UNIVERSITY OF SOUTHAMPTON

FACULTY OF NATURAL AND ENVIRONMENTAL SCIENCES

School of Chemistry

Studies of Oxygen Electrochemistry on Spinel Oxides

by

Turgut Sönmez

Thesis for the degree of Doctor of Philosophy

June 2017

UNIVERSITY OF SOUTHAMPTON

ABSTRACT

FACULTY OF NATURAL AND ENVIRONMENTAL SCIENCES

Chemistry

Thesis for the degree of Doctor of Philosophy

Studies of Oxygen Electrochemistry on Spinel Oxides

Turgut Sönmez

Electrochemical studies of the spinels, Co_3O_4 and $NiCo_2O_4$, in alkaline media were conducted and show that the products and the oxygen reduction mechanisms vary. The $4e^-$ reduction strongly predominates at $NiCo_2O_4$, a substantial amount of the $2e^-$ reduction product (H_2O_2), 43%, is formed at the cobalt spinel. $NiCo_2O_4$ is a significantly better catalyst than Co_3O_4 in terms of both the overpotential for reduction and its limiting current density. The differences come from the enhanced rate of O – O bond cleavage early in the reduction sequence at the mixed spinel.

Based on the full physical, spectroscopic and electrochemical studies of a wide range of Mn content ($Mn_xCo_{3-x}O_4$, $0.0 \leq x \leq 2.0$) in spinel cobalt oxide, the phase transition (from cubic to tetragonal), particle size, surface area, crystallinity and electrochemical activities towards the ORR can be tuned with Mn content in spinel cobalt oxide. The Mn ions are in oxidation state +3 and they have tendency to occupy tetrahedral sites rather than octahedral sites in the spinels. In terms of the highest limiting current and lowest onset potential for oxygen reduction, cubic phase $MnCo_2O_4$ ($x = 1.0$) possesses the highest catalytic activity amongst Mn doped spinels and follows the $4e^-$ reduction mechanism with early cleavage of the O – O bond.

Three different synthesis methods for $MnCo_2O_4$ (co-precipitation, thermal decomposition and hydrothermal method) and the influence of conditions within hydrothermal method were investigated. The preparation conditions and methods were found to affect the morphology, phase, crystallinity, and ORR activity of the catalyst. Co-precipitation produced the catalyst with the highest surface area, smallest particle size, highest crystallinity and the highest ORR activity.

Table of Contents

DECLARATION OF AUTHORSHIP

I, Turgut Sönmez, declare that this thesis and the work presented in it are my own and has been generated by me as the result of my own original research.

Studies of Oxygen Electrochemistry on Spinel Oxides

I confirm that:

1. This work was done wholly or mainly while in candidature for a research degree at this University;
2. Where any part of this thesis has previously been submitted for a degree or any other qualification at this University or any other institution, this has been clearly stated;
3. Where I have consulted the published work of others, this is always clearly attributed;
4. Where I have quoted from the work of others, the source is always given. With the exception of such quotations, this thesis is entirely my own work;
5. I have acknowledged all main sources of help;
6. Where the thesis is based on work done by myself jointly with others, I have made clear exactly what was done by others and what I have contributed myself;
7. Parts of this work have been published as:
    1. T. Sönmez, S. J. Thompson, S. W. Price, D. Pletcher and A. E. Russell, *J. Electrochem. Soc.*, 2016, **163**, H884-H890.
    2. D. Pletcher, X. Li, S. W. Price, A. E. Russell, T. Sönmez and S. J. Thompson, *Electrochim. Acta*, 2016, **188**, 286-293.

Signed: .....

Date: .....

Acknowledgements

First of all, I would like to express my sincere gratitude to my supervisor Professor Andrea E. Russell for her ongoing support, guidance, encouragement and enthusiasm during the journey of this PhD. Without her advice and continuous support, this PhD would not have been achievable.

Professor Derek Pletcher is owed a special thank you for his valuable advice and useful discussions during any problem I have faced in electrochemistry. I have gained lots of experience from his immense knowledge in science as well as life. I would like to thank my advisor Assoc. Professor Guy Denuault for his valuable comments and help whenever I needed. Further, I would like to acknowledge Professor Andrew L. Hector for research discussions, teaching and helping me for XRD data analysis. I would also like to thank Dr Laura Calvillo from University of Padova, Italy for obtaining XPS measurements and Ms Lucia Lupica-Spagnolo for helping me with TGA analysis. Another big thanks goes to Dr Veronica Celorrio for her help during XANES measurements and her comments on data analysis.

My sincere thanks also goes to the past and current group members Danai P., David I., Alex K., Andy S. L., Haoliang H., Alex P., Penny W., Sandra M., Waldemir, Abu B. N., Mike P. and Scott G. for being there whenever I need any help and especially Stephen T. for helping me to do first electrochemical experiments and his insightful comments. I would also like to thank all my friends in 6th floor Hisham, Marta, Gabriella, David, Anna, Saiful and Firas. Without group members and friends, this PhD journey would not have been this enjoyable.

I thank all the support staff at University of Southampton; especially Alistair, Sally, Ann and people in the glass blowing workshop, the mechanical workshop and store.

I would also like to thank my undergraduate supervisor Prof Gulfeza Kardas as without the encouragement, I would not have continued my studies further.

Last but not the least, my most special thanks goes to my departed mom, Muhteber, my dad, Izzettin, my sisters and brothers for always being there and supporting me materially and spiritually. Thank you.

Chapter 1: Introduction

The rapid growth in energy demand, the depletion of fossil fuels, and the concern about climate change due to the emission of large amounts of carbon dioxide and other adverse gases from the combustion of fossil fuels in the atmosphere have become highly important in recent years. Therefore, renewable energy sources such as wind and solar have drawn attention since they are environmentally friendly. However, these clean energy sources are intermittent and limited by geographical and seasonal features.[1, 2] Energy conversion and storage systems (such as fuel cells, water electrolysers, and batteries) could play critical roles for effective utilisation of renewable energy sources. The feasibility of these energy conversion and storage systems depends on electrocatalysts, as critical components in these systems. Therefore, the discovery of efficient, stable and cost effective catalysts for use in the aforementioned systems is a major scientific research area.[3]

Both the oxygen reduction reaction (ORR) and oxygen evolution reaction (OER) are important and the central to the efficiencies of fuel cells, water electrolysers, and metal-air batteries.[3] Precious metal electrocatalysts such as Pt, IrO_2, and RuO_2 have been used in these systems. However, their high cost and low abundancy are bottlenecks for the practical use of such precious metal electrocatalysts.[4] The best known ORR catalysts are Pt or alloys of Pt. In contrast, Pt shows only moderate activity for the OER due to the formation of insulating platinum oxides.[4, 5] IrO_2 and RuO_2 have shown the best catalytic activity for the OER, however, they are not very active for the ORR.[5] Additionally, RuO_2 is not stable at high potentials due to the formation of soluble ruthenium oxides with a higher oxidation state. IrO_2 is known as the most active and stable OER catalyst so far.[4] The fabrication of highly active, stable, abundant and low-cost non-precious bifunctional catalysts is therefore of great interest.

Transition metal oxides (such as perovskites, pyrochlore and spinels) have shown reasonable activity for both the ORR and OER processes at neutral and alkaline conditions.[3, 6] The advantages of alkali over acid are as follows: *I)* the ORR is more facile and a much broader range of materials (non-precious metals) are more stable in alkaline than acid.[7-9] *II)* Alkaline media inhibits metal or metal oxide corrosion.[10]

The development of highly active catalysts is slowed by the shortage of fundamental understanding of both the mechanism of the oxygen reduction reaction and the properties of the catalyst that govern the catalytic activity.[3] In this thesis, spinel type metal oxides (Co, Ni

and Mn based) have been investigated in alkaline media in order to understand the mechanism of the oxygen reduction reaction and structural properties of materials, which play key role in the ORR mechanism. Spinels as oxygen electrodes have applications in fuel cells, water electrolysers and metal-air batteries, which are briefly explained in the next section. The ORR, OER and in general spinel structure will be discussed in the rest of this chapter.

1.1. Applications of ORR and OER

Spinel metal oxides can potentially be applied in energy storage and conversion systems (fuel cells, water electrolysers and metal-air batteries). A fuel cell is an electrochemical device where the chemical energy of fuel is directly converted to electrical energy. Fuel cells have a lower environmental effect since there is no fuel combustion in fuel cells.[11-15] H_2, methanol, ethanol etc. act as fuels and O_2 reduction occurs at cathode. Electricity, water and heat are produced.[11] It is highly possible to use the electricity and heat produced from fuel cell simultaneously and this is called co-generation.[16] More details about fuel cells may be found in the literature.[14, 16, 17]

A water electrolyser transfers electrical energy into chemical energy in the form of hydrogen and oxygen.[18] If the electrical energy comes from renewable energy sources then this is truly green technology.[19] In the water electrolysis process, an electrical current passes through anode and cathode electrodes to split water into hydrogen and oxygen.[18] This process has been known for around 200 years even though it only represents 4% of hydrogen production in the world.[20] The rest of hydrogen production is produced from fossil fuel feedstock using high temperature, gas phase reactions.[19] Ultra high purity hydrogen (> 99.9%) can be only produced via water electrolysis since oxygen is the only impurity.[19, 21, 22] The cathodic hydrogen evolution reaction (HER) and anodic oxygen evolution reaction (OER) are the half-cell reactions in water electrolysers and it is considered that OER is the major contributor to the overpotential.[1, 23]

Metal-air batteries are unique compared to traditional batteries since oxygen, the electroactive cathode material, is not required to be stored in the battery as it can be accessed from the environment.[24, 25] Metal-air batteries have similarities to conventional fuel cells, in which oxygen is continuously supplied to their porous cathode electrodes from the surrounding air. However, they also have similarities to the traditional batteries since the negative electrode is a metal.[26] Much higher theoretical energy densities (2-10 fold) can be

easily obtained with metal-air batteries compared to those of lithium-ion batteries since the cathode active material (oxygen) is not stored.[26-28] Zinc-air, to name but one example, is made of two electrodes (a negative zinc electrode and a positive air electrode) and typically uses alkaline media.[26] In the battery discharge process, Zn is oxidised to soluble zincate ions ($Zn(OH)_4^{2-}$) in the aqueous electrolyte. Then, insoluble zinc oxide (ZnO) can be formed from the decomposition of zincate ions. At the air electrode, oxygen from the atmosphere penetrates through the porous gas diffusion electrode and oxygen is reduced at the air electrode catalyst in contact with the liquid electrolyte. The anodic and cathodic reactions during discharge process in zinc-air batteries are shown below.[26, 29]

Negative electrode: $Zn + 4OH^- \rightarrow Zn(OH)_4^{2-} + 2e^-$ (**1.1**)

Positive electrode: $O_2 + 4e^- + 2H_2O \rightarrow 4OH^-$ (**1.2**)

Overall reaction: $2Zn + O_2 + 4OH^- + 2H_2O \rightarrow 2Zn(OH)_4^{2-}$ (**1.3**)

1.2. Oxygen Reduction Reaction (ORR)

Due to the importance and ongoing challenges of the oxygen reduction reaction (ORR) for fuel cells and metal air-batteries, cathodic oxygen reduction is one of the most investigated electrochemical reactions in recent decades.[30, 31] The ORR mechanism is quite complicated and many intermediates are involved in the process.[32] It is clearly a multistep mechanism and both the reaction overpotential and products strongly depend on the cathode material. The oxygen reduction pathway in alkaline media is illustrated in **Figure 1.1**.

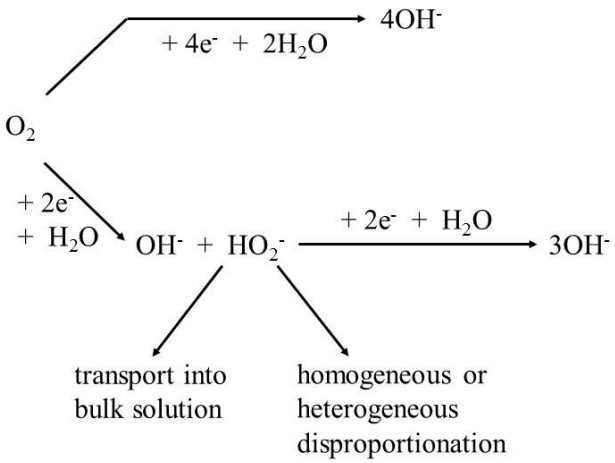

Figure 1.1. Pathways for cathodic O_2 reduction in aqueous alkaline media, based on references [33] and [34].

The direct $4e^-$ reduction pathway is predicted to result from mechanisms where the O – O bond cleavage occurs in the early stage of the reaction sequence. On the other hand, alternative pathways involve $2e^-$ reduction steps with hydrogen peroxide formation. Hydrogen peroxide can stay in the electrolyte as a final product or as an intermediate further reduced or undergoing chemical disproportionation. The cathode and reaction conditions strongly effect the rate of the further hydrogen peroxide reduction and chemical decomposition. It is highly preferred that oxygen undergoes the full $4e^-$ reduction for fuel cells or batteries due to the following reasons:[35]

- ***I)*** The equilibrium potential of the O_2/H_2O couple is positive to that for the O_2/H_2O_2 couple leading to a higher battery voltage.
- ***II)*** The current density at any potential is twice as large.
- ***III)*** The energy storage capability/mole of oxygen is double.

However, the observation of the direct $4e^-$ reduction alone does not distinguish two reaction pathways direct $4e^-$ reduction and the $2x2e^-$ reduction where the second $2e^-$ reduction of H_2O_2 is rapid.[35]

More detail mechanisms of the ORR in alkaline media have been proposed by Cheng et al.[36] as shown in **Figure 1.2**.

a)

b) $M + O_2 \rightarrow M\text{---}O_2$ (adsorption)

$M\text{---}O_2 + e^- + H_2O \rightarrow M\text{---}HO_2 + OH^-$

$M\text{---}HO_2 + e^- \rightarrow M + HO_2^-$

c) $M + O_2 \rightarrow M\text{---}O_2$ (adsorption)

$M\text{---}O_2 + 2e^- + 2H_2O \rightarrow M\text{---}2OH + 2OH^-$

$M\text{---}2OH + 2e^- \rightarrow M + 2OH^-$

d) $M^{m+}\text{—}O^{2-} + H_2O + e^- \rightarrow M^{(m-1)+}\text{—}OH^- + OH^-$

$O_2 + e^- \rightarrow O_2^-$ (ads.)

$M^{(m-1)+}\text{—}OH^- + O_2^-$ (ads.) $\rightarrow M^{m+}\text{—}O\text{—}O^{2-} + OH^-$

$M^{m+}\text{—}O\text{—}O^{2-} + H_2O + e^- \rightarrow M^{(m-1)+}\text{—}O\text{—}OH^- + OH^-$

$M^{(m-1)+}\text{—}O\text{—}OH^- + e^- \rightarrow M^{m+}\text{—}O^{2-} + OH^-$

Figure 1.2. a) Different configurations of O_2 adsorption on catalyst surfaces: on top end-on, bridge end-on, bridge side-on one site, and bridge side-on two sites, from left to right. The blue atom represents oxygen while brown and yellow are catalytic atom 1 and atom 2 (normally metal), respectively. Mechanisms suggested for the ORR on metal surfaces in the case of **b)** end-on O_2 adsorption, and **c)** bidentate O_2 adsorption, corresponding to the $2e^-$ reduction (with generated peroxide species) and the direct $4e^-$ reduction, respectively. **d)** One of the proposed catalytic ORR pathways at a metal oxide/alkaline electrolyte interface. **Figure 1.2** is based on the figure from "Chem. Soc. Rev., 2012, **41**, 2172-2192" with the author's permission.[36]

Because the mechanism of ORR can involve adsorbed O species, the mechanism and kinetics of the ORR are very surface sensitive. Several adsorption geometries have been proposed[36] as shown in **Figure 1.2.a**. With each geometry, the reduction involves multiple steps (for $4e^-$ reduction, $4e^-$ steps and 4 protonations) and it is difficult to identify precise pathways. Cheng et al.[36] suggest mechanisms for each O adsorption geometry, see **Figure 1.2.b – 1.2.d**. Other mechanisms have been suggested, see reference[37]. The end-on way supports mainly $2e^-$ pathway (see **Figure 1.2.b**) since only one O atom is coordinated vertically to the active site and one electron transfer to oxygen is happened. On the other hand, horizontally coordinated two oxygen atoms adsorbing on the active sites support O_2 dissociation[36] (the ability of O_2 to adsorb in a way to catalyse O – O cleavage clearly depends on the nature and separation of atoms within the surface. It is often suggested that O – O cleavage occurs simultaneously with M – O bond formation) and this is most likely cause to direct $4e^-$ pathway (see **Figure 1.2.c**). Even though there is not an exact idea about how $4e^-$ oxygen reduction reaction mechanism works, **Figure 1.2.d** shows a proposed four-step catalytic mechanism at the transition metal-oxides' surfaces.[36]

As mentioned earlier, Pt and alloys of Pt are known as the most active and favourable catalysts for ORR process. However, the weak durability, rare abundancy in the Earth's crust and high cost of Pt make it hard to be used in a wide applications of aforementioned systems.[38, 39] Therefore, non-noble metal oxides[38-42], metal free nitrogen doped carbon materials[43, 44], nitrogen coordinated metal on carbon matrices[45] and non-precious metal oxides on nitrogen-doped graphene[46] alternatives to noble metals for ORR have been widely studied in order to overcome these bottlenecks. The ORR mechanism on spinel type non precious metal oxides will be investigated in details in **Chapter 3, 4** and **5**.

1.3. Oxygen Evolution

The large anodic overpotential of the oxygen evolution reaction (OER) limits the practical efficiency of water electrolysis. Anodes of RuO_2 and IrO_2 demonstrate the lowest OER overpotentials at a practical current density.[47] However, the high cost and abundancy of these precious-metal electrocatalysts as well as instability of RuO_2 at high potentials[5] make them unfavourable OER catalysts. From non-precious metal oxides, cobalt and nickel oxides (Co_3O_4, $NiCo_2O_4$) have been widely studied for decades since they are highly stable and efficient in alkaline media for OER.[4] The OER mechanism on perovskites (ABO_3)[48] and spinels (AB_2O_4)[49] have been widely studied and some possible OER mechanisms have been

proposed on the basis of electrochemical parameters such as reaction orders and Tafel slopes.[50-53] It is also highly important to point out that the nature of the active sites on the electrocatalysts play a role for the oxygen evolution. That is, the oxygen evolution process happens on a species with a high oxidation state.[51] Highly oxidised $Co^{+3/+4}$ and $Ni^{+3/+4}$ couples are known as the active OER centres.[4, 8, 52]

1.4. Spinel Structure

Spinel type transitional metal oxides (AB_2O_4, A, B = metals) have a structure where A^{+2} and B^{+3} cations occupy the tetrahedral and octahedral sites, respectively, of a distorted face-center cubic (fcc) oxygen sublattice.[39, 49] One cubic unit cell consists of 8 AB_2O_4 formal units, therefore it shows $A_8B_{16}O_{32}$.[54]

1.4.1. Co_3O_4

Cobalt oxides can be classified to three well-defined oxides, which are CoO (cubic), Co_2O_3 (hexagonal) and Co_3O_4 (normal spinel structure, space group $Fd\bar{3}m$).[55, 56] The cationic distribution in the stoichiometric spinel Co_3O_4 is $Co^{+2}[2Co^{+3}]O_4^{-2}$ and **Figure 1.3** illustrates the unit cell of spinel Co_3O_4, where 8 Co^{+2} ions ($3d^7$) occupy the tetrahedral A sites while the octahedral B sites are occupied by 16 Co^{+3} ions ($3d^6$) in the lattice.[55, 57-59]

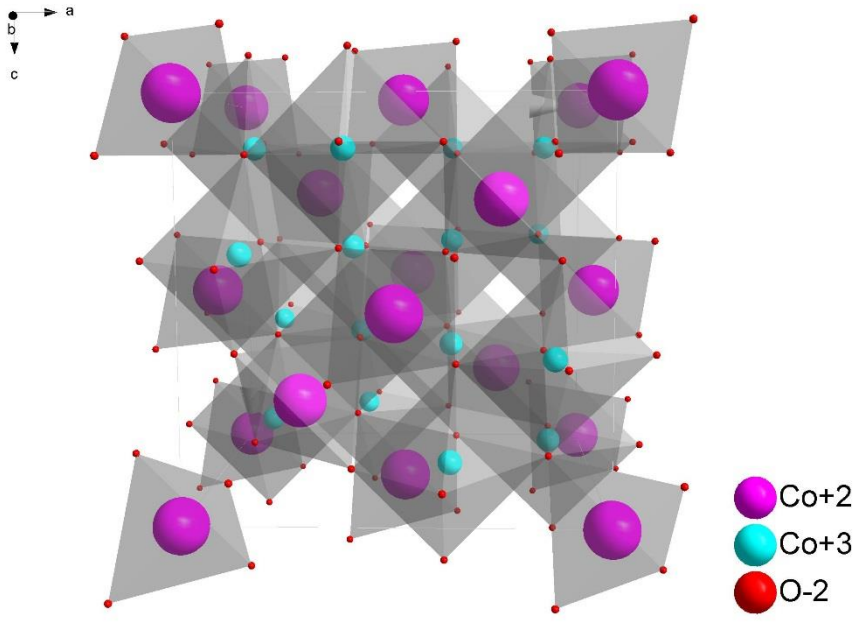

Figure 1.3. The unit cell of Co_3O_4.

Spinel Co_3O_4 is a p-type semiconductor with a poor electronic conductivity due to the impossibility of electronic transfer between Co^{+2} ions (in tetrahedral sites) and Co^{+3} ions (in octahedral sites).[56, 60] The electronic transfer takes place only between Co^{+3} ions in octahedral sites since there is no stabilization for Co^{+3} ions in tetrahedral sites.[56] It has been proposed that while changing a metal in the octahedral (B) sites of Co_3O_4, the ORR activity is increased since the cations placed in B sites have a critical role assisting O_2 chemisorption via their cationic d-orbitals.[59, 61]

A wide range of metal cations (Ni, Mn, Cu, Li etc.) with different oxidation states can be accommodated in a spinel Co_3O_4 and the metal ions substitution can change the cationic distribution, increase the electrochemical activity, electrical conductivity, as well as stability.[38, 56, 62] **Table 1.1** presents some recent studies of spinel cobalt based samples, precursors, preparation methods, electrochemical activities for ORR/OER in alkaline media and related references. It has been shown that[31, 35, 63] mixed metal oxides show much superior catalytic activity than that single metal oxide for ORR[64] since mixed metal oxides show good electrical conductivities through electron hopping process, which results in an increase in the electrocatalytic activities.[61, 64] Ternary $NiCo_2O_4$, to name but one example, has much higher ORR and OER activities in alkaline media compared to binary Co_3O_4 due to its better electrical conductivity and higher electrochemical activity, which is attributed to Ni ions substitution for Co in Co_3O_4.[35, 62, 65] In a similar way, ternary $CoMn_2O_4$ and $MnCo_2O_4$ possess much higher catalytic activity as well as stability in alkaline media compared to binary Co_3O_4 because of Mn incorporation into spinel Co_3O_4.[62] Co, Ni and Mn based spinel oxides can be produced via different synthesis methods as well as with different ratio of metal cations in the lattice (see **Table 1.1**).

Oxides	Precursor(s)	Preparation Method	Electrochemical Activity (ORR/OER)	References
Co_3O_4	Nitrate	Precipitation, Solution Combustion, Hard Template	OER	[66]
Co_3O_4	Chloride	The Solvent-Mediated Method	ORR	[59]
Co_3O_4	Sulphate	Chemical Synthesis + Post Calcination	ORR/OER	[67]
Co_3O_4	Acetate	Hydrothermal	ORR/OER	[68]
Co_3O_4/ $NiCo_2O_4$	Nitrates	Thermal Decomposition (two-step strategy)	OER	[69]
$NiCo_2O_4$	Nitrates	Thermal Decomposition / Electrophoretic Deposition/ Alloy Oxidation	OER	[70]
$NiCo_2O_4$	Nitrates	Co-precipitation + Post Calcination	ORR/OER	[71]
$NiCo_2O_4$	Nitrates	Hard Template	ORR/OER	[72]
$NiCo_2O_4$	Nitrates	Thermal Decomposition	ORR	[73]
$Ni_{1.5}Co_{1.5}O_4$	Sulphates	Electrodeposition with Anodization	OER	[74]
$CoMn_2O_4$	Acetates	Co-precipitation	ORR	[39]
$MnCo_2O_4$	Nitrates	Hydrothermal + Post Calcination	ORR/OER	[75]
$MnCo_2O_{4.5}$	Chlorides	A Facile Two-Step Approach	ORR	[62]
$Mn_xCo_{3-x}O_4$	Acetates	Sonochemical Reaction Method	ORR	[64]
$CoMn_2O_4$ & $MnCo_2O_4$	Carbonates	Thermal Decomposition	ORR/OER	[76]
$Mn_xCo_{3-x}O_4$	Nitrates	Hydrothermal + Post Calcination	ORR	[77]

Table 1.1. Literature survey of some recent studies of spinel metal oxides, their precursors, preparation method, electrochemical activities for ORR/OER and related references.

1.4.2. $NiCo_2O_4$

As previously mentioned, spinel cobalt oxide is a semiconductor and it has low electronic conductivity. Therefore, doping Ni into spinel Co_3O_4 not only increases the surface area and roughness of material but also increases the electronic conductivity of Co_3O_4 by up to five orders of magnitude.[71, 78, 79] It has been suggested by Windisch et al.[79] that the electrical conductivity properties of Co-Ni oxide, at least partly, depend on the structure and the composition on the octahedral sites in the spinel. Based on the results from Powder X-ray Diffraction (XRD), X-ray Absorption Spectroscopy (EXAFS and XANES)

and X-ray Photoemission Spectroscopy (XPS) in the literature, the cationic distribution of $NiCo_2O_4$ has been proposed.[80] The results from the literature[80, 81] show that Ni ions are located on the octahedral sites in the spinel structure. Even though Ni ions with different oxidation states (Ni^{+2} and Ni^{+3}) occupy octahedral sites, the ratio of Ni^{+2} and Ni^{+3} can vary in the exact cationic distribution of the bulk since the exact cationic distribution of the bulk highly depends on the preparation procedure.[80] $[Co^{+2}][Ni^{+3}Co^{+3}]$ ([82]), $[Co^{+2}_{0.8}Co^{+3}_{0.2}][Ni^{+2}_{0.2}Ni^{+3}_{0.8}Co^{+3}]$ ([81]), $[Co^{+2}_{0.65}Co^{+3}_{0.35}][Ni^{+2}_{0.37}Ni^{+3}_{0.61}Co^{+3}]$, $[Co^{+2}_{0.81}Co^{+3}_{0.19}][Ni^{+2}_{0.24}Ni^{+3}_{0.75}Co^{+3}]$, and $[Co^{+2}_{0.96}Co^{+3}_{0.04}][Ni^{+2}_{0.14}Ni^{+3}_{0.85}Co^{+3}]$ ([80]) are some of the proposed cationic distributions for $NiCo_2O_4$ in the literature.

1.4.3. $Mn_xCo_{3-x}O_4$ ($0.0 \leq x \leq 2.0$)

The electrochemical activity of Mn doped spinels are higher than pure cobalt oxide in alkaline media, which is not only from increased electrical conductivity but also from the Mn^{+3}/Mn^{+4} species considerable to be more active ORR sites than Co species in the lattice.[62] Two phases (cubic and tetragonal) are formed while Mn is incorporated into Co_3O_4, which depends on the atomic ratio of Mn in the lattice.[83] A single stable phase of cubic spinel is the only formed phase at 1000 ^oC when the range of solid solution of manganese is between $0.0 \leq x \leq 1.3$. While both cubic and tetragonal phases exist in the ratio of $1.3 \leq x \leq 1.9$, there is only tetragonal phase when $x > 1.9$.[63, 84] Cubic spinel ($x = 1.8$) may be possible to observe at high temperature (700 ^oC) and the phase transition from cubic to tetragonal can be obtained when the materials are quenched from 700 ^oC since the cubic phase is not stable at low temperature.[84-86] **Figure 1.4** shows the cubic phase (space group $Fd\bar{3}m$) and tetragonal phase (space group $I41/amd$) of Co_3O_4 ($x = 0$) and Mn_2CoO_4 ($x = 2.0$), respectively.

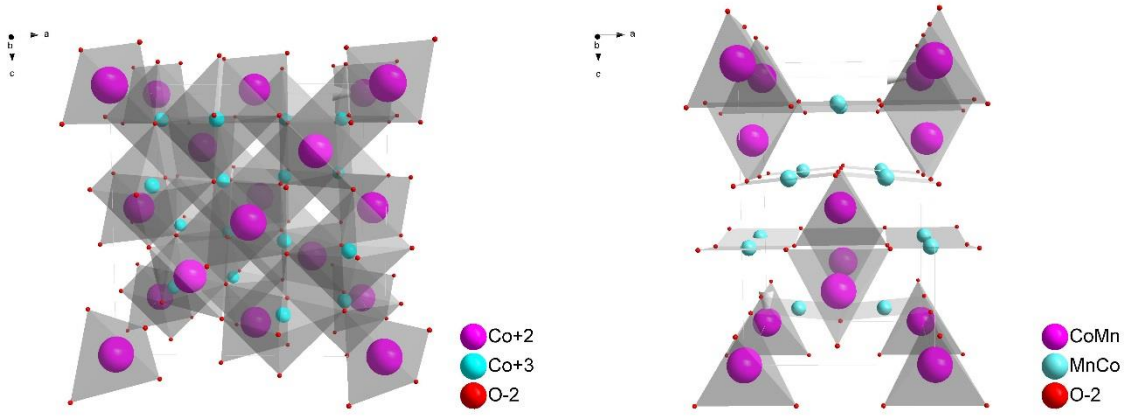

Figure 1.4. Schematic representation of cubic Co_3O_4 (**left**) and tetragonal Mn_2CoO_4 (**right**) spinels. Cations and anions are as shown in the figure.

According to Wickham et al.[83], when more than a critical fraction (60-65 %) of the octahedral sites are occupied by Mn^{+3} cations, tetragonal distortion from cubic symmetry is shown. This has been pointed out by Bordeneuve et al. as well.[87] This lattice distortion is theoretically caused by Jahn-Teller effect of Mn^{+3} ($3d^4$) in octahedral sites. Jahn-Teller effect would be dominant when Mn^{+3} cations exceed the critical fraction and the spinels could not have cubic phase anymore.[84] Therefore, it is doable but it remains a big challenge to produce Mn/Co spinels with desired atomic ratio and controlled phase in the spinel structure especially with a wider composition range, which has a critical importance for structure sensitive applications.[84]

As reported in details by Restovic et al[61]., many cationic distributions have been proposed for Mn doped spinel Co_3O_4 and the variations in cationic distributions are based on different preparations methods and calcination temperature. Therefore, there could be different cationic distributions for the same composition prepared in different conditions.

The reason that spinel type cobalt-based oxides have been studied in this thesis is that the mixed valence oxides with spinel structure are a highly important class of non precious metal oxides, which show high catalytic activity as well as stability in alkaline media for the ORR and OER.[73] Due to the advantages of their low cost, environmental friendliness, easy synthesis, high activity and stability, cobalt based spinel type metal oxides have been taking a great interest.[73] In particular, Ni and Mn metal cations in the spinel Co_3O_4 are highly active and stable metal oxides. Therefore, it is crucial to understand the structural properties of these materials with varying metal cations incorporation, wide atomic ratios, and the change

in the phase with increased content ratio, the synthesis methods and conditions within the same preparation method, which greatly effect the oxygen reduction pathway in these systems.

Physical and spectroscopic characterisation techniques such as Powder X-ray Diffraction (XRD), Brunauer-Emmet-Teller (BET), Raman Spectroscopy, Scanning Electron Microscopy and Energy Dispersive X-ray (SEM-EDX), Transmission Electron Microscopy (TEM), X-ray Photoemission Spectroscopy (XPS), Thermogravimetric Analysis (TGA) and X-ray Absorption Spectroscopy (XAS) are mainly used for the structural characterisation of transition metal oxides. Rotating Disc Electrode (RDE) and Rotating Ring Disc Electrode are electrochemical characterisation techniques, which are commonly used especially for mechanistic studies at spinels. All of these physical, spectroscopic and electrochemical characterisation techniques mentioned above were employed in this thesis.

1.5. Thesis Outline

The work reported in this thesis is made of a series of chapters as shown below.

Chapter 2: Information about all physical, spectroscopic and electrochemical characterisation methods used in this project are mentioned. The physical and spectroscopic methods allow us to characterise the structural features of spinels and the results obtained from them are correlated with the results collected from electrochemical methods in order to have a full understanding about how and why electrochemical activities and oxygen reduction mechanism pathways are different at each material. This chapter also includes information about reagent materials, instrumentation, some error and testing calculation related to electrochemical studies.

Chapter 3: This chapter investigates the bifunctional properties of spinel type oxides (Co_3O_4 and $NiCo_2O_4$) and compares the oxygen reduction reaction mechanisms on these materials under similar conditions. Although both spinels demonstrate the catalytic activity towards oxygen reduction and evolution, the catalytic activity for both the ORR and OER at $NiCo_2O_4$ is much higher than that at Co_3O_4. The results also show that oxygen reduction mechanism pathways are quite different at both spinels. The results obtained for this part of PhD formed the basis of two published papers.[35, 65]

Chapter 4: Chapter 4 focusses on the effect of manganese as a dopant into the spinel Co_3O_4 with a much wider dopant ratios ($Mn_xCo_{3-x}O_4$ ($0.0 \leq x \leq 2.0$)). Co_3O_4 and $MnCo_2O_4$ have

been widely studied in the literature but the intermediate compositions and phase transitions (from cubic to tetragonal phase) were not studied in detail. In this chapter, full physical and electrochemical characterisations are carried out. The same results are obtained with two different preparation methods (thermal decomposition and co-precipitation). Desired atomic ratios (Co:Mn) are confirmed with XPS studies. Ex-situ X-ray Absorption Spectroscopy (XAS) measurements are used to determine the oxidation states of Co and Mn species in the bulk. Based on XPS, ex-situ XAS and fit statistics from XRD data, the cationic distribution of all spinels are proposed. The oxygen reduction mechanism pathways are deeply investigated at pure spinel Co_3O_4 and Mn doped spinel Co_3O_4 samples.

Chapter 5: The final part of this thesis is to compare the effect of preparation conditions within the same preparation method and three different synthesis methods (co-precipitation, thermal decomposition, and a hydrothermal method) towards oxygen reduction activity at $MnCo_2O_4$ since using different conditions within a single method and different preparation routes show important variations in the rate of oxygen reduction in alkaline media. This chapter also includes full physical, spectroscopic and electrochemical characterisation of spinel $MnCo_2O_4$ samples.

Chapter 6: The conclusion chapter highlights the concluding remarks from **Chapter 3**, **4** and **5**.

1.6. References

1. X. Li, X. Hao, A. Abudula and G. Guan, *J. Mater. Chem. A*, 2016, **4**, 11973-12000.
2. A. Z. Weber, M. M. Mench, J. P. Meyers, P. N. Ross, J. T. Gostick and Q. Liu, *J. Appl. Electrochem.*, 2011, **41**, 1137.
3. J. Suntivich, H. A. Gasteiger, N. Yabuuchi, H. Nakanishi, J. B. Goodenough and Y. Shao-Horn, *Nat. Chem.*, 2011, **3**, 647-647.
4. T. Maiyalagan, K. A. Jarvis, S. Therese, P. J. Ferreira and A. Manthiram, *Nat. Commun.*, 2014, **5**.
5. Y. Gorlin and T. F. Jaramillo, *J. Am. Chem. Soc.*, 2010, **132**, 13612-13614.
6. L. Jorissen, *J. Power Sources*, 2006, **155**, 23-32.
7. Y. Liang, H. Wang, J. Zhou, Y. Li, J. Wang, T. Regier and H. Dai, *J. Am. Chem. Soc.*, 2012, **134**, 3517-3523.
8. M. Hamdani, R. N. Singh and P. Chartier, *Int. J. Electrochem. Sci.*, 2010, **5**, 556-577.

9. P. Cox and D. Pletcher, *J. Appl. Electrochem.*, 1990, **20**, 549-554.
10. A. J. Esswein, M. J. McMurdo, P. N. Ross, A. T. Bell and T. D. Tilley, *J. Phys. Chem. C*, 2009, **113**, 15068-15072.
11. S. J. Peighambardoust, S. Rowshanzamir and M. Amjadi, *Int. J. Hydrog. Energy*, 2010, **35**, 9349-9384.
12. Z. P. Shao and S. M. Haile, *Nature*, 2004, **431**, 170-173.
13. U. Lucia, *Renew. Sust. Energ. Rev.*, 2014, **30**, 164-169.
14. Y. Wang, K. S. Chen, J. Mishler, S. C. Cho and X. C. Adroher, *Appl. Energy*, 2011, **88**, 981-1007.
15. E. Gülzow, *J. Power Sources*, 1996, **61**, 99-104.
16. L. Carrette, K. A. Friedrich and U. Stimming, *ChemPhysChem*, 2000, **1**, 162-193.
17. L. Carrette, K. A. Friedrich and U. Stimming, *Fuel Cells*, 2001, **1**, 5-39.
18. J. D. Holladay, J. Hu, D. L. King and Y. Wang, *Catal. Today*, 2009, **139**, 244-260.
19. D. Pletcher and X. H. Li, *Int. J. Hydrog. Energy*, 2011, **36**, 15089-15104.
20. K. Zeng and D. K. Zhang, *Prog. Energy Combust. Sci.*, 2010, **36**, 307-326.
21. E. Varkaraki, N. Lymberopoulos, E. Zoulias, D. Guichardot and G. Poli, *Int. J. Hydrog. Energy*, 2007, **32**, 1589-1596.
22. J. Turner, G. Sverdrup, M. K. Mann, P. C. Maness, B. Kroposki, M. Ghirardi, R. J. Evans and D. Blake, *Int. J. Energy Res.*, 2008, **32**, 379-407.
23. X. Wu and K. Scott, *Int. J. Hydrog. Energy*, 2013, **38**, 3123-3129.
24. K. F. Blurton and A. F. Sammells, *J. Power Sources*, 1979, **4**, 263-279.
25. K. M. Abraham and Z. Jiang, *J. Electrochem. Soc.*, 1996, **143**, 1-5.
26. Y. G. Li and H. J. Dai, *Chem. Soc. Rev.*, 2014, **43**, 5257-5275.
27. A. Kraytsberg and Y. Ein-Eli, *J. Power Sources*, 2011, **196**, 886-893.
28. D. Capsoni, M. Bini, S. Ferrari, E. Quartarone and P. Mustarelli, *J. Power Sources*, 2012, **220**, 253-263.
29. P. Pei, K. Wang and Z. Ma, *Appl. Energy*, 2014, **128**, 315-324.
30. N. A. Anastasijevic, V. Vesovic and R. R. Adzic, *J. Electroanal. Chem.*, 1987, **229**, 305-316.
31. Y. Liang, H. Wang, J. Zhou, Y. Li, J. Wang, T. Regier and H. Dai, *J. Am. Chem. Soc.*, 2012, **134**, 3517-3523.
32. C. Song and J. Zhang, in *PEM fuel cell electrocatalysts and catalyst layers*, Springer, 2008, pp. 89-134.

33. M. Tarasevich, A. Sadkowski and E. Yeager, in *Comprehensive treatise of electrochemistry*, Springer, 1983, pp. 301-398.
34. V. Bagotsky, M. Tarasevich and V. Y. Felinovskii, *Soviet Electrochem.*, 1969, **5**, 1158.
35. T. Sönmez, S. J. Thompson, S. W. Price, D. Pletcher and A. E. Russell, *J. Electrochem. Soc.*, 2016, **163**, H884-H890.
36. F. Cheng and J. Chen, *Chem. Soc. Rev.*, 2012, **41**, 2172-2192.
37. K. Kinoshita, *Electrochemical oxygen technology*, John Wiley & Sons, 1992.
38. R. J. Toh, A. Y. S. Eng, Z. Sofer, D. Sedmidubsky and M. Pumera, *Chemelectrochem*, 2015, **2**, 982-987.
39. Y. Liu, Y. Wang, X. Xu, P. Sun and T. Chen, *RSC Adv.*, 2014, **4**, 4727-4731.
40. H. Liu, X. Zhu, M. Li, Q. Tang, G. Sun and W. Yang, *Electrochim. Acta*, 2014, **144**, 31-41.
41. L. Mao, T. Sotomura, K. Nakatsu, N. Koshiba, D. Zhang and T. Ohsaka, *J. Electrochem. Soc.*, 2002, **149**, A504-A507.
42. J. Valencia, N. Arias, O. Giraldo and A. Rosales-Rivera, *Phys. B*, 2012, **407**, 3155-3157.
43. K. P. Gong, F. Du, Z. H. Xia, M. Durstock and L. M. Dai, *Science*, 2009, **323**, 760-764.
44. R. L. Liu, D. Q. Wu, X. L. Feng and K. Mullen, *Angew. Chem.-Int. Edit.*, 2010, **49**, 2565-2569.
45. M. Hui, F. Jaouen, E. Proietti, M. Lefevre and J. P. Dodelet, *Electrochem. Commun.*, 2009, **11**, 1986-1989.
46. M. Prabu, P. Ramakrishnan and S. Shanmugam, *Electrochem. Commun.*, 2014, **41**, 59-63.
47. M. E. G. Lyons and S. Floquet, *Phys. Chem. Chem. Phys.*, 2011, **13**, 5314-5335.
48. B. Han, M. Risch, Y.-L. Lee, C. Ling, H. Jia and Y. Shao-Horn, *Phys. Chem. Chem. Phys.*, 2015, **17**, 22576-22580.
49. F. Y. Cheng, J. A. Shen, B. Peng, Y. D. Pan, Z. L. Tao and J. Chen, *Nat. Chem.*, 2011, **3**, 79-84.
50. J. O. Bockris and T. Otagawa, *J. Phys. Chem.*, 1983, **87**, 2960-2971.
51. P. Rasiyah, A. C. C. Tseung and D. B. Hibbert, *J. Electrochem. Soc.*, 1982, **129**, 1724-1727.
52. P. Rasiyah and A. C. C. Tseung, *J. Electrochem. Soc.*, 1983, **130**, 2384-2386.

53. R.-N. Singh, M. Hamdani, J.-F. Koenig, G. Poillerat, J. Gautier and P. Chartier, *J. Appl. Electrochem.*, 1990, **20**, 442-446.
54. E. Rios, P. Lara, D. Serafini, A. Restovic and J. L. Gautier, *J. Chil. Chem. Soc.*, 2010, **55**, 261-265.
55. P. Rasiyah and A. C. C. Tseung, *J. Electrochem. Soc.*, 1983, **130**, 365-368.
56. G. Godillot, L. Guerlou-Demourgues, L. Croguennec, K. M. Shaju and C. Delmas, *J. Phys. Chem. C*, 2013, **117**, 9065-9075.
57. F. Svegl, B. Orel, I. Grabec-Svegl and V. Kaucic, *Electrochim. Acta*, 2000, **45**, 4359-4371.
58. F. Moro, S. V. Y. Tang, F. Tuna and E. Lester, *J. Magn. Magn. Mater.*, 2013, **348**, 1-7.
59. J. Xu, P. Gao and T. Zhao, *Energy Environ. Sci.*, 2012, **5**, 5333-5339.
60. Y. L. Li, J. Z. Zhao, Y. Y. Dan, D. C. Ma, Y. Zhao, S. N. Hou, H. B. Lin and Z. C. Wang, *Chem. Eng. J.*, 2011, **166**, 428-434.
61. A. Restovic, E. Rıos, S. Barbato, J. Ortiz and J. Gautier, *J. Electroanal. Chem.*, 2002, **522**, 141-151.
62. J. Li, N. Zhou, H. Wang, H. Li, Z. Xie, H. Chu, Y. Tang, L. Sun and Z. Peng, *J. Electrochem. Soc.*, 2015, **162**, A2302-A2307.
63. E. Rios, J. L. Gautier, G. Poillerat and P. Chartier, *Electrochim. Acta*, 1998, **44**, 1491-1497.
64. E. Lee, J. H. Jang and Y. U. Kwon, *J. Power Sources*, 2015, **273**, 735-741.
65. D. Pletcher, X. Li, S. W. Price, A. E. Russell, T. Sönmez and S. J. Thompson, *Electrochim. Acta*, 2016, **188**, 286-293.
66. A. H. Monteverde Videla, P. J. Stelmachowski, G. Ercolino and S. Specchia, *J. Appl. Electrochem.*, 2017, **47**, 295-304.
67. F. Kong, *Electrochim. Acta*, 2012, **68**, 198-201.
68. Y. Liang, Y. Li, H. Wang, J. Zhou, J. Wang, T. Regier and H. Dai, *Nat. Mater.*, 2011, **10**, 780-786.
69. H. Hu, B. Guan, B. Xia and X. W. Lou, *J. Am. Chem. Soc.*, 2015, **137**, 5590-5595.
70. B. Chi, H. Lin, J. Li, N. Wang and J. Yang, *Int. J. Hydrog. Energy*, 2006, **31**, 1210-1214.
71. C. Jin, F. Lu, X. Cao, Z. Yang and R. Yang, *J. Mater. Chem. A*, 2013, **1**, 12170-12177.

72. Y. Li, L. Zou, J. Li, K. Guo, X. Dong, X. Li, X. Xue, H. Zhang and H. Yang, *Electrochim. Acta*, 2014, **129**, 14-20.
73. H. Zhang, H. Qiao, H. Wang, N. Zhou, J. Chen, Y. Tang, J. Li and C. Huang, *Nanoscale*, 2014, **6**, 10235-10242.
74. Y. Yang, H. Fei, G. Ruan, C. Xiang and J. M. Tour, *ACS Nano*, 2014, **8**, 9518-9523.
75. X. Ge, Y. Liu, F. T. Goh, T. A. Hor, Y. Zong, P. Xiao, Z. Zhang, S. H. Lim, B. Li and X. Wang, *ACS Appl. Mater. Interfaces*, 2014, **6**, 12684-12691.
76. P. W. Menezes, A. Indra, N. R. Sahraie, A. Bergmann, P. Strasser and M. Driess, *ChemSusChem*, 2015, **8**, 164-171.
77. H. Yang, F. Hu, Y. Zhang, L. Shi and Q. Wang, *Nano Res.*, 2016, **9**, 207-213.
78. Y. Li, P. Hasin and Y. Wu, *Adv. Mater.*, 2010, **22**, 1926-1929.
79. C. F. Windisch, G. J. Exarhos, K. F. Ferris, M. H. Engelhard and D. C. Stewart, *Thin Solid Films*, 2001, **398**, 45-52.
80. J. F. Marco, J. R. Gancedo, M. Gracia, J. L. Gautier, E. Rios and F. J. Berry, *J. Solid State Chem.*, 2000, **153**, 74-81.
81. M. Lenglet, R. Guillamet, J. Dürr, D. Gryffroy and R. Vandenberghe, *Solid State Commun.*, 1990, **74**, 1035-1039.
82. D. Mehandjiev and E. Nikolova-Zhecheva, *Thermochim. Acta*, 1981, **51**, 343-351.
83. D. G. Wickham and W. J. Croft, *J. Phys. Chem. Solids*, 1958, **7**, 351-360.
84. C. Li, X. P. Han, F. Y. Cheng, Y. X. Hu, C. C. Chen and J. Chen, *Nat. Commun.*, 2015, **6**.
85. E. Vila, R. M. Rojas, J. L. M. deVidales and O. GarciaMartinez, *Chem. Mat.*, 1996, **8**, 1078-1083.
86. J. L. Martin de Vidales, E. Vila, R. M. Rojas and O. Garcia-Martinez, *Chem. Mat.*, 1995, **7**, 1716-1721.
87. H. Bordeneuve, S. Guillemet-Fritsch, A. Rousset, S. Schuurman and V. Poulain, *J. Solid State Chem.*, 2009, **182**, 396-401.

Chapter 2: Experimental

This chapter discusses the experimental aspects of techniques that have been used for physical characterization and electrochemical measurements in this thesis. The preparation of the catalyst materials will be discussed in the relevant chapters (**3**, **4** and **5**).

2.1. Reagents and Materials

Table 1 List of the materials and reagents used in this thesis along with their suppliers

Material/Reagent	**Supplier**
Ammonium hydroxide (35 %)	Fisher Scientific
Aqueous Nafion® solution (10.0 % solids)	Sigma Aldrich
Boron nitride (powder, 1 micron, 98 %)	Sigma Aldrich
Carbon powder (XC-72R)	Johnson Matthey
Cobalt (II) nitrate hexahydrate (99 %)	Acros Organics
Cobalt (II) oxide (≥ 99.99 % trace metals basis)	Sigma Aldrich
Cobalt (II, III) oxide (nonstoichiometric compound, 99.995 % trace metals basis)	Sigma Aldrich
Diethylene glycol (≥ 99 %)	Sigma Aldrich
Ethanol (absolute)	Fisher Scientific
Hydrochloric acid (≈ 37 %)	Fisher Scientific
Hydrogen peroxide 100 (>30 % w/v)	Fisher Scientific
Isopropyl alcohol (99 %)	Fisher Scientific
Lithium cobalt (III) oxide, 99.5 % (metals basis)	Alfa Aesar
Manganese (II) nitrate tetrahydrate (≥ 97 %)	Sigma Aldrich
Manganese (II) oxide (≥ 99.99 % trace metals basis)	Sigma Aldrich
Manganese (III) oxide (99.9 % trace metals basis)	Sigma Aldrich
Manganese (IV) oxide (≥ 99.99 % trace metals basis)	Sigma Aldrich
Mercury	Fluka Chemika
Mercury (II) oxide (99.999 % trace metals basis)	Sigma Aldrich
Micro-cloth	Buhler
Micro-polish Alumina (0.05 µm)	Buhler
Micro-polish Alumina (1 µm)	Buhler
Nitric acid (70 %)	Fisher Scientific
Nitrogen	BOC
Oxygen	BOC
Platinum black (fuel cell grade)	E-TEK
Polyamide filter	Whatman

Potassium hydroxide (85 %)	Acros Organics
Sodium Bicarbonate	Fisher Scientific
Sodium hydroxide (> 98 %)	Fisher Scientific
Toray Carbon Paper (45365)	Alfa Aesar
Water (18 MΩ cm)	Purite water purifier

2.2. Physical Characterization

Prepared materials were first characterized by X-ray Diffraction (XRD), BET Surface Area Measurements, Raman Spectroscopy, Scanning Electron Microscopy-Energy Dispersive X-ray (SEM-EDX), Transmission Electron Microscopy (TEM), X-Ray Photoemission Spectroscopy (XPS) and Thermogravimetric Analysis (TGA) in order to investigate crystallite size, phase, surface area, morphology, elemental distribution, particle size, atomic ratio and decomposition.

2.2.1. Powder X-ray Diffraction (XRD)

Powder X-ray diffraction (XRD) was used to determine the phase of the materials via refinement of the diffraction patterns using the PDXL[1] (Rigaku) and GSAS[2] software packages in order to determine unit cell and lattice parameters. Additionally, the average crystallite size was calculated from the widths of diffraction peaks by using the Scherrer equation (**Equation 2.1**). Where L is the average crystallite size, K is the Scherrer constant (typically 0.9 but this is not certain due to different approximation methods), λ is the wavelength of the incident X-rays, β is the full width half maximum of the diffraction peak in radians and θ is the Bragg angle.[3]

$$L = \frac{K\lambda}{\beta cos\theta} \qquad \textbf{Equation 2.1}$$

All materials were finely ground and sieved (53 μm) as part of the preparation method (see **Chapters 3-5**). Therefore, for the XRD measurements, each sample was directly transferred into sample holder and packed using a clean cover glass, which was removed prior to the measurements. The sample holder was then placed in Bruker D2 Phaser diffractometer with a fluorescence filtering detector. The radiation source used with this diffractometer is

Cu - *K*α (λ = 1.5418 Å). All materials were scanned from 10° to 80° 2θ with a 0.2 seconds step time, 0.0162° step size, 935 seconds exposure time and 8 scans.

2.2.2. BET Surface Area Analysis (BET)

The specific surface area of the powdered samples was measured by the physical adsorption of N_2 gas using Brunauer-Emmet-Teller (BET) isotherm.[4] **Equation 2.2**

$$\frac{P}{V(P_0-P)} = \frac{1}{V_m C} + \frac{C-1}{V_m C}\frac{P}{P_0} \qquad \textbf{Equation 2.2}$$

Where *P* is equilibrium pressure, P_0 is the vapour pressure of the adsorbate gas at standard conditions, *V* is the volume of the adsorbed gas at a particular partial pressure ($\frac{P}{P_0}$), V_m is the volume of gas required to achieve monolayer coverage and *C* is the temperature dependent BET constant. The specific surface area (S) of the material ($m^2\ g^{-1}$) was then calculated (**Equation 2.3**). Where *A* (m^2) is the area of adsorbate molecule, *m* the mass of the sample (g) and N_A is Avagadro's number.

$$S = \frac{V_m}{m}\frac{N_A}{V_A}A \qquad \textbf{Equation 2.3}$$

All samples were first dried in glass sample holders under vacuumed condition at 180 °C for 2 hours and dryness was confirmed by periodically weighing each sample once cooled to room temperature until a constant weight was achieved. Then sample was placed in Micromeritrics-Gemini/Micromeritrics-TriStar II 3020 Instruments to obtain the isotherm data at nitrogen temperature (77 K). Nitrogen gas was used for all BET surface area measurements as the adsorbate gas.

2.2.3. Raman Spectroscopy

Powder samples were packed as a thin layer between two cover glass slides and before focusing a specific point of sample with microscope and taking the spectra, the top slide was removed. A 50x microscope lens was used with 785 nm wavelength Near IR Laser

(100 mW). The spectrometer was a Renishaw inVia. The laser power was chosen as 0.5 % and accumulating time was 60 seconds. The baseline was subtracted for each spectra using the Origin 2015 software package.

2.2.4. Scanning Electron Microscopy and Energy Dispersive X-ray (SEM-EDX)

Small amounts of the powdered samples were sprinkled onto adhesive carbon tabs on aluminium sample studs and the excess was removed by shaking. Then aluminium sample studs were placed in the Philips XL30 ESEM environmental scanning electron microscope (running at 15 kV) operating in the wet mode with a secondary electron (SE) detector. The microscope was fitted with a Thermo Scientific NSS X-ray Analysis System with ultra-dry EDX detector. SEM images and EDX data were collected after the microscope was evacuated.

For SEM imaging of the glassy carbon (GC) electrodes, an ink was prepared as described below in **2.4.6** and this was drop coated onto GC electrode, which was fitted into the microscope and the microscope was evacuated.

2.2.5. Transmission Electron Microscopy (TEM)

Powdered samples were sprinkled onto carbon coated Cu TEM grids, prepared by Mr. Anton Page of the Biomedical Imaging Unit, Southampton General Hospital, before using a FEI Tecnai 12 Transmission Electron Microscope running at 100 kV.

2.2.6. X-Ray Photoemission Spectroscopy (XPS)

X-ray photoemission spectroscopy measurements for powdered samples were carried out by Dr Laura Calvillo, University of Padova, Italy. Photoemission data were obtained in a custom designed UHV system equipped with an EA 125 Omicron electron analyser with five channeltrons, working at a base pressure of 10^{-10} mbar. Core level photoemission spectra (C 1s, O 1s, Mn 2p and Co 2p regions) were collected in normal emission at room temperature with a non-monochromatized Al K_α X-ray source (1486.7 eV) and using 0.1 eV steps, 0.5 s collection time and 20 eV pass energy. The binding energies (BE) were referenced to the C 1s peak at 284.6 eV.

2.2.7. Thermogravimetric Analysis (TGA)

$Co(NO_3)_2.6H_2O$ and $Mn(NO_3)_2.4H_2O$ (2:1) were used as starting materials in order to produce spinel $MnCo_2O_4$ via a thermal decomposition method (see **Chapter 4**).

Therefore, the mixture of these salts was heated on a hot plate to obtain a solid sample prior to TGA analysis in order to define the composition of sample and thermal stability prior to investigation of the optimum temperature to produce spinels. Thermogravimetric analysis (TGA) was performed using a TG 209 F1 Libra (Netzsch). Sample was heated in a ceramic crucible from 30 to 900 ^{o}C with a temperature ramp of 10 ^{o}C min^{-1} under air flow atmosphere (air flow rate 50 mL min^{-1}). The TGA experiment was carried out with the help of Ms Lucia Lupica-Spagnolo in the Chemistry Department at the University of Southampton.

2.3. Electrochemical Characterization

Electrochemical techniques are critical tools to probe the electrochemical activities and behaviours of the prepared catalysts. Techniques that have been used in this thesis are mainly Cyclic Voltammetry (CV) and Linear Sweep Voltammetry (LSV) at Rotating Disc Electrodes (RDE) and Rotating Ring Disc Electrodes (RRDE).[5-8] CV was used to investigate changes in oxidation state of transition metals within surface layers. **Figure 2.1** is an example of cyclic voltammetry of cobalt oxide (Co_3O_4) in 1 molar potassium hydroxide at 25 ^{o}C measured with 10 mV s^{-1} scan rate between potentials of 0.0 and 0.6 V *vs* Hg/HgO.

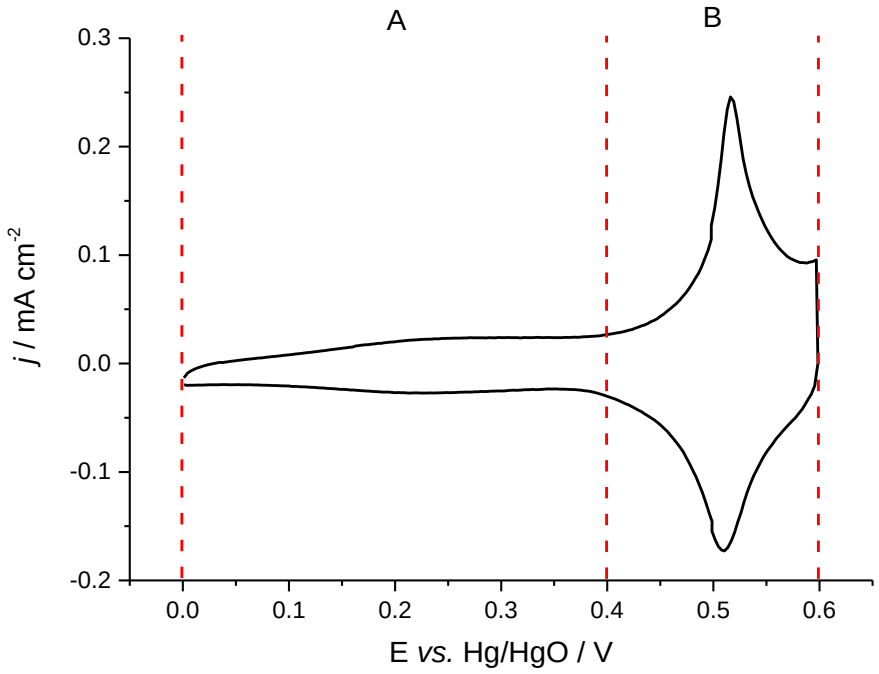

Figure 2.1. Cyclic voltammetry of Co_3O_4 (see **Chapter 3** for preparation) coated on to a glassy carbon electrode (0.19 cm^2) in 1 M KOH. Temperature: 25 ^{o}C; Potential scan rate: 10 mV s^{-1}.

The figure is divided to two sections, A, double layer region and B, oxidation and reduction region. Double layer charging currents, a charge formed in the interphase between electrode surface and electrolyte, can be seen between 0.0 and 0.4 V *vs.* Hg/HgO.[5, 9] The surface oxidation begins around 0.4 V and a well-formed oxidation peak is observed when the surface oxidation ends around 0.6 V. After 0.6 V, oxygen evolution starts. The surface reduction begins at 0.6 V and ends around 0.4 V in the back scan. These oxidation and reduction peaks are due to the change in the oxidation states of Co.[10] Further details related to oxidation/reduction states of Co will be explained in **Chapter 3**.

2.4. Electrochemical Experimental Details

Experimental details related to the electrochemical cell design and electrolyte, the reference electrode (Hg/HgO) preparation, instrumentation, rotating disc electrode (RDE) test experiment, catalyst preparation, electrode coatings, electrode surface coverage mapping and electrode surface coverage error calculation will be explained in this section.

2.4.1. Electrochemical Cell and Electrolyte

RDE and RRDE were used and all the electrochemical measurements were carried out in a beaker cell (volume ≈ 200 mL) with a water jacket thorough which water was passed for temperature control as shown in **Figure 2.2.**

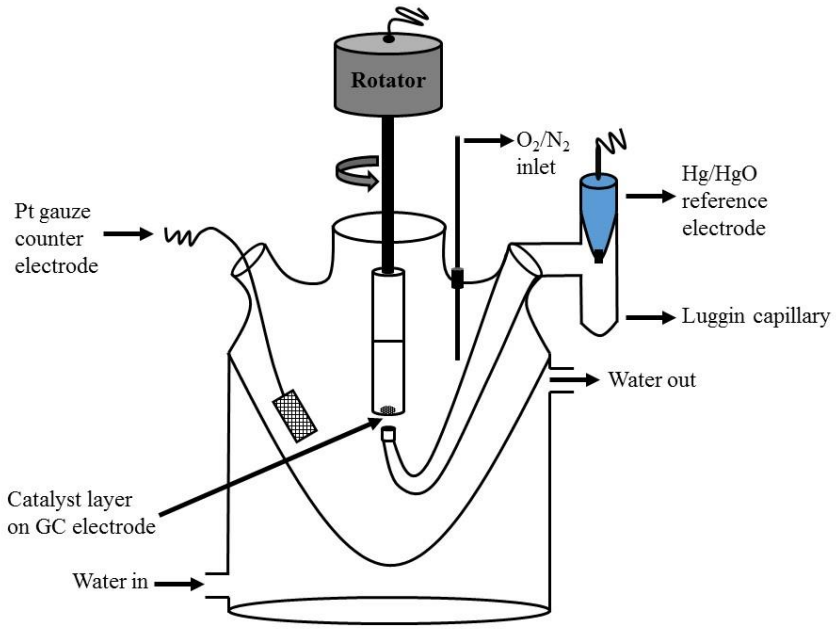

Figure 2.2. Schematic of electrochemical cell used for RDE and RRDE measurements.

Pt gauze and home made Hg/HgO (1 M KOH) electrodes were used as counter and reference electrodes, respectively. The glassy carbon (GC) electrode (Disc OD: 5 mm, 0.196 cm^2) was an AF3M electrode (Pine Instrument). The rotating ring disc electrode was made of a glassy carbon disc (0.25 cm^2) and Pt ring (0.19 cm^2) (AFE7R9GCPT, Pine Instrument) with a collection efficiency (*N*) of 0.37 (see **Figure 2.3**). Prior to each experiment, GC and GC/Pt electrodes were polished on separate micro-cloths (Buehler) with alumina slurries of 1.0 μm and then 0.05 μm particle sizes. The tips of electrodes were then immersed in deionized water for ultrasonic irradiation (≈ 10 minutes) before final rinsing. All experiments were carried out in 1 M KOH degassed with nitrogen or pre-saturated with oxygen.

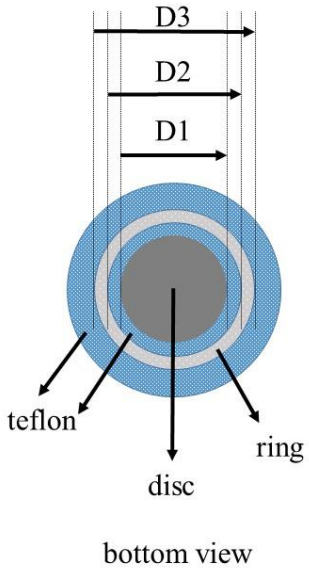

Figure 2.3. The schematic design of rotating-ring disc electrode (RRDE).

The geometric surface areas of disc and ring can be calculated from diameters (Disc OD (D1): 5.61 mm, Ring ID (D2): 6.25 mm and Ring OD (D3): 7.92 mm).

2.4.2. The Reference Electrode (Hg/HgO) Preparation

Mercury/Mercury Oxide (Hg/HgO), an ideal reference electrode for alkaline media, was used as a reference electrode in all electrochemical measurements. **Figure 2.4** shows the homemade Hg/HgO reference electrode and its labelled parts. The glass part of the reference electrode was made in the glass blowing workshop in the Chemistry Department

at the University of Southampton. The empty glass tube, which has a platinum wire in and connected to nickel wire, was filled with liquid mercury (≈ 1/4 of tube) in contact with Pt wire. Then HgO (red solid powder) was packed in the tube (≈ 1/4 of tube). Glass wool, which was already soaked into deionised water, was used to hold the Hg/HgO in place. Finally, the whole glassware was filled with 1 M KOH. The concentration of electrolyte in the reference electrode should be the same of the electrolyte in electrochemical cell in order to eliminate any liquid junction potential.[11] The potential of Hg/HgO is +866 mV *vs.* SHE with 1 M KOH.

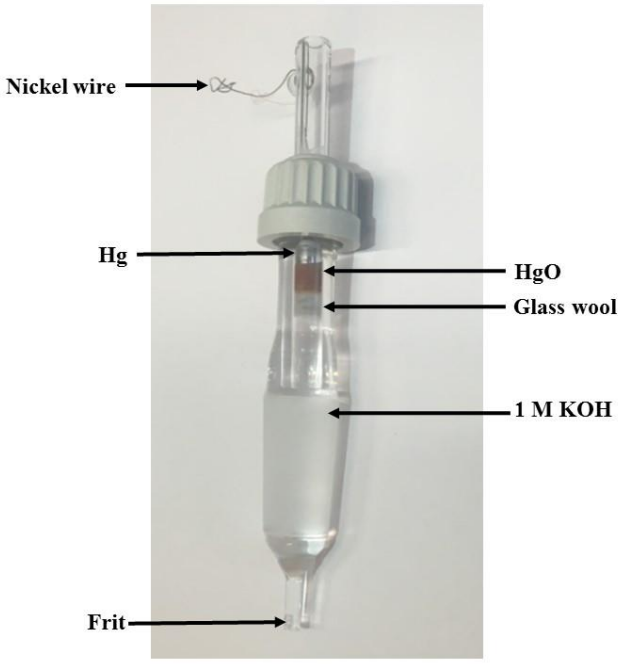

Figure 2.4. The image of homemade Hg/HgO reference electrode in 1 M KOH.

2.4.3. Instrumentation

Electrochemical measurements were carried out with an Autolab PGSTAT instrument with Nova 1.11[12] and GPES software packages. A Pine Instrument Rotator, type CPR or MSR, was used to control the rotating rates of electrodes. Origin 2015[13] was used for processing electrochemical data.

2.4.4. Rotating Disc Electrode (RDE) Test Experiment

Rotating disc electrode (RDE) and rotating ring disc electrode (RRDE) test measurements were periodically carried out with 3 mM $K_3Fe(CN)_6$ in 1 M KOH purged with N_2 in order to ensure RDE and RRDE systems were working properly. $K_3Fe(CN)_6$ was used for all the test experiments since $Fe(CN)_6^{-3}$/ $Fe(CN)_6^{-4}$ is a good redox couple, which has a very fast reversible electronic transfer process.[14]

The role of mass transport is very important at mass transfer limited condition at RDE/RRDE experiments. The Levich equation (**Equation 2.4**) shown below applies only when the reaction is fully mass-transfer limited at the RDE and limiting current density is proportional to c and $\omega^{1/2}$.[6, 14]

$$j_L = 0.62nFD^{2/3}\, cv^{-1/6}\omega^{1/2} \qquad \textbf{Equation 2.4}$$

Where j_L is limiting current density (A cm^{-2}), n is number of electrons participate in electrode reaction, F is the Faraday constant (96,485 C mol^{-1}), D is diffusion coefficient (cm^2 s^{-1}), c is the concentration of electroactive species (mol cm^{-3}), v is the kinematic viscosity of the electrolyte (cm^2 s^{-1}) and ω is the rotating rate of electrode (radians s^{-1}). Therefore, the proportionality between limiting current density and rotating rate has been shown in the RDE test experiment (see **Figure 2.5). Figure 2.5** shows the linear sweep voltammetry of the reduction of 3 mM $Fe(CN)_6^{-3}$ to $Fe(CN)_6^{-4}$ in 1 M KOH (purged with N_2) with different rotating rates at room temperature with 5 mV s^{-1} scan rate.

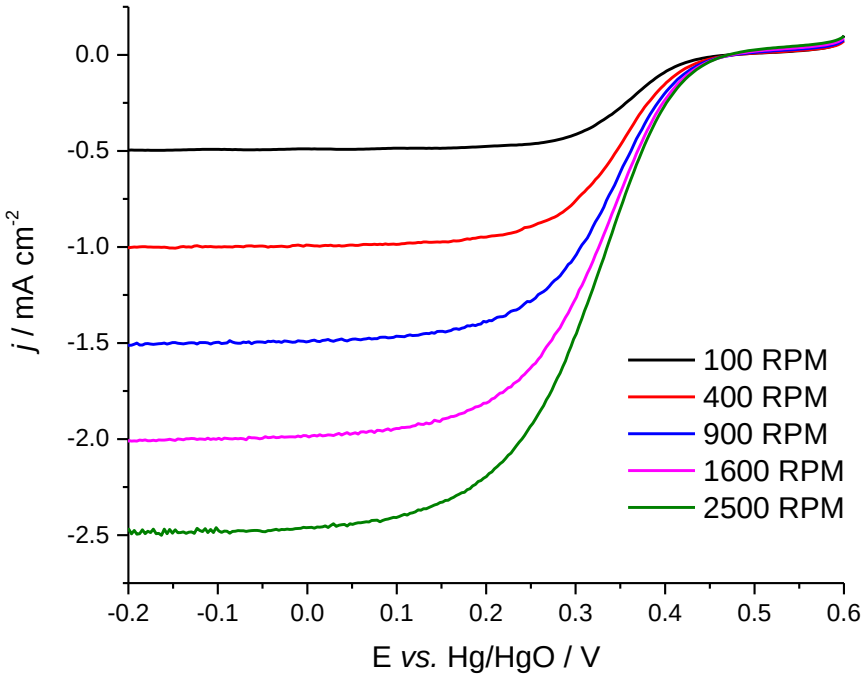

Figure 2.5. Linear sweep voltammetry of 3 mM $K_3Fe(CN)_6$ in 1 M KOH purged with N_2 (≈ 30 minutes). Temperature: 25 ºC; Potential scan rate: 5 mV s^{-1}.

The linearity between j_L *vs.* $\omega^{1/2}$ (at -0.1 V potential) can be seen in **Figure 2.6** as it is expected from the Levich equation (**Equation 2.4**). These results show that RDE system does work properly. The same test experiment was also applied to RRDE (results are not shown) and similar results were obtained. In addition to the test experiment, diffusion coefficient of $Fe(CN)_6^{-3}$ (D) can be also calculated from the slope of the Levich plot (see **Figure 2.6**) as shown below:

$$Slope = 0.62\, n\, F D^{\frac{2}{3}} (m^2 s^{-1}) v^{-\frac{1}{6}} (m^2 s^{-1})\, c\, (mol\, m^{-3}) \qquad \textbf{Equation 2.5}$$

(n = 1; F = 96500 C mol^{-1}; v (1 M KOH)[15]: 1 10^{-6} m^2 s^{-1}; c: 3 mol m^{-3})

1.5262 = 0.62 x 1 x 96,500 x $D^{\frac{2}{3}}$ x (1 10^{-6})$^{-1/6}$ x 3

D = 7.8 10^{-10} m^2 s^{-1}

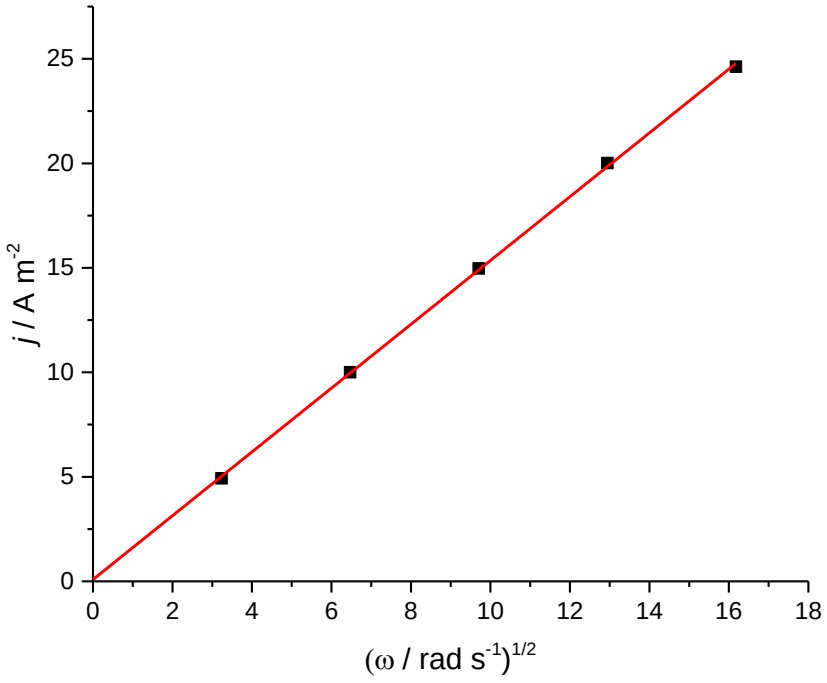

Figure 2.6. Plot of j_L *vs.* $\omega^{1/2}$ produced from **Figure 2.5** at -0.1 V potential. Slope: 1.5262 (± 0.01503).

2.4.5. Catalyst Preparation

Thermal decomposition, co-precipitation and hydrothermal methods were used for catalysts preparations. Details of material preparations will be discussed in relevant chapters (**3-5**).

2.4.6. Electrode Coatings

Ink preparation and electrode coating for all rotating disc electrode and rotating ring disc electrode measurements are the same. 2 mg of each catalyst were placed with 6 mL deionized water. Then each sample was placed in an ultrasonic bath (Fisherbrand FB15046) for 30 minutes followed by 2 minutes shear force stirring in a homogeniser (Fisher Powergen 1000). The prepared ink remained in the sonicator while depositing 3x15 µL of prepared ink on to a clean GC electrode surface (0.196 cm^2) to generate loading of 75 µg cm^{-2}. Finally, 15 µL of 1 % Nafion in water (prepared from aqueous Nafion solution, 10 % solids) was added and the coating again dried. The GC electrode was dried with an IR heat lamp after each ink and Nafion drop.

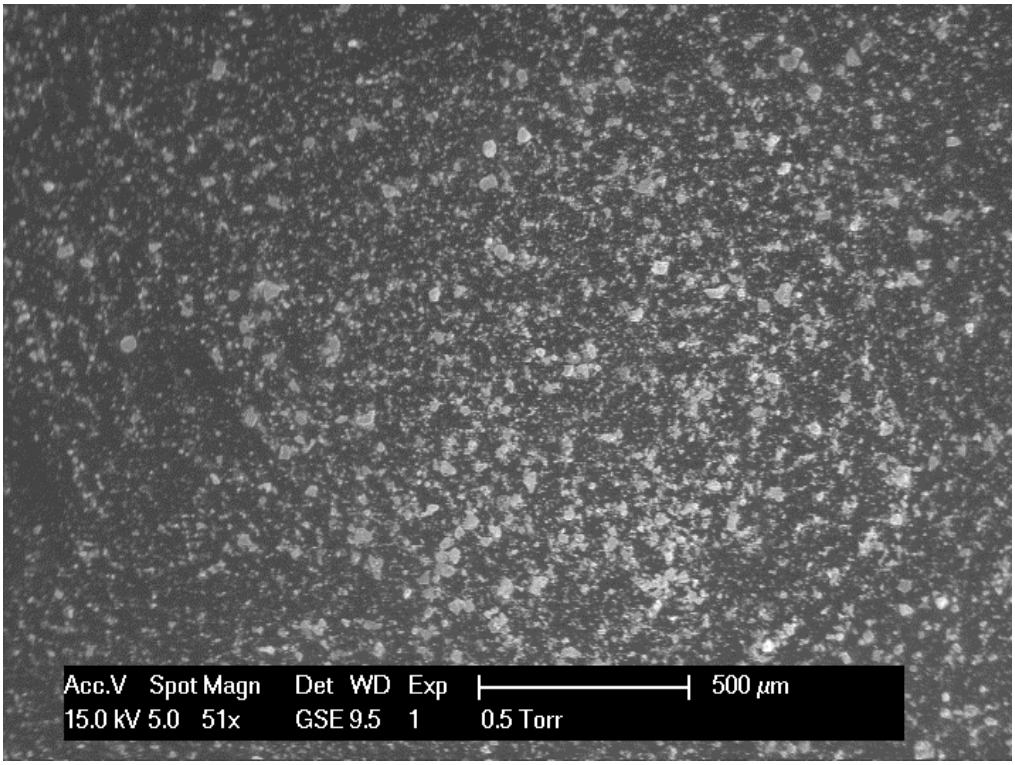

Figure 2.7. SEM image of $MnCo_2O_4$ (prepared via thermal decomposition method) coated on a GC electrode. Image scale: 500 µm. The image was taken from the middle of catalyst coated GC electrode.

The uniformity of coated ink on GC electrode was checked by SEM and it can be seen in **Figure 2.7**. On a low magnification, the coating appears uniform. On a high magnification, it can be seen that the catalyst is present as individual particles with a size up to 10 µm.

2.4.7. Electrode Surface Coverage Mapping

Electrode surface coverage mapping was carried out on the same GC electrode after collecting **Figure 2.7** to analyse elemental mapping as well as the electrode coverage since catalysts appear as individual particles in **Figure 2.7**.

As can be seen from SEM elemental mapping of $MnCo_2O_4$ coated on the GC electrode (**Figure 2.8**), each element mapping is perfectly matching to the SEM image in **Figure 2.8**. It is shown in the SEM image (**Figure 2.7)** of catalyst coated on GC electrode, there are some parts at the GC electrode, which are not completely covered with ink. However, elemental mapping shows there are some nanoscale particles which are still covering GC

electrode with a less intensity of catalyst material on the surface. **Figure 2.8** and its full EDX scale of $MnCo_2O_4$ (**Figure 2.9**) are complementary results with SEM image (**Figure 2.7**).

All of these results show that there is a uniform layer of catalyst material on GC electrode in which the intensity of materials are different in some points due to agglomeration of particles in the ink.

It is also worth to note that elemental mapping (**Figure 2.8)** does also show a uniform distribution of Co and Mn within the individual particles.

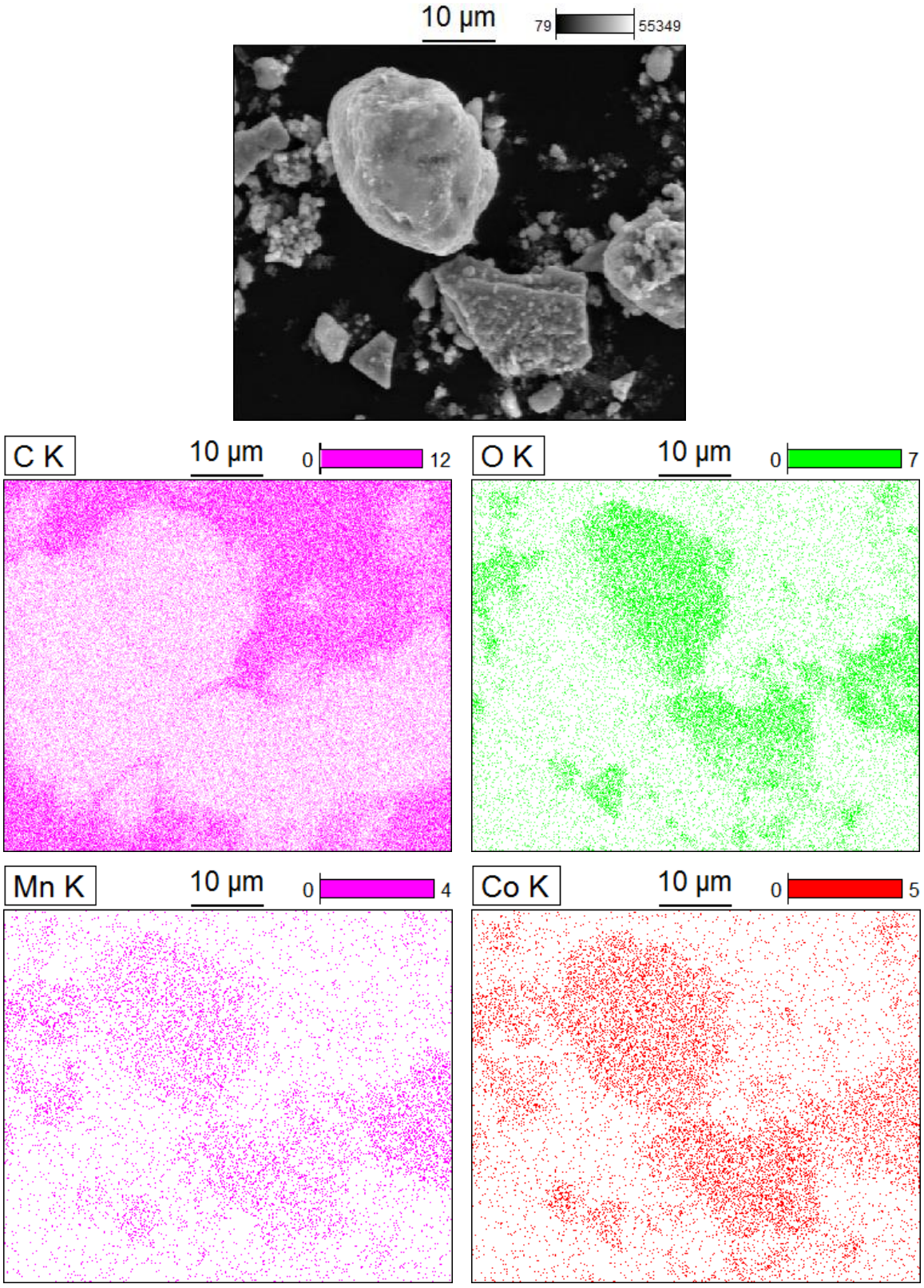

Figure 2.8. SEM elemental mapping of $MnCo_2O_4$ coated on GC electrode. Image is from the middle of the electrode. For SEM image, parameters: Data type: Counts; Image resolution: 512 by 426; image pixel size: 0.12 µm; map resolution: 512 by 426; map pixel size: 0.12 µm; acc. voltage: 15.0 kV; magnification: 2000.

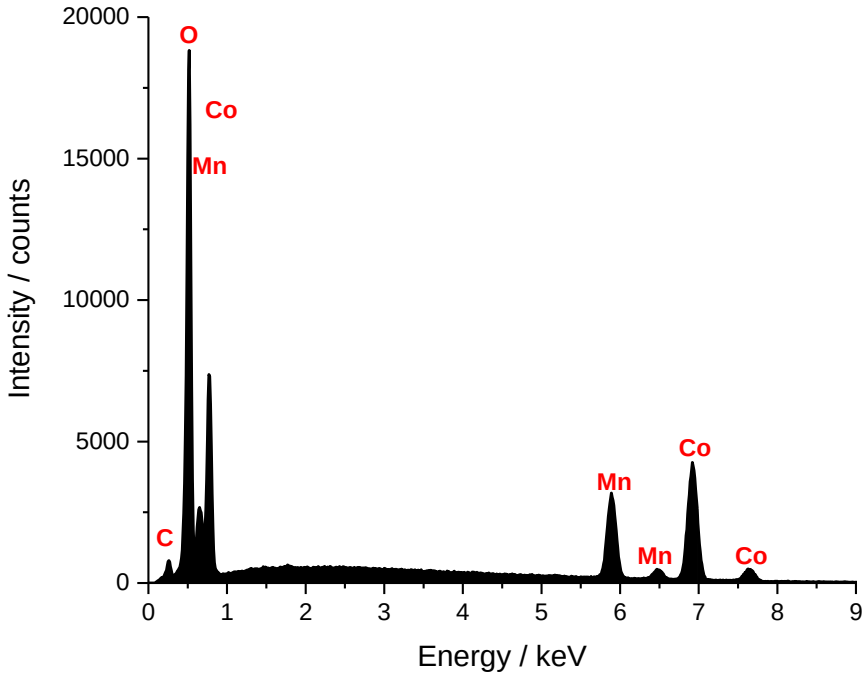

Figure 2.9. SEM full scale EDX of $MnCo_2O_4$ coated on GC from the middle of GC electrode. Full scale counts: 18822.

2.4.8. Electrode Surface Coverage Error Calculation

Knowledge of the electrode area is critical in comparing electrocatalysis. With the preparation of the thin film electrodes, errors could arise from ***a)*** incomplete coverage of the GC disc ***b)*** the oxide film extending over the polytetrafluoroethylene (PTFE) shroud. These errors were investigated by SEM imaging of catalyst coated GC electrode. **Figure 2.10** shows one of six SEM images (see all 6 images in **Appendix**, **Figure A2.1.**) of catalyst coated GC electrode edges at six different points on the circumference. Film, uncovered distance between film and GC electrode edge, GC edge, PTFE edge and PTFE are as shown in **Figure 2.10.**

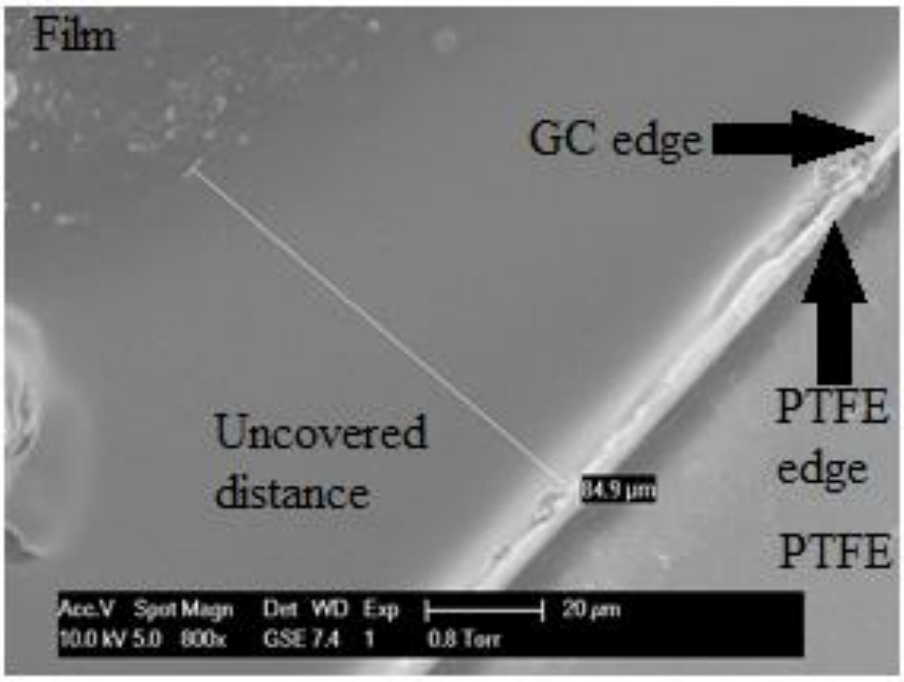

Figure 2.10. SEM image of $MnCo_2O_4$ coated GC electrode (one of 6 images from 6 different positions on the GC electrode edge).

The average of uncovered surface distances (AUSD) from the edge of GC electrode (6 points) is calculated from **Figure 2.10** (five images are not shown here) and shown below.

$$\text{AUSD} = \frac{87.9 + 75.9 + 84.9 + 71.1 + 84.0 + 83.0}{6} = 81.1\ \mu\text{m}$$

The exact surface area of GC is $1.9635\ 10^{-5}$ m^2. The uncoated surface area of GC electrode, which was calculated from AUSD, is $1.253\ 10^{-6}$ m^2.

$$\text{Electrode surface coverage error } = -\frac{1.253\ 10^{-6}}{1.9635\ 10^{-5}}\ 100 = -6.4\%$$

Electrode surface coverage error has been found as -6.4%. This result indicates that electrochemical results for the same material under the same condition may vary roughly in

the range of ±10%. This difference was observed while carrying out reproducibility experiments.

2.5. X-ray Absorption Spectroscopy (XAS)

X-ray absorption spectroscopy (XAS)[16, 17] measurements were carried out in transmission mode at Diamond Light Source-B18. There are some steps of processing the raw XAS data produced by the beamline using the ATHENA software program.[18, 19] The raw XAS data are first imported into ATHENA in order to normalise, calibrate and carry out the background subtraction. Prior to normalisation and calibration, multiple spectra collected for each sample were merged to improve the signal to noise ratio. Then, XAS spectra were normalised to 1 and normalisation was continued by ***I)*** fitting a linear function through the pre-edge; *II)* fitting a quadratic function to post-edge and *III)* subtracting both of these from the raw data as a final stage.[18, 20]

A Mn foil spectrum was also measured for calibrating each sample. The calibration is achieved by shifting the peak of the first derivative of the metal foil reference samples to the tabulated absorption energy. Then, the shift in absorption energy is applied to all spectra of samples in order to ensure the same energy scale.[20]

The adsorption edge energy (E_o) can be identified either selecting half-way up the adsorption edge (white line peak) or the first peak in the first derivative of the spectrum.[20] Half-way of the white line peak was chosen for E_o in XANES studies for this thesis.

2.5.1. Ex-Situ XANES Measurements

Ex-situ XAS measurements were carried out to investigate how oxidation states of powdered samples are changing with different atomic compositions and preparation methods. Ex-situ XANES measurements were conducted with the help of Professor Andrea E. Russell and Dr Veronica Celorrio.

2.5.1.1. Pellet Preparation

Boron nitride was mixed with catalysts (amount of active material varies from 5 mg to 20 mg based on X-ray absorption calculation for each active material) to prepare pellets (≈ 120 mg total composition) for ex-situ XANES measurements. The mixture of boron nitride and active material was mixed in a pestle and mortar prior to applying 5 tons pressure for 15 seconds.

2.6. References

1. *The Rigaku Journal* 2010, **26**, 23-27.
2. S. C. Vogel, *J. Appl. Crystallogr.*, 2011, **44**, 873-877.
3. A. L. Patterson, *Phys. Rev.*, 1939, **56**, 978-982.
4. S. Brunauer, P. H. Emmett and E. Teller, *J. Am. Chem. Soc.*, 1938, **60**, 309-319.
5. D. Pletcher, *A First Course in Electrode Processes*, Royal Society of Chemistry, 2009.
6. B. A. J. and F. L. R., *Electrochemical methods: Fundamentals and Applications*, John Wiley & Sons, Inc., 2nd edn., 2001.
7. F. Opekar and P. Beran, *J. Electroanal. Chem.*, 1976, **69**, 1-105.
8. P. W. Atkins, *Physical Chemistry*, Oxford University, 4th edn., 1990.
9. P. Kissinger and W. R. Heineman, *Laboratory Techniques in Electroanalytical Chemistry, revised and expanded*, CRC press, 1996.
10. D. Pletcher, X. Li, S. W. Price, A. E. Russell, T. Sönmez and S. J. Thompson, *Electrochim. Acta*, 2016, **188**, 286-293.
11. R. Thacker, *J. Chem. Educ*, 1968, **45**, 180.
12. http://www.ecochemie.nl/Products/Echem/Software/Nova.html, (accessed October 4, 2016).
13. http://www.originlab.com/index.aspx?go=PRODUCTS/Origin, (accessed October 24, 2016).
14. J. Nikolic, E. Expósito, J. Iniesta, J. González-García and V. Montiel, *J. Chem. Educ.*, 2000, **77**, 1191.
15. J. Qiao, L. Xu, L. Ding, P. Shi, L. Zhang, R. Baker and J. Zhang, *Int. J. Electrochem. Sci.*, 2013, **8**, 1189.
16. S. Calvin, *XAFS for Everyone*, CRC Press, 2013.
17. D. Koningsberger, B. Mojet, G. Van Dorssen and D. Ramaker, *Top. Catal.*, 2000, **10**, 143-155.
18. B. Ravel and M. Newville, *J. Synchrot. Radiat.*, 2005, **12**, 537-541.
19. M. Newville, *J. Synchrot. Radiat.*, 2001, **8**, 322-324.
20. S. Thompson, *Bi-functional oxygen catalysts for metal-air flow-batteries*, PhD Thesis, University of Southampton, 2016.

Chapter 3: Spinel Co_3O_4 and $NiCo_2O_4$ as Bifunctional Oxygen Catalysts in Alkaline Media

This chapter will first explain the oxygen reduction reaction (ORR) and oxygen evolution reaction (OER) behaviours at bifunctional spinel type Co_3O_4 and $NiCo_2O_4$ catalyst electrodes in alkaline media. The main focus then will be comparing the oxygen reduction reaction mechanism at these spinels.

3.1. Introduction

The oxygen reduction reaction (ORR) and the oxygen evolution reaction (OER) are highly important processes in metal-air batteries, fuel cells and water electrolysis. Therefore, electrocatalysts, where oxygen reduction or oxygen evolution take place, are crucial components of these systems. Transition metal oxides especially spinels[1-8] and perovskites[9-12] have been widely studied for their electrochemical activities towards oxygen reduction and oxygen evolution in the alkaline system.

Co_3O_4 and $NiCo_2O_4$ have drawn the most attention amongst spinel oxides due to their relatively high electrochemical activity and stability in alkaline media. Due to the advantages of their high catalytic activity, thermodynamic stability, abundancy, cheapness, low electrical resistance and environmental friendliness, spinel type Co_3O_4 and $NiCo_2O_4$ are highly favourable as electrode materials in energy conversion and storage systems.[6, 13] Alkaline media is more favourable than acidic media for spinel metal oxides since they are more stable in alkaline media.[13-15] Therefore, many studies[2-4, 16-18] were carried out of their electrochemistry in alkaline media.

Although OER properties of Co_3O_4 and $NiCo_2O_4$ have been extensively investigated since the 1980s[2-4, 19, 20], ORR studies of these bifunctional spinels have not been extensively reported in the literature. In most studies, carbon powder is used with oxide based electrodes since carbon increases the conductivity of the catalyst layer, which results in an enhancement for the catalytic activity of materials for ORR.[21-23] However, carbon itself shows catalytic activity towards ORR by reducing oxygen via the $2e^-$ pathway, which produces hydrogen peroxide. This confuses or makes it hard to identify the mechanism of ORR at spinel oxides. It is also not desirable to use carbon component in a bifunctional oxygen electrode since carbon itself corrodes under the oxygen evolution conditions.[24-27]. Two recent papers from

Southampton University show the oxygen reduction on $NiCo_2O_4$ based gas diffusion electrodes (GDE) in alkaline media without any carbon additive.[16, 17] Many other reports also show the oxygen reduction behaviour on nanostructured Co_3O_4 and $NiCo_2O_4$ spinel oxides.[28-37] However, the evaluation of these results are limited by the deficiency of the data at standard surfaces (such as Pt, carbon or bare glassy carbon) in order to make an accurate comparison.

An intense search of the literature shows the oxygen reduction reaction (ORR) process has not been fully understood at spinel Co_3O_4 and $NiCo_2O_4$ electrodes. Therefore, the main aim of the study shown in this chapter is to investigate oxygen reduction reaction process in alkaline media on pure spinel Co_3O_4 and $NiCo_2O_4$ (without a graphitic carbon component) by analysing the rotation dependent limiting currents for oxygen reduction and hydrogen peroxide oxidation and reduction. These catalysts can be investigated in three different ways; as pure powders, as powders with carbon black (XC-72R) or as spray and thermal coatings on a metal substrate. Catalysts used in this study are pure powders. Moreover, they were used to make bound films on an inert (vitreous carbon) rotating disc electrode (RDE) and rotating ring disc electrode (RRDE). The results compared to those obtained at the standard Pt black and graphitic carbon electrodes in order to make a logical assessment.

Early parts of this work were carried out by Dr Stephen W.T. Price and Dr Stephen J. Thompson, who investigated the design and fabrication of gas diffusion electrode (GDE) with spinel $NiCo_2O_4$.[17] The work in this chapter is partially the continuation of this work, however, the aspect here is to investigate the bifunctional properties of Co_3O_4 and $NiCo_2O_4$ and the comparison of the ORR mechanism pathways at these powdered pure spinels since the amount of intermediate product (H_2O_2) and oxygen reduction pathways are quite different. The results shown in this chapter formed the basis of two published papers.[38, 39]

3.2. Experimental

3.2.1. Co_3O_4 synthesis

5 g $Co(NO_3)_2 6H_2O$ was dissolved in 20 cm^3 of deionised water. The solution was evaporated to dryness and heated at 105 ^oC for 3 hours. The residue was ground and then calcined at 400 ^oC for 12 hours. The resulting black solid was reground and then sieved through a 53 μm sieve.

3.2.2. $NiCo_2O_4$ synthesis

29 g $Co(NO_3)_2.6H_2O$ and 14.5 g $Ni(NO_3)_2.6H_2O$ were dissolved in 100 cm^3 of deionised water to give a deep red solution. 56 g KOH and 53.9 g $NaHCO_3$ were dissolved in 1500 cm^3 of deionised water and the Ni (II)/Co (II) solution was slowly added drop wise to this solution with vigorous stirring. After complete addition, the solution was heated at 80 ^oC for 20 hours. The green opaque suspension was filtered through a 0.02 μm polyamide filter and dried at 100 ^oC. It was then ground before being calcined at 375 ^oC for 4 hours. The resulting black solid was reground and then sieved through a 53 μm sieve. This sample was produced by Dr Stephen J. Thompson.

3.2.3. Electrode Coating

Ink preparation and electrode coating are as described in **Chapter 2**, section **2.4.6**. All current densities are based on geometric area of the vitreous carbon disc.

3.3. Physical Characterization

This section will describe the physical characterization of powdered spinels (Co_3O_4 and $NiCo_2O_4$) via XRD, BET, SEM and TEM.

3.3.1. XRD

The spinel structures of Co_3O_4 and $NiCo_2O_4$ were confirmed by XRD as shown in **Figure 3.1.**

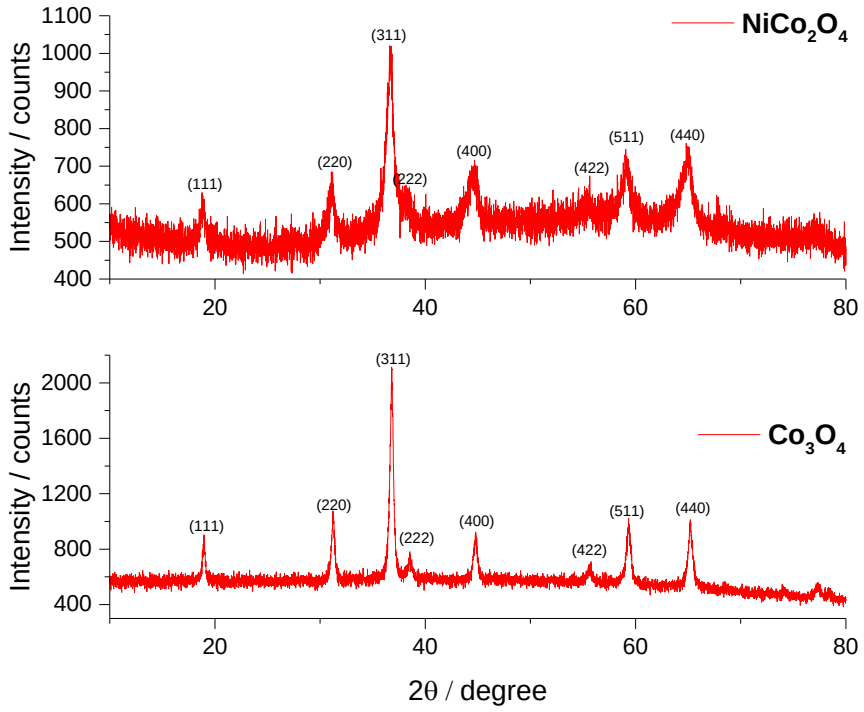

Figure 3.1. XRD patterns of the two spinels Co_3O_4 (**bottom**) and $NiCo_2O_4$ (**top**).

The powder patterns of $NiCo_2O_4$ are noisier compared to those for Co_3O_4, due to higher fluorescence. The structural refinements were also carried out and **Table 3.1** shows the structural parameters of both spinels obtained by analysing of the XRD patterns.

Powder	**Space group**	**Lattice constant a=b=c (Å)**	**V (Å^3)**	**Average crystallite size / nm**
Co_3O_4	$Fd\bar{3}m$	8.08574(5)	530	23
$NiCo_2O_4$	$Fd\bar{3}m$	8.1082(1)	533	12

Table 3.1. Summary of XRD structure refinement of the patterns shown in **Figure 3.1.**

The results from **Table 3.1** show that adding nickel into cobalt oxide expands the cell volume as well as lattice constant as expected.[40] As already shown in **Chapter 1**, cobalt has two different oxidation states, Co^{+2} in the tetrahedral sites, Co^{+3} in the octahedral sites. Ni ions occupy the octahedral sites.[41, 42]

3.3.2. BET

BET measurements of the surface areas of the materials were carried out twice with two different instruments. The results from Micromeritrics-Gemini Instrument are: 30 m^2/g for Co_3O_4 and 68 m^2/g for $NiCo_2O_4$. The results from Micromeritrics-TriStar II 3020 instrument (a more sophisticated instrument) are shown in **Table 3.2.**

Powder	BET Surface Area (m^2/g)	Average Aggregate Size (nm)	Median Pore Width (Å)
Co_3O_4	35	172	13.5
$NiCo_2O_4$	77	78	12.8

Table 3.2. Summary of BET surface area measurements from Micromeritrics-TriStar II 3020

3.3.3. SEM

Elemental analysis of the $NiCo_2O_4$ showed the Ni:Co ratio is close to 1:2, carried out by inductive coupled plasma optical emission spectroscopy (ICP-MS) by Medac Ltd. EDAX analysis also confirmed this ratio as 1:2. **Figure 3.2** is SEM images of both spinels and indicates that the solids were made up of irregular particles with dimensions of 10 – 50 μm.

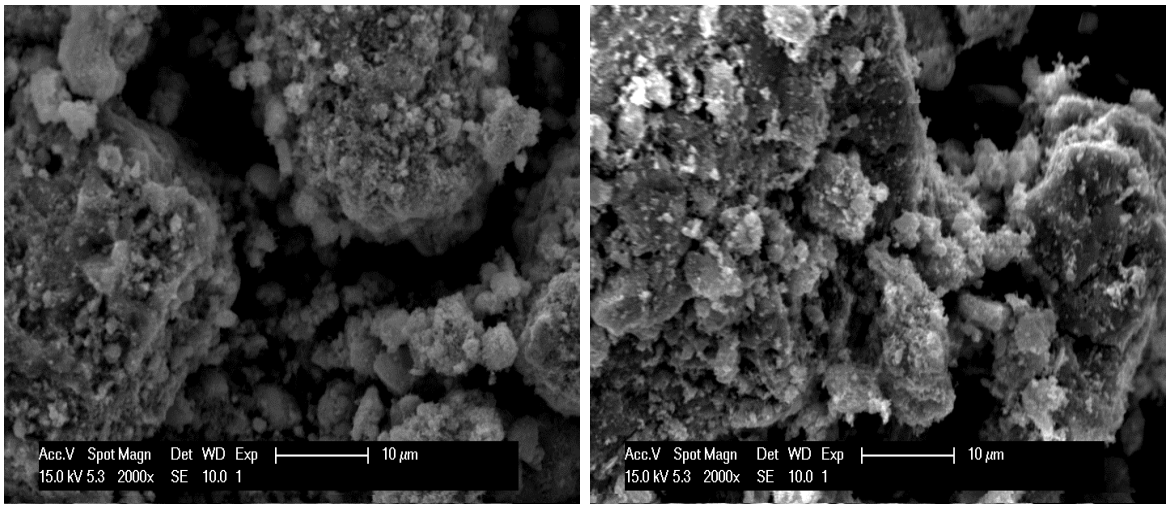

Figure 3.2. Scanning electron microscope (SEM) of Co_3O_4 (**left**) and $NiCo_2O_4$ (**right**). Scale bar is 10 micron.

3.3.4. TEM

Figure 3.3 shows the TEM images of Co_3O_4 and $NiCo_2O_4$. TEM images and the width of the peaks in the XRD suggest that these particles are masses of particles with typical size of 10 to 20 nm.

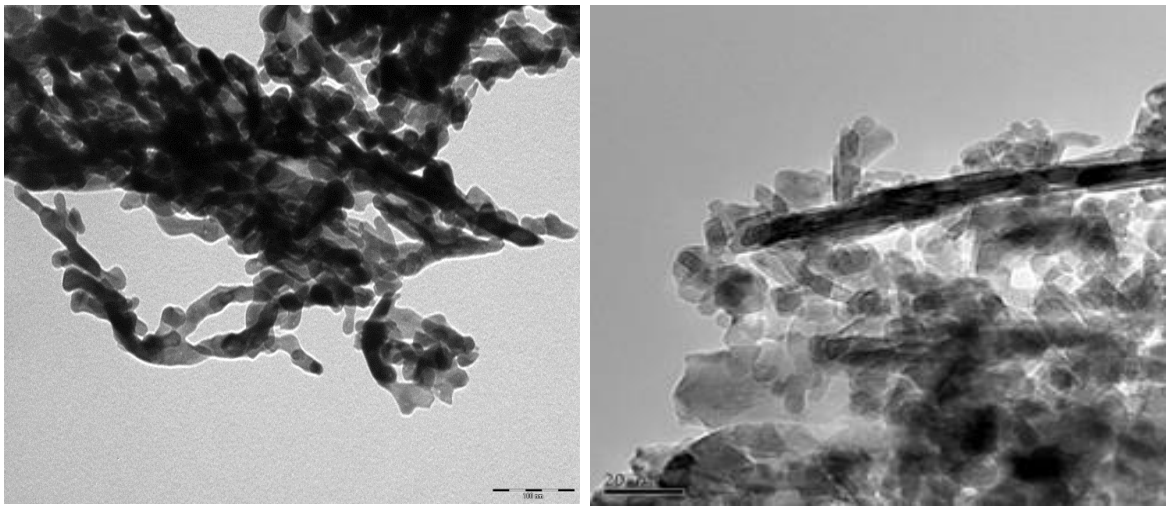

Figure 3.3. Transmission electron microscopy (TEM) of Co_3O_4 (**left**) and $NiCo_2O_4$ (**right**). Scale bar: 100nm (**left**) and 20 nm (**right**).

3.4. Electrochemical Characterization

This section will explain the electrochemical behaviours of the catalysts in alkaline media. The experimental details are as described in **Chapter 2**.

3.4.1. Cyclic Voltammetry and Oxidation States

Co_3O_4 and $NiCo_2O_4$ spinels were coated on the GC electrode and used for cyclic voltammetry under the conditions involving 1 M KOH electrolyte at 25 ^oC with a potential scan rate of 10 mV s^{-1} between open circuit potential and a potential before oxygen evolution *vs* Hg/HgO. Results from **Figure 3.4** are typical cyclic voltammograms for Co_3O_4 and $NiCo_2O_4$ in alkaline media in agreement with those in the literature.[4, 14, 16, 18, 43-45] Well-formed oxidation peaks (forward scans) and reduction peaks (back scans) are due to the change in the oxidation states of Co and mixed Co/Ni ions in the spinel structures. It is believed in the literature that these peaks are the oxidation of Co (III) to Co (IV), which is

attributed to the oxidation reaction of CoOOH at the surface of thin film electrode (see **Reaction 3.1**). This is a reversible surface reaction (see **Reaction 3.2**).[4, 6, 13, 29, 43-45]

$$CoOOH + OH^- \rightarrow CoO_2 + H_2O + e^- \quad (\mathbf{3.1})$$

$$CoO_2 + H_2O + e^- \rightarrow CoOOH + OH^- \quad (\mathbf{3.2})$$

It is known that the surface of a thin film Co_3O_4 electrode is partially changed to CoOOH at open circuit potential.[13] Peak potentials at E = 0.517 V (E_{pa}) and E = 0.510 V (E_{pc}) were obtained for Co_3O_4, which gives formal redox potential (E = (E_{pa} + E_{pc})/2) 0.514 V. This is almost what is recorded in the literature for formal redox potential (E = 0.515 V).[13] The anodic peak potential (E_{pa}) and cathodic peak potential (E_{pc}) for $NiCo_2O_4$ are about 0.465 V and 0.390 V, respectively. While the potential between anodic and cathodic peaks for $NiCo_2O_4$ is around 0.075 V, it is around 0.007 V for Co_3O_4. It is also worth noting that the oxidation and reduction peaks at $NiCo_2O_4$ at less positive potentials. These results are in a good agreement with the literature.[13]

Co_3O_4

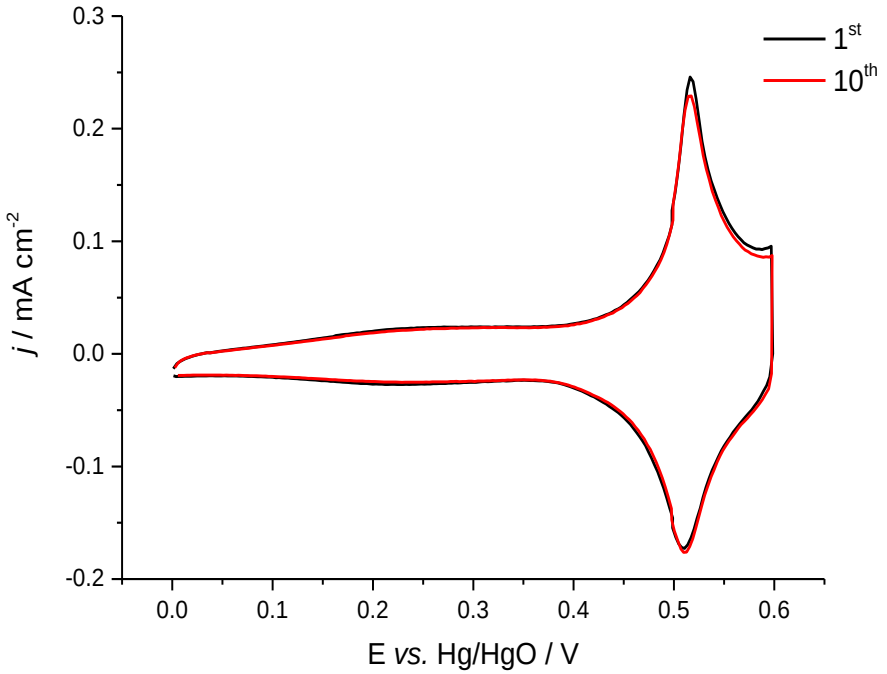

$NiCo_2O_4$

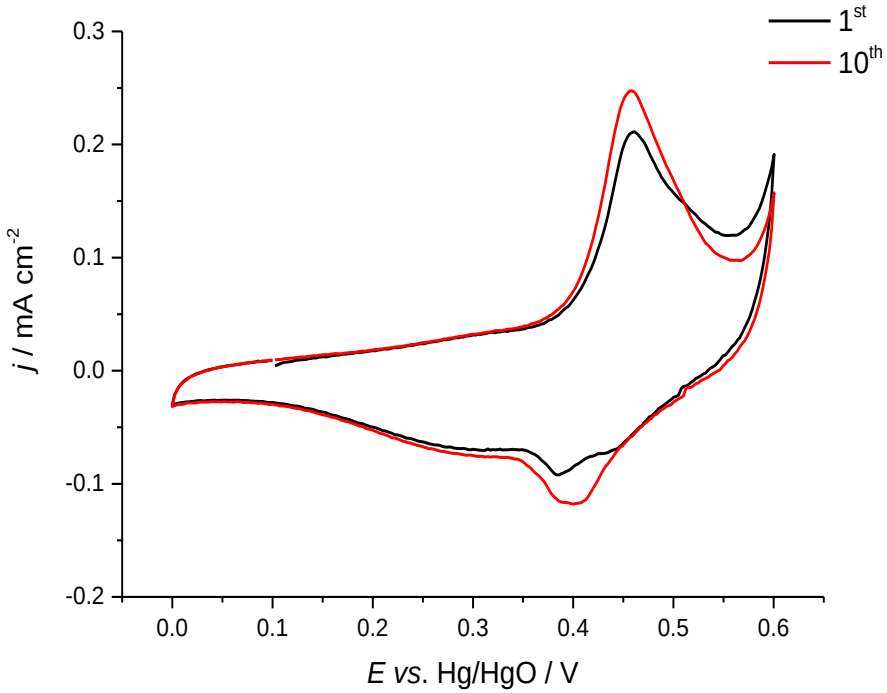

Figure 3.4. Cyclic voltammograms - 1st (black) and 10th cycles (red) for Co_3O_4 (**top**) and $NiCo_2O_4$ (**bottom**) layer in 1 M KOH. Temperature: 25 °C; Potential scan rate: 10 m V s^{-1}.

Figure 3.4 also shows that the kinetics of electron transfer reaction at Co_3O_4 are relatively rapid compared to those at $NiCo_2O_4$ as evidenced by the narrower oxidation/reduction peaks at Co_3O_4. In contrast, the reverse scan of $NiCo_2O_4$ shows two broad features extending down towards the negative potential limit, which may come from more complex electron transfer kinetics. In fact, some papers[20, 36, 46-53] reported cyclic voltammetry of $NiCo_2O_4$ under similar conditions and those results show significant variation, which is probably due to different preparations. All peak current densities increased with increased scan rates. Moreover, the total charge under the oxidation peaks is equal to the total charge under the reduction peaks at all scan rates indicating that the charge passed is limited by the availability of species on the electrode surface. Therefore, all chemistry is reversible. Since the charge associated with oxidation/cathodic peak (1.5 mC cm^{-2}) is small compared to that for 1 e^- oxidation/reduction of all the nickel and cobalt ions in the film on GC electrode (≈ 30 mC cm^{-2}), it is clear that only the surface layers of the spinels are oxidised/reduced during potential cycling.

It can also be seen from **Figure 3.4** that there is almost no difference between the 1st and 10th cycles. However, it seems there is a small increase for oxidation and reduction peaks at $NiCo_2O_4$ attributable to a slight increase in the surface area at $NiCo_2O_4$ coating during cycling. Overall, there is no important change for the spinel in a complete potential cycle. Both spinels are returned to their original compositions and structures after oxidation and reduction processes. Moreover, it is important to note that oxygen evolution and reduction take place at surfaces characterised by different oxidation states of Ni/Co since oxygen evolution occurs at higher potentials and oxygen reduction occurs at lower potentials (see **3.4.2** and **3.4.3**). Therefore, it is expected that the oxidation and reduction of transition metal ions rather than oxygen evolution and reduction will occur during battery operation as the immediate reaction after switching between charge and discharge. The charge in these conversions is highly important in gas diffusion electrodes (GDE) with high loadings of spinels and will influence the battery performance.[16, 17]

In order to confirm the change in oxidation state of the spinel surfaces, the open circuit potential of spinel layers were investigated. The steady state open circuit potentials for both spinels are around + 0.1 V *vs* Hg/HgO after or prior to any measurement. **Figure 3.5** shows the open circuit potentials as a function of time after a 1 minute periods of oxygen evolution and reduction.

Co_3O_4

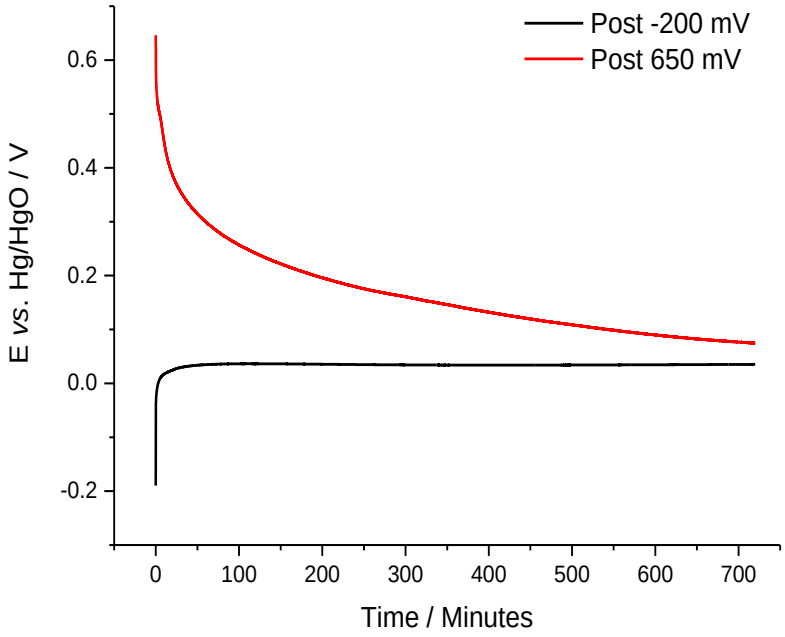

$NiCo_2O_4$

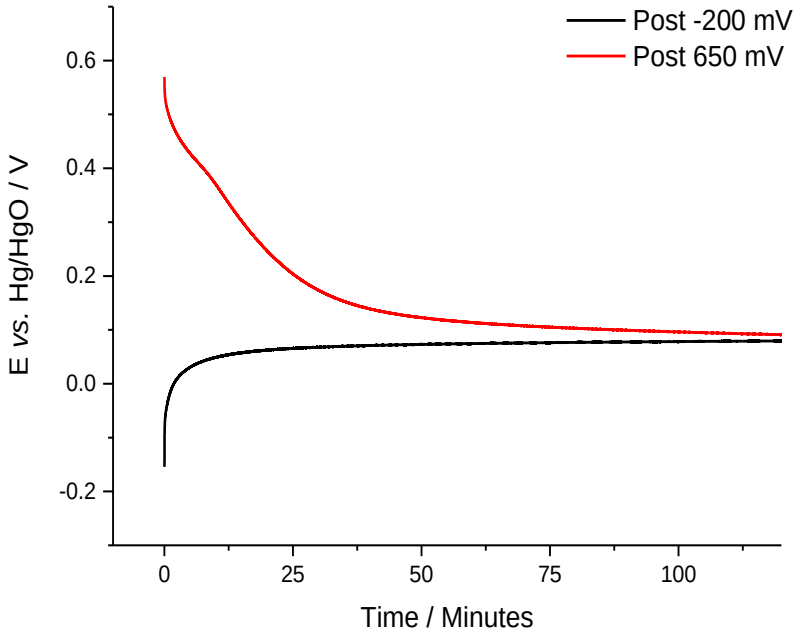

Figure 3.5. Open circuit potential as a function of time after a 1 minute period of oxygen evolution (red curves) or oxygen reduction (black curves). Catalyst coated glassy carbon discs Co_3O_4 (**top**) and $NiCo_2O_4$ (**bottom**). Oxygen saturated 1 M KOH. Temperature: 25 ^oC.

As can be seen in **Figure 3.5**, the open circuit potentials of both spinels rapidly relax towards that for a freshly prepared spinel electrode potential (≈ +0.1 V) after oxygen reduction at - 0.2 V and it is obvious that there is no oxidation change between oxygen reduction and that in fresh/prepared spinels. On the other hand, after the oxygen evolution period for 1 minute at 0.65 V, the open circuit potentials slowly relax to +0.1 V, which is the potential of fresh spinels. The relaxation for Co_3O_4 takes much longer compared to $NiCo_2O_4$.

Oxygen evolution takes place on the surface of spinels with the metal ions in a higher oxidation state[43, 45] and Ni and Co ions slowly react with the electrolyte in order to return the spinels to their original oxidation states at open circuit potential (≈ +0.1 V). This reaction seems much faster with $NiCo_2O_4$ than Co_3O_4 since the former regains an open circuit potential of +0.1 V rather more rapidly.

3.4.2. Oxygen Reduction

Figure 3.6 shows voltammograms of Co_3O_4, $NiCo_2O_4$, platinum black, carbon powder (XC-72R) and uncoated glassy carbon electrodes in oxygen saturated 1 M KOH at 25 °C with a rotation rate of 400 RPM.

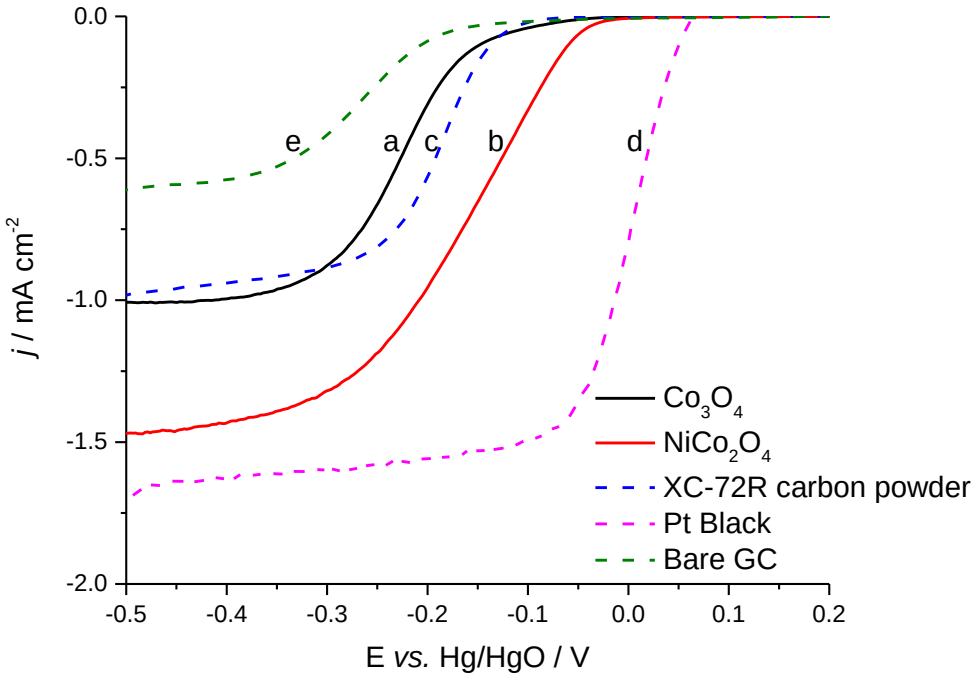

Figure 3.6. Voltammograms of Co_3O_4 (**a**), $NiCo_2O_4$ (**b**), XC-72R carbon powder (**c**) and Pt black (**d**) at coated glassy carbon and bare GC (**e**) RDE in O_2 saturated 1 M KOH. Temperature: 25 °C; Rotation rate: 400 RPM; Potential scan rate: 5 mV s^{-1}.

Characteristic sigmoidal reduction waves for each sample were obtained, however, they have large differences with regard to current densities and oxygen reduction potentials. The uncoated glassy carbon electrode also shows oxygen reduction behaviour as also reported in the literature.[54-56] However, there is an obvious shift towards to positive potential with spinel coated electrodes and large increase in the limiting current densities is observed for some cases. The oxygen reduction voltammogram at a Pt black coated electrode is also shown in **Figure 3.6** in order to make a comparison with a catalyst reducing oxygen via a $4e^-$ pathway. As it was pointed out at the beginning of this chapter that catalysed coatings in this study are carbon free, however, the response at carbon powder (XC-72R) is important to this work since it defines the response at a particle-based coating supporting the $2e^-$ mechanism[57] similar to the spinel coating studied in this chapter. High area carbon is generally added to the catalyst ink or as a layer on gas diffusion electrode (GDE) in order to increase the conductivity of catalyst. However, this influence is often unknown in the literature. A number of important points should be noted;

a) Pt black shows the best catalytic activity under these conditions. However, the onset potential of oxygen reduction at $NiCo_2O_4$ is 110 mV higher (see **Figure 3.6**) than Pt black at low current densities (i.e. at potentials where gas diffusion electrode would be expected to operate). Values of the potentials are shown in **Table 3.3** at low current density (-0.1 mA cm^{-2}).

b) Carbon powder (XC-72R) shows a moderate increase in the onset potential compared to Pt black while the limiting current density is almost half of the current density of Pt black. The response of carbon black points out the importance of checking the activity of any carbon component used in studies where as a catalyst layer or mixed with electrocatalyst. This result shows that graphitic carbon influences the current and there is a possibility of parallel oxygen reduction pathways on the surface of the graphitic carbon and spinel. In addition to this influence of carbon, carbon corrodes under the conditions where oxygen evolution occurs. Due to these points, carbon powder was not added to spinel catalysts layers.

c) The limiting current densities vary with the catalyst. As expected, oxygen is reduced via $4e^-$ reduction pathway at Pt black while it is reduced via $2e^-$ reduction pathway at the graphitic carbon (the charge efficiency of ≈ 80% for the production of H_2O_2 in NaOH was obtained with fuel cell electrodes based on carbon[57]). The ratio of limiting currents is also consistent with this expectation. The limiting currents at Co_3O_4 and

$NiCo_2O_4$ differ strongly. While the limiting current at $NiCo_2O_4$ is slightly less than that at Pt black, the limiting current at Co_3O_4 is almost the same of that at graphitic carbon. However, an analysis of this voltammetry alone does not allow someone to determine whether this limiting current comes from a $2e^-$ reduction or a strongly kinetically limited $4e^-$ reduction. Therefore, further investigation will be explained in sections **3.4.5**, **3.4.7** and **3.4.8.**

Before this further investigation with RDE and RRDE studies in order to determine the oxygen reduction mechanism and kinetics at spinels, oxygen evolution behaviours and electrolyte and temperature effects on oxygen reduction and evolution at spinels will be explained.

3.4.3. Oxygen Evolution

Oxygen evolution behaviours at spinels, platinum black and bare glassy carbon in 1 M KOH at 25 ^oC are shown in **Figure 3.7.**

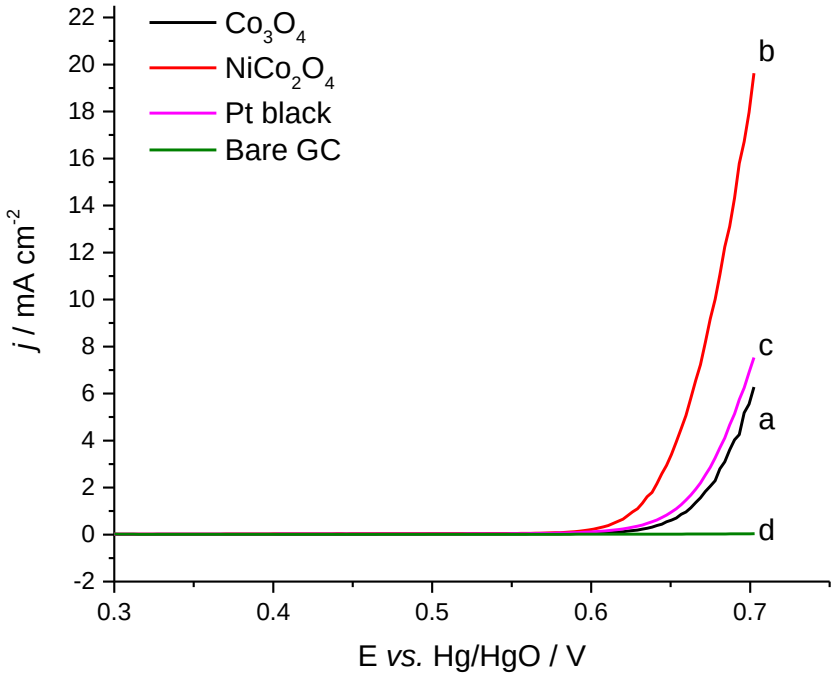

Figure 3.7. Voltammograms for Co_3O_4 (**a**), $NiCo_2O_4$ (**b**), Pt black (**c**) coated at glassy carbon and bare GC (**d**) RDE in 1 M KOH. Temperature: 298 K; Potential scan rate: 1 mV s^{-1}; Rotation rate: 400 RPM.

It can be seen in **Figure 3.7** that both spinels show catalytic activity for oxygen evolution. Moreover, the highest activity and lowest onset potential for oxygen evolution is obtained at $NiCo_2O_4$. Combination of results from oxygen reduction and evolution behaviours of spinels shows that both spinels have bifunctional behaviours for oxygen reduction and evolution. $NiCo_2O_4$ even has much better catalytic activity than Pt black under similar conditions. Therefore, this somewhat improves the comparison with Pt black as a bifunctional catalyst.

3.4.4. Electrolyte and Temperature Effects on Oxygen Reduction and Evolution

Figure 3.8 compares voltammograms for both oxygen evolution and reduction at a $NiCo_2O_4$ catalysed glassy carbon rotating disc electrode in two different O_2 saturated electrolyte concentrations (1 M KOH and 8 M KOH) at 25 ^oC (note that the current density scales for oxygen evolution and reduction are different).

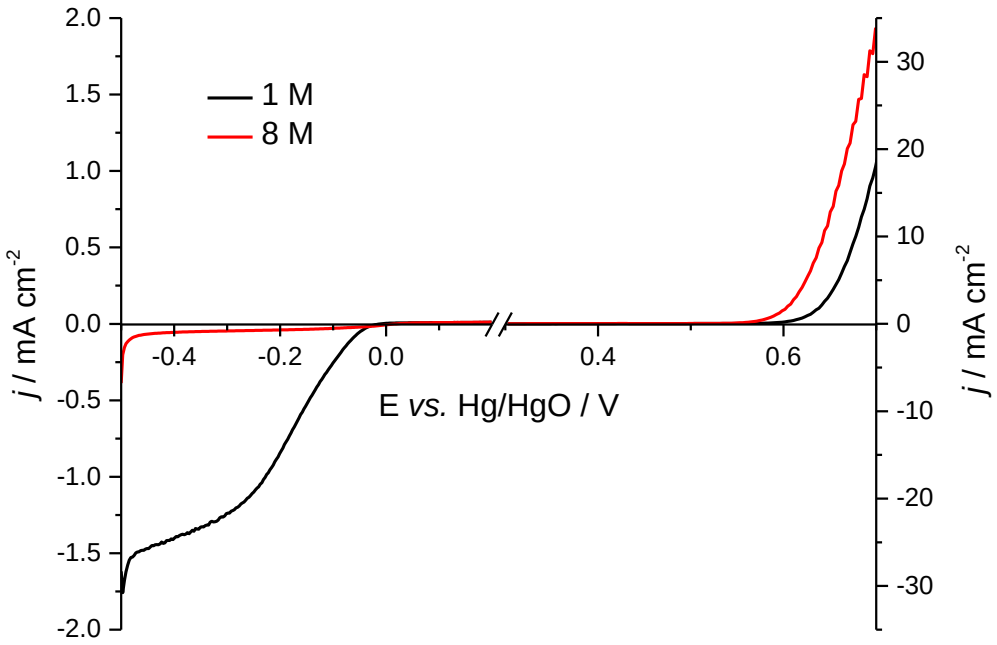

Figure 3.8. Voltammograms for O_2 reduction and evolution at a $NiCo_2O_4$ catalysed glassy carbon RDE in O_2 saturated 1 M KOH (black) and 8 M KOH (red) at 25 ^oC. Note the different current density scales for O_2 reduction and evolution. Rotation rate: 400 rpm; Potential scan rate: 1 mV s^{-1}.

The potential for oxygen evolution is shifted to less positive potential by increasing KOH concentration as expected. The current density for oxygen evolution is also increased with

increased electrolyte concentration. In contrast, there is a dramatic decrease in the current density for oxygen reduction by increasing the electrolyte concentration. The current density for oxygen reduction in 8 M KOH is almost 10 time smaller than that in 1 M KOH. This is due to the much decreased the solubility of oxygen with increasing KOH concentration. Moreover, there is also a significant decrease in the diffusion coefficient due to higher viscosity of 8 M KOH.[55, 58, 59]

Comparing the responses in **Figure 3.8** (see voltammogram 1 M KOH, 25 ^oC) and **Figure 3.9** (see voltammogram 8 M, 25 ^oC) show that there is a positive shift for the onset potential of the reduction wave with increase in KOH concentration at 25 ^oC.

Figure 3.9 also compares voltammograms for both oxygen evolution and reduction at a $NiCo_2O_4$ catalysed glassy carbon rotating disc electrode in O_2 saturated 8 M KOH at two different temperatures (25 ^oC and 60 ^oC) (note here also that the current density scales for oxygen evolution and reduction are different).

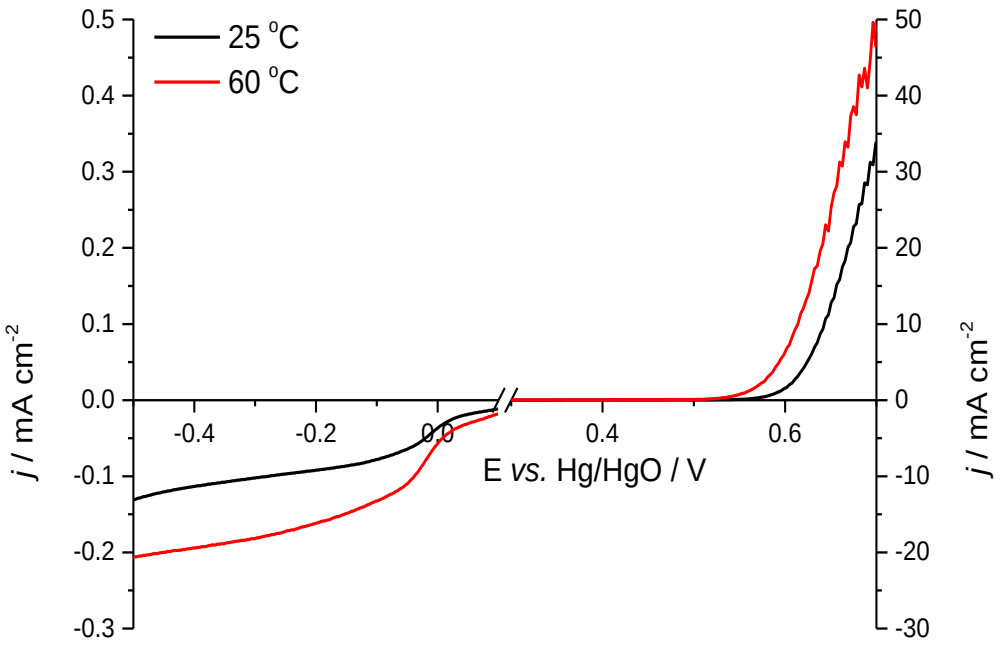

Figure 3.9. Voltammograms for O_2 reduction and evolution at a $NiCo_2O_4$ catalysed glassy carbon RDE in O_2 saturated 8 M KOH at temperatures of 25 ^oC (black) and 60 ^oC (red). Note the different current density scales for O_2 reduction and evolution. Reduction currents were recorded at 900 rpm and oxidation current at 400 rpm; Potential scan rate: 1 mV s^{-1}.

As shown in **Figure 3.9**, the current densities for both oxygen evolution and reduction are increased when the temperature is increased. It is also known that the solubility of oxygen is decreased while the oxygen diffusion coefficient increases with increased temperature.[59] Therefore, the direct comparison of the current densities for oxygen reduction at two temperatures is difficult.

Results from **Figure 3.8** and **Figure 3.9** show that the difference in potential between oxygen reduction and evolution is decreased by the increase in KOH concentration. There is even a further decrease between oxygen evolution and reduction potential in elevated temperature as shown in **Figure 3.9**. This confirms that operating a cell with 8 M KOH at 60 ^oC provides a smaller overpotential difference between oxygen reduction and evolution in addition to providing a maximum in the electrolyte conductivity, which is a reason normally to use potassium hydroxide rather than sodium hydroxide as electrolyte in such cells.

3.4.5. Rotating Rate Dependency of Oxygen Reduction Reaction (ORR)

The rotating rate dependency of voltammograms for oxygen reduction at spinels, Pt black and the graphitic carbon (XC-72R) was further investigated in order to gain further information about oxygen reduction pathway(s) at spinels. Well-formed sigmoidal reduction waves were obtained with all rotation rates for all four coatings. **Figure 3.10** shows the limiting current densities versus rotation rate dependency of oxygen reduction voltammograms at Co_3O_4 and $NiCo_2O_4$ coated electrodes under similar conditions. The limiting current density is observed for all rotation rates and the current density values are much higher at $NiCo_2O_4$ than that at Co_3O_4. It is also worth to note that the rate determining step in the electrode reaction at a potential in the plateau region can be either mass transport or a chemical step. There is no possibility for electron transfer since there is no current density change with potential change.

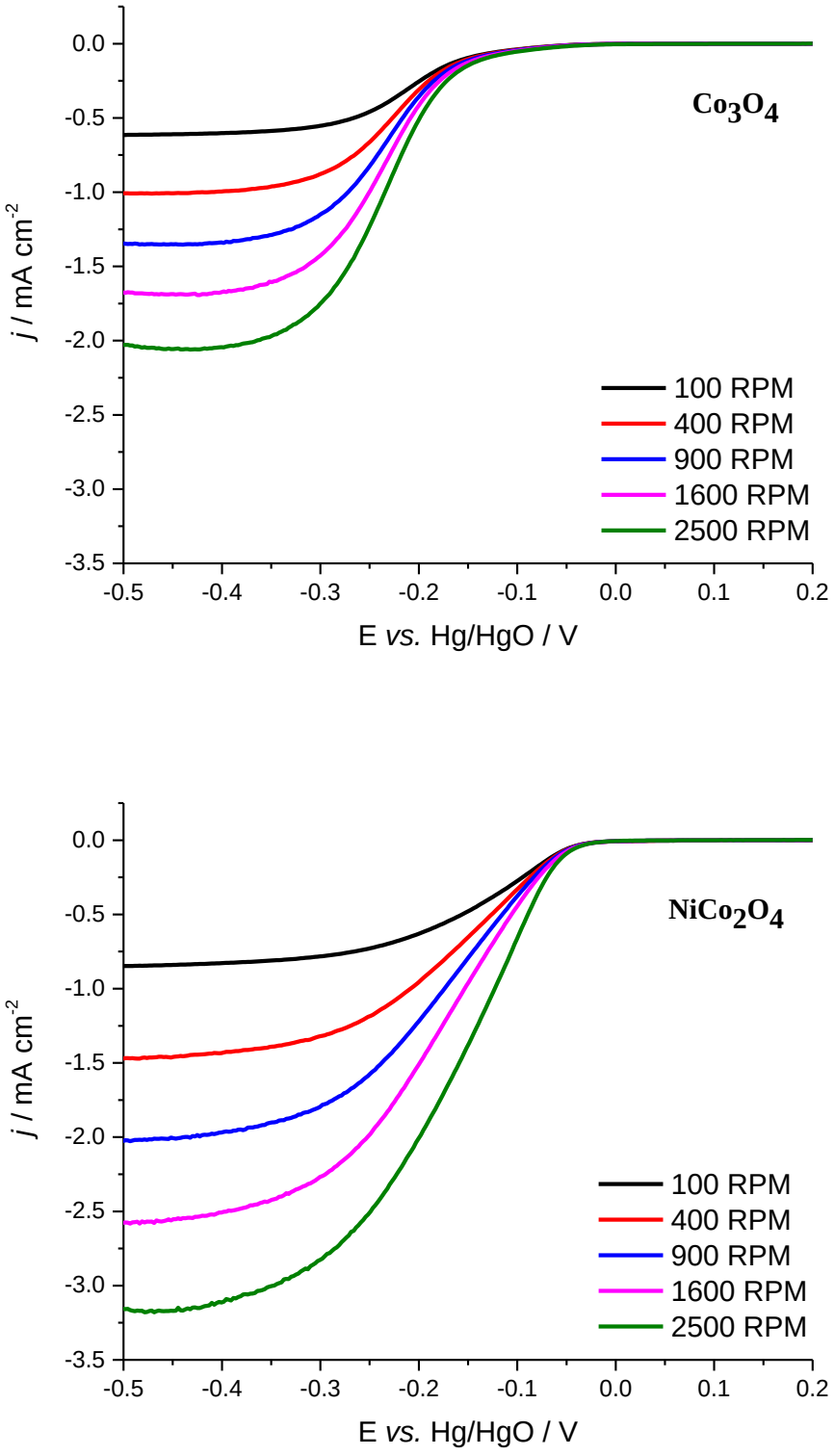

Figure 3.10. Rotation rate dependence of the voltammograms for the reduction of O_2 in oxygen saturated 1 M KOH at Co_3O_4 (**top**) and $NiCo_2O_4$ (**bottom**) coatings. Rotation rates are as shown. Temperature: 25 ^oC; Potential scan rate: 5 mV s^{-1}.

The limiting current densities at both spinel coatings are increased by increasing the rotation rates, however, the oxygen reduction is not fully mass transport controlled since the linear responses for both spinels do not pass through the origin as shown in **Figure 3.11**. These deviations from zero intercepts suggest that the measurements are not under pure mass transport control and suggest a kinetic limitation. The limiting current densities obtained at Pt black and XC-72R carbon coated electrodes are proportional to the square root of the rotation rates. However, the slopes of the Levich plots vary by a factor of 2, consistent with n = 2 at carbon and n = 4 at Pt black.

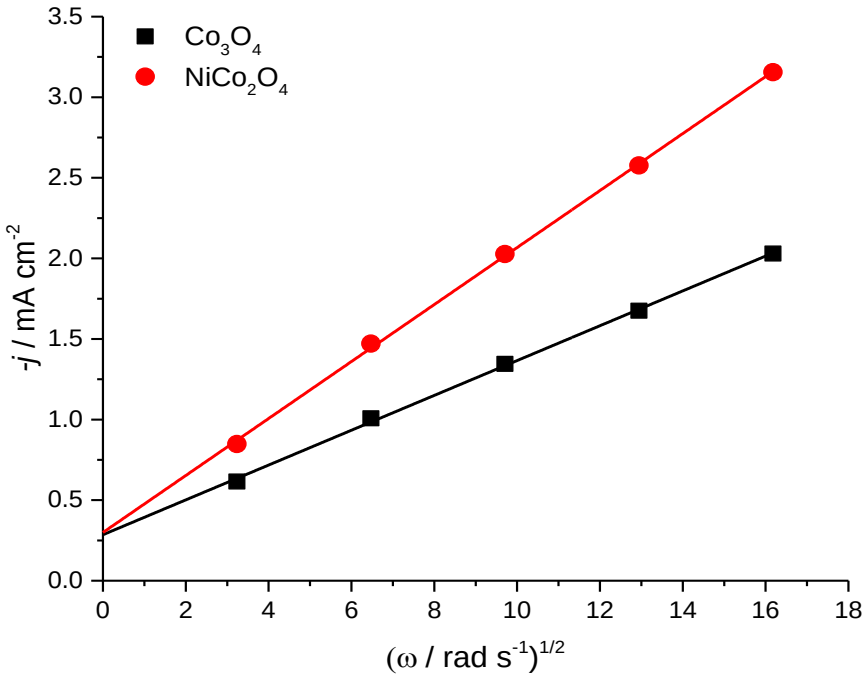

Figure 3.11. Levich plots of Co_3O_4 and $NiCo_2O_4$ coated on GC RDE in oxygen saturated 1 M KOH at 25 ^oC. The limiting current densities taken at -0.5 V *vs* Hg/HgO *vs* the rotation rates from **Figure 3.10**.

Since the limiting current densities (j_L) are partially limited by chemical step, they were further analysed with the Koutecky – Levich (**K – L**) equation (**Equation 3.1**):

$$\frac{1}{j_L} = \frac{1}{\mathrm{n\,F\,k}\,c_{o_2}} + \frac{1}{0.62\,n\,F\,D^{2/3}\,\nu^{-1/6}\,c_{o_2}\,\omega^{1/2}} \qquad \textbf{Equation 3.2}$$

Where j_L, n, F, k, c_{O_2}, D, v and ω are limiting current density, number of electrons/O_2 transferred during reaction, the Faraday constant, the rate constant for the chemical step in the reduction mechanism, the oxygen concentration in the electrolyte, the diffusion coefficient of O_2, the kinematic viscosity of the electrolyte and the rotation rate of the disc, respectively. Therefore, a Koutecky – Levich plot can be produced by plotting $1/j_L$ *vs* $1/\omega^{1/2}$, in which the comparative values of slopes provide information about "the number of electrons" involved in the reduction while the intercepts reflect the rate of the chemical step.

Figure 3.12 is Koutecky – Levich plots ($-1/j_L$ *vs* $1/\omega^{1/2}$) for the four coated electrodes. The slopes and intercepts from these plots are reported in **Table 3.3.**

Catalyst	**RDE data§**			**Koutecky – Levich**	
	$E_{-0.1\ mA\ cm^{-2}}$ *vs* Hg/HgO/ mV	**$E_{3/4} - E_{1/4}$/ mV**	**j_L/ mA cm^{-2}**	**Slope/ $mA^{-1}\ cm^2\ rpm^{-1/2}$**	**Intercept/ $mA^{-1}\ cm^2$**
Pt black	+ 50	- 53.7	- 1.6 (± 0.1)	- 11.0 (±0.1)	- 0.06 (±0.01)
Carbon (XC-72R)	- 137	- 63.3	- 1.0 (± 0.1)	- 17.0 (±0.3)	- 0.16 (±0.02)
Co_3O_4	- 149	- 75.8	- 1.01 (± 0.1)	- 13.1 (±0.5)	- 0.32 (±0.03)
$NiCo_2O_4$	- 61	- 117	- 1.5 (± 0.1)	- 10.2 (±0.3)	- 0.16 (±0.02)

Table 3.3. Comparison of catalyst materials RDE data. O_2 saturated 1 M KOH. Temperature: 25 ^oC; Rotation rate: 400 RPM. § Data taken for voltammograms recorded at 400 RPM. (Slopes and intercepts for all materials shown in the table are only from the first three points, corresponding to rotation rates of 100, 400 and 900 RPM).

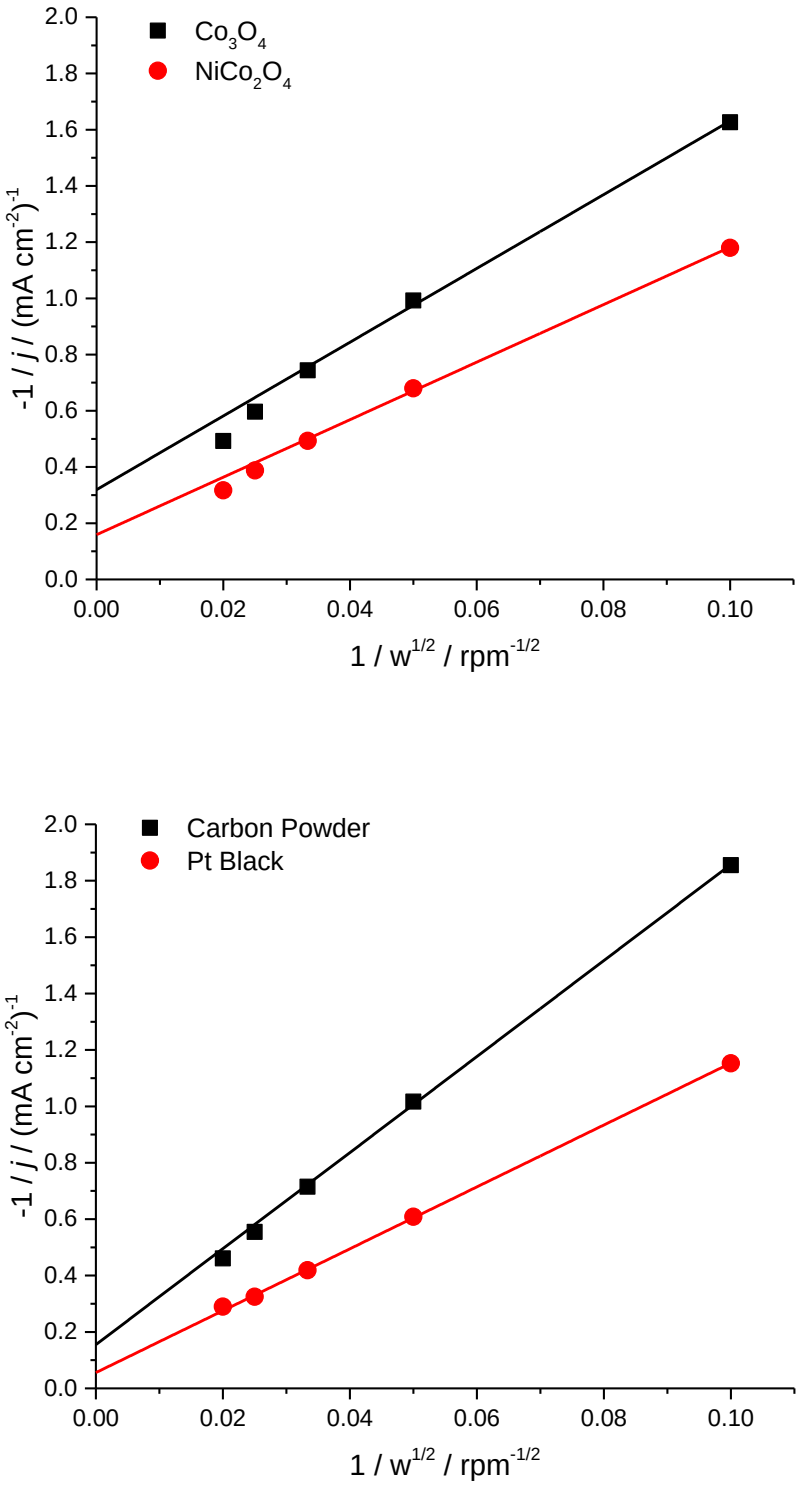

Figure 3.12. Koutecky – Levich plots for O_2 reduction in oxygen saturated 1 M KOH with Co_3O_4, $NiCo_2O_4$, carbon powder (XC-72R), Pt black coatings on glassy carbon. Data taken at -500 mV *vs* Hg/HgO in the plateau regions of the voltammograms. Temperature: 25 ^oC; Potential scan rate: 5 mV s^{-1}. Lines shown are best fits through only the three lowest rotation rates (100, 400, and 900 rpm), as discussed in the text.

As can be seen from **Figure 3.12**, the K – L plots of Pt black and carbon are linear and only have small intercepts on -1/j_L axis, however, they have different slopes as expected. These results for Pt black and carbon are consistent with mass transport limited currents but different values of n (n = 4e^- for Pt, n = 2 e^- for Carbon). **Figure 3.12** also shows the K – L plots for the spinels and here linear fit goes through first 3 or 4 data points at low rotation rates, but there is an obvious deviation at higher rotation rates (small values of $1/\omega^{1/2}$) especially for Co_3O_4. The slopes of K – L plots for spinels at low rotation rates are similar to the K – L slope for Pt black (see **Table 3.3**), confirming that the number of electrons involved in the reduction process are 4e^-. Moreover, there is a clear non-zero intercept on - 1/j_L axis for both spinels, which confirms a component of kinetic control to the limiting currents. The intercept for $NiCo_2O_4$ is much smaller than that for Co_3O_4. This indicates that the chemical step is more rapid at $NiCo_2O_4$. The deviation at higher rotation rates is likely because of a higher involvement of 2e^- reduction as also evident by the increase in slope (see **Table 3.3**).

3.4.6. Tafel plot

Figure 3.13 shows Tafel plots for the spinels made from the oxygen reduction voltammograms at 400 RPM between 0.0 and -0.2 V (from **Figure 3.6**). No further analyses were carried out for Tafel plots to gain information about the kinetics parameters since there is not a pure kinetic controlled region and thus no obvious linear portion of the Tafel plots.

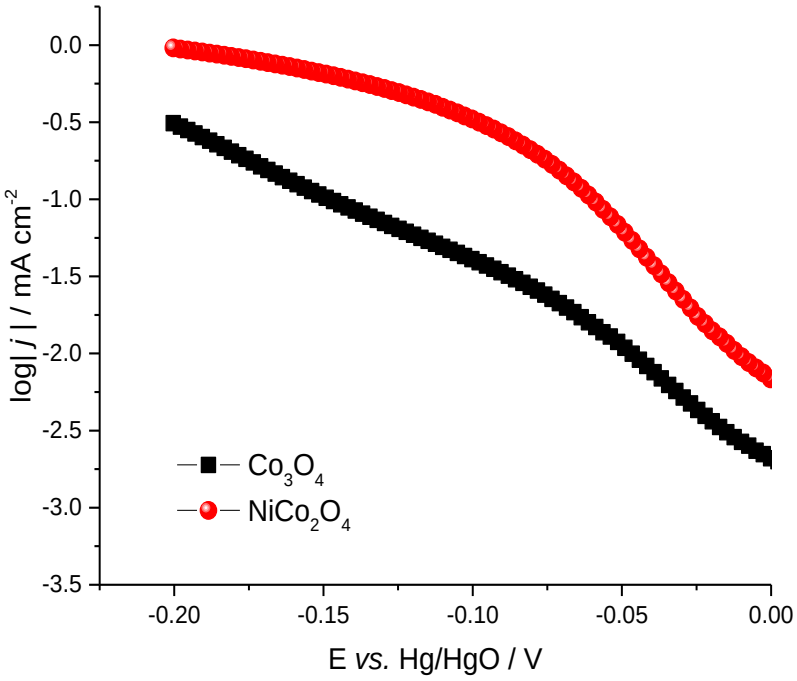

Figure 3.13. Tafel plots of Co_3O_4 and $NiCo_2O_4$ made from ORR voltammograms of spinels at 400 RPM (**Figure 3.6**). Data taken between 0.0 V and -0.2 V *vs* Hg/HgO.

3.4.7. Hydrogen Peroxide Formation as an Intermediate Product

All four samples (Pt black, carbon powder (XC-72R), Co_3O_4 and $NiCo_2O_4$) coated on the glassy carbon disc of a C/Pt ring electrodes with rotating ring disc electrode (RRDE) were further studied under similar conditions in order to investigate the formation of hydrogen peroxide (H_2O_2) as an intermediate in oxygen reduction. The potential of the disc (glassy carbon) was scanned while the ring electrode (Pt) potential was held at 0.2 V *vs* Hg/HgO, a potential where oxidation of H_2O_2 at Pt ring electrode is mass transport controlled.[60] **Figure 3.14** shows set of responses from Co_3O_4 and $NiCo_2O_4$ catalysed disc electrodes. The ratio of limiting currents for O_2 reduction and H_2O_2 oxidation were used to calculate the current efficiency for H_2O_2 formation during O_2 reduction. The current efficiencies are reported in **Table 3.4**. Although there is hydrogen peroxide formation on both spinels, the magnitudes of the ring currents are quiet different. The results in **Table 3.4** show that hydrogen peroxide collected at Pt ring represents a very low current efficiency for hydrogen peroxide (9% at 400 RPM) with $NiCo_2O_4$. In fact, SEM images of the edges of the catalyst coated glassy carbon electrode (see **2.4.8** section in **Chapter 2**) showed that the surface of glassy carbon electrode was not completely covered with ink.

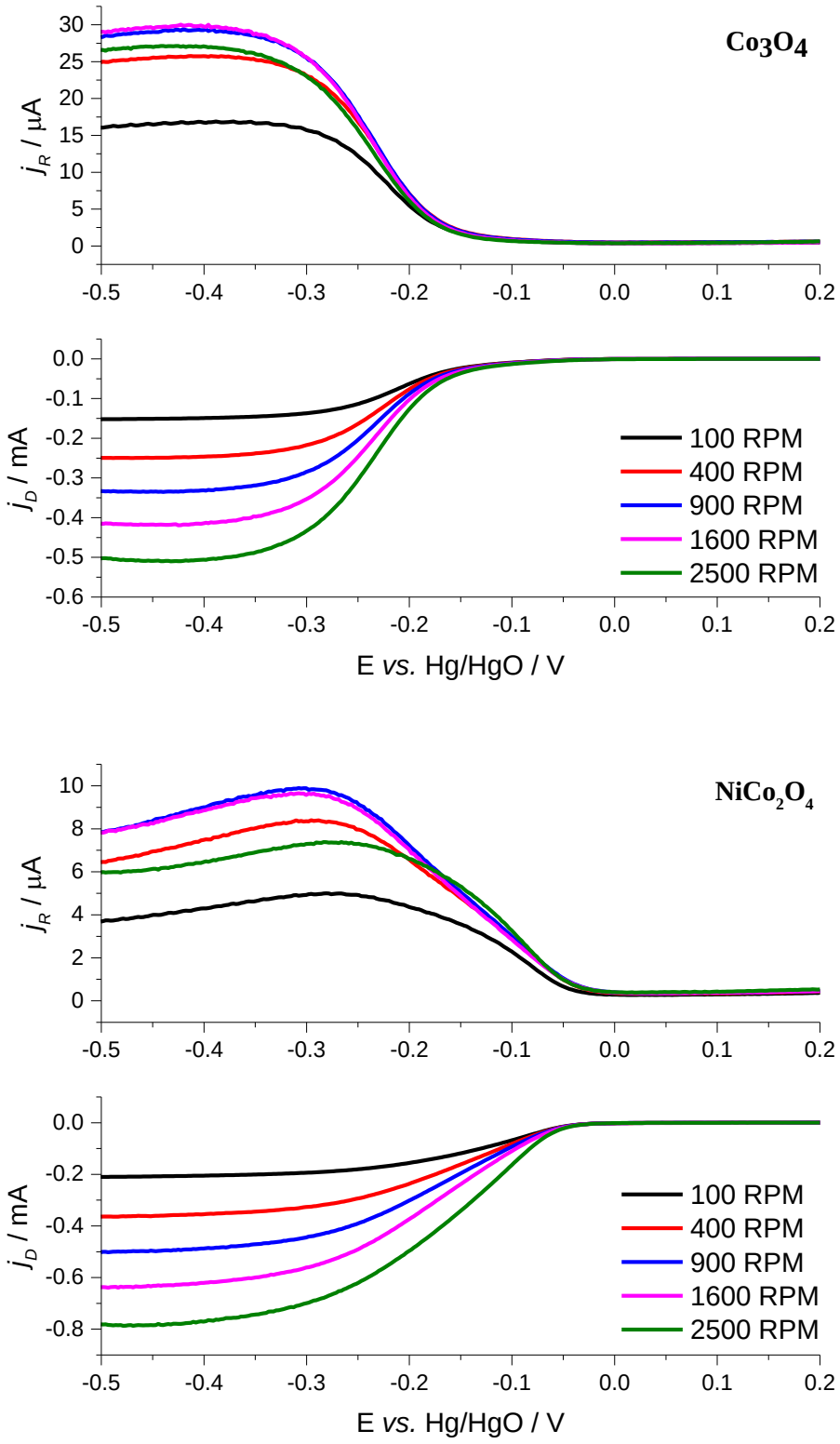

Figure 3.14. Disc and ring responses for O_2 reduction at Co_3O_4 and $NiCo_2O_4$ coated glassy carbon discs. The potential of the discs is scanned while the Pt ring electrode is held at + 200 mV *vs* Hg/HgO. Rotation rates as shown. O_2 saturated 1 M KOH; Temperature: 25 ^oC; Potential scan rate: 5 mV s^{-1}; The collection efficiency of the RRDE: 0.37.

Catalyst	% H_2O_2[§]
Pt black	< 1.0
Carbon (XC-72R)	59.5 (± 3.0)
Co_3O_4	42.5 (± 2.1)
$NiCo_2O_4$	9.0 (± 0.5)

Table 3.4. Comparison of catalyst materials RRDE data. O_2 saturated 1 M KOH. Temperature: 25 ^oC; § data rotation rate: 400 RPM.

This uncovered glassy carbon electrode surface close to the PTFE surround was exposed to substrate and this could easily account for the small amount of hydrogen peroxide formation since oxygen reduction occurs on glassy carbon electrode via hydrogen peroxide formation pathway ($2e^-$). On the other hand, hydrogen peroxide formation (42.5% at 400 RPM) is significant at the Co_3O_4 catalyst coated disc. The results obtained for H_2O_2 oxidation at Pt black and carbon powder (at 400 RPM) are <1% and 59.5%, respectively. While the formation of hydrogen peroxide is a minor contribution at the Pt black coated electrode, it becomes a main reaction with carbon powder since 59.5% of the charge at the disc with carbon electrode leads to H_2O_2 and this is expected from the known performance of carbon based GDEs.[57]

3.4.8. Hydrogen Peroxide Oxidation and Reduction

The oxidation and reduction voltammograms of 10 mM hydrogen peroxide in N_2 purged 1 M KOH with different rotation rates at Co_3O_4 and $NiCo_2O_4$ coated electrodes are shown in **Figure 3.15.** Oxidation and reduction are observed at both electrodes, however, the current densities for reduction are much smaller than that for oxidation (both the oxidation and the reduction of hydrogen peroxide involve $2e^-$, therefore the mass transfer controlled current densities were expected to be equal). It is also obvious that the oxidation limiting currents are not fully mass transport controlled at both spinels. It is partially mass transport controlled at low rotation rates (100 and 400 RPM), however, there is not any proportionality between the limiting currents and the square root of rotation rates. In addition, all the currents are low compared to those expected for the estimated concentration of hydrogen peroxide.

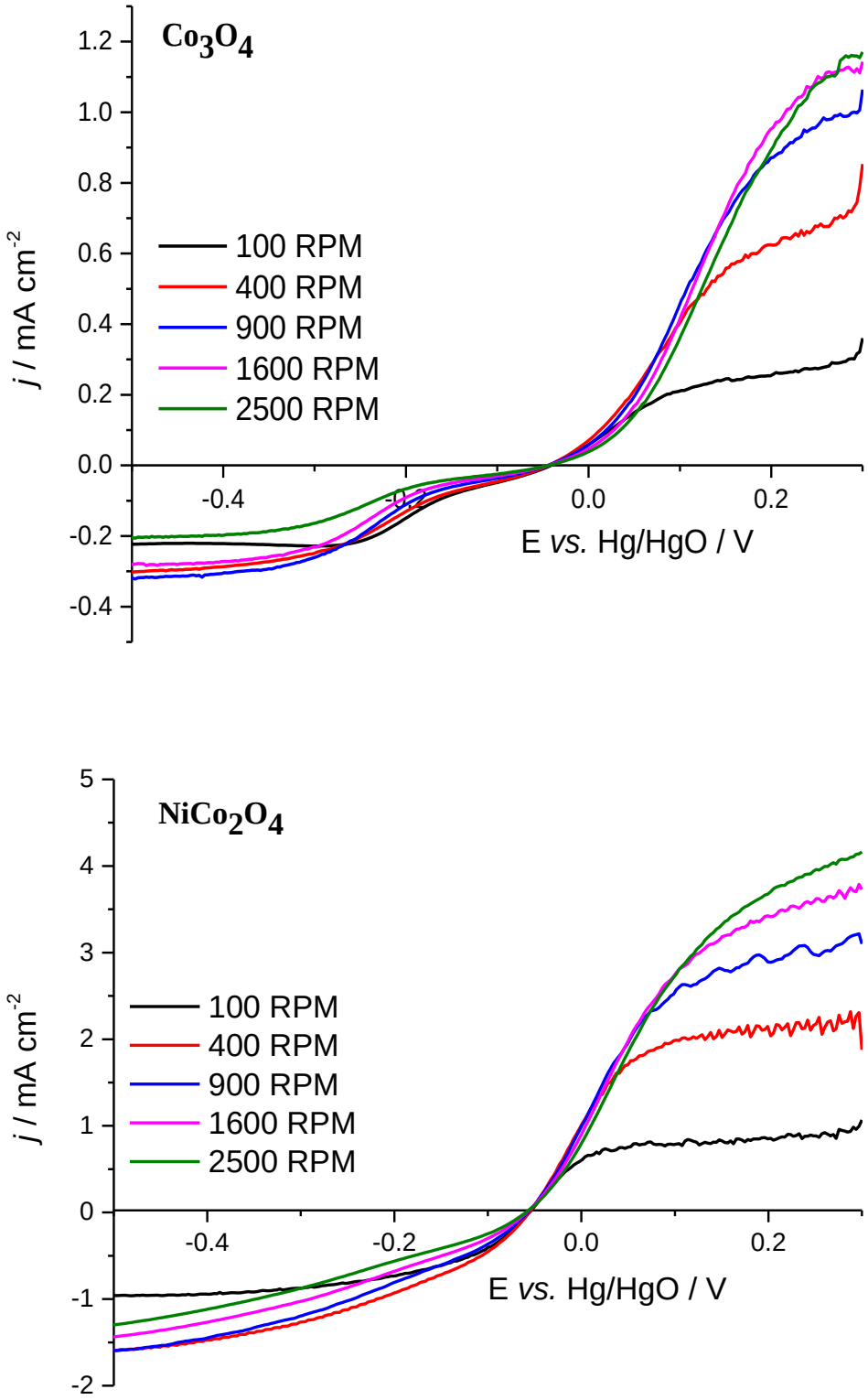

Figure 3.15. Rotation rate dependence of the voltammogram for the reduction of ≈ 10 mM H_2O_2 in N_2 purged 1 M KOH at Co_3O_4 and $NiCo_2O_4$ coated glassy carbon. Rotation rates are as shown. Temperature: 25 ^oC; Potential scan rate: 1 mV s^{-1}.

On the other hand, the limiting currents for the hydrogen peroxide reduction are almost completely independent of the rotation rates confirming that there is a strong kinetic limitation to the reduction of hydrogen peroxide at both spinels. According to results from **Figure 3.15**, a $2e^- + 2e^-$ mechanism for a $4e^-$ reduction is improbable due to a strong kinetic limitation/slow rate for the reduction of hydrogen peroxide at the spinel coatings.

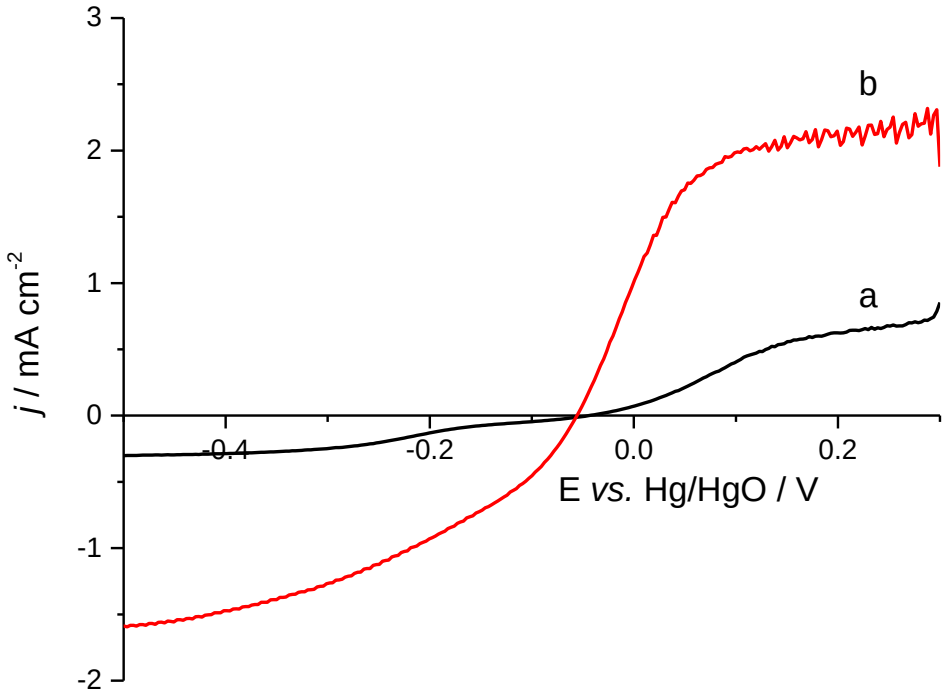

Figure 3.16. Voltammograms at glassy carbon RDE coated with (**a**) Co_3O_4 (**b**) $NiCo_2O_4$ for ≈ 10 mM H_2O_2 in N_2 purged 1 M KOH. Temperature: 25 ^oC; Rotation rate: 400 rpm; Potential scan rate: 1 mV s^{-1}.

Figure 3.16 compares the voltammograms of oxidation and reduction of hydrogen peroxide (H_2O_2) at spinels (at 400 RPM). It is obvious that oxidation and reduction of hydrogen peroxide are more rapid at $NiCo_2O_4$ than that at Co_3O_4 since the limiting currents for oxidation and reduction obtained at $NiCo_2O_4$ are higher (almost 4 times) than that at Co_3O_4.

3.5. Discussion

Transition metal oxides (the perovskite, pyrochlore and spinel structure) have been widely studied as alternative electrocatalysts to noble metals for oxygen reduction.[6, 11, 13, 61,

[62] Many of these oxides can be easily produced from cheap starting materials (such as nitrates, acetates, carbonates) and they can be conductive and sometimes show electrocatalytic activity for oxygen reduction as well as oxygen evolution. Conductive Co_3O_4 and $NiCo_2O_4$ both have spinel structures and they can easily be produced from aqueous nitrates solutions. Their electrochemical properties can be screened by drop casting graphitic carbon free catalyst ink onto an inert RDE.

In this study, physical characterization techniques (XRD, BET, SEM and TEM) proved that Co_3O_4 and $NiCo_2O_4$ have spinel structure and the high surface area of powdered spinels were obtained (the surface area of $NiCo_2O_4$ is higher (more than twice) than Co_3O_4). Irregular nano scale size particles were shown by SEM and TEM.

Cyclic voltammetry shows that well-formed oxidation and reduction peaks at both spinels are characteristic for cobalt, nickel and mixed Co/Ni oxides due to the change in the oxidation states of Co(III)/Co(IV) at the surface of thin film electrode in alkaline media. The charge under the anodic peak (1.5 mC cm^{-2}) is the same as that of the cathodic peak (1.5 mC cm^{-2}), confirming that all chemistry is reversible. Results also show that only surface layer of thin electrode is oxidised and reduced during potential cycling since the oxidation/reduction peak charge is almost 20 times smaller than the charge for all the nickel and cobalt ions in the film electrode. Open circuit potential experiments confirmed that oxygen reduction occurs on the surface of spinels in low oxidation state since there is no oxidation change between the oxygen reduction and that in prepared spinels. In contrast, oxygen evolution takes place on the surface of spinels in a “higher oxidation state” and Ni and Co ions are slowly reacting with the electrolyte in order to return the spinels to their original oxidation states at open circuit potential ($\approx +0.1$ V). This relaxation takes much longer with Co_3O_4.

Oxygen reduction and oxygen evolution behaviours were shown at both spinels with a large limiting current densities between spinels. Oxygen reduction occurs at Co_3O_4 with much less limiting current density and at a higher onset potential than that at $NiCo_2O_4$. While the limiting current at Co_3O_4 is almost the same of that at carbon (XC-72R), the limiting current at $NiCo_2O_4$ is slightly less than Pt black. The oxygen evolution results at both spinels and Pt black show that both spinels have oxygen evolution behaviours. Even higher oxygen evolution activity and lower onset potential were observed at $NiCo_2O_4$ than that at Pt black. Therefore, this much higher oxygen evolution and slightly less oxygen reduction activity

somewhat make $NiCo_2O_4$ as an important non-noble bifunctional catalyst compared to Pt black.

To compare oxygen reduction mechanism at spinels, $NiCo_2O_4$ an effective catalyst for oxygen reduction shows $4e^-$ reduction (like Pt) in alkaline media at a rate approaching mass transport control even though it has a slightly larger over-potential (110 mV) than Pt. On the other hand, Co_3O_4 is a poor catalyst for oxygen reduction with larger overpotential and half the limiting current compared to Pt black. The voltammetry shows that $4e^-$ reduction occurs at some mass transport conditions (especially low rotation rates), however, it also implies slow kinetics in the $4e^-$ pathway (most likely the initial cleavage of the O – O bond) allowing the $2e^-$ pathway to overcome especially at higher rotation rates of convection. Therefore, the limiting currents are pretty much below than the one for a mass transfer controlled $4e^-$ reaction. In addition, RRDE studies also show that a substantial fraction of charge passed leads to hydrogen peroxide formation. It is also shown in the literature[6, 62] that the cobalt spinel is a poor oxygen reduction catalyst and high amount of hydrogen peroxide formation is observed.[63] Even in a recent Co_3O_4 and cobalt based oxide review[13], the oxygen reduction properties of cobalt oxide were not mentioned. In contrast, N. Heller-Ling et al.[40] found that the full $4e^-$ reduction was catalysed by Co_3O_4 coatings. In addition, several recent studies on electrode coatings containing nanostructured Co_3O_4 show very good oxygen reduction activities with mainly $4e^-$ reduction pathway.[29, 30, 34, 64] The reason for the inconsistency with the work in this chapter and these reports are not clear. A recent study[34] shows the oxygen reduction activity of Co_3O_4 nanochains since Co_3O_4/C catalyst has even higher current density than Pt/C. However, all these coatings have an active carbon, a graphitic carbon powder or graphene. The effect of adding carbon is not generally explained in these reports. However, the effect of the nanostructured Co_3O_4 could increase the catalytic activity towards ORR if Co_3O_4 has a high density of the active sides, promoting the cleavage of O – O bond.

With $NiCo_2O_4$ coating, RDE data show that oxygen is reduced via $4e^-$ pathway, which is consistent with RRDE data since there is a very low hydrogen peroxide formation (9%). Hydrogen peroxide reduction data show that the cathodic reduction of H_2O_2 at $NiCo_2O_4$ is strongly kinetically limited and this rules out a reaction pathway for oxygen reduction where H_2O_2 is produced and rapidly further reduced. Therefore, oxygen should be reduced at $NiCo_2O_4$ via a mechanism where the O – O bond is cleaved in an initial step. It has been shown by Levich and Koutecky – Levich plots that oxygen reduction is not completely mass transport controlled. Even in the limiting current plateau, it is in some degree kinetically

controlled by the rate of this O – O cleavage reaction. At high rotation rate, there is more pressure on the chemical step, presumed to be cleavage of the O – O bond, and because of this, the opportunity for electron transfer is increased as the first step and hence for the formation of H_2O_2 in a $2e^-$ step and slight deviation from the linearity of K – L plot for $NiCo_2O_4$.

With Co_3O_4 coating, the results are consistent with a similar mechanism, however, the chemical step is much slower in this mechanism. Therefore, $2e^-$ reduction role is larger in this case. The RRDE experiment proves that the hydrogen peroxide formation is massive and the Koutecky – Levich plot has much larger intercept. It has been also seen from K – L plot that oxygen is reduced with $4e^-$ at low rotation rates, however, K – L slope is largely deviated toward that for $2e^-$ reduction slope at higher rotation rates.

Therefore, it can be concluded that $2e^-$ and $4e^-$ reduction pathways are happening in parallel for oxygen reduction and the relative importance of two mechanisms changes with mass transport conditions at intermediate rate constants for the chemical step. As can be seen in the K – L plots, there is a deviation at higher rotation rates, implying that increasing rotation rate increases the pressure on the chemical step in the direct $4e^-$ reduction. It is probably right to say that the $2e^-$ reduction is, in general, the "default mechanism" owing to slow cleavage rate of O – O bond. The potentials for electron addition to O_2 are only slightly negative to that for the direct $4e^-$ reduction initiated by a chemical step such as O – O bond cleavage. Of course, the effect of electrocatalyst and the kinetics of the chemical step on catalyst's surface are critical in determining the potential for the $4e^-$ reduction. With a catalyst and carbon layer, it is definitely possible that two mechanisms happen in competition with the relative importance of the two routes depending on the O – O bond cleavage rate at the other catalyst.

Oxygen is predominantly reduced by a $4e^-$ reaction at $NiCo_2O_4$ coated cathode electrode, which is leading to water with almost no intermediate (H_2O_2) product. A chemical step controls the rate limitation and this is most likely the cleavage of the O – O bond on the surface of the spinel. In contrast, oxygen is reduced with much lower current densities at Co_3O_4 coated cathode electrode and it can be said that the rate of cleavage of the O – O bond and hence the $4e^-$ reduction is significantly slower, which is leading to an important contribution from a competing mechanism. Almost half of the charge passed at a Co_3O_4 coating leads to hydrogen peroxide formation.

According to the literature and the studies in **Chapter 5**, spinels prepared via different methods (such as, thermal decomposition, spray pyrolysis, electrostatic spray deposition, sol gel, precipitation, electrospinning, anodic oxidation of alloys, rheological phase reaction and pyrolysis, gel hydrothermal oxidation, electrodeposition, etc.)[13] and using different conditions within a single method show a large variation in the rate of oxygen reduction, however, the reasons cannot be explained from the information available (probably it is from different crystallite size, surface area, or a small variation in the composition of mixed oxides, etc.).

3.6. References

1. P. Rasiyah and A. C. C. Tseung, *J. Electrochem. Soc.*, 1983, **130**, 365-368.
2. P. Rasiyah, A. C. C. Tseung and D. B. Hibbert, *J. Electrochem. Soc.*, 1982, **129**, 1724-1727.
3. P. Rasiyah and A. C. C. Tseung, *J. Electrochem. Soc.*, 1983, **130**, 2384-2386.
4. R. N. Singh, J. F. Koenig, G. Poillerat and P. Chartier, *J. Electrochem. Soc.*, 1990, **137**, 1408-1413.
5. M. De Koninck, S.-C. Poirier and B. Marsan, *J. Electrochem. Soc.*, 2006, **153**, A2103-A2110.
6. V. Nikolova, P. Iliev, K. Petrov, T. Vitanov, E. Zhecheva, R. Stoyanova, I. Valov and D. Stoychev, *J. Power Sources*, 2008, **185**, 727-733.
7. P. W. Menezes, A. Indra, N. R. Sahraie, A. Bergmann, P. Strasser and M. Driess, *ChemSusChem*, 2015, **8**, 164-171.
8. R. Ning, J. Q. Tian, A. M. Asiri, A. H. Qusti, A. O. Al-Youbi and X. P. Sun, *Langmuir*, 2013, **29**, 13146-13151.
9. J. Suntivich, K. J. May, H. A. Gasteiger, J. B. Goodenough and Y. Shao-Horn, *Science*, 2011, **334**, 1383-1385.
10. J. Suntivich, H. A. Gasteiger, N. Yabuuchi, H. Nakanishi, J. B. Goodenough and Y. Shao-Horn, *Nat. Chem.*, 2011, **3**, 647-647.
11. J. Suntivich, H. A. Gasteiger, N. Yabuuchi and Y. Shao-Horn, *J. Electrochem. Soc.*, 2010, **157**, B1263-B1268.
12. A. Grimaud, K. J. May, C. E. Carlton, Y. L. Lee, M. Risch, W. T. Hong, J. G. Zhou and Y. Shao-Horn, *Nat. Commun.*, 2013, **4**.
13. M. Hamdani, R. N. Singh and P. Chartier, *Int. J. Electrochem. Sci.*, 2010, **5**, 556-577.

14. P. Cox and D. Pletcher, *J. Appl. Electrochem.*, 1990, **20**, 549-554.
15. B. Chi, J.-B. Li, Y.-S. Han and J.-H. Dai, *Mater. Lett.*, 2004, **58**, 1415-1418.
16. X. H. Li, D. Pletcher, A. E. Russell, F. C. Walsh, R. G. A. Wills, S. F. Gorman, S. W. T. Price and S. J. Thompson, *Electrochem. Commun.*, 2013, **34**, 228-230.
17. S. W. T. Price, S. J. Thompson, X. H. Li, S. F. Gorman, D. Pletcher, A. E. Russell, F. C. Walsh and R. G. A. Wills, *J. Power Sources*, 2014, **259**, 43-49.
18. C. Bocca, A. Barbucci, M. Delucchi and G. Cerisola, *Int. J. Hydrog. Energy*, 1999, **24**, 21-26.
19. C. R. Davidson, G. Kissel and S. Srinivasan, *J. Electroanal. Chem.*, 1982, **132**, 129-135.
20. I. Nikolov, R. Darkaoui, E. Zhecheva, R. Stoyanova, N. Dimitrov and T. Vitanov, *J. Electroanal. Chem.*, 1997, **429**, 157-168.
21. T. Poux, F. S. Napolskiy, T. Dintzer, G. Kerangueven, S. Y. Istomin, G. A. Tsirlina, E. V. Antipov and E. R. Savinova, *Catal. Today*, 2012, **189**, 83-92.
22. A. Tseung and K. Yeung, *J. Electrochem. Soc.*, 1978, **125**, 1003-1005.
23. S. Malkhandi, P. Trinh, A. K. Manohar, K. C. Jayachandrababu, A. Kindler, G. K. S. Prakash and S. R. Narayanan, *J. Electrochem. Soc.*, 2013, **160**, F943-F952.
24. N. Staud and P. Ross, *J. Electrochem. Soc.*, 1986, **133**, 1079-1084.
25. P. N. Ross and M. Sattler, *J. Electrochem. Soc.*, 1988, **135**, 1464-1470.
26. N. Staud, H. Sokol and P. N. Ross, *J. Electrochem. Soc.*, 1989, **136**, 3570-3576.
27. S. Müller, F. Holzer, H. Arai and O. Haas, *J. New Mater. Electrochem. Syst.*, 1999, **2**, 227-232.
28. Y. Liang, Y. Li, H. Wang, J. Zhou, J. Wang, T. Regier and H. Dai, *Nat. Mater.*, 2011, **10**, 780-786.
29. J. Xu, P. Gao and T. Zhao, *Energy Environ. Sci.*, 2012, **5**, 5333-5339.
30. Y. J. Sa, K. Kwon, J. Y. Cheon, F. Kleitz and S. H. Joo, *J. Mater. Chem. A*, 2013, **1**, 9992-10001.
31. C. Jin, F. Lu, X. Cao, Z. Yang and R. Yang, *J. Mater. Chem. A*, 2013, **1**, 12170-12177.
32. D. U. Lee, B. J. Kim and Z. Chen, *J. Mater. Chem. A*, 2013, **1**, 4754-4762.
33. M. Prabu, K. Ketpang and S. Shanmugam, *Nanoscale*, 2014, **6**, 3173-3181.
34. P. W. Menezes, A. Indra, D. González-Flores, N. R. Sahraie, I. Zaharieva, M. Schwarze, P. Strasser, H. Dau and M. Driess, *ACS Catal.*, 2015, **5**, 2017-2027.
35. F. Kong, *Electrochim. Acta*, 2012, **68**, 198-201.

36. J. Shen, X. Li, N. Li and M. Ye, *Electrochim. Acta*, 2014, **141**, 126-133.
37. Z.-Q. Liu, Q.-Z. Xu, J.-Y. Wang, N. Li, S.-H. Guo, Y.-Z. Su, H.-J. Wang, J.-H. Zhang and S. Chen, *Int. J. Hydrog. Energy*, 2013, **38**, 6657-6662.
38. D. Pletcher, X. Li, S. W. Price, A. E. Russell, T. Sönmez and S. J. Thompson, *Electrochim. Acta*, 2016, **188**, 286-293.
39. T. Sönmez, S. J. Thompson, S. W. Price, D. Pletcher and A. E. Russell, *J. Electrochem. Soc.*, 2016, **163**, H884-H890.
40. N. Heller-Ling, M. Prestat, J.-L. Gautier, J.-F. Koenig, G. Poillerat and P. Chartier, *Electrochim. Acta*, 1997, **42**, 197-202.
41. J. Marco, J. Gancedo, M. Gracia, J. Gautier, E. Rios and F. Berry, *J. Solid State Chem.*, 2000, **153**, 74-81.
42. M. Lenglet, R. Guillamet, J. Dürr, D. Gryffroy and R. Vandenberghe, *Solid State Commun.*, 1990, **74**, 1035-1039.
43. F. Svegl, B. Orel, I. Grabec-Svegl and V. Kaucic, *Electrochim. Acta*, 2000, **45**, 4359-4371.
44. G. Spinolo, S. Ardizzone and S. Trasatti, *J. Electroanal. Chem.*, 1997, **423**, 49-57.
45. R. Boggio, A. Carugati and S. Trasatti, *J. Appl. Electrochem.*, 1987, **17**, 828-840.
46. J. Haenen, W. Visscher and E. Barendrecht, *J. Electroanal. Chem.*, 1986, **208**, 323-341.
47. M. El Baydi, S. K. Tiwari, R. N. Singh, J.-L. Rehspringer, P. Chartier, J. F. Koenig and G. Poillerat, *J. Solid State Chem.*, 1995, **116**, 157-169.
48. P. Nkeng, J.-F. Koenig, J. Gautier, P. Chartier and G. Poillerat, *J. Electroanal. Chem.*, 1996, **402**, 81-89.
49. B. Chi, J. Li, Y. Han and Y. Chen, *Int. J. Hydrog. Energy*, 2004, **29**, 605-610.
50. B. Chi, H. Lin, J. Li, N. Wang and J. Yang, *Int. J. Hydrog. Energy*, 2006, **31**, 1210-1214.
51. Y. Q. Wu, X. Y. Chen, P. T. Ji and Q. Q. Zhou, *Electrochim. Acta*, 2011, **56**, 7517-7522.
52. N. Padmanathan and S. Selladurai, *Ionics*, 2013, **19**, 1535-1544.
53. M. A. Prathap and R. Srivastava, *Nano Energy*, 2013, **2**, 1046-1053.
54. H. H. Yang and R. L. McCreery, *J. Electrochem. Soc.*, 2000, **147**, 3420-3428.
55. D. Zhang, J. Wu, L. Mao, T. Okajima, F. Kitamura, T. Ohsaka and T. Sotomura, *Indian J. Chem., Sect. A*, 2003, **42**, 801-806.

56. A. Sarapuu, K. Vaik, D. J. Schiffrin and K. Tammeveski, *J. Electroanal. Chem.*, 2003, **541**, 23-29.
57. P. Foller and R. Bombard, *J. Appl. Electrochem.*, 1995, **25**, 613-627.
58. K. E. Gubbins and R. D. Walker, *J. Electrochem. Soc.*, 1965, **112**, 469-471.
59. R. Davis, G. Horvath and C. Tobias, *Electrochim. Acta*, 1967, **12**, 287-297.
60. N. M. Markovic, H. A. Gasteiger and P. N. Ross Jr, *J. Phys. Chem.*, 1995, **99**, 3411-3415.
61. L. Jorissen, *J. Power Sources*, 2006, **155**, 23-32.
62. V. Neburchilov, H. Wang, J. J. Martin and W. Qu, *J. Power Sources*, 2010, **195**, 1271-1291.
63. S. Jiang, Z. Lin and A. Tseung, *J. Electrochem. Soc.*, 1990, **137**, 764-769.
64. Y. Y. Liang, Y. G. Li, H. L. Wang, J. G. Zhou, J. Wang, T. Regier and H. J. Dai, *Nat. Mater.*, 2011, **10**, 780-786.

Chapter 4: Spinel Manganese-Cobalt Oxides ($Mn_xCo_{3-x}O_4$, $0.0 \leq x \leq 2.0$) as ORR Catalyst

This chapter will focus on the effect of manganese as a dopant into the spinel Co_3O_4 with a wide dopant ratio ($Mn_xCo_{3-x}O_4$ ($0.0 \leq x \leq 2.0$). The main focus will be on the effects of the structural features, on the catalytic activity for oxygen reduction/evolution and the oxygen reduction mechanism at these materials in alkaline media.

4.1. Introduction

At the beginning of this study, five materials with different Co:Mn atomic ratios (Co_3O_4, $Mn_{0.5}Co_{2.5}O_4$, $MnCo_2O_4$, $Mn_{1.5}Co_{1.5}O_4$ and Mn_2CoO_4) were produced via a thermal decomposition method by calcining a mixture of cobalt and manganese nitrates sequentially at 260 and 600 ^oC in an electric furnace. All electrochemical characterisations of these materials showed that doping manganese into cobalt oxide increases the catalytic activity for ORR. The highest ORR activity and lowest onset potential were observed with $MnCo_2O_4$. The oxygen reduction pathway (ratio of mechanisms, $2e^-$ or $4e^-$) also varied. However, X - ray Diffraction (XRD) results show that there was more than a single phase, especially with $MnCo_2O_4$. Therefore, the materials with the same atomic ratios were produced again with a "co-precipitation method" and in this case only a single crystalline phase was observed for $MnCo_2O_4$ in the XRD measurements. All electrochemical and physical characterisations were then completed on these Mn/Co materials with different atomic ratios produced via the co-precipitation method. The electrochemical results and the oxygen reduction activities on spinel Mn/Co materials produced via both thermal decomposition and co-precipitation methods generally showed the same results and the highest ORR activity was observed with $MnCo_2O_4$, which shows a cubic spinel structure. All physical, spectroscopic and electrochemical characterisation results shown in this chapter are from $Mn_xCo_{3-x}O_4$ ($0.0 \leq x \leq 2.0$) materials produced via "co-precipitation method" unless otherwise stated.

4.2. Experimental

In general, a co-precipitation method was used for the materials reported for this chapter. However, five spinel samples ($Mn_xCo_{3-x}O_4$ ($0.0 \leq x \leq 2.0$)) were also produced via a thermal decomposition method and these samples will be mentioned in some sections.

Therefore, the preparation of the materials produced via "thermal decomposition" is also described in this section. The amount of nitrates for each sample and preparation details are described in the next sections. The concentration of mixed solutions ($Co(NO_3)_2.6H_2O$/$Mn(NO_3)_2.4H_2O$ and deionised H_2O) was kept around 0.2 M. Higher concentration (> 0.2 M) of the precursors mixture results in larger nanoparticles[1], which is less favourable for electrocatalysis. As shown in the synthesis parts, there are two calcination steps (260 and 600 ^oC). The reason for choosing these calcination temperatures comes from a thermogravimetric (TG) analysis. TG analysis (see **Figure 4.1**) was first applied to the mixture of nitrate salts (1.910 g $Co(NO_3)_2.6H_2O$ and 0.8413 g $Mn(NO_3)_2.4H_2O$ in 50 cm^3 deionised water) in order to choose the correct calcination temperature. There are two main weight losses (see **Figure 4.1**) at 31-150 ^oC and 150-280 ^oC. While the first weight loss comes from water evaporation, the decomposition of the nitrates is observed in the second weight loss.[2] The nitrate decomposition occurs at the same time with water evaporation or right after water evaporation. The decomposition process is quite complicated since there are many unstable intermediates such as $MnONO_3$, CoO, Co_2O_3, $CoO.CoONO_3$, $Co_2(NO_3)_2(OH)_2$, $MnO_{1.2}(NO_3)_{0.8}$ and Co_2ONO_3.[2, 3] The spinel structure forms between 280 and 900 ^oC, which is consistent with the literature.[3] Spinel materials can be produced over this temperature range with varying particle size, surface area and extent of crystallinity.

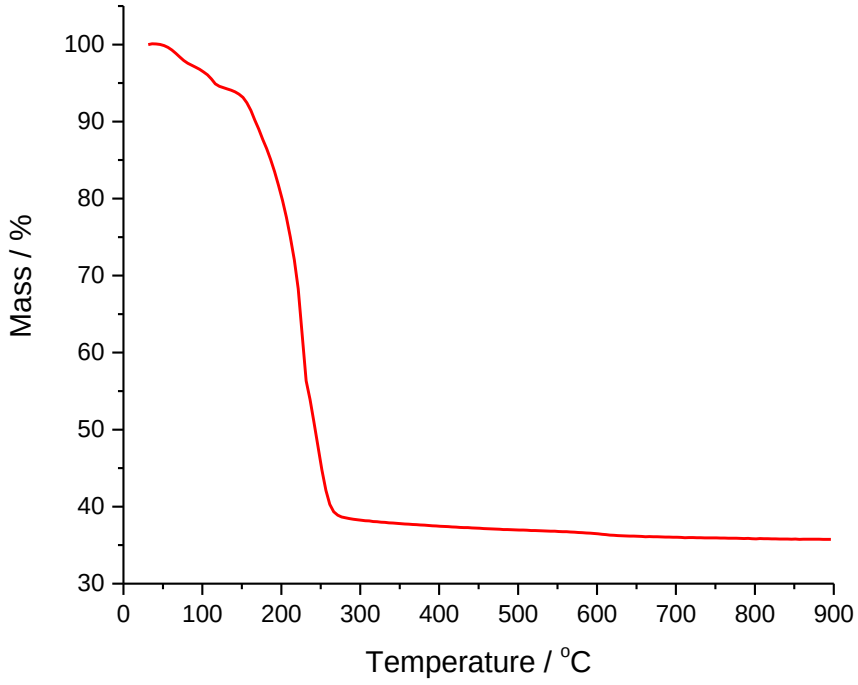

Figure 4.1. TG analysis of nitrate salts mixture ($Co(NO_3)_2.6H_2O$ and $Mn(NO_3)_2.4H_2O$)

4.2.1. $Mn_xCo_{3-x}O_4$ ($0.0 \leq x \leq 2.0$) Synthesis via Co – Precipitation

4.2.1.1. Co_3O_4 Synthesis via Co - Precipitation

2.8652 g $Co(NO_3)_2.6H_2O$ was first dissolved in 50 cm^3 of deionised water. The solution was added dropwise into 200 cm^3 of 4 M NH_4OH while the NH_4OH was stirred.

The stirring of the mixed solution was continued at 25 ^oC for 40 minutes. The whole solution was then evaporated to dryness by heating at ≈ 110 ^oC for 6 hours. The solid residue was ground and calcined at 260 ^oC for 4 hours. The black powder was again ground and calcined at 600 ^oC for 12 hours. As a final stage, the resulting black solid was reground and then sieved through a 53 μm sieve.

4.2.1.2. $Mn_{0.5}Co_{2.5}O_4$ Synthesis via Co - Precipitation

2.3875 g $Co(NO_3)_2.6H_2O$ and 0.4205 g $Mn(NO_3)_2.4H_2O$ were dissolved in 50 cm^3 of deionised water. The rest of the preparation is the same as described in the second paragraph of the Co_3O_4 synthesis (see **4.2.1.1**).

4.2.1.3. $MnCo_2O_4$ Synthesis via Co - Precipitation

1.9102 g $Co(NO_3)_2.6H_2O$ and 0.8415 g $Mn(NO_3)_2.4H_2O$ were dissolved in 50 cm^3 of deionised water. The rest of the preparation is the same as described in the second paragraph of the Co_3O_4 synthesis (see **4.2.1.1**).

4.2.1.4. $Mn_{1.5}Co_{1.5}O_4$ Synthesis via Co - Precipitation

1.4327 g $Co(NO_3)_2.6H_2O$ and 1.2612 g $Mn(NO_3)_2.4H_2O$ were dissolved in 50 cm^3 of deionised water. The rest of the preparation is the same as described in the second paragraph of the Co_3O_4 synthesis (see **4.2.1.1**).

4.2.1.5. Mn_2CoO_4 Synthesis via Co - Precipitation

0.955 g $Co(NO_3)_2.6H_2O$ and 1.681 g $Mn(NO_3)_2.4H_2O$ were dissolved in 50 cm^3 of deionised water. The rest of the preparation is the same as described in the second paragraph of the Co_3O_4 synthesis (see **4.2.1.1**).

4.2.2. $Mn_xCo_{3-x}O_4$ ($0.0 \leq x \leq 2.0$) Synthesis via Thermal Decomposition

4.2.2.1. Co_3O_4 Synthesis via Thermal Decomposition

2.865 g $Co(NO_3)_2.6H_2O$ was first dissolved in 50 cm^3 of deionised water.

The solution was then stirred for ≈ 30 minutes on a hot plate (≈ 110 ºC), then evaporated to dryness by heating at ≈ 110 ºC for 6 hours. The solid sample was then ground and heated at 260 ºC for 4 hours in an electric furnace. The black material was again reground and calcined at 600 ºC for 12 hours in the second stage of calcination process. As a final stage, the resulting black solid was reground and then sieved through a 53 µm sieve.

4.2.2.2. $Mn_{0.5}Co_{2.5}O_4$ Synthesis via Thermal Decomposition

2.3876 g $Co(NO_3)_2.6H_2O$ and 0.4204 g $Mn(NO_3)_2.4H_2O$ were dissolved in 50 cm^3 of deionised water. The rest of the preparation is the same as described in the second paragraph of the Co_3O_4 synthesis (see **4.2.2.1**).

4.2.2.3. $MnCo_2O_4$ Synthesis via Thermal Decomposition

1.910 g $Co(NO_3)_2.6H_2O$ and 0.8413 g $Mn(NO_3)_2.4H_2O$ were dissolved in 50 cm^3 of deionised water. The rest of the preparation is the same as described in the second paragraph of the Co_3O_4 synthesis (see **4.2.2.1**).

4.2.2.4. $Mn_{1.5}Co_{1.5}O_4$ Synthesis via Thermal Decomposition

1.4326 g $Co(NO_3)_2.6H_2O$ and 1.2611 g $Mn(NO_3)_2.4H_2O$ were dissolved in 50 cm^3 of deionised water. The rest of the preparation is the same as described in the second paragraph of the Co_3O_4 synthesis (see **4.2.2.1**).

4.2.2.5. Mn_2CoO_4 Synthesis via Thermal Decomposition

0.955 g $Co(NO_3)_2.6H_2O$ and 1.681 g $Mn(NO_3)_2.4H_2O$ were dissolved in 50 cm^3 of deionised water. The rest of the preparation is the same as described in the second paragraph of the Co_3O_4 synthesis (see **4.2.2.1**).

4.2.3. Electrode Coating

Ink preparation and electrode coating are as described in **Chapter 2**, section **2.4.6**. All current densities are based on geometric area of the vitreous carbon disc.

4.3. Physical Characterisation

The results from XRD, Raman, BET, TEM, XPS and XANES techniques used for the physical characterisation of powdered manganese doped spinel cobalt oxide materials ($Mn_xCo_{3-x}O_4$ ($0.0 \leq x \leq 2.0$) will be shown and described in this section.

4.3.1. XRD

XRD measurements were carried out in order to confirm spinel structures and see the changes in the phase (from cubic to tetragonal) with increasing Mn ions in the spinel Co_3O_4. **Figure 4.2** shows XRD powder patterns of five samples.

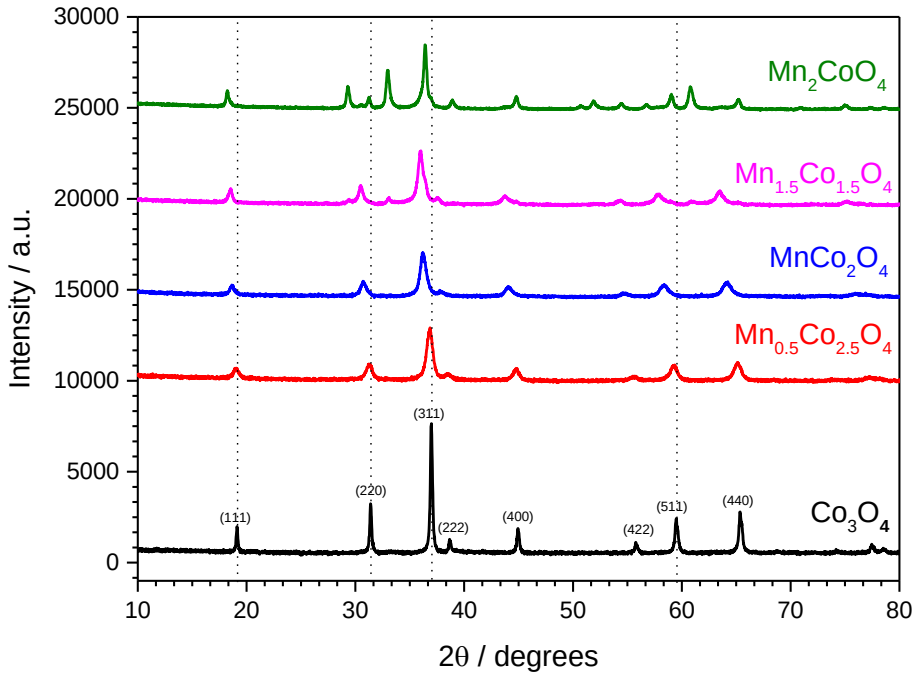

Figure 4.2. XRD powder patterns of $Mn_xCo_{3-x}O_4$ ($0.0 \leq x \leq 2.0$) prepared with different Mn content.

As seen in **Figure 4.2**, there are two types of spinel phases, which depend on the atomic ratio of Mn/Co. While the Mn content is low, the XRD patterns of Co_3O_4, $Mn_{0.5}Co_{2.5}O_4$ and $MnCo_2O_4$ are indexed with cubic unit cells. However, when Mn content is increased ($x > 1.3$), XRD patterns of $Mn_{1.5}Co_{1.5}O_4$ and Mn_2CoO_4 no longer correspond to the cubic phase. While the XRD pattern of $Mn_{1.5}Co_{1.5}O_4$ is a mixture of cubic (83.5%) and tetragonal phases (16.5%) (based on Rietveld refinement fit data), Mn_2CoO_4 shows a clear diffractogram for the tetragonal phase.[4-7] The peak pattern of Co_3O_4 indexed on the basis of cubic space group Fd-3ms (ICSD collection code: 36256) is very sharp and clear, which is a very good cubic spinel structure.[1, 8, 9] There are obvious changes in the diffractograms from Co_3O_4 to $MnCo_2O_4$ such as the peak intensities, the sharpness of peaks and the shift in the location of peaks. As already mentioned in **Chapter 1**, samples with Mn content up to 1.0

still show cubic phase, however, the peaks for $MnCo_2O_4$ are smaller and much wider than Co_3O_4, $Mn_{0.5}Co_{2.5}O_4$ samples due to larger Jahn-Teller distortion[10-12]. It is known that Jahn-Teller distortion decreases the crystallographic symmetry when Mn is introduced into Co_3O_4.[13] Peak positions (as shown with parallel lines in **Figure 4.2**) are also shifted to lower degrees by increasing Mn content. Jahn-Teller distortion exceeds the critical fraction (60 - 65%) for $Mn_{1.5}Co_{1.5}O_4$ and Mn_2CoO_4 samples and these spinels no longer correspond to the cubic phase.

Almost the same XRD results were obtained for samples prepared via "thermal decomposition method" as shown in **Figure 4.3**. However, more than a single phase is observed especially for $MnCo_2O_4$ prepared via thermal decomposition, which was the reason that all materials were reproduced via co-precipitation method.

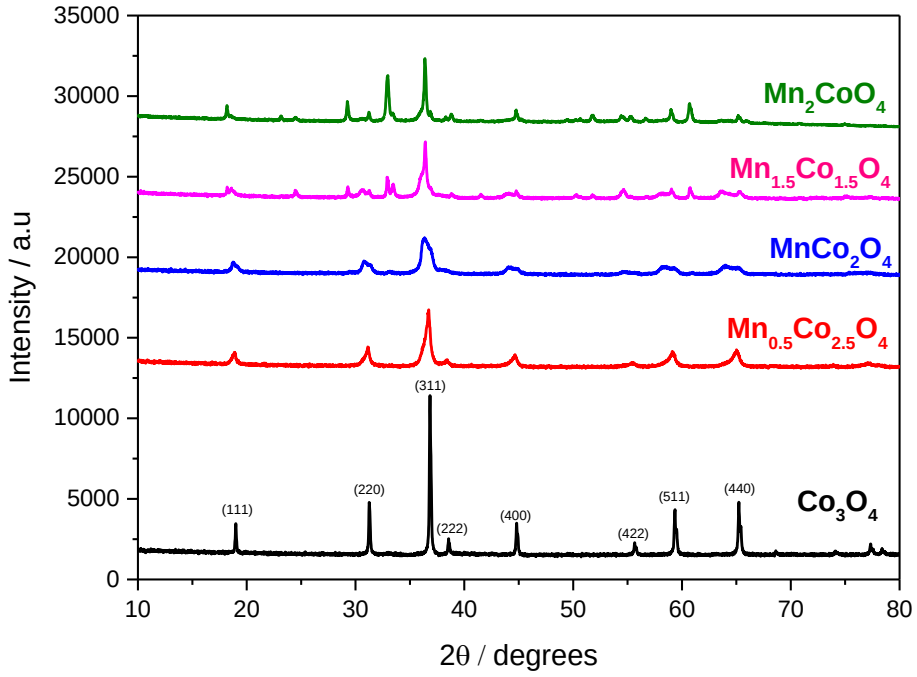

Figure 4.3. XRD of $Mn_xCo_{3-x}O_4$ ($0.0 \leq x \leq 2.0$) produced via "thermal decomposition method".

Rietveld analysis was carried out for all five spinels produced via co-precipitation by using the GSAS software with their CIF files obtained from ICSD. **Figure 4.4** shows that the measured diffraction patterns of all samples agree with pure spinel structures. A summary of the Rietveld analysis for all the spinels is shown in **Table 4.1**. Lattice constants are

increased by doping Mn ions into Co_3O_4. While the lattice constant (unit cell) is 8.08 Å for Co_3O_4, it is 8.11 and 8.20 Å for $Mn_{0.5}Co_{2.5}O_4$ and $MnCo_2O_4$, respectively, for cubic phase materials. These results are expected and consistent with the literature[8, 9, 14, 15] and this increase can be explained with larger ionic size of Mn^{+3} (0.78 Å) than Co^{+3} (0.65 Å).[15, 16] The same trend is observed for volume per formula unit (see **Table 4.1**). Rietveld analysis also shows that while Mn_2CoO_4 is pure tetragonal phase, $Mn_{1.5}Co_{1.5}O_4$ sample has two phases and the major phase is cubic phase (see **Table 4.1**).

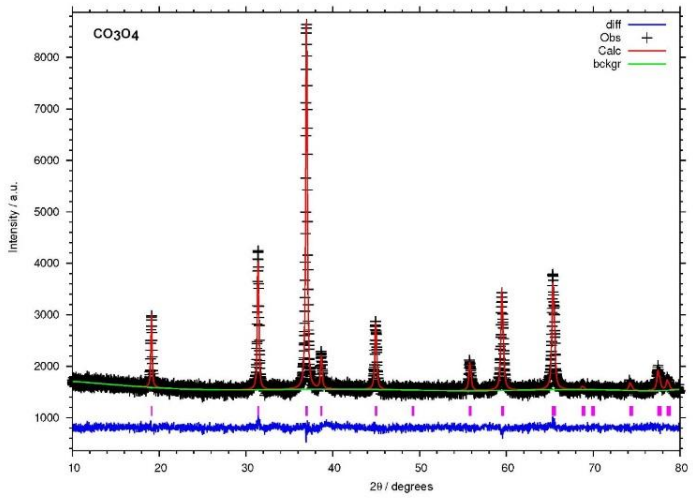
Co3O4
diff
Obs
Calc
bckgr
Intensity / a.u.
2θ / degrees

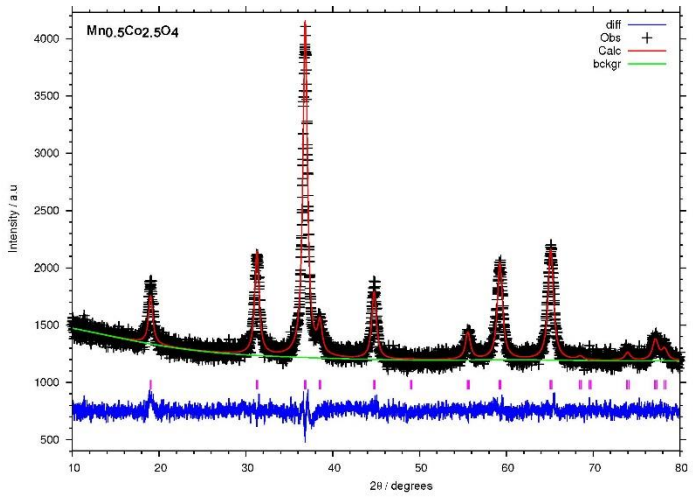
Mn0.5Co2.5O4
diff
Obs
Calc
bckgr
Intensity / a.u
2θ / degrees

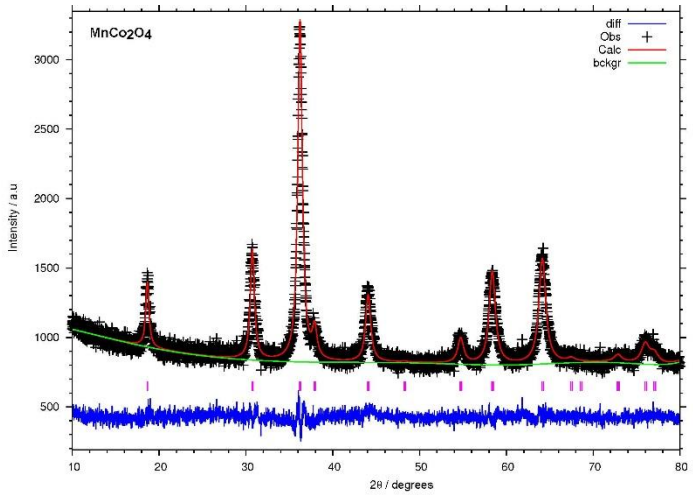
MnCo2O4
diff
Obs
Calc
bckgr
Intensity / a.u
2θ / degrees

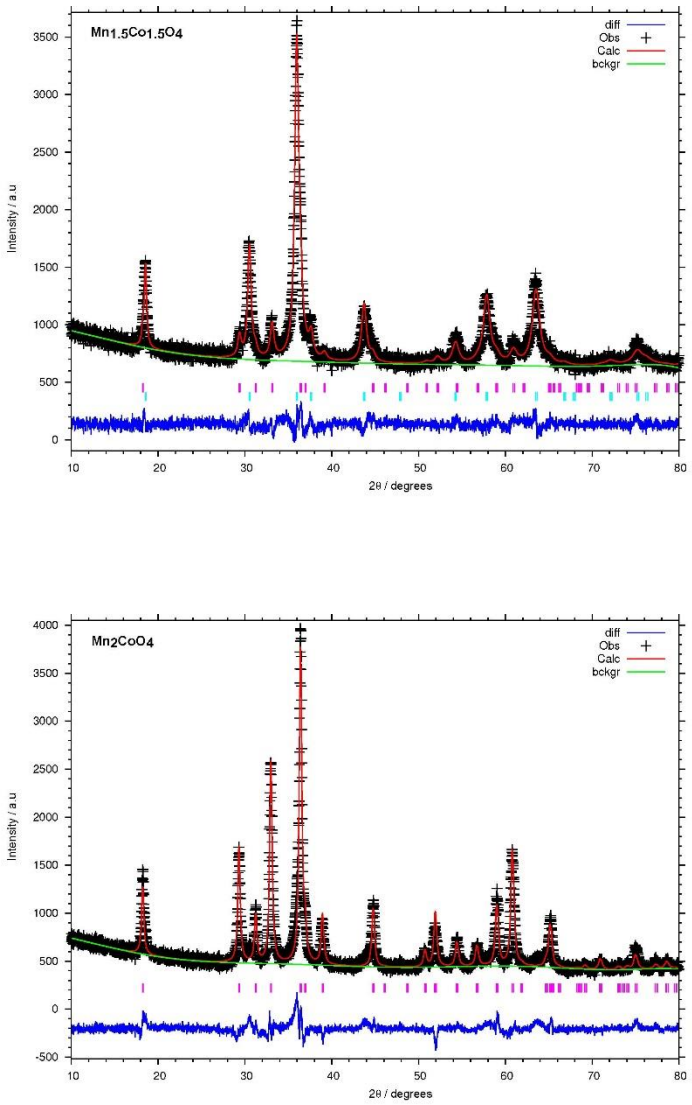

Figure 4.4. XRD patterns of Co_3O_4, $Mn_{0.5}Co_{2.5}O_4$, $MnCo_2O_4$, $Mn_{1.5}Co_{1.5}O_4$ and Mn_2CoO_4. Black crosses: observed intensities; Red line: Rietveld refinement fit; Green line: background fit; Blue line: difference between observed and fitted pattern. In first three graphs the pink lines indicate the peaks for cubic phase while in the last two graphs the pink lines indicate the peaks for tetragonal phase. The turquois lines in $Mn_{1.5}Co_{1.5}O_4$ sample indicates the peaks for cubic phase.

As already mentioned in **Chapter 2**, the average crystallite size can be estimated from the widths of diffraction peaks by using Scherrer equation (**Equation 2.1** in **Chapter 2**). Therefore, average crystallite sizes were calculated using "a derivation of the Scherrer equation" (**Equation 4.1**).

$$average\ crystallite\ size = \frac{18000\lambda K}{\pi L_x} \qquad \textbf{Equation 4.1}$$

Where the numerical constant K: 0.9 and λ: 1.5418 Å were used in this equation for average crystallite size (nm) calculations. As shown in **Table 4.1**, Mn incorporation into spinel Co_3O_4 increases volume per formula and this increase continues also in tetragonal phase samples.

Average particle sizes obtained using **Equation 4.1** may not yield the same results shown in BET and TEM measurements since the numerical constant (K: 0.9) used in Scherrer equation is not certain due to different approximation methods.[17] However, it may still be useful to compare the average crystallite sizes of all five spinels calculated from Scherrer equation to show the effect of Mn incorporation.

It is highly important to note that fit statistics from the XRD refinement show that Mn occupies a tetrahedral site in the spinel structure rather than a octahedral site because a lower Fitted wRp / % was obtained. This result along with XPS and XANES data allows us to propose the cationic distributions for all five spinels (see section **4.5. Discussion**).

XRD studies from materials prepared via co-precipitation and thermal decomposition methods show the phase transition from cubic to tetragonal phase with increasing Mn content in spinel Co_3O_4.

Catalyst	Space Group	Phase Fraction	Lattice Constant a, b, c (Å)	Volume per formula unit / (Å^3) (Cubic = V/8 Tetragonal = V/4)	Average crystallite size / nm	X^2	Fitted wRp / %	L_x
Co_3O_4	Fd-3ms	100%	8.0843(2) (a = b = c)	66.0(2)	72	1.150	2.63	11.09
$Mn_{0.5}Co_{2.5}O_4$	Fd-3mz	100%	8.1128(2) (a = b = c)	66.8(3)	14.5	1.233	3.02	54.81
$MnCo_2O_4$	Fd-3mz	100%	8.2026(9) (a = b = c)	69.0(1)	27.1	1.216	3.58	29.36
$Mn_{1.5}Co_{1.5}O_4$	Fd-3mz	83.5(3)%	8.2831(10) (a = b = c)	71.0(1)	235.9	1.590	4.40	3.37
	I41/amds	16.5(3)%	a = 5.730(2) c = 9.202(3) (b = a)	75.53(16)	89.5	1.590	4.40	8.88
Mn_2CoO_4	I41/amds	100%	a = 5.7243(4) c = 9.2503(8) (b = a)	75.78(4)	26.8	2.712	6.76	29.72

Table 4.1. The summary of Rietveld analysis of $Mn_xCo_{3-x}O_4$ ($0.0 \leq x \leq 2.0$) catalysts synthesised via co-precipitation method. The value of fitted wRp was kept < 10% to make a fit considered acceptable. ICSD collection codes for each samples are shown in brackets. Co_3O_4 (36256), $Mn_{0.5}Co_{2.5}O_4$ (291110), $MnCo_2O_4$ (201314), $Mn_{1.5}Co_{1.5}O_4$ (both of 201314 and 39197 were used) and Mn_2CoO_4 (39197). The values in the parentheses for phase fraction, lattice constants and volume per formula unit are standard deviations.

4.3.2. Raman

Raman studies were also carried out on spinel samples prepared via "thermal decomposition method" in order to see the phase transition from cubic phase to tetragonal phase. **Figure 4.5** shows five Raman peaks (Raman active modes), which are correspond to E_g (476 cm^{-1}), 3 F_{2g} (193.7, 517 and 614 cm^{-1}) and A_{1g} (683 cm^{-1}) for cubic phase samples as also shown in Raman spectra. These five Raman peaks were also reported in the literature for Co_3O_4.[16, 18, 19]

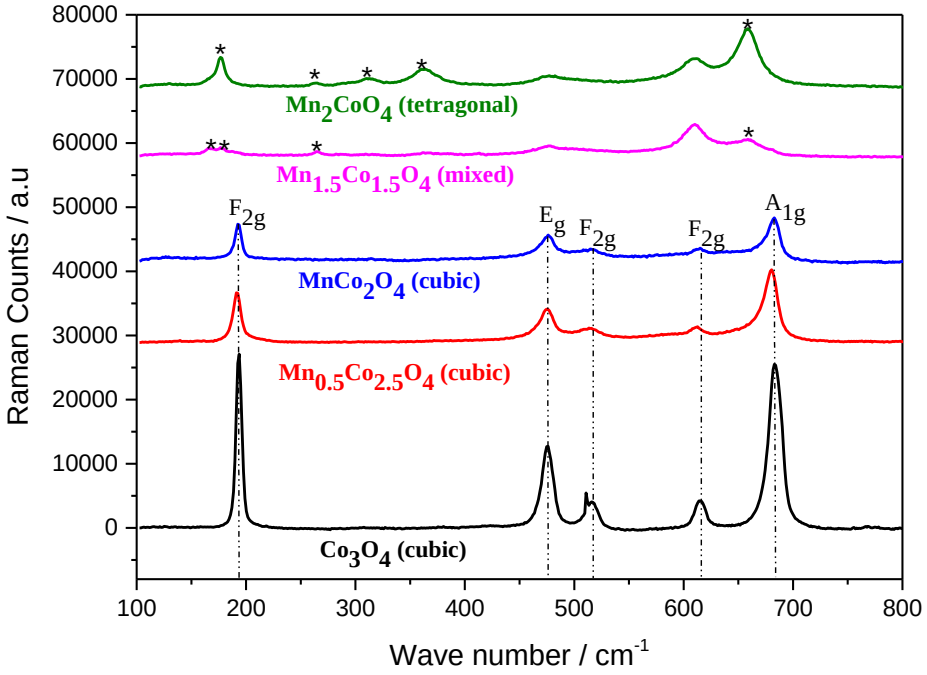

Figure 4.5. Raman spectra of $Mn_xCo_{3-x}O_4$ ($0.0 \leq x \leq 2.0$) samples produced via "thermal decomposition method". Laser power (785 nm): 0.5 %; Accumulating time: 60 s. Baseline was subtracted for each spectra.

Raman spectra of five spinels produced via thermal decomposition also show the phase transition from the cubic phase to the tetragonal phase with increased Mn ions in Co_3O_4. The main peak positions for cubic phase samples (Co_3O_4, $Mn_{0.5}Co_{2.5}O_4$, $MnCo_2O_4$) are the same while there is a decrease in peak intensities with incorporation of Mn into Co_3O_4 (see parallel lines, which are only for cubic phase samples, in **Figure 4.5**). On the other hand, the

appearances of new peaks (shown with asterisks) and disappearances of cubic phase peaks are observed for samples ($Mn_{1.5}Co_{1.5}O_4$ and Mn_2CoO_4), which are not cubic phase anymore.

4.3.3. BET

Brunauer, Emmett and Teller (BET) surface area measurements were carried out and **Table 4.2** shows the surface areas of the spinels. As shown in **Table 4.2**, the surface area of cobalt oxide is 4.8 m^2/g and the surface area is increased several times with all other samples, which contain Mn ions. The highest surface area (50 m^2/g) is observed with $MnCo_2O_4$. 50 m^2/g is regarded as high for the surface area of pure metal oxide (without carbon additive). It is worth mentioning here that carbon based materials (such as nitrogen-doped reduced graphene oxide (N-rGO), carbon nanotubes (CNT) and carbon powder (XC-72R)) not only increase conductivity but also help the dispersion of oxide materials to prevent agglomeration, which results in higher surface area and better accessibility of electrolyte to the surface area of metal oxides.[20, 21] Therefore, it would be possible to obtain spinels with larger surface areas than the results in **Table 4.2** if there was carbon material as additive in the preparation process.

Catalyst	BET Surface Area (m^2/g)	Average Aggregate Diameter (nm)	Max Pore Volume at P/P° (0.15) (cm^3/g)	Median Pore Width (nm)
Co_3O_4	4.8	1245.0	0.0017	1.34
$Mn_{0.5}Co_{2.5}O_4$	49.7	120.6	0.0190	1.32
$MnCo_2O_4$	50.0	120.5	0.0190	1.34
$Mn_{1.5}Co_{1.5}O_4$	20.6	290.5	0.0079	1.33
Mn_2CoO_4	23.6	254.0	0.0092	1.33

Table 4.2. Summary of BET surface area measurements of $Mn_xCo_{3-x}O_4$ ($0.0 \leq x \leq 2.0$) catalysts prepared via co-precipitation.

The average aggregate diameter has the same trend with BET surface area of materials. The lowest aggregate size is observed with $MnCo_2O_4$ while Co_3O_4 has the largest. It is also important to note that BET results are well consistent with TEM images (see **4.3.4**).

4.3.4. TEM

Transmission electron microscopy (TEM) images of each of the spinels prepared via co-precipitation are shown in **Figure 4.6**.

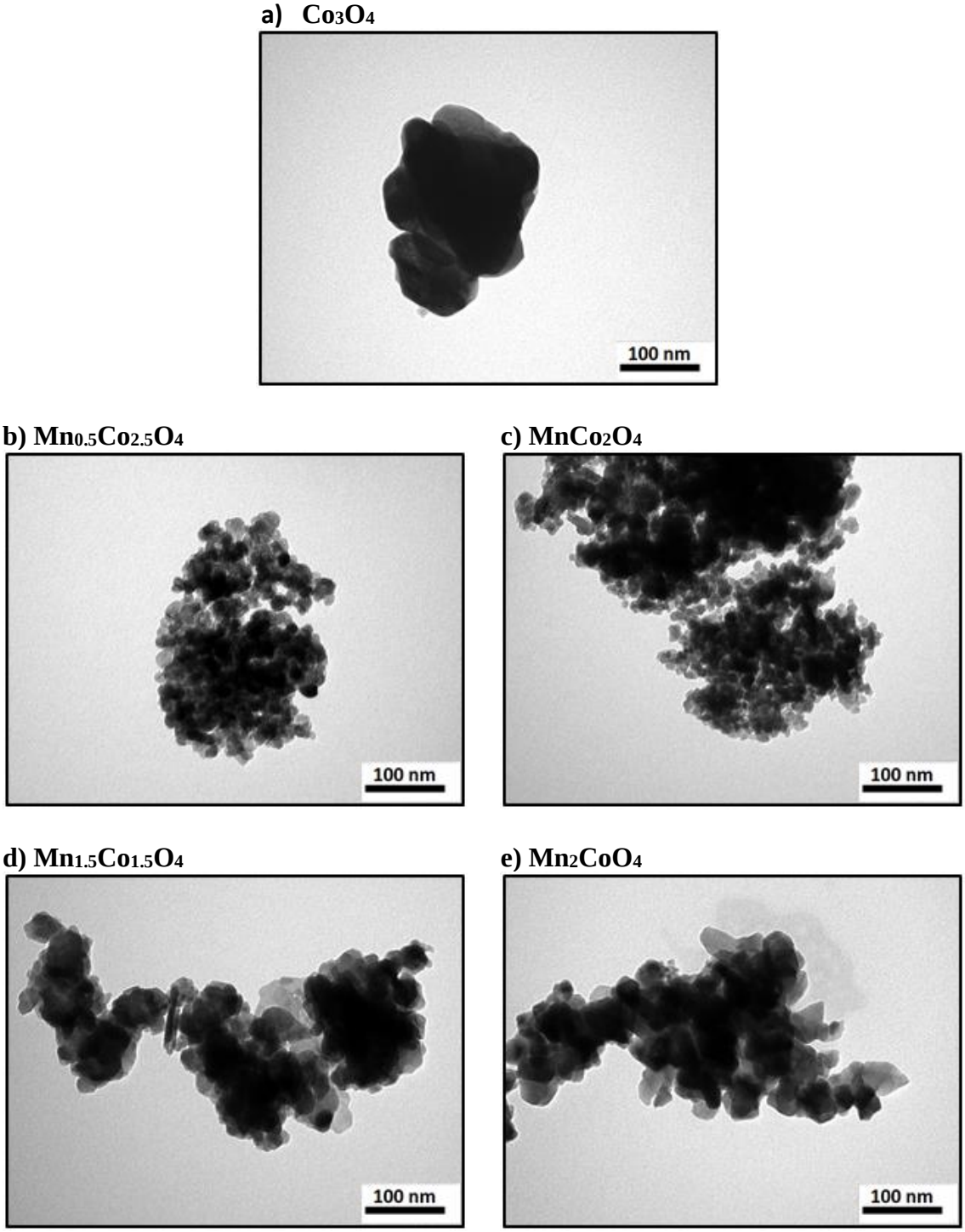

Figure 4.6. TEM images of **a)** Co_3O_4 **b)** $Mn_{0.5}Co_{2.5}O_4$ **c)** $MnCo_2O_4$ **d)** $Mn_{1.5}Co_{1.5}O_4$ and **e)** Mn_2CoO_4. Scale bar is 100 nm.

As shown, Co_3O_4 has the largest particle size. The smallest particles are observed with $Mn_{0.5}Co_{2.5}O_4$ and $MnCo_2O_4$ samples with size of ≈ 7 nm. On the other hand, the particle size of Co_3O_4 was measured as ≈ 233 nm. TEM results are consistent with XRD and BET results.

4.3.5. XPS

X-ray photoelectron spectroscopy (XPS) analysis of manganese doped spinel cobalt oxides was also carried out in order to study the Mn:Co surface atomic ratios as well as the oxidation states of Co and Mn in the as prepared samples. The binding energies were referenced to the C 1s peaks at 284.6 eV. **Figure 4.7** shows the photoemission lines obtained during the survey. The spectra (see **Figure 4.7**) show the elemental peaks of Co, Mn and O as expected. Also presented is the C peak, which comes from adventitious carbon species.[22]

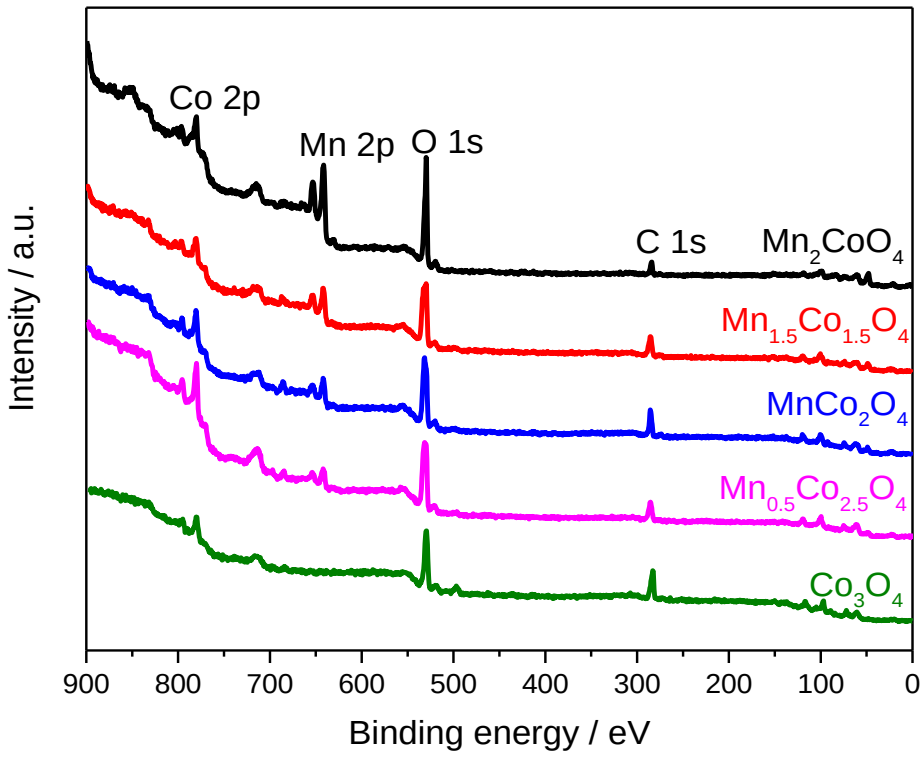

Figure 4.7. Survey photoemission spectra taken in normal emission using non-monochromatized Al K_α X-ray source for the $Mn_xCo_{3-x}O_4$ samples.

The photoemission lines obtained in the Mn 2p and Co 2p regions are shown in **Figure 4.8**.

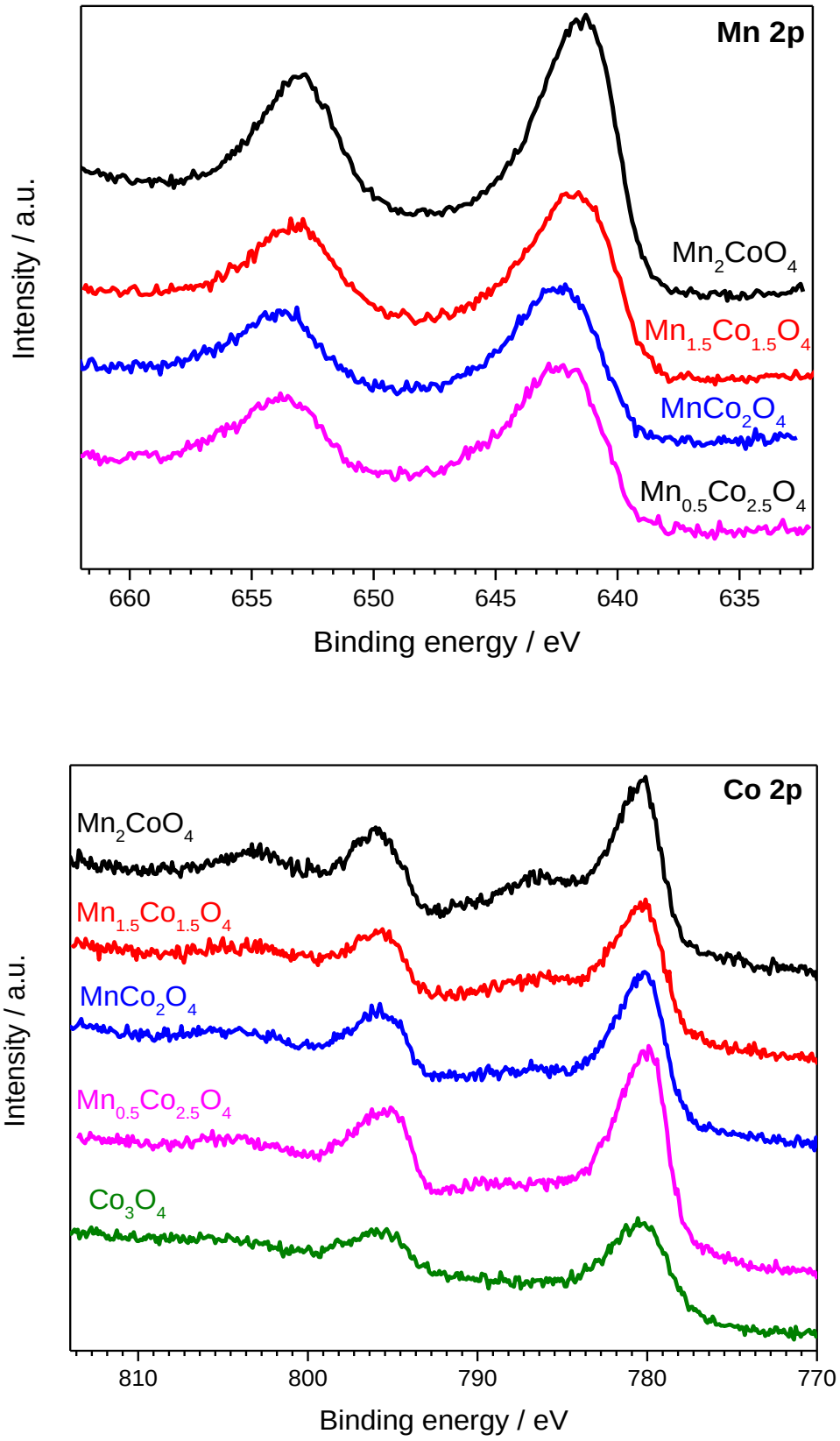

Figure 4.8. Mn 2p (top) and Co 2p (bottom) photoemission spectra taken in normal emission using non-monochromatized Al K_α X-ray source for the $Mn_xCo_{3-x}O_4$ samples.

The surface composition of the $Mn_xCo_{3-x}O_4$ ($0.0 \leq x \leq 2.0$) samples was calculated from the Mn 2p and Co 2p regions and the corresponding sensitivity factors. As seen in **Table 4.3**, the surface composition for each sample is close to the nominal one, although some surface segregation of Mn is observed in the samples with $x < 2$. It is worth noting that XPS data are very sensitive to the surface state due to all species adsorbed on the surface (such as water or hydroxyl groups). Therefore, while the trends along the series can be safely taken as correct, the absolute values should be taken with caution.

Catalyst	Mn:Co	Stoichiometry
$Mn_{0.5}Co_{2.5}O_4$	30:70	$Mn_{0.9}Co_{2.1}$
$MnCo_2O_4$	40:60	$Mn_{1.2}Co_{1.8}$
$Mn_{1.5}Co_{1.5}O_4$	57:43	$Mn_{1.7}Co_{1.3}$
Mn_2CoO_4	60:40	$Mn_{1.8}Co_{1.2}$

Table 4.3. Mn:Co surface atomic ratios calculated from XPS for the $Mn_xCo_{3-x}O_4$ ($0.0 \leq x \leq 2.0$) samples. (Mn enrichment of surface for those $x < 2.0$).

High resolution Co 2p photoemission lines for all the $Mn_xCo_{3-x}O_4$ ($0.0 \leq x \leq 2.0$) samples are shown in **Figure 4.9**. In addition to satellite peaks (shown as "sat." in **Figure 4.9**), there are two main peaks are observed at ≈ 796 and ≈ 780.5 eV with spin-orbit splitting of ≈ 15 eV, which are due to Co $2p_{1/2}$ and Co $2p_{3/2}$, respectively.[22] As seen in **Figure 4.9**, there are significant changes in the Co 2p lines with the decrease of the Mn amount. From Mn_2CoO_4 ($x = 2$) to Co_3O_4 ($x = 0$), the shape of the Co 2p line changes from the typical shape of Co^{+2} to the one of Co_3O_4 sample (Co^{+2} and Co^{+3}). Moreover, the binding energies are shifted from higher binding energies (≈ 780 eV, typical for Co^{+2}) to lower binding energies (≈ 779.6 eV, typical for Co_3O_4) from Mn_2CoO_4 to Co_3O_4, well consistent with the literature.[23] As also seen in **Figure 4.9**, there are other changes such as the decrease of the satellite at around 787 eV and the decrease of the spin-orbit splitting (the distance between the Co $2p_{3/2}$ and Co $2p_{1/2}$). These results mean that only Co^{+2} is present in Mn_2CoO_4 (by considering Mn prefers tetrahedral site from fit statistics in XRD refinement, in this case the cationic distribution is $[Mn^{+3}]_{Th}[Co^{+2}Mn^{+3}]_{Oh}O_4$, where Co^{+2} ions are in octahedral (Oh) sites while Mn^{+3} can be observed in both tetrahedral (Th) and octahedral (Oh) sites) and the amount of Co^{+3} increases

when x (Mn dopant) decreases, for example $[Mn^{+3}]_{Th}[Co^{+2}Co^{+3}]_{Oh}O_4$ in $MnCo_2O_4$,[22] or $[Co^{+2}]_{Th}[Co^{+3}{}_2]_{Oh}O_4$ in Co_3O_4.

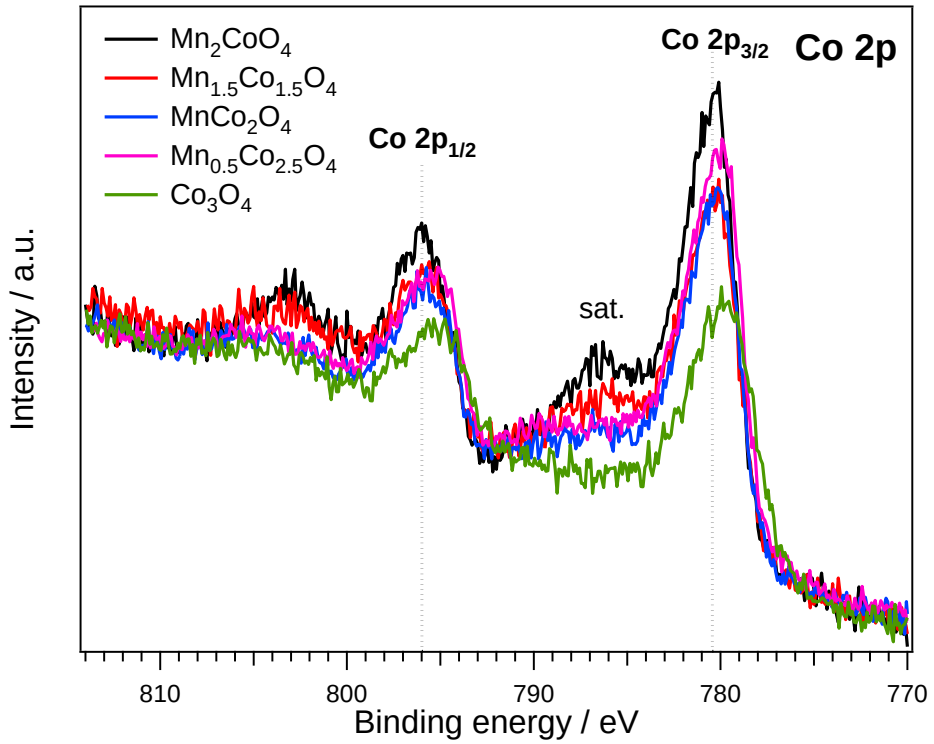

Figure 4.9. Co 2p photoemission lines for the $Mn_xCo_{3-x}O_4$ ($0.0 \leq x \leq 2.0$) samples.

As for the Mn 2p high resolution spectrum shown in **Figure 4.10**, there are two main peaks observed for all Mn containing spinel samples at around 642 and 653.7 eV for Mn $2p_{3/2}$ and Mn $2p_{1/2}$, respectively. These two peaks are characteristic of the Mn(III) cation.[24] The Mn 2p region is similar for all samples as seen in **Figure 4.10**. In this case, it is not possible to separate the Mn 2p photoemission line into single chemical components due to the very small differences in bonding energies. When the x value is 2 (Mn_2CoO_4), the Mn 2p line is narrower compared to the other samples. As mentioned above, the oxidation state of Mn is +3 due to the characteristic peak positions (642 and 653.7 eV) as expected.[24] As seen in **Figure 4.10**, for the samples with $x < 2$, the $2p_{3/2}$ peak shifts about 0.4 eV towards the higher bonding energy and becomes slightly broader at higher bonding energies. This could be from the presence of both Mn^{+3} and Mn^{+4} species on the surface. Looking at **Table 4.3,** the

existence of Mn^{+4} could be explained owing to the slight excess of Mn on the surface of the samples (with respect to the nominal composition) that could form MnO_2 in contact with air.

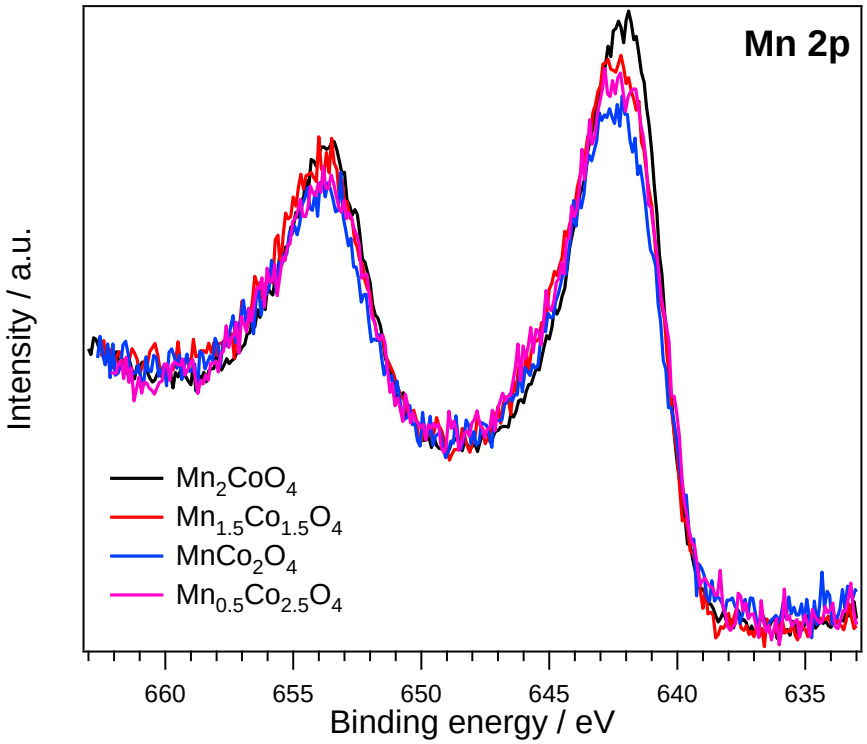

Figure 4.10. Mn 2p photoemission lines for the $Mn_xCo_{3-x}O_4$ ($0.0 \leq x \leq 2.0$) samples.

As shown in **Figure 4.10**, there is no observation of the characteristic satellite of Mn^{+2} at 647 eV for any of the samples.[23] However, a small amount of Mn^{+2} in samples with $x < 2$ cannot be excluded. It is worth mentioning that these samples show significant amount of adsorbed species on the surface (such as water and hydroxyl groups).

The adsorbed species on the surface were also investigated by analysing the O 1s photoemission spectra as shown in **Figure 4.11**. The O 1s photoemission spectra can be divided into three photoelectron peaks as labelled on the figure. The peaks at 529.6, 531.6 and 533.0 eV belong to the oxygen in the spinel lattice (metal-oxygen bonds), the oxygen of hydroxide ions, and the oxygen of the water that is physically adsorbed on the surface,

respectively. All these results are in agreement with the values found in the literature for the $Mn_xCo_{3-x}O_4$ ($0.0 \leq x \leq 2.0$) samples.[22, 25]

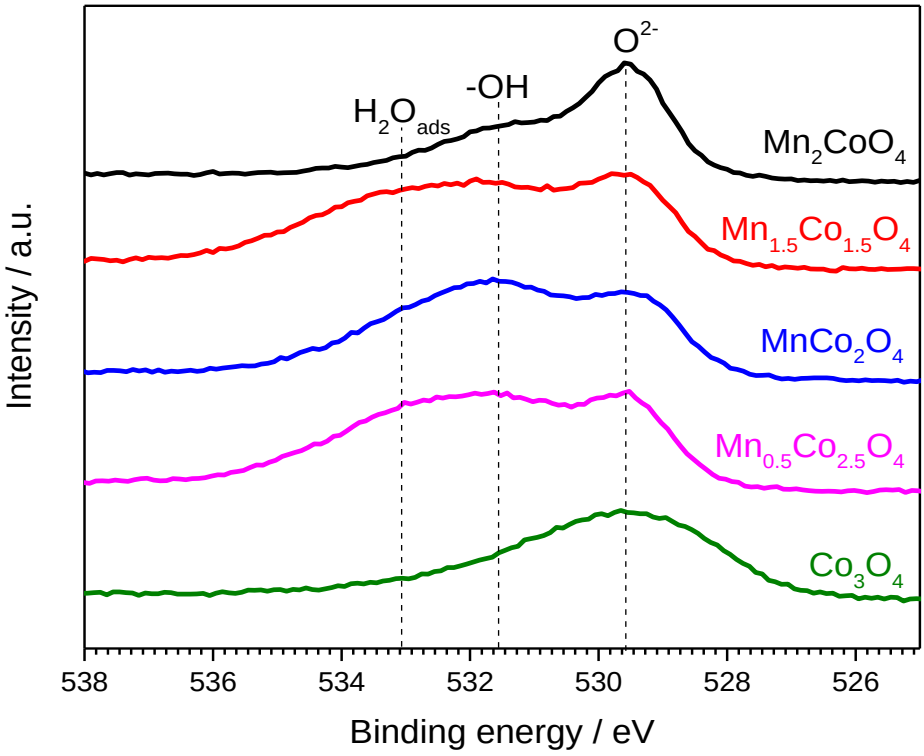

Figure 4.11. O 1s photoemission spectra taken in normal emission using non-monochromatized Al K_α X-ray source for the $Mn_xCo_{3-x}O_4$ samples.

4.3.6. Ex situ XANES

Synchrotron X-ray Absorption Spectroscopy (XAS) was used to identify the oxidation states of Co and Mn in spinels $Mn_xCo_{3-x}O_4$ ($0.0 \leq x \leq 2.0$) as well as the cationic distributions in these materials since X-ray Absorption Near-Edge Structure (XANES) allows one to obtain information on the oxidation state of an atom of interest and the site symmetry.[26-28]

4.3.6.1. Co Edge

Figure 4.12 illustrates K-edge XANES of Co in spinels Co_3O_4, $Mn_{0.5}Co_{2.5}O_4$, and $MnCo_2O_4$ and reference Co oxides. K-edge XANES spectra of standard cobalt oxide particles of CoO (+2), Co_3O_4 (+2.66) and $LiCoO_2$ (+3) were included for comparison purpose. K-edge XANES of Co in both $Mn_{1.5}Co_{1.5}O_4$ and Mn_2CoO_4 samples were not included in **Figure 4.12** since absorption was not high enough due to less Co in both samples. The inset in **Figure 4.12** shows XANES spectra of spinels and reference Co oxides more clearly. As shown in the inset, the K-edge Co XANES of three spinels are varied between reference CoO (+2) and Co_3O_4 (+2.66). However, more clear results can be seen in **Figure 4.13**, in which the reference Co oxides were used to make a linear relationship between Co oxidation states in three spinels and K-edge absorption energies.[11]

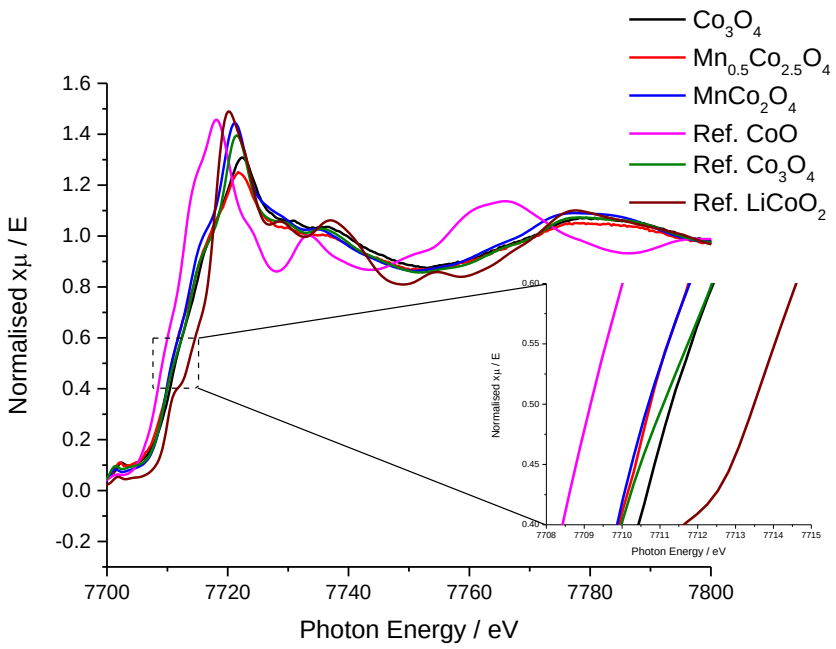

Figure 4.12. K-edge XANES patterns of Co in spinel Co_3O_4, $Mn_{0.5}Co_{2.5}O_4$, $MnCo_2O_4$ and the reference oxides (CoO, Co_3O_4 and $LiCoO_2$). Inset shows XANES patterns of three spinels and reference oxides in the photon energy scale between 7708 and 7715 eV.

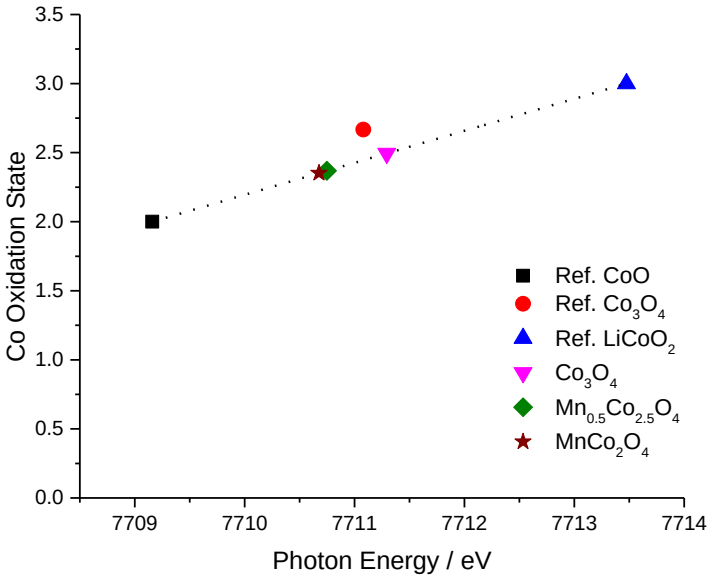

Figure 4.13. Fitted linear relationship between Co oxidation states in spinel Co_3O_4, $Mn_{0.5}Co_{2.5}O_4$, $MnCo_2O_4$ and the corresponding photon energies. The plot was made from **Figure 4.12** at 0.5 E, which is commonly selected as half-way up the absorption edge.[29] Ref. Co_3O_4 was excluded to produce linear fit. The same result for Ref. Co_3O_4 is shown by Li et al.[11] Data points for the prepared Co_3O_4, $Mn_{0.5}Co_{2.5}O_4$ and $MnCo_2O_4$ samples were placed onto the calibration line.

A list of the Co oxidation states in cubic phase spinels and reference Co oxides and their corresponding K-edge absorption energies (eV) is reported in **Table 4.4**. The error in oxidation states (see **Table 4.4**) was calculated based on the energy resolution shift, which is 0.1 eV since the detector of B18 can measure the XANES with an energy resolution of 0.1 eV, in the calibration curve.[29] According to XANES measurements for Co edge (see **Figure 4.13** and **Table 4.4**) in cubic phase spinels, the mean Co valence were determined to be 2.5 for Co_3O_4, 2.4 for $Mn_{0.5}Co_{2.5}O_4$ and 2.4 for $MnCo_2O_4$. By increasing Mn cations in spinel Co_3O_4, the mean Co valence value is decreased, suggesting that Mn^{+3} cations substitute for Co^{+3} in spinel.[11] It may be worth noting that the oxidation state for Co_3O_4 is 2.5 rather than 2.66, which might be coming from either small impurity of CoO or the surface

oxidation state of the Co nanoparticles might be different from that of the bulk. However, the trends along the series (from x = 0 to 1) can be safely taken as correct.

Catalyst	Energy / eV (±0.1)	Oxidation State (±0.023)
Ref. CoO	7709.2	2
Ref. Co_3O_4	7711.1	2.66
Ref. $LiCoO_2$	7713.5	3
Co_3O_4	7711.3	2.50
$Mn_{0.5}Co_{2.5}O_4$	7710.8	2.37
$MnCo_2O_4$	7710.7	2.35

Table 4.4. List of the mean Co oxidation states in reference oxides, spinel Co_3O_4, $Mn_{0.5}Co_{2.5}O_4$, $MnCo_2O_4$ samples and their corresponding K-edge energies (eV).

XANES measurements for Co in cubic phase spinels are confirming XPS measurements (see section **4.3.5. XPS**) by showing that the ratio of Co^{+2}/Co^{+3} increases when x (Mn dopant) increases due to substitution of Mn for the Co^{+3}.

4.3.6.2. Mn Edge

Mn K-edge XANES profiles of four spinels ($Mn_{0.5}Co_{2.5}O_4$, $MnCo_2O_4$, $Mn_{1.5}Co_{1.5}O_4$, and Mn_2CoO_4) and reference Mn oxides are shown in **Figure 4.14**. XANES spectra of reference Mn oxide particles of MnO (+2), Mn_2O_3 (+3) and MnO_2 (+4) were also included for comparison purpose. The difference between XANES spectra can be seen more clearly in the inset in **Figure 4.14**. The reference Mn oxides were used to establish a linear relationship between K-edge absorption energy and the metal valence.[11, 30]

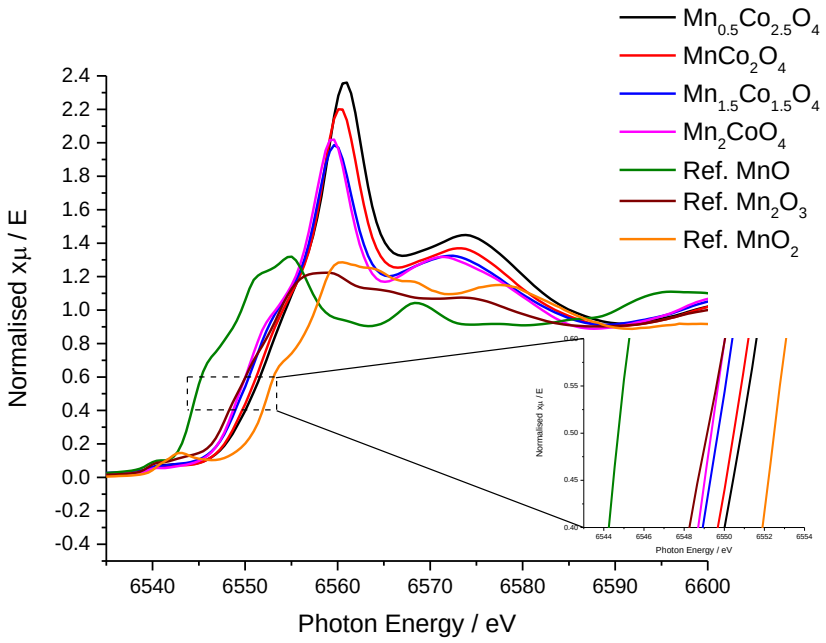

Figure 4.14. K-edge XANES patterns of Mn in spinel $Mn_{0.5}Co_{2.5}O_4$, $MnCo_2O_4$, $Mn_{1.5}Co_{1.5}O_4$, Mn_2CoO_4 samples and the reference oxides (MnO, Mn_2O_3 and MnO_2). Inset shows XANES patterns of three spinels and reference oxides in the photon energy scale between 6543 and 6554 eV.

Figure 4.15 illustrates a linear fit, which was made of reference Mn oxides with their corresponding energies, to show the oxidation state of Mn in four spinels and their corresponding photon energies (eV). The results from **Figure 4.15** were reported in **Table 4.5** show the mean Mn oxidation states for four spinels, reference Mn oxides and their corresponding Mn K-edge photon energies. The error in oxidation states (see **Table 4.5**) was again calculated from the energy resolution shift (0.1 eV) as mentioned in **Co Edge** section. **Figure 4.15** and **Table 4.5** show that the mean Mn oxidation states for four spinels are between 3 and 4 confirming the existence of Mn^{+3} and Mn^{+4} in all spinels. As already shown in XPS measurements, the existence of Mn^{+4} was observed in all spinels and the existence of Mn^{+4} might be coming from the slight excess of Mn on the surface of the samples, which could form MnO_2 due to the contact with air. By comparing the mean Mn oxidation states in four spinels, it is obvious to see that the mean Mn oxidation state decreases when x (Mn dopant) increases. These results mean that doped Mn ions are Mn^{+3} and Mn^{+3} ions replace

in Co^{+3} in the spinels since the mean Mn valence values for all four samples are larger than 3. It might be considered that the amount of Mn^{+4} on the surface of spinels are roughly fixed and the incorporated Mn ions must have +3 oxidation state since the mean Mn oxidation state is getting closer to 3 rather than 4 (see **Table 4.5**).

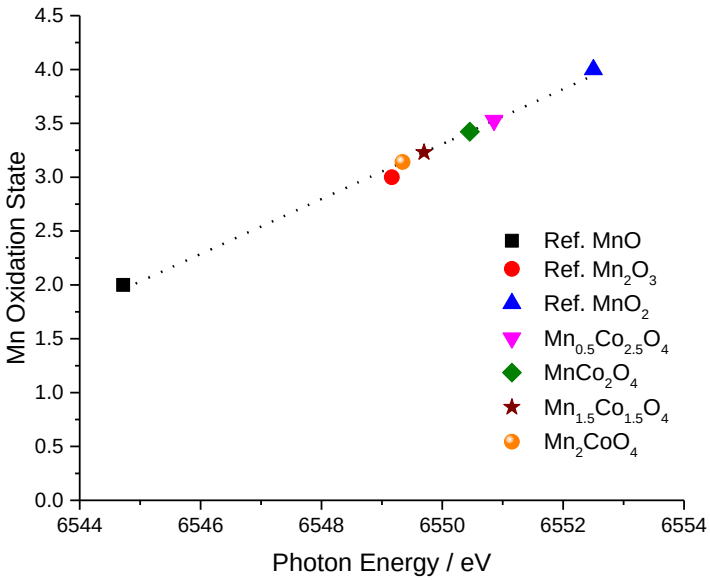

Figure 4.15. Fitted linear relationship between Mn oxidation states in spinel $Mn_{0.5}Co_{2.5}O_4$, $MnCo_2O_4$, $Mn_{1.5}Co_{1.5}O_4$, Mn_2CoO_4 samples and the corresponding photon energies. The plot was made from **Figure 4.14** at 0.5 E (half-way up the absorption edge). Data points for the prepared $Mn_{0.5}Co_{2.5}O_4$, $MnCo_2O_4$, $Mn_{1.5}Co_{1.5}O_4$, Mn_2CoO_4 samples were placed onto the calibration line.

Mn edge XANES results are consistent with Co edge XANES measurements by showing that doped Mn^{+3} ions substitute Co^{+3} ions in four spinels.

Catalyst	Energy / eV (±0.1)	Oxidation State (±0.025)
Ref. MnO	6544.7	2
Ref. Mn_2O_3	6549.2	3
Ref. MnO_2	6552.5	4
$Mn_{0.5}Co_{2.5}O_4$	6550.9	3.53
$MnCo_2O_4$	6550.5	3.42
$Mn_{1.5}Co_{1.5}O_4$	6549.7	3.23
Mn_2CoO_4	6549.3	3.14

Table 4.5. List of the mean Mn oxidation states in reference oxides, spinel $Mn_{0.5}Co_{2.5}O_4$, $MnCo_2O_4$, $Mn_{1.5}Co_{1.5}O_4$, Mn_2CoO_4 samples and their corresponding K-edge energies (eV).

4.4. Electrochemical Characterization

This part will explain the electrochemical studies on Mn doped spinel cobalt oxides in alkaline media. Again, experimental details are set out in **Chapter 2**. In order to make a reasonable comparison between all spinels, experimental conditions were kept as consistent as possible by using fresh electrolyte, making fresh ink, uniform electrode coating, keeping the same electrolyte temperature and purging electrolyte with O_2/N_2 in each measurement.

4.4.1. Cyclic Voltammetry

Cyclic voltammograms of Co_3O_4 samples prepared via co-precipitation and thermal decomposition methods are compared in **Figure 4.16.** In contrast to other $Mn_xCo_{3-x}O_4$ samples, with Co_3O_4 there were significant differences with the preparation. Both samples showed oxidation and reduction peaks between 500 and 550 mV, but there are large differences in magnitude. The origin of peaks are not known clearly, however, as already discussed in more details in **Chapter 3**, it has been proposed in the literature[18, 31-36] that they may be attributed to the Co (III/IV) couple at the electrode surface due to the oxidation reaction of CoOOH formed on the surface.[37] It is known that the surface of Co_3O_4 immediately turns into CoOOH in alkaline media.[15] Therefore, the surface redox reaction is from the oxidation of CoOOH and the reverse reaction.

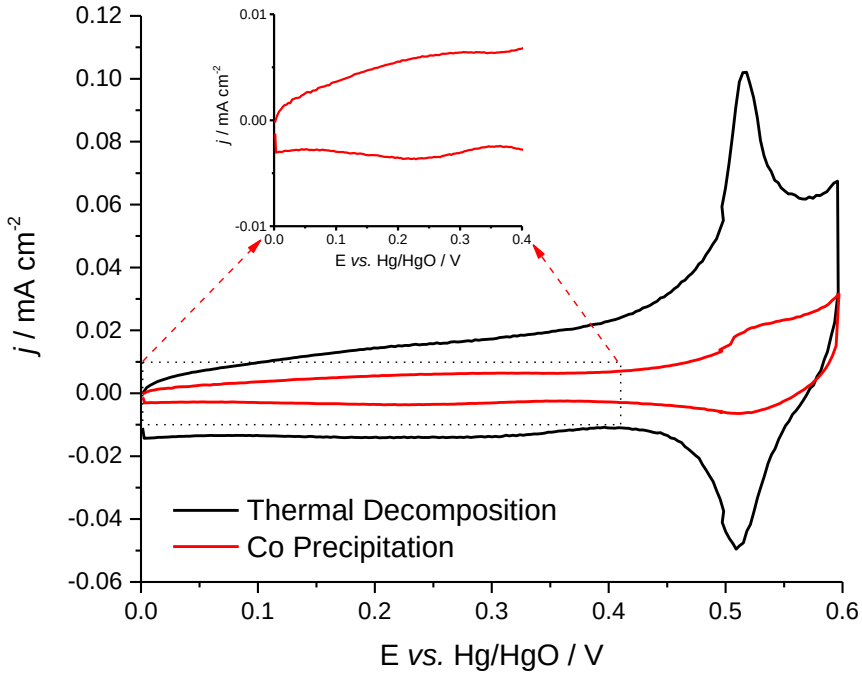

Figure 4.16. Cyclic voltammograms of Co_3O_4 catalysts (prepared via thermal decomposition (black) and co-precipitation (red) methods) coated on GC electrode in 1 M KOH. Temperature: 25 ^oC; Potential scan rate: 20 mV/s.

As seen in **Figure 4.16**, the oxidation and reduction peaks' sizes at Co_3O_4 produced with thermal decomposition are much larger than at one prepared via co-precipitation. While the oxidation/reduction peaks at Co_3O_4 produced via thermal decomposition are much more clear and distinct, the sample produced by co-precipitation shows much wider and lower intensity peaks. The reason for the large difference between CVs of Co_3O_4 prepared via thermal decomposition and co-precipitation is not know. However, these may come from different particle sizes, crystallinity, morphologies and the surface areas (BET surface areas of Co_3O_4 via thermal decomposition: 7.7 m^2 g^{-1}; co-precipitation: 4.8 m^2 g^{-1}), which are strongly affected by preparation methods.[35, 38, 39] It is an important evidence that morphology of Co_3O_4 influences the probability of Co(III) species to be exposed in alkaline media differently.[35] Therefore, it is expected to obtain cyclic voltammetry somewhat similar even though there are some difference in peak intensities. The integrated areas of Co(III) oxidation peaks were calculated and the integrated area of oxidation peak at Co_3O_4 produced

via thermal decomposition is almost 12 times larger than at the one produced via co-precipitation.

The inset present in **Figure 4.16** shows a small oxidation and reduction peaks, which are normally hard to see in the scale of typical CV of Co_3O_4 without zooming, at Co_3O_4 prepared via the co-precipitation method. It has been suggested that these peaks are assigned to the Co(II/III) oxidation and reduction.[18, 40, 41] These oxidation and reduction peaks are not always visible in the literature. According to Belova et al., it is common to observe very small oxidation/reduction peaks for Co(II/III) couple since the amount Co^{+2} is half of Co^{+3} and due to tetrahedral site location of Co^{+2}, it is harder to oxidise Co^{+2} compared to Co^{+3}.[41, 42] Probably, this is why it is not obvious to see these peaks in general CVs of Co_3O_4.

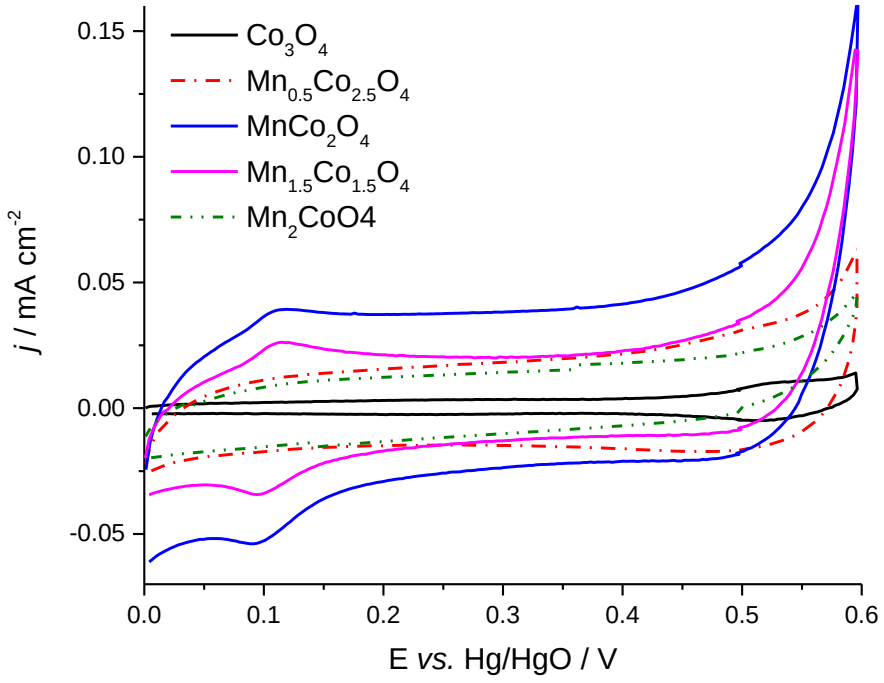

Figure 4.17. Cyclic voltammograms of Mn doped $Mn_xCo_{3-x}O_4$ ($0.0 \leq x \leq 2.0$) catalysts coated on GC electrode in 1 M KOH. Temperature: 25 ^oC; Potential scan rate: 10 mV s^{-1}.

Cyclic voltammograms of five spinels coated on GC electrode 1 M KOH at 25 ^oC with 10 mV s^{-1} potential scan rate are present in **Figure 4.17**. As shown, there are three major points to highlight:

I) There is an increase in the current densities for O_2 evolution around 0.6 V from cubic phase Co_3O_4 to $MnCo_2O_4$ and then the current density is decreased from $MnCo_2O_4$ to Mn_2CoO_4 (when the phase is changed from cubic to tetragonal phase).

II) Cyclic voltammograms also show the small oxidation and reduction peaks for $MnCo_2O_4$ and $Mn_{1.5}Co_{1.5}O_4$ samples between 50 and 150 mV. Lee et al. suggest that these oxidation and reduction peaks are for the $MnOOH/MnO_2$ couple because of the increased content of Mn^{+3} on the nanoparticle surface.[15] The oxidation/reduction peak intensities are different with different Mn content. While Mn^{+3} ions in spinels (from $MnCo_2O_4$ to Mn_2CoO_4) increase there is a decrease in peak current densities for oxidation and reduction peaks. No peaks are observed in this region for the oxidation and reduction at Mn_2CoO_4 coated sample. Lee et al. believe that when the Mn^{+3} ion content is increased in the tetragonal phase of $Mn_xCo_{3-x}O_4$ ($0.0 \leq x \leq 2.0$), the stabilization of Mn^{+3} is increased by Jahn – Teller distortion.[15] Therefore, the oxidation of Mn^{+3} to Mn^{+4} is becoming harder and there is no oxidation at pure tetragonal phase (Mn_2CoO_4). However, the charge associated with these peaks are $\approx$ 30 $\mu C\ cm^{-2}$ and this corresponds to a small fraction of a monolayer oxidation/reduction charge ($\approx$ 150 $\mu C\ cm^{-2}$) on an atomically smooth surface. Therefore, these peaks are not associated with conversion of ions in the structure. These peaks are most probably from impurity or very minor species (such as iron couple) on the surface of these samples.

III) The addition of Mn ions into spinel Co_3O_4 further suppresses the Co redox couple at around +500 mV for all Mn containing spinels. According to XPS and XANES data, Mn^{+3} ions replace with Co^{+3} in the spinel cobalt oxide. This is an important finding from the data in this chapter, and supports the assertion that the oxidation and reduction peaks around +500 mV for Co_3O_4 are most likely from the Co(III/IV) redox couple.

4.4.2. Oxygen Reduction

Oxygen reduction reaction properties at spinel $Mn_xCo_{3-x}O_4$ ($0.0 \leq x \leq 2.0$) catalysts coated on glassy carbon electrodes were investigated by linear sweep voltammetry (LSV) in O_2 saturated 1 M KOH at 25 ^oC with 5 mV s^{-1} potential scan rate at 400 RPM and as shown

in **Figure 4.18**. Carbon powder (XC-72R) and Pt black were also included for comparison purpose. The activity was assessed from both the current density in the foot of the reduction waves and from the limiting current densities. In both cases, there is an obvious increase in the catalytic activities of all Mn containing spinels towards ORR compared to pure Co_3O_4. This is an expected results since mixed metal oxides show higher catalytic activity for ORR[8, 9, 15, 43, 44] as introduced in **Chapter 1**.

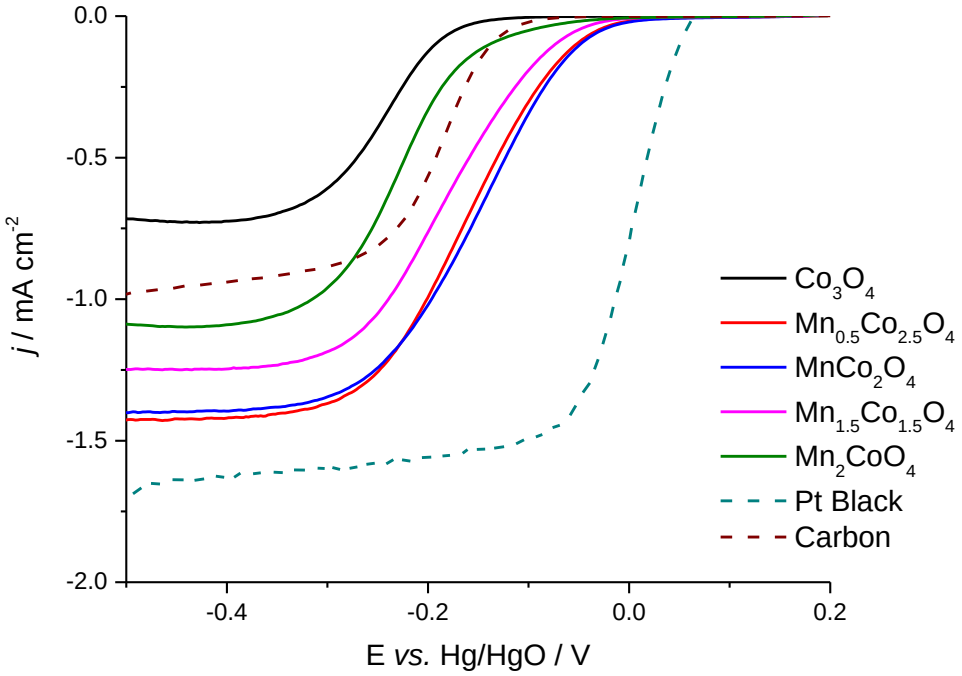

Figure 4.18. ORR voltammograms of Mn doped $Mn_xCo_{3-x}O_4$ ($0.0 \leq x \leq 2.0$) catalysts, Pt black and Carbon (XC-72R) in O_2 saturated 1 M KOH. Temperature: 25 ^oC; Potential scan rate: 5 mV s^{-1}; Rotation rate: 400 RPM.

The reduction waves show two distinct regions:

a) <u>Foot of wave:</u> In this region, there is a large potential dependency and the rate determining step must be an electron transfer reaction.

b) <u>Plateau region:</u> The current is independent of potential and the rate determining step is either a chemical step or mass transport in this region.

4.4.2.1. Foot of Wave

Figure 4.19 shows the variation of the current density at – 0.15 V with Mn content. There is an increase in the catalytic activities of cubic phase samples (Co_3O_4, $Mn_{0.5}Co_{2.5}O_4$ and $MnCo_2O_4$) with Mn content but the trend is reversed with the tetragonal phase. The results show that the highest ORR activities are observed with cubic phase $MnCo_2O_4$ (almost similar to $Mn_{0.5}Co_{2.5}O_4$). Rios et al. show the same increase in ORR activity for cubic phase samples ($Mn_xCo_{3-x}O_4$ ($0.0 \leq x \leq 1.0$)).[9] It is also worth noting that $MnCo_2O_4$ approaches the ORR activity of Pt black with only ≈ 100 mV larger onset potential at a current density of – 0.1 mA cm^{-2}.

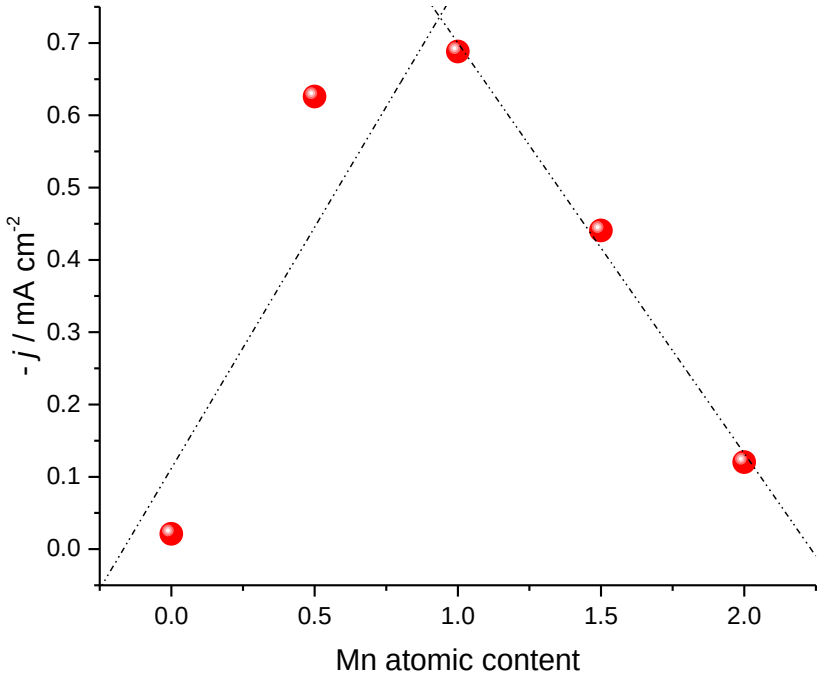

Figure 4.19. ORR activities (current density) versus Mn atomic content in spinels $Mn_xCo_{3-x}O_4$ ($0.0 \leq x \leq 2.0$) at – 0.15 V. The lines shown are the best fit through the three data points on either side of the peak.

ORR activities of samples can be also compared with their potentials at a specific current density. **Figure 4.20** compares potentials versus Mn content in spinels at a chosen specific current density (– 0.03 mA cm^{-2}). The same trends can be seen in these results also since the

lowest onset potential is observed with $MnCo_2O_4$. According to results (especially in **Figure 4.19**), oxygen reduction activity at cubic phase sample (0.69 mA cm^{-2} for $MnCo_2O_4$) is almost 6 times higher than tetragonal phase sample (0.12 mA cm^{-2} for Mn_2CoO_4). The similar result was also provided by Garg et al. who showed that cubic phase $MnCo_2O_4$ nanocubes has 5 times higher oxygen reduction activity than tetragonal phase Mn_2CoO_4 nanocubes.[5] The slight difference between their results and the results in this chapter might be coming from different preparation methods.

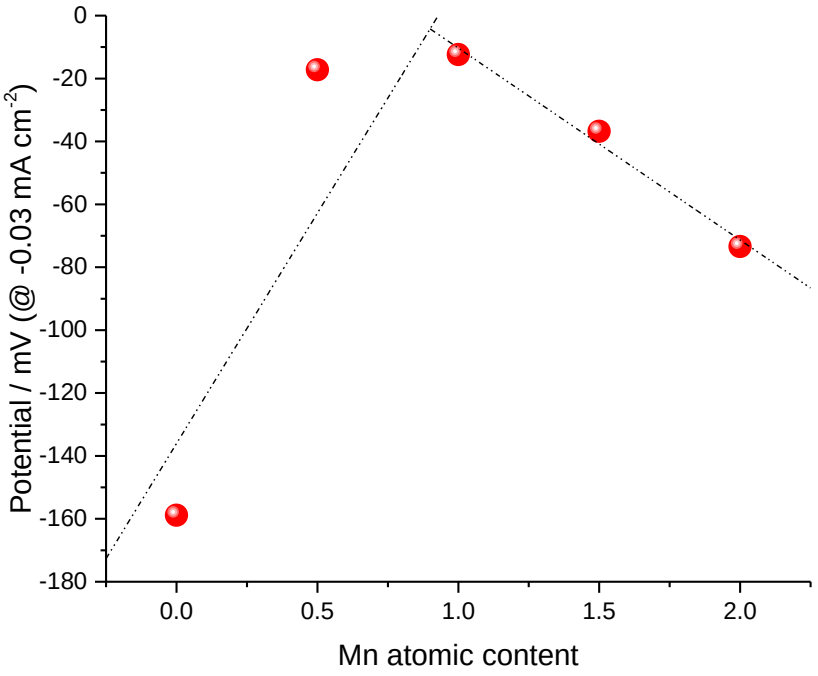

Figure 4.20. ORR potentials versus Mn atomic content in spinels $Mn_xCo_{3-x}O_4$ ($0.0 \leq x \leq 2.0$) at – 0.03 mA cm^{-2}. The lines shown are the best fit through the three data points on either side of the peak.

The literature commonly investigates and compares the kinetics of the ORR using Tafel plots. **Figure 4.21** shows Tafel plots for all 5 spinels, which are created from the ORR voltammograms at 400 RPM between 0.0 and – 0.2 V *vs* Hg/HgO in **Figure 4.18**. As shown, there is not a clear range where the log | *j* | *vs* E are linear. Therefore, no further analyses were carried out from Tafel plots.

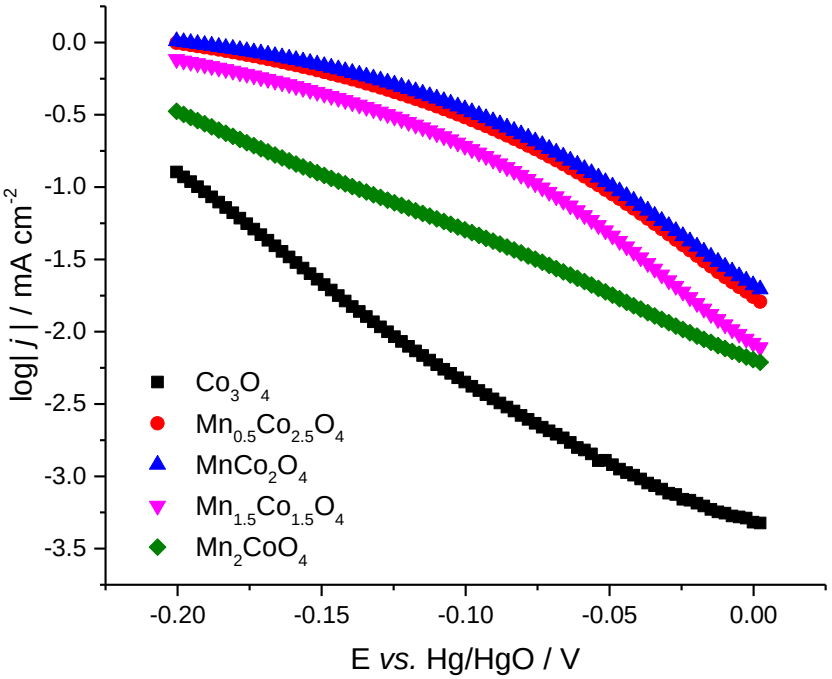

Figure 4.21. Tafel plots of Mn doped $Mn_xCo_{3-x}O_4$ ($0.0 \leq x \leq 2.0$) catalysts made from ORR voltammograms of spinels at 400 RPM (**Figure 4.18**). Data taken between 0.0 V and – 0.2 V *vs* Hg/HgO.

4.4.2.2. Plateau region

The rotation rate dependency of the voltammograms at all five spinels coated on GC electrode were further investigated and **Figure 4.22** reports the rotation rate dependencies of the responses at these materials in 1 M KOH. Well formed sigmoidal voltammograms were obtained for each rotation rate at each spinel. The value of limiting current densities at those containing Mn ions are much higher than that at Co_3O_4.

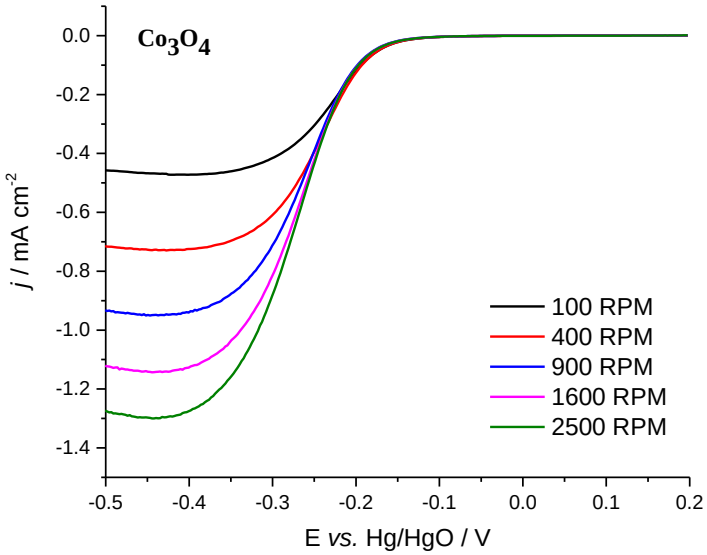
Co3O4
j / mA cm-2
E vs. Hg/HgO / V
100 RPM
400 RPM
900 RPM
1600 RPM
2500 RPM

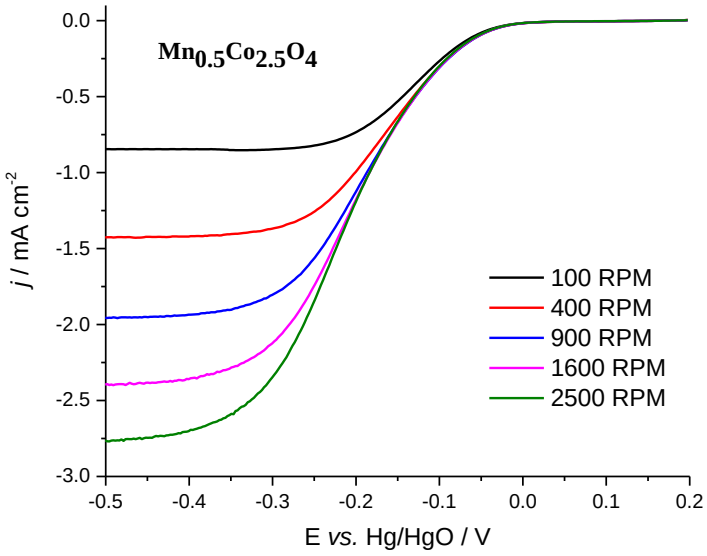
Mn0.5Co2.5O4
j / mA cm-2
E vs. Hg/HgO / V
100 RPM
400 RPM
900 RPM
1600 RPM
2500 RPM

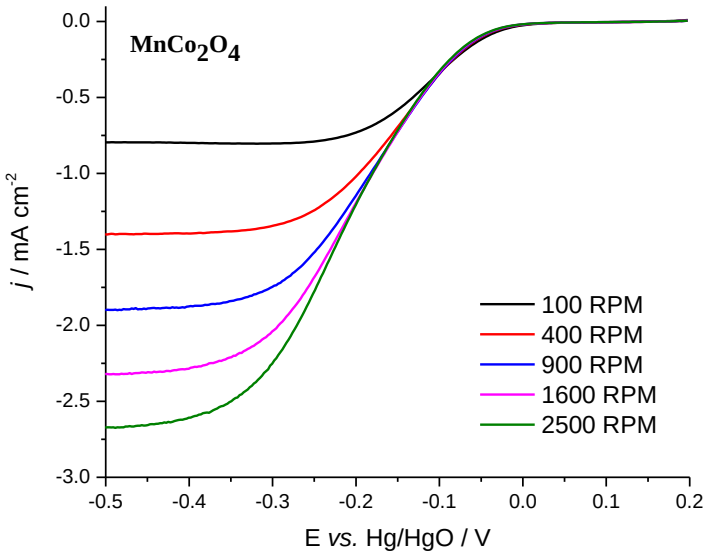
MnCo2O4
j / mA cm-2
E vs. Hg/HgO / V
100 RPM
400 RPM
900 RPM
1600 RPM
2500 RPM

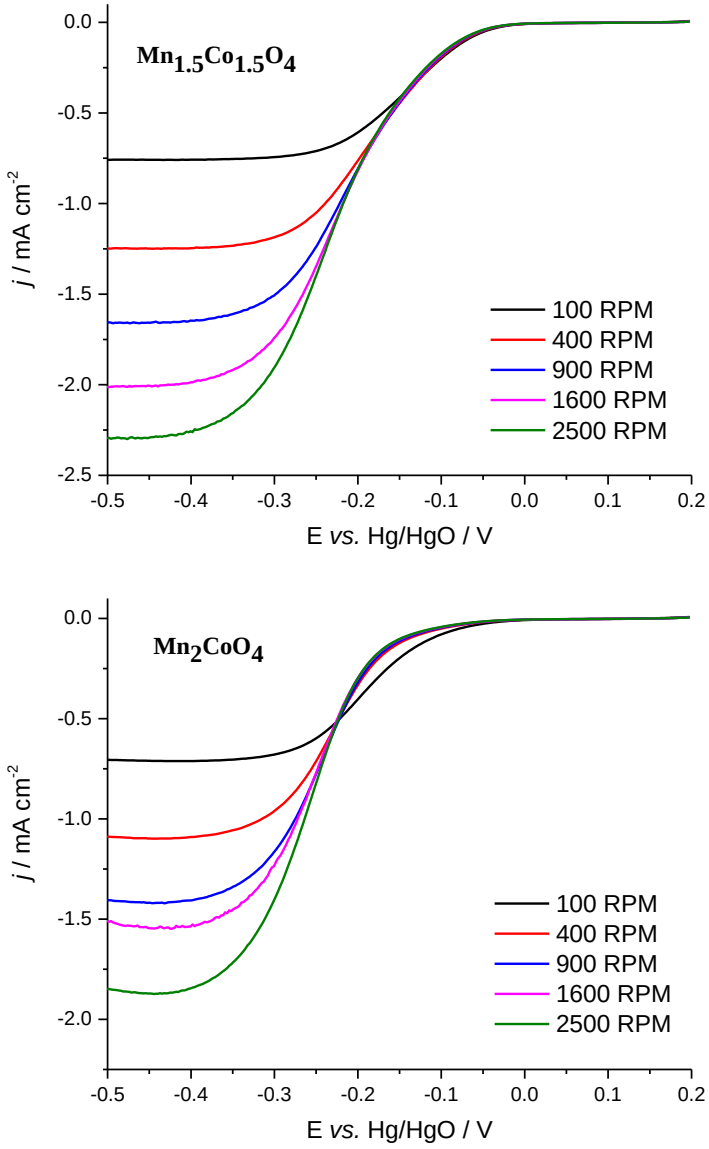

Figure 4.22. ORR voltammograms of Mn doped $Mn_xCo_{3-x}O_4$ ($0.0 \leq x \leq 2.0$) catalysts coated glassy carbon in O_2 saturated 1 M KOH. Temperature: 25 ^oC; Potential scan rate: 5 mV s^{-1}.

Again to point out, the rate determining step in the limiting current plateau region can be either limited by mass transport or a chemical step. It is obvious that the limiting current densities are increased with an increase in the speed of rotation rate for all five samples (see **Figure 4.22**). However, the oxygen reduction is not completely mass transport controlled since the limiting current densities versus the square root of rotation rates (Levich Plots, not shown) are not linear passing through the origin. Also intercepts are different at the different spinels. According to these results, the oxygen reduction is partially limited by a chemical

step for all five spinels. Therefore, further data analysis was carried out using the Koutecky – Levich (K – L) equation (see **Equation 3.1,** in **Chapter 3**) in order to gain further information about the number of transferred electrons (n) per oxygen molecule from K – L slopes and the rate of chemical step from the intercepts.

Figure 4.23 reports plots of $1 / j_L$ *vs* $1 / \omega^{1/2}$ for five spinels (top) and Pt black and carbon XC– 72R (bottom) coated electrodes. The slopes and intercepts from these plots are reported in **Table 4.6**. The linear fit through data points goes through 3 points (100, 400 and 900 rpm) for all samples and it is obvious that there is a deviation at higher rotation rates (1600 and 2500 rpm, small $1 / \omega^{1/2}$ values) especially for Co_3O_4. Again K – L plots of Pt black and carbon powder were used in this chapter for comparison purpose since oxygen is reduced on Pt via $4e^-$ reduction while it is $2e^-$ reduction on carbon. As shown from K – L plots, there are clear intercepts at all spinels, which proves the oxygen reduction is partially limited by a chemical step. A small intercept indicates a rapid chemistry while a large value indicates a slow chemical rate determining step. The values of the intercepts are reported in **Table 4.6**, and it is clear that the smallest intercept was obtained at cubic phase $MnCo_2O_4$ while the highest was observed at Co_3O_4. Smaller intercept means larger rate of chemical step (see **Equation 3.1**, **Chapter 3**), therefore, O – O cleavage is faster and more favourable when the rate of chemical step is large. It is also worth noting that the intercept value of $MnCo_2O_4$ is slightly larger than Pt black.

As to the comparison of slopes (see **Table 4.6**), it is obvious that slopes of all spinels except Co_3O_4 are very close to Pt black and especially the slope of $MnCo_2O_4$ is the same of Pt black, confirming that oxygen is reduced via $4e^-$ at all Mn containing spinels. The slope of Co_3O_4 is slightly smaller than carbon black and the larger deviation at higher rotation rate also confirms that oxygen reduction is predominantly occurred via $2e^-$ reduction at Co_3O_4.

The number of apparent electron (n_{app}) transferred per oxygen molecule and the formation of hydrogen peroxide will be investigated from RRDE data in section **4.4.4**.

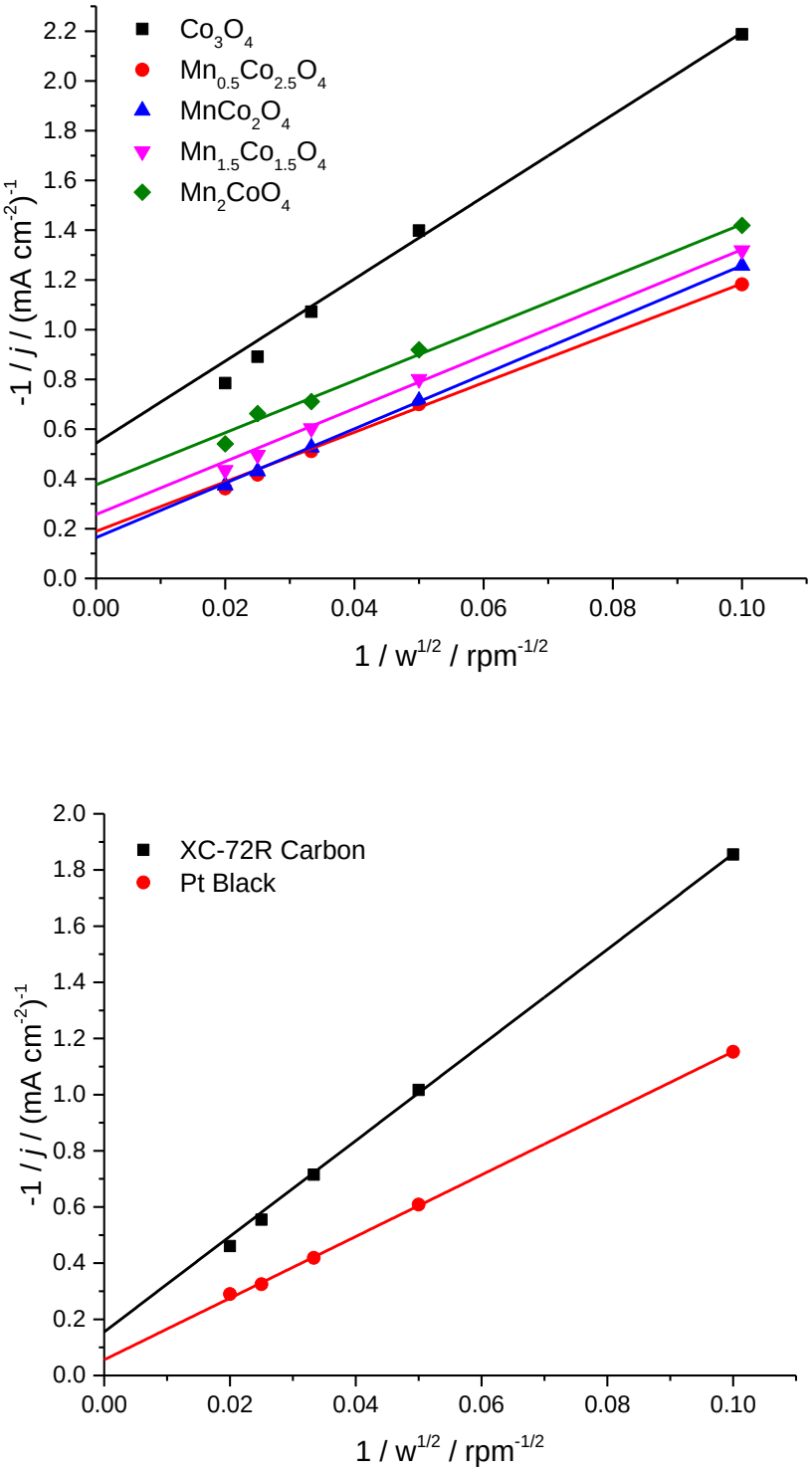

Figure 4.23. Koutecky-Levich plots for O_2 reduction in O_2 purged 1 M KOH with Mn doped $Mn_xCo_{3-x}O_4$ ($0.0 \leq x \leq 2.0$) catalysts, Pt black and carbon powder (XC-72R) coated glassy carbon. Data taken at – 500 mV *vs* Hg/HgO, in the plateau regions of the voltammograms. Temperature: 25 ^oC; Potential scan rate: 5 mV s^{-1}. Lines shown are best fits through only the three lowest rotation rates (100, 400 and 900 RPM).

Catalyst	Koutecky – Levich		% H_2O_2*	n_{app} / Apparent electron number*
	Slope / mA^{-1} cm^2 $rpm^{-1/2}$	Intercept / mA^{-1} cm^2		
Co_3O_4	-16.5 (±0.8)	-0.54 (±0.05)	76 (±4)	2.48
$Mn_{0.5}Co_{2.5}O_4$	-9.96 (±0.3)	-0.19 (±0.02)	18 (±1)	3.64
$MnCo_2O_4$	-10.94 (±0.1)	-0.16 (±0.01)	16 (±1)	3.68
$Mn_{1.5}Co_{1.5}O_4$	-10.65 (±0.3)	-0.26 (±0.02)	33 (±2)	3.35
Mn_2CoO_4	-10.48 (±0.5)	-0.38 (±0.03)	41 (±2)	3.18
Pt Black	-10.97 (±0.1)	-0.06 (±0.01)	<1	-
Carbon (XC-72R)	-17.02 (±0.3)	-0.16 (±0.02)	59.5 (±3.0)	2.81

Table 4.6. Comparison of catalyst materials with Pt black and Carbon (XC – 72R) RDE and RRDE data. O_2 saturated 1 M KOH; Temperature: 25 ^oC; Potential scan rate: 5 mV s^{-1}; Rotation rate: 400 RPM. *****Data were collected at 400 RPM where potential was – 0.5 V. Slopes and intercepts for all materials shown in the table are only from first three points, corresponding to rotation rates of 100, 400 and 900 RPM.

4.4.3. Oxygen Evolution

The oxygen evolution reaction (OER) behaviours at $Mn_xCo_{3-x}O_4$ ($0.0 \leq x \leq 2.0$) spinels were carried out in order to investigate the bifunctional properties at these materials and to assess the effect of Mn content towards OER. **Figure 4.24** shows OER voltammograms at five spinels, bare GC and Pt black in 1 M KOH at room temperature with 5 mV s^{-1} potential scan rate. The results show that oxygen evolution activities increase from cubic phase Co_3O_4 to $MnCo_2O_4$ and then the activities decrease from cubic phase $MnCo_2O_4$ to tetragonal phase Mn_2CoO_4, yielding a similar trend to the ORR activities. The highest oxygen reduction and evolution activities and lowest onset potentials for both ORR and OER at $MnCo_2O_4$ (with x =1) make this sample the most active bifunctional catalyst amongst manganese doped Co_3O_4 series ($Mn_xCo_{3-x}O_4$ ($0.0 \leq x \leq 2.0$)). The results reported in this chapter show that adding Mn into spinels, which have pure cubic phase, increases OER activity. On the other hand, according to some studies[9, 34, 45, 46], adding Mn into Co_3O_4 decreases the OER activities. The origins of this discrepancy between our work and these studies are not known.

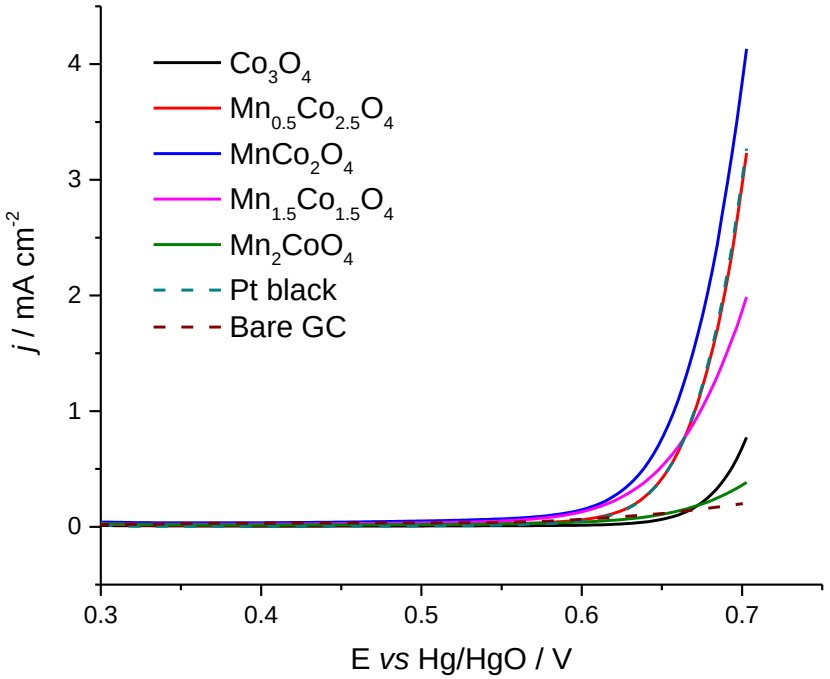

Figure 4.24. OER voltammograms of Mn doped $Mn_xCo_{3-x}O_4$ ($0.0 \leq x \leq 2.0$) catalysts, Pt black and bare GC in O_2 saturated 1 M KOH. Temperature: 25 ^oC; Potential scan rate: 5 mV s^{-1}.

4.4.4. Hydrogen Peroxide Formation as Intermediate Product

RRDE studies were also carried out to investigate hydrogen peroxide formation as intermediate product in the oxygen reduction at five catalysts coated on GC disc/Pt ring electrodes. While the potential of the ring was held at 0.2 V *vs* Hg/HgO, where the oxidation of hydrogen peroxide is mass transport controlled at Pt,[44, 47] the GC disc electrode was scanned from 0.2 V to – 0.5 V *vs* Hg/HgO, where oxygen is reduced. **Figure 4.25** shows the responses from the disc and ring under similar conditions at five spinels. The percentage (%) of the reduction currents, which lead to H_2O_2, at these spinels, Pt black and carbon powder are estimated using **Equation 4.2** and reported in **Table 4.6**;[43]

$$H_2O_2\ \% = 200\frac{I_R/N}{I_D+I_R/N} \qquad \textbf{Equation 4.2}$$

Where I_D is disc current, I_R is ring current and N is current collection efficiency (0.37). As can be seen from **Figure 4.25** and H_2O_2 % in **Table 4.6**, there is peroxide formation at all spinel catalysts although the H_2O_2 % at each material are very different.

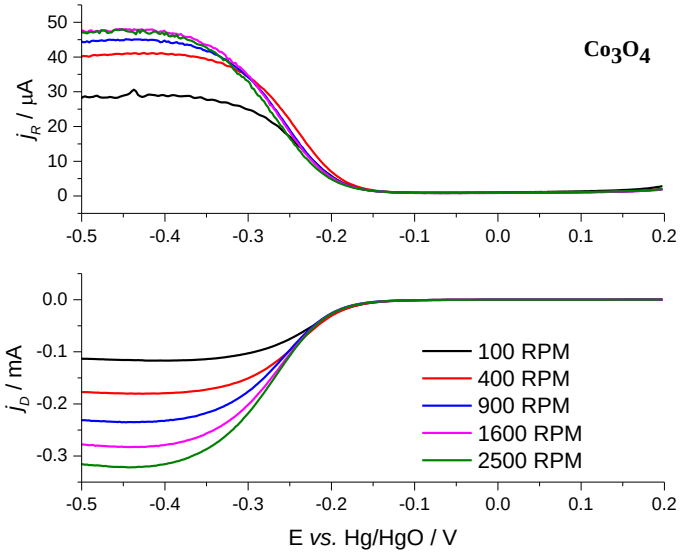
Co3O4
jR / µA
jD / mA
100 RPM
400 RPM
900 RPM
1600 RPM
2500 RPM
E vs. Hg/HgO / V

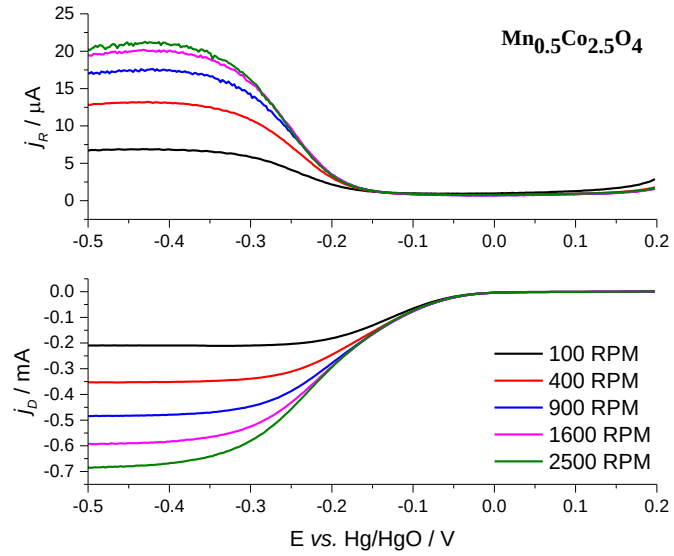
Mn0.5Co2.5O4
jR / µA
jD / mA
100 RPM
400 RPM
900 RPM
1600 RPM
2500 RPM
E vs. Hg/HgO / V

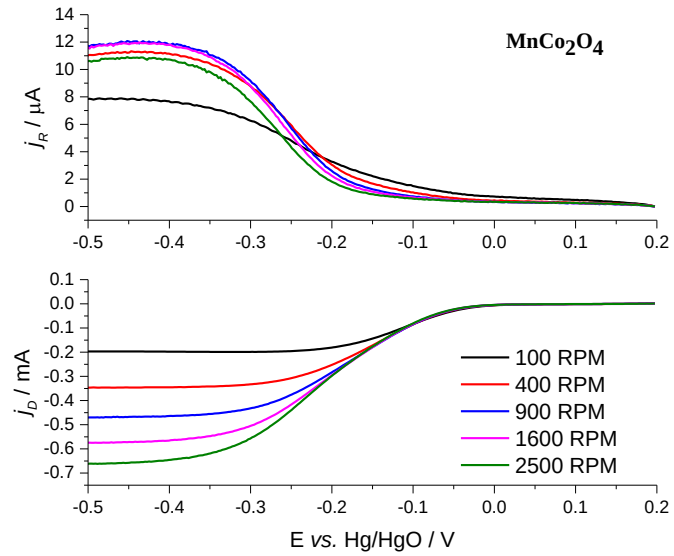
MnCo2O4
jR / µA
jD / mA
100 RPM
400 RPM
900 RPM
1600 RPM
2500 RPM
E vs. Hg/HgO / V

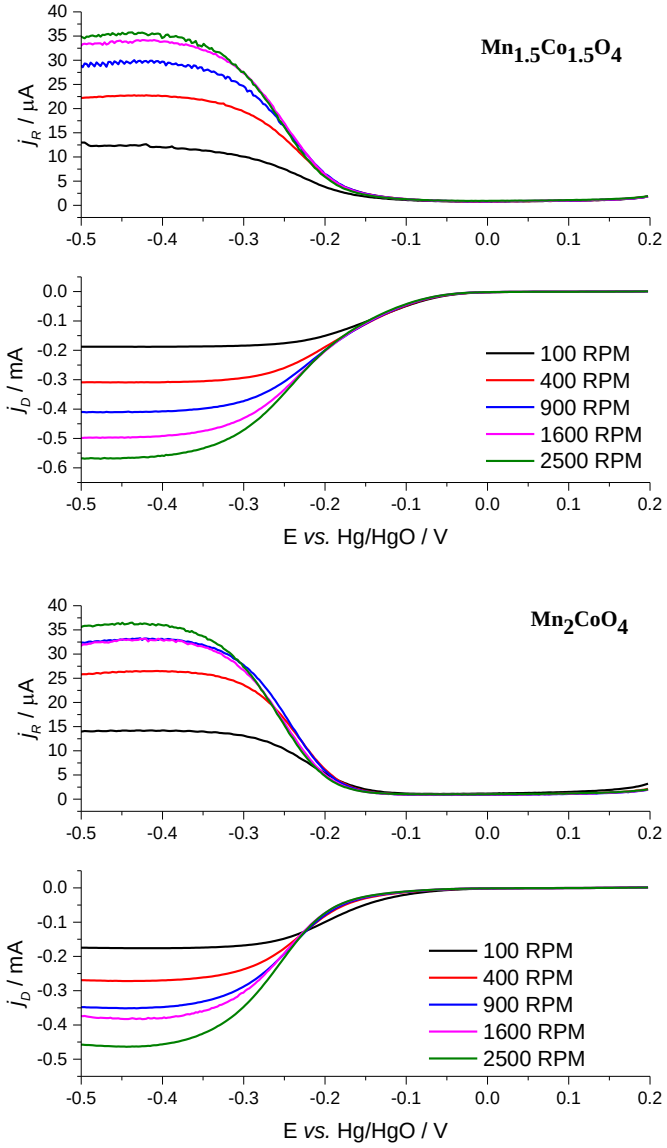

Figure 4.25. Ring (top) and disc (bottom) responses for O_2 reduction at Mn doped $Mn_xCo_{3-x}O_4$ ($0.0 \leq x \leq 2.0$) catalysts coated glassy carbon discs. The potential of the discs is scanned while the Pt ring electrode is held at + 200 mV *vs* Hg/HgO. Rotation rates as shown. O_2 saturated 1 M KOH. Temperature: 25 ^oC; Potential scan rate: 5 mV s^{-1}. The disc area: 0.2475 cm^2; The ring area: 0.1866 cm^2. The collection efficiency of the RRDE is 0.37. Prior to each rotating, KOH was purged with O_2 for ≈ 8 mins.

As already shown in Plateau region section (**4.4.2.2**), oxygen reduction is mainly $2e^-$ reduction at Co_3O_4 coated electrode, which implied that high amount of hydrogen peroxide was expected. The result (H_2O_2 %) in **Table 4.6** confirms this outcome by showing large

amount of H_2O_2 formation (≈ 76 %) at Co_3O_4. RRDE results also confirm that Mn containing cubic phase spinels ($Mn_{0.5}Co_{2.5}O_4$ and $MnCo_2O_4$) are more favourable than tetragonal phase sample (Mn_2CoO_4) for oxygen to be reduced via $4e^-$ pathway. With $MnCo_2O_4$, hydrogen peroxide detected at Pt ring was the smallest, ≈ 16 % at 400 RPM. In fact, SEM images of GC electrode edge showed (see **Figure A2.1**, in **Appendix**) that there was uncovered GC close to PTFE surround (This error was calculated in **Chapter 2** as –6.4 %) and this may contribute to the final hydrogen peroxide percentages reported in **Table 4.6**.

Hydrogen peroxide formation at Pt and carbon black are the same as reported in **Chapter 3**. It is clear that hydrogen peroxide formation reaction is predominant at carbon black as expected from known the performance of gas diffusion electrodes (GDE)[48] while it is a minor contribution at Pt black.

The number of apparent electrons (n_{app}) transferred per oxygen molecule can be also calculated from Rotating Ring Disc Electrode (RRDE) data by using the equation below; [43, 49-51]

$$n_{app} = 4\frac{I_D}{I_D + \frac{I_R}{N}} \qquad \textbf{Equation 4.3}$$

I_D, I_R and N are disc current, ring current and current collection efficiency, respectively. Apparent electron numbers for oxygen reduction at all spinels were calculated from RRDE data (see **Figure 4.25**) collected with 400 RPM at – 0.5 V by using **Equation 4.3** and reported in **Table 4.6**. Results show that apparent electron numbers are much higher at Mn containing spinels compared to those at Co_3O_4. These results confirm the results obtained in section (**4.4.2.2**) that oxygen is mainly reduced via the $2e^-$ reduction pathway at Co_3O_4 while it is the $4e^-$ reduction pathway at Mn containing spinels. The highest apparent electron numbers (n_{app} = 3.68) were observed at cubic phase $MnCo_2O_4$ as expected. The results also prove that cubic phase is more favourable than tetragonal phase as shown from apparent electron numbers for all spinels. The number of transferred electrons are not exactly $4e^-$ for Mn containing samples, in which the deviations are caused by the varied rate of chemical steps involved in ORR process. Samples with higher values of intercept (small rate of chemical step) showed smaller apparent electron numbers (see **Table 4.6**).

4.4.5. Hydrogen Peroxide Oxidation and Reduction

The voltammetry of H_2O_2 oxidation and reduction at spinel Mn doped cobalt oxides ($Mn_xCo_{3-x}O_4$, $0.0 \leq x \leq 2.0$) materials are highly important to define exact oxygen reduction pathways, which can be direct $4e^-$ reduction or $2x2e^-$ reduction pathway, at these materials. In some cases, the oxygen reduction pathway may look like $4e^-$ reduction even though it may be $2x2e^-$ reduction if the second $2e^-$ is fast. To show the simple case of H_2O_2 oxidation and reduction, the voltammetry of 10 mM H_2O_2 in N_2 purged 1 M KOH at Pt black is reported in **Figure 4.26**. The limiting currents for oxidation and reduction are equal and the actual values are large compared to all Mn containing spinels.

Figure 4.27 reports the oxidation and reduction voltammograms of ≈ 10 mM H_2O_2 in N_2 purged 1 M KOH with different rotation rates at five spinels (all experiments were carried out on the same day in order to make a logical comparison since H_2O_2 decomposes with time (see **Figure A4.1**, in **Appendix** for the degree of H_2O_2 decomposition in 12 hours)).

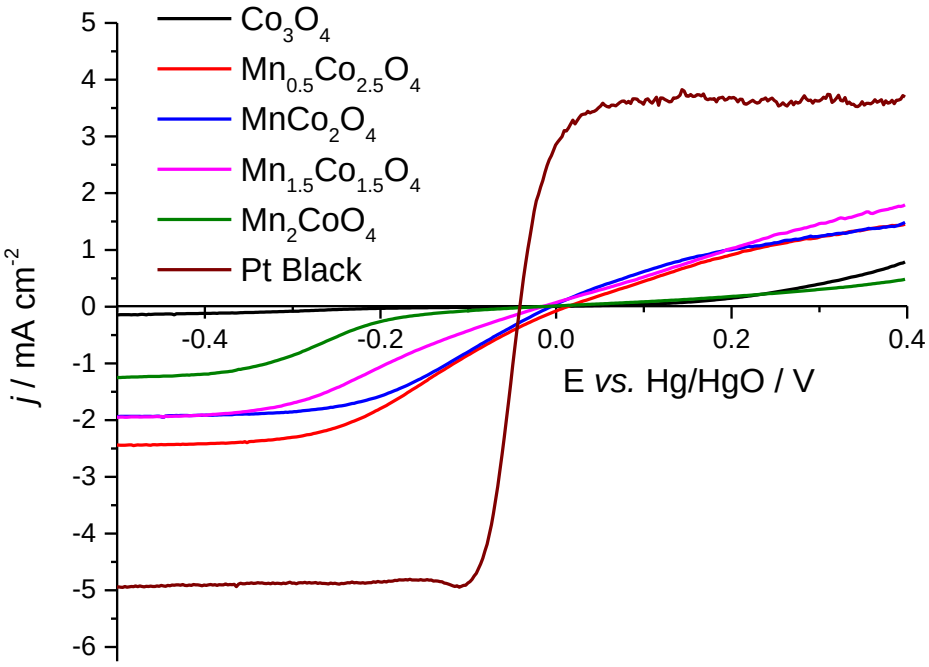

Figure 4.26. Voltammograms of the reduction and oxidation of ≈ 10 mM H_2O_2 in N_2 purged 1 M KOH at Mn doped $Mn_xCo_{3-x}O_4$ ($0.0 \leq x \leq 2.0$) catalysts and Pt black coated glassy carbon. Rotation rate: 400 RPM; Temperature: 25 ^oC; Potential scan rate: 5 mV s^{-1}.

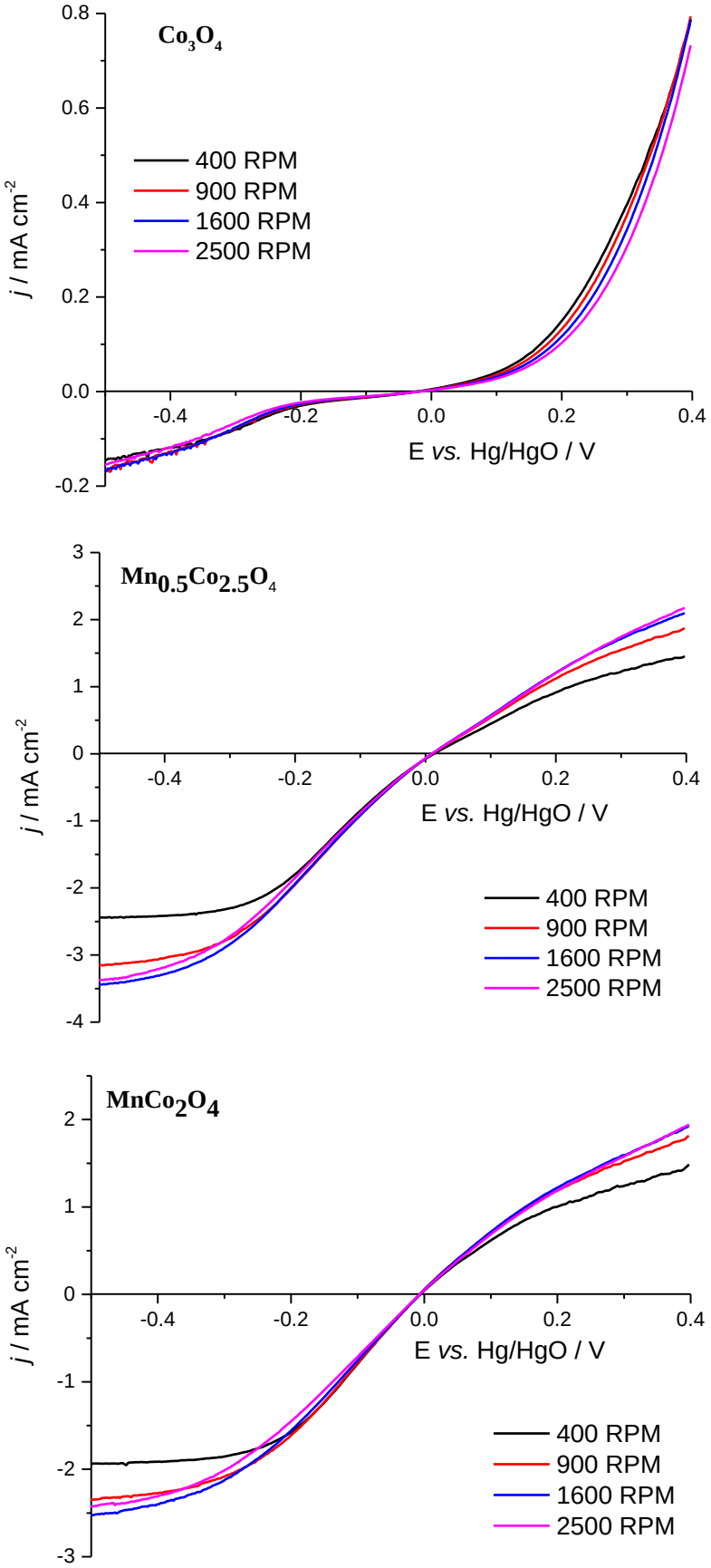
Co3O4
400 RPM
900 RPM
1600 RPM
2500 RPM
j / mA cm-2
E vs. Hg/HgO / V
Mn0.5Co2.5O4
MnCo2O4

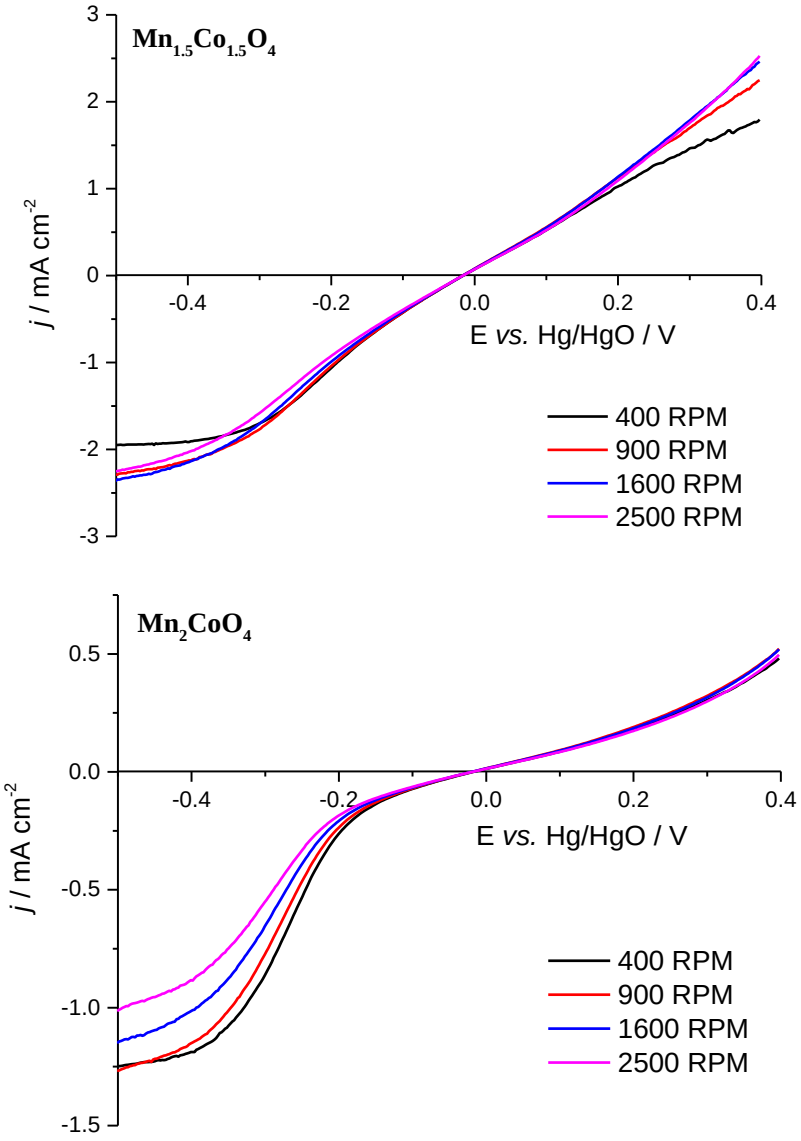

Figure 4.27. Rotation rate dependence of the voltammograms for the reduction and oxidation of ≈ 10 mM H_2O_2 in N_2 purged 1 M KOH at Mn doped $Mn_xCo_{3-x}O_4$ ($0.0 \leq x \leq 2.0$) catalysts coated glassy carbon. Rotation rates are as shown. Temperature: 25 ^oC; Potential scan rate: 5 mV s^{-1}. Electrolyte was purged with N_2 for ≈ 5 minutes prior to each measurement.

As seen in **Figure 4.27**, the oxidation and reduction current densities at all spinels show little dependency on rotation rate, confirming that hydrogen peroxide reduction and oxidation are strongly kinetically limited with these spinels. According to results in **Figure 4.26**, showing that the current densities at spinels are much lower than expected, and **Figure 4.27**, the

intermediate product (H_2O_2) can not be rapidly reduced to hydroxide due to strong kinetic limitation. Therefore, it is obvious that a 2x2e$^-$ mechanism for a 4e$^-$ reduction is not possible at the aforementioned spinels.

4.5. Discussion

Spinel type manganese cobalt oxides were synthesised with a wide manganese composition range ($Mn_xCo_{3-x}O_4$, $0.0 \leq x \leq 2.0$) via co-precipitation method. Physical characterisation results show that samples with Mn content up to x = 1.0 have a cubic phase. On the other hand, the mixture of cubic and tetragonal phase is obtained with $Mn_{1.5}Co_{1.5}O_4$ while the phase is only tetragonal with Mn_2CoO_4. The crystallinity of sample is decreased by increasing Mn in pure Co_3O_4. This decrease in crystallographic symmetry is caused by a Jahn – Taller distortion[11-13], which was turned to be more dominant when Mn^{+3} ions exceed the critical fraction (60 – 65 %). It was also shown that Mn incorporation into pure Co_3O_4 increases the surface area and decreases the particle sizes. With $MnCo_2O_4$, the highest surface area (50 $m^2\ g^{-1}$) and smallest particle size (≈ 7 nm) material was obtained. Thus, the morphology of materials can be tuned with composition, which highly affects the intrinsic properties of spinels for oxygen reduction/evolution.

XPS studies proved that the surface elemental compositions were close to the bulk atomic ratios although some surface segregation of Mn was observed. The slight deviation from the bulk Mn:Co composition is due to the surface state, which is affected by all species adsorbed on the surface (such as OH^- and H_2O_{ads}). It was also shown by high resolution Co 2p photoemission lines that the amount of Co^{+3} in octahedral sites was decreased when x (Mn dopant) was increased, showing that Mn^{+3} ions substitute for Co^{+3} in Co_3O_4. High resolution Mn 2p spectrum presents the characteristic two peaks of Mn(III) cation. These results were also supported with electrochemical measurements and literature data[5, 15] by showing that no oxidation and reduction peaks for Co^{+3}/Co^{+4} couple in cyclic voltammograms of Mn containing spinels. Ex-situ XANES studies are well consistent with XPS measurements for five spinel samples $Mn_xCo_{3-x}O_4$ ($0.0 \leq x \leq 2.0$) (see **Table 4.7**). According to XANES and XPS results, substituted Mn ions' oxidation states are +3 and by doping Mn ions, the mean oxidation states of Co is getting closer to 2, suggesting that Mn^{+3} ions replace in Co^{+3} in all spinels. The XPS data also revealed the existence of Mn^{+4} ions. This most likely comes from an excess of Mn ions on the surface of the catalysts. This supports the ex-situ XANES data

where the mean manganese oxidation states are all greater than +3 (see **Table 4.7**). Moreover, by considering statistical fits from XRD refinement, Mn^{+3} ions prefer to occupy tetrahedral sites rather than octahedral sites in the spinels. According to these findings (statistical fits from XRD refinement, XPS and ex-situ XANES), the cationic distribution of all five spinels is as suggested in **Table 4.8**.

	XPS		**Ex-Situ XANES**	
Catalyst	**Co^{+2}/Co^{+3} ratio (qualitative)**	**Mn^{+3} (qualitative)**	**Mean Co Oxidation State (± 0.023)**	**Mean Mn Oxidation State (± 0.025)**
Co_3O_4	smallest ratio ↓ largest ratio	-	2.5	-
$Mn_{0.5}Co_{2.5}O_4$		least amount ↓ greatest amount	2.37	3.53
$MnCo_2O_4$			2.35	3.42
$Mn_{1.5}Co_{1.5}O_4$			-	3.23
Mn_2CoO_4			-	3.14

Table 4.7. Comparison of the XPS and Ex-Situ XANES data of $Mn_xCo_{3-x}O_4$ ($0.0 \leq x \leq 2.0$). (XPS data also show the existence of Mn^{+4} species on the surface of materials).

Catalyst	**Suggested Cationic Distribution**
Co_3O_4	$[Co^{+2}]_{Th}[Co^{+3}{}_2]_{Oh}O_4$
$Mn_{0.5}Co_{2.5}O_4$	$[Mn^{+3}{}_{0.5}\,Co^{+2}{}_{0.5}]_{Th}[Co^{+3}{}_{1.5}\,Co^{+2}{}_{0.5}]_{Oh}O_4$
$MnCo_2O_4$	$[Mn^{+3}]_{Th}[Co^{+3}\,Co^{+2}]_{Oh}O_4$
$Mn_{1.5}Co_{1.5}O_4$	$[Mn^{+3}]_{Th}[Co^{+3}\,Co^{+2}]_{Oh}O_4$ (83.5%) + $[Mn^{+3}]_{Th}[Co^{+2}Mn^{+3}]_{Oh}O_4$ (16.5%)
Mn_2CoO_4	$[Mn^{+3}]_{Th}[Co^{+2}Mn^{+3}]_{Oh}O_4$

Table 4.8. Catalysts and their suggested cationic distributions based on XPS, ex-situ XANES and statistical fits from XRD refinement.

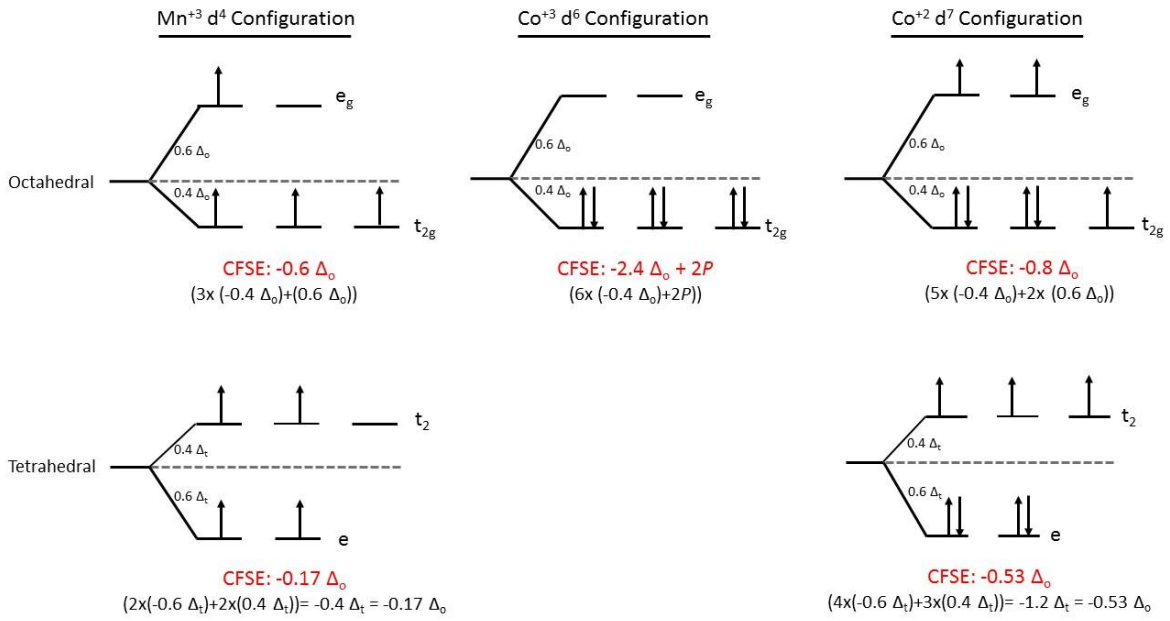

Figure 4.28. The d-orbital configurations for Mn^{+3}, Co^{+3} and Co^{+2} ions in octahedral and tetrahedral coordination. CFSE: Crystal Field Stabilization Energy; Δ: The ligand-field splitting parameter; *P*: Pairing energy; $\Delta_t = 4/9\ \Delta_o$.

Figure 4.28 shows the possible d orbital configurations and calculated crystal field splitting energies (CFSE) of the various ions (Mn^{+3}, Co^{+3} and Co^{+2}) in spinels ($Mn_xCo_{3-x}O_4$, $0.0 \leq x \leq 2.0$). Based on XPS and ex-situ XANES data, the oxidation state of Mn doped in spinel Co_3O_4 is +3 (d^4) and as already known (see **Chapter 1**) the oxidation states of Co in spinel Co_3O_4 are +2 (d^7) and +3 (d^6). Therefore, the cationic distributions of all five spinels may be proposed from crystal field theory. From crystal field theory, the suggested cationic distribution of $MnCo_2O_4$, to name but one example, is $[Co^{+2}]_{Th}[Co^{+3}Mn^{+3}]_{Oh}O_4^{-2}$ since the calculated crystal field stabilization energy (CFSE) of $[Co^{+2}]_{Th}[Co^{+3}Mn^{+3}]_{Oh}O_4^{-2}$ is estimated as - $3.53\Delta_o$+2P, which is smaller than that for $[Mn^{+3}]_{Th}[Co^{+3}Co^{+2}]_{Oh}O_4^{-2}$ at - $3.37\Delta_o$+2P. However, based on the experimental studies (XRD fit statistics, XPS, and ex-situ XANES), the suggested cationic distribution for $MnCo_2O_4$ is $[Mn^{+3}]_{Th}[Co^{+3}Co^{+2}]_{Oh}O_4^{-2}$, which suggest that Mn ions occupy tetrahedral sites rather than octahedral sites. The origin of the inconsistency between the experimental results in this thesis and the results from crystal field theory is not clear. However, it should be noted that Δ_o values will vary for the

different ions, so the simple addition of the CFSE values is not fully valid. Since the CFSE values are close, these deviations could be significant.

Electrochemical measurements report that all spinels prepared as layers without carbon have bifunctional properties toward oxygen reduction and evolution in alkaline media. Cubic phase $MnCo_2O_4$ is the most active bifunctional catalyst amongst the five spinels, and it is especially more favourable for oxygen reduction reaction in terms of current density (at – 0.15 V) and onset potential (at – 0.03 mA cm^{-2}). The highest ORR activity was observed for the cubic phase $MnCo_2O_4$ (which is close to Pt black with a slightly less limiting current density and only ≈ 100 mV larger onset potential at – 0.1 mA cm^{-2}). This is because cubic phase has higher catalytic active sites and more strongly binding O_2 properties than tetragonal phase material(s).[5, 11, 13] It has been also believed that Mn^{+3} and Mn^{+4} are more active than Co species for ORR.[9, 43, 49, 52] Further analyses were conducted with Tafel plots, but Tafel plots show no linear region to obtain the kinetic parameters for comparing ORR activities of spinels in terms of rate constants.

The mechanistic studies of oxygen reduction at five spinels in alkaline media also show that pure Co_3O_4 is a poor catalyst (follow mainly $2e^-$ reduction) for oxygen reduction while Mn doped spinels are more effective catalysts (largely follow $4e^-$ reduction). Rotation rate dependency voltammograms were conducted and used for Koutecky – Levich (K – L) plots. K – L plots suggest that oxygen is mainly reduced via $2e^-$ pathway at Co_3O_4 since it shows somewhat similar slope to carbon black (XC – 72R), in which oxygen is reduced via $2e^-$ pathway. In this case, the suggested mechanism for O adsorption geometry at spinel Co_3O_4 could involve end-on O_2 adsorption (see **Chapter 1**, **Figure 1.2.b**). In contrast, it is followed via $4e^-$ pathway with Mn doped spinels since the slopes of Mn doped spinels are quite close to Pt black's, in which oxygen is reduced via $4e^-$ pathway. Therefore, the suggested mechanism for O adsorption geometry at Mn containing spinels should be bidentate O_2 adsorption (see **Chapter 1**, **Figure 1.2.c-d**). The slope of $MnCo_2O_4$ (-10.94) is the closest to Pt black's slope (-10.97) under similar conditions showing the oxygen reduction is $4e^-$ reduction on $MnCo_2O_4$. From the intercepts obtained from K – L plots, it can be suggested that oxygen reduction is partially limited by chemical steps at five materials to a varied degree. Again $MnCo_2O_4$ shows the highest rate of chemical step amongst five spinels, confirming that the fastest O – O cleavage is observed at this sample.

Figure 4.29 shows oxygen reduction mechanism at different potentials (– 0.1 V, where oxygen reduction is electron transfer controlled, and – 0.4 V, where oxygen reduction is mainly mass transport/chemical reaction controlled). There are possible oxygen reduction reactions shown in the foot of wave region and plateau region (see **Figure 4.29**):

I) Reaction in the foot of wave region (at – 0.1 V): O – O cleavage happens and then oxygen atoms can reduce with $4e^-$ reduction to form hydroxide. In this region, not all the O_2 is reduced but the rate of the reduction shows a large potential dependency; the rate determining step is electron transfer (slow) since electron transfer depends on potential. There is no chemical limitation or mass transport limitation in the oxygen reduction mechanism. O_2 cleavage (the rate of chemical step) is independent of the potential while it depends on the catalyst. The highest rate of the chemical step was obtained at $MnCo_2O_4$ amongst five spinels as mentioned above.

II) Reactions in the Plateau region (at – 0.4 V): There are two oxygen reduction mechanisms in this region. O – O cleavage continues to occur and oxygen atoms can be reduced with $4e^-$ reduction to form hydroxide but the current is now limited by chemical step. Any O_2 at the surface not consumed in O – O cleavage can now undergo direct electron transfer, initially to give superoxide (O_2^-). But the plateaux of the waves coincide with potentials where the reduction of O_2 to O_2^- is mass transport controlled, see voltammogram at carbon in **Figure 4.18**. There are two competing reaction mechanisms in plateau region, which are $4e^-$ reduction and $2e^-$ reduction (hydrogen peroxide formation). The kinetics and thermodynamics of electron transfer to oxygen atom and electron transfer to oxygen molecule are entirely different.

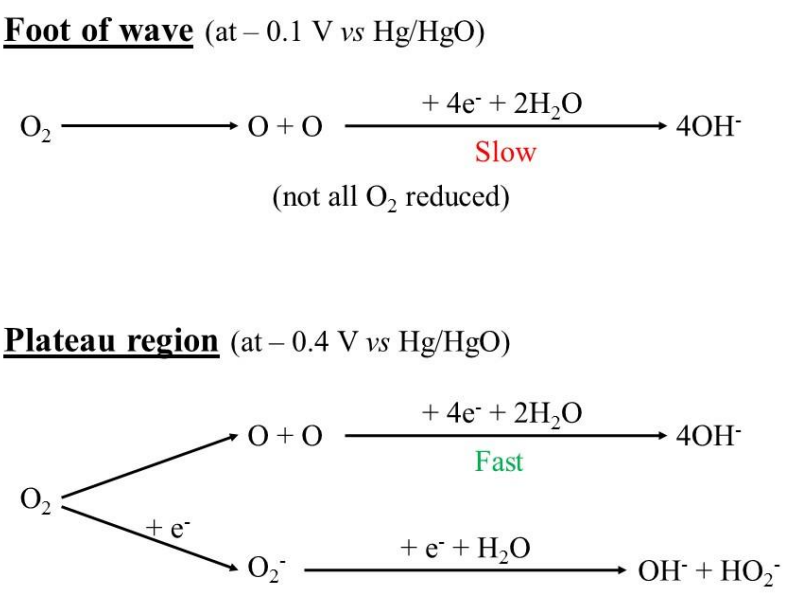

Figure 4.29. ORR mechanism at different potentials at Foot of wave (– 0.1 V) and Plateau region (– 0.4 V) in **Figure 4.18**.

Oxygen evolution behaviours of the spinels showed that adding Mn in pure Co_3O_4 increases OER activity up to x = 1.0, which is still cubic phase, and the activity is decreased from cubic phase sample ($MnCo_2O_4$) to tetragonal phase sample (Mn_2CoO_4). The OER results in this chapter suggest that adding Mn into Co_3O_4 increases OER activity up to x = 1.0 Mn content and cubic phase is more favourable than tetragonal phase for oxygen evolution, which does not agree with the results reported by some studies.[5, 13]

Hydrogen peroxide formation percentages (% H_2O_2) and the apparent electron number (n_{app}) are present (see **Table 4.6**) from the RRDE data. % H_2O_2 formations show that the lowest H_2O_2 % formation (16%) was observed with cubic phase $MnCo_2O_4$ sample while the highest amount of H_2O_2 formation (76%) was obtained at Co_3O_4. Adding Mn into pure Co_3O_4 decreases dramatically hydrogen peroxide formation. Again, cubic phase Mn containing spinels ($Mn_{0.5}Co_{2.5}O_4$ and $MnCo_2O_4$) show less hydrogen peroxide formation compared to those which are the mixture of cubic and tetragonal phase ($Mn_{1.5}Co_{1.5}O_4$) and only tetragonal phase (Mn_2CoO_4). The apparent electron number (n_{app}) is changed between 2.48 (Co_3O_4) to 3.68 ($MnCo_2O_4$). These are more accurate results to show that O_2 reduction is dominantly

$2e^-$ at Co_3O_4 while it is $4e^-$ at $MnCo_2O_4$. The deviation from $4e^-$ is due to chemical step in plateau region as shown in previous sections, and the rate of this deviation from $4e^-$ reduction is different for each Mn containing spinels, which is caused by different Mn content and phase (cubic or tetragonal). These results are also in a good agreement with the rotation rate dependency results as shown before.

As mentioned in **Chapter 1**, there are two main oxygen reduction pathways ($4e^-$ and $2e^-$ pathways) in alkaline media.[44, 53-55] The full $4e^-$ reduction can occur by either direct $4e^-$ reduction, where no H_2O_2 formation occurs due to early O – O bond cleavage, or $2x2e^-$ mechanism, where H_2O_2 formation is observed but H_2O_2 can be rapidly converted into hydroxide with fast reduction kinetics on the catalyst surface.[44] H_2O_2 oxidation and reduction studies proved that both the oxidation and reduction are not mass transport controlled at all spinels, confirming that there is a strong kinetic limitation at all catalysts. The current densities from the oxidation and reduction of 10 mM H_2O_2 at five spinels compared to Pt black show that the current densities were much lower compared to those expected for 10 mM H_2O_2, which proves that the sluggish H_2O_2 reduction at all five spinels rule out $2x2e^-$ mechanism. Therefore, it can be concluded that O_2 reduction at spinels occur via direct $4e^-$ reduction pathway where O – O bond cleavage is happening in early stage.

To sum up, the effect of composition is a major impact for the phase, morphology, surface area and the intrinsic properties of catalysts towards the oxygen reduction reaction and the oxygen evolution reaction.

4.6. References

1. Y. Dong, K. He, L. Yin and A. Zhang, *Nanotechnology*, 2007, **18**, 435602.
2. T. Nissinen, M. Leskela, M. Gasik and J. Lamminen, *Thermochim. Acta*, 2005, **427**, 155-161.
3. S. A. A. Mansour, *Mater. Chem. Phys.*, 1994, **36**, 317-323.
4. G. Salek, P. Dufour, S. Guillemet-Fritsch and C. Tenailleau, *Mater. Chem. Phys.*, 2015, **162**, 252-262.
5. N. Garg, M. Mishra and A. K. Ganguli, *RSC Adv.*, 2015, **5**, 84988-84998.
6. P. Lavela, J. L. Tirado and C. Vidal-Abarca, *Electrochim. Acta*, 2007, **52**, 7986-7995.

7. J. L. Martin de Vidales, E. Vila, R. M. Rojas and O. Garcia-Martinez, *Chem. Mat.*, 1995, **7**, 1716-1721.
8. A. Restovic, E. Rıos, S. Barbato, J. Ortiz and J. Gautier, *J. Electroanal. Chem.*, 2002, **522**, 141-151.
9. E. Rios, J. L. Gautier, G. Poillerat and P. Chartier, *Electrochim. Acta*, 1998, **44**, 1491-1497.
10. H. Bordeneuve, S. Guillemet-Fritsch, A. Rousset, S. Schuurman and V. Poulain, *J. Solid State Chem.*, 2009, **182**, 396-401.
11. C. Li, X. P. Han, F. Y. Cheng, Y. X. Hu, C. C. Chen and J. Chen, *Nat. Commun.*, 2015, **6**.
12. P. W. Menezes, A. Indra, N. R. Sahraie, A. Bergmann, P. Strasser and M. Driess, *ChemSusChem*, 2015, **8**, 164-171.
13. F. Y. Cheng, J. A. Shen, B. Peng, Y. D. Pan, Z. L. Tao and J. Chen, *Nat. Chem.*, 2011, **3**, 79-84.
14. E. Vila, R. M. Rojas, J. L. M. deVidales and O. GarciaMartinez, *Chem. Mat.*, 1996, **8**, 1078-1083.
15. E. Lee, J. H. Jang and Y. U. Kwon, *J. Power Sources*, 2015, **273**, 735-741.
16. H. Liu and G. R. Patzke, *Nanostructured Materials and Nanotechnology VII*, 2014, 75-86.
17. A. L. Patterson, *Phys. Rev.* 1939, **56**, 978-982.
18. A. H. Monteverde Videla, P. J. Stelmachowski, G. Ercolino and S. Specchia, *J. Appl. Electrochem.*, 2017, **47**, 295-304.
19. V. Hadjiev, M. Iliev and I. Vergilov, *J. Phys. C: Solid State Phys.*, 1988, **21**, L199.
20. X. Ge, Y. Liu, F. T. Goh, T. A. Hor, Y. Zong, P. Xiao, Z. Zhang, S. H. Lim, B. Li and X. Wang, *ACS Appl. Mater. Interfaces*, 2014, **6**, 12684-12691.
21. G. Kerangueven, S. Royer and E. Savinova, *Electrochem. Commun.*, 2015, **50**, 28-31.
22. S. Wang, Y. Hou and X. Wang, *ACS Appl. Mater. Interfaces*, 2015, **7**, 4327-4335.
23. M. C. Biesinger, B. P. Payne, A. P. Grosvenor, L. W. Lau, A. R. Gerson and R. S. C. Smart, *Appl. Surf. Sci.*, 2011, **257**, 2717-2730.
24. J. Li, S. Xiong, X. Li and Y. Qian, *Nanoscale*, 2013, **5**, 2045-2054.
25. H. Liu, X. Fu, X. Weng, Y. Liu, H. Wang and Z. Wu, *J. Chem-NY.*, 2014, **2014**.

26. J.-K. Chang, M.-T. Lee, W.-T. Tsai, M.-J. Deng and I.-W. Sun, *Chem. Mat.*, 2009, **21**, 2688-2695.
27. K.-W. Nam, M. G. Kim and K.-B. Kim, *J. Phys. Chem. C*, 2007, **111**, 749-758.
28. Y.-Y. Hu, Z. Liu, K.-W. Nam, O. J. Borkiewicz, J. Cheng, X. Hua, M. T. Dunstan, X. Yu, K. M. Wiaderek and L.-S. Du, *Nat. Mater.*, 2013, **12**, 1130-1136.
29. S. Thompson, *Bi-functional oxygen catalysts for metal-air flow-batteries*, PhD Thesis, University of Southampton, 2016.
30. F. Jiao and H. Frei, *Chem. Commun.*, 2010, **46**, 2920-2922.
31. R. Boggio, A. Carugati and S. Trasatti, *J. Appl. Electrochem.*, 1987, **17**, 828-840.
32. P. Nkeng, J.-F. Koenig, J. Gautier, P. Chartier and G. Poillerat, *J. Electroanal. Chem.*, 1996, **402**, 81-89.
33. I. Nikolov, R. Darkaoui, E. Zhecheva, R. Stoyanova, N. Dimitrov and T. Vitanov, *J. Electroanal. Chem.*, 1997, **429**, 157-168.
34. R. N. Singh, J. F. Koenig, G. Poillerat and P. Chartier, *J. Electrochem. Soc.*, 1990, **137**, 1408-1413.
35. J. Xu, P. Gao and T. Zhao, *Energy Environ. Sci.*, 2012, **5**, 5333-5339.
36. G. Spinolo, S. Ardizzone and S. Trasatti, *J. Electroanal. Chem.*, 1997, **423**, 49-57.
37. M. Hamdani, R. N. Singh and P. Chartier, *Int. J. Electrochem. Sci.*, 2010, **5**, 556-577.
38. E. Rios, P. Lara, D. Serafini, A. Restovic and J. L. Gautier, *J. Chil. Chem. Soc.*, 2010, **55**, 261-265.
39. T. Nissinen, Y. Kiros, M. Gasik and M. Lampinen, *Mater. Res. Bull.*, 2004, **39**, 1195-1208.
40. E. Castro, C. Gervasi and J. Vilche, *J. Appl. Electrochem.*, 1998, **28**, 835-841.
41. P. Nkeng, G. Poillerat, J. F. Koenig, P. Chartier, B. Lefez, J. Lopitaux and M. Lenglet, *J. Electrochem. Soc.*, 1995, **142**, 1777-1783.
42. I. Belova, Y. E. Roginskaya, R. Shifrina, S. Gagarin, Y. V. Plekhanov and Y. N. Venevtsev, *Solid State Commun.*, 1983, **47**, 577-584.
43. Y. Liang, H. Wang, J. Zhou, Y. Li, J. Wang, T. Regier and H. Dai, *J. Am. Chem. Soc.*, 2012, **134**, 3517-3523.
44. T. Sönmez, S. J. Thompson, S. W. Price, D. Pletcher and A. E. Russell, *J. Electrochem. Soc.*, 2016, **163**, H884-H890.

45. R.-N. Singh, M. Hamdani, J.-F. Koenig, G. Poillerat, J. Gautier and P. Chartier, *J. Appl. Electrochem.*, 1990, **20**, 442-446.
46. E. Rios, P. Chartier and J.-L. Gautier, *Solid State Sci.*, 1999, **1**, 267-277.
47. N. M. Marković, H. A. Gasteiger and P. N. Ross, *J. Phys. Chem.*, 1996, **100**, 6715-6721.
48. P. Foller and R. Bombard, *J. Appl. Electrochem.*, 1995, **25**, 613-627.
49. M. De Koninck and B. Marsan, *Electrochim. Acta*, 2008, **53**, 7012-7021.
50. Y. J. Sa, K. Kwon, J. Y. Cheon, F. Kleitz and S. H. Joo, *J. Mater. Chem. A*, 2013, **1**, 9992-10001.
51. C. Song and J. Zhang, in *PEM fuel cell electrocatalysts and catalyst layers*, Springer, 2008, pp. 89-134.
52. J. Li, N. Zhou, H. Wang, H. Li, Z. Xie, H. Chu, Y. Tang, L. Sun and Z. Peng, *J. Electrochem. Soc.*, 2015, **162**, A2302-A2307.
53. M. Tarasevich, A. Sadkowski and E. Yeager, in *Comprehensive treatise of electrochemistry*, Springer, 1983, pp. 301-398.
54. V. Bagotsky, M. Tarasevich and V. Y. Felinovskii, *Soviet Electrochem.*, 1969, **5**, 1158-1161.
55. L. Jorissen, *J. Power Sources*, 2006, **155**, 23-32.

Chapter 5: The Effect of Preparation Methods on Spinel $MnCo_2O_4$

In this chapter, the effect of preparation methods and conditions on the electrochemical activity of $MnCo_2O_4$ in alkaline media will be investigated. $MnCo_2O_4$ materials will be prepared via three different synthesis methods (thermal decomposition, hydrothermal and co-precipitation) and under three different conditions in the hydrothermal method. Electrochemical activities and the oxygen reduction mechanisms at these $MnCo_2O_4$ samples will be compared. Their stabilities under long term measurements will be also investigated.

5.1. Introduction

The physicochemical properties of Mn-based spinel oxides depend on the composition, phase, crystalline structure, surface area, cationic distribution, and oxidation states of metal ions, which are largely determined by the synthetic conditions.[1-9]

In general, spinel metal oxides have been produced by a variety of methods such as hydrothermal/solvothermal[9-15], sol-gel[4, 16-18], co-precipitation[19-21], microwave synthesis/assisted[7, 22, 23], thermal decomposition[3, 24-27], the wet method[28], combustion reaction[29], the Pechini method using a polymeric precursor[30], spray pyrolysis[31, 32], and electrostatic spray deposition[33]. With some of these methods, oxides can be produced as powder or thin film. The differences between these preparation methods are distinguished based on the homogeneity of oxides, purity of phase, crystallinity, specific surface area, particle size, stability, morphology, cost of reagents/preparation, and resulting electrochemical properties.[34] All of the aforementioned properties are highly affected by the preparation method, conditions within the preparation, and starting precursors.[34]

Thermal decomposition of metallic salts is the most common technique for the preparation of powder catalysts or sometimes, the solution of metallic salts with a desired molar ratio are used to form a thin film on a conductive support (such as Ni foam) and then calcined.[34-38] Large particle size and low specific surface area catalysts are obtained with this method.[1] Moreover, the shape and particle size of the resulting catalyst are not controlled. It is also hard to produce materials with pure spinel phase via thermal decomposition.[33] Nitrates, citrates and carbonates have been used as precursors in this method at different calcination temperatures.[23] Sugawara et al. show that larger surface area catalysts can be produced with

carbonates rather than citrates and also materials with larger surface area are produced at lower temperature.[26] Schwickardi et al. prepared metal oxides produced using nitrates, alkoxides, chlorides, acetates and acetylacetonates metal salts and showed that the highest surface area was obtained with nitrates.[39] Nitrates as precursors are more favourable for oxide preparation with temperature treatment due to their high solubility in water and low contamination of the final catalysts.[40]

Hydrothermal (or solvothermal) method possesses the advantage of controlling the morphology of nanosize materials at lower temperatures and high pressures.[41] It is easily possible with hydrothermal method to produce crystal synthesis or crystal growth from precursors, which are insoluble under normal temperature and pressure (< 100 ^{o}C, < 1 atm).[42] The solubility and dielectric constants of many solvents under supercritical conditions change dramatically (dielectric constant for H_2O: 78 at 25 ^{o}C, < 10 at supercritical conditions).[8, 42] The reaction rate is then much greater under supercritical conditions due to the decrease in dielectric constant. While some studies[9, 11, 13, 43] use hydrothermal methods for producing the spinels $MnCo_2O_4$/Mn_2CoO_4 without further treatment, others[44, 45] do post high thermal treatment after hydrothermal process.

Co-precipitation is another commonly used preparation method for producing metal oxides at relatively low temperatures.[46, 47] In some cases, there is an additional thermal treatment at high temperature for producing spinel oxides.[19, 20, 48] Co-precipitation involves mixing of the precursor metal salts to a high degree and the only concern in this method is the removal of any impurities come from the precipitating agents.[38] For example, NaOH often contains trace of Fe. Metallic salt solutions precipitated with alkaline (such as NaOH, NH_4OH and etc.) and metal hydroxides are observed to precipitate from metal salts (nitrates).[38] Metallic salt solutions may be added as dropwise to alkaline solution under vigorous stirring conditions or vice versa. In addition, metallic salt solutions and alkaline solution can be also added into a buffer solution with an adjusted pH.[38]

In this chapter, $MnCo_2O_4$ samples (the composition of Mn:Co (1:2) shows the highest ORR and OER activity as shown in **Chapter 4**), produced via thermal decomposition, co-precipitation and hydrothermal methods with varying conditions, are discussed. The physicochemical properties of each catalyst were determined. The mechanism of oxygen reduction, hydrogen peroxide formation and material stability at each $MnCo_2O_4$ are compared.

As already discussed in previous chapters, the conductivity, dispersion of nanoparticles and the electrochemical activity of metal oxides are significantly increased by adding carbon or carbon based materials to metal oxides.[49, 50] In addition, even though carbon addition into the catalyst preparation results in 4 – 20 times larger surface area than catalyst without carbon, all carbon materials show ORR activity ($2e^-$ reduction) in alkaline media and this can mislead studies of the oxygen reduction pathway at such materials.[39, 49, 51, 52] Therefore, there is no addition of carbon or carbon based materials in all catalyst preparations in this chapter.

5.2. Experimental

5.2.1. $MnCo_2O_4$ Synthesis via Thermal Decomposition

This sample is the same $MnCo_2O_4$ sample as shown in **Chapter 4** (section **4.2.2.3**). This sample will be called **MCO – TD** for convenience.

5.2.2. $MnCo_2O_4$ Synthesis via Hydrothermal Method

1.9101 g $Co(NO_3)_2.6H_2O$, 0.8414 g $Mn(NO_3)_2.4H_2O$ and 4.028 g NaOH were dissolved in a mixture of deionised H_2O (40 cm^3) and diethylene glycol (40 cm^3). The resulting solution was then stirred for 2 hours at room temperature prior to being placed into a 120 cm^3 Teflon-lined stainless steel autoclave, sealed and maintained at 200 ^oC for 20 hours in an electric furnace with 8 ^oC/min ramping speed. The stainless steel autoclave was cooled down to room temperature and the top (liquid part) of the mixture was removed. The residue was first mixed with ethanol and the mixture was centrifuged to collect the product. This process was repeated two times with ethanol. After this step, the product was mixed with deionised water and the same process was repeated with deionised water to wash the product. The residue was then dried in an electric furnace at 80 ^oC for 2 hours. The dark green product was then divided into three parts:

- The first part was stored without any further thermal treatment and this sample will be called as **MCO – No Calcination**.
- The second part was calcined at 600 ^oC for 12 hours under air flow with a heat rate of 8 ^oC/min in a tubular furnace. The resulting black solid was ground and then sieved through a 53 µm sieve. This sample will be called as **MCO – Air – HT.**

- The third part was calcined at 600 ºC for 12 hours under argon flow with a heat rate of 8 ºC/min in a tubular furnace. The resulting black solid was ground and then sieved through a 53 µm. This sample will be called as **MCO – Ar – HT.**

5.2.3. $MnCo_2O_4$ Synthesis via Co – Precipitation

This sample is the same $MnCo_2O_4$ sample as shown in **Chapter 4** (section **4.2.1.3**). This sample will be called as **MCO – CP.**

5.2.4. Electrode Coating

Ink preparation and electrode coating are as described in **Chapter 2**, section **2.4.6**. All current densities are based on geometric area of the vitreous carbon disc.

5.3. Physical Characterization

The results from XRD, BET, SEM, TEM and XANES techniques used for the physical characterization of $MnCo_2O_4$ samples prepared via different synthesis methods (thermal decomposition, hydrothermal method and co-precipitation) and under different conditions within the hydrothermal method will be shown in this section.

5.3.1. XRD

5.3.1.1. XRD of $MnCo_2O_4$ Samples Synthesised Under Different Conditions

Figure 5.1 shows the powder XRD patterns of MCO – No calcination, MCO – Air – HT and MCO – Ar – HT. As shown, MCO – No calcination does not have a spinel structure. This sample had no further temperature treatment and the XRD shows impurities, which might be coming from undecomposed nitrates in the composition. Some studies[9, 11, 13, 43] have produced spinel $MnCo_2O_4$ without further temperature treatment although the crystallinity of materials was low and the XRD patterns reported have large noisy backgrounds. On the other hand, other reports[15, 44] produced $MnCo_2O_4$ via hydrothermal method and post temperature treatment. XRD powder pattern of MCO – Ar – HT shows a pattern close to the spinel structure, but there are additional peaks (shown with asterisks) and the absence of some peaks from spinel pattern, suggesting that MCO – Ar – HT does not have a pure spinel structure. As mentioned in preparation section, this sample was calcined under argon flow at 600 ºC for 12 hours, therefore we propose oxygen deficiency in the lattice due to lack of oxygen in the calcination process. This point can be proved by looking at XRD powder pattern of MCO – Air – HT, synthesised under air

flow at 600 ºC for 12 hours and indeed MCO – Air – HT does have a spinel pattern for cubic phase $MnCo_2O_4$ with a good quality of material crystallinity.

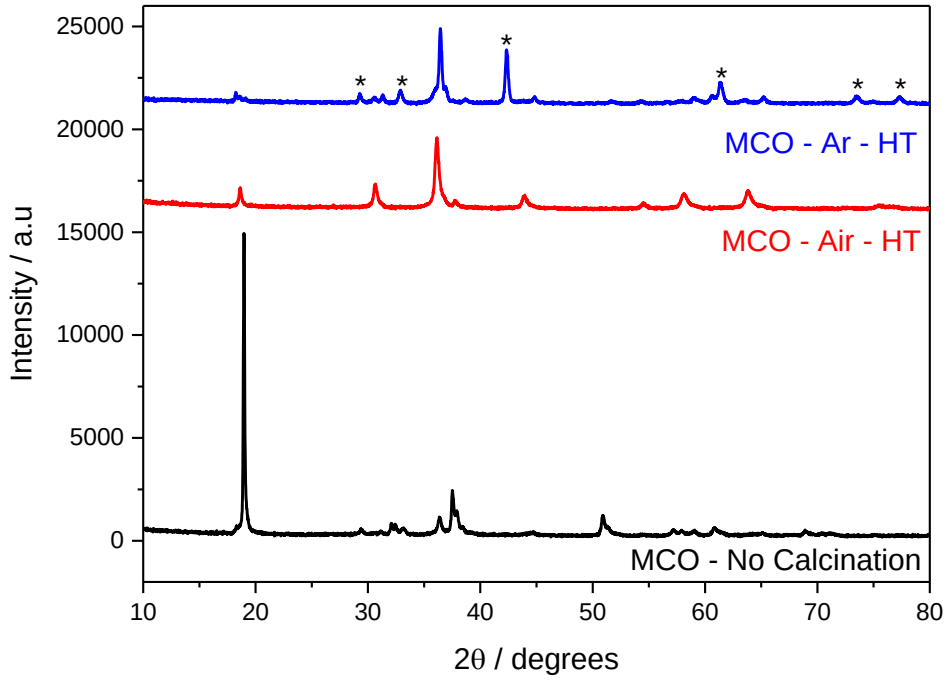

Figure 5.1. XRD patterns of $MnCo_2O_4$ samples synthesised under different conditions within hydrothermal method: MCO – No Calcination (black), MCO – Air – HT (red) and MCO – Ar – HT (blue).

5.3.1.2. XRD of $MnCo_2O_4$ Samples Synthesised with Different Methods

Figure 5.2 shows XRD powder patterns of MCO – TD, MCO – Air – HT and MCO – CP. All three have spinel structures. While MCO – Air – HT and MCO – CP possess single phase spinel structures, MCO – TD has more than a single phase. With MCO – TD, peaks are much broader and the intensity of peaks are lower. The highest crystallinity was observed with MCO – Air – HT. It is also worth noting that peak positions are not exactly on the same 2θ positions for all samples.

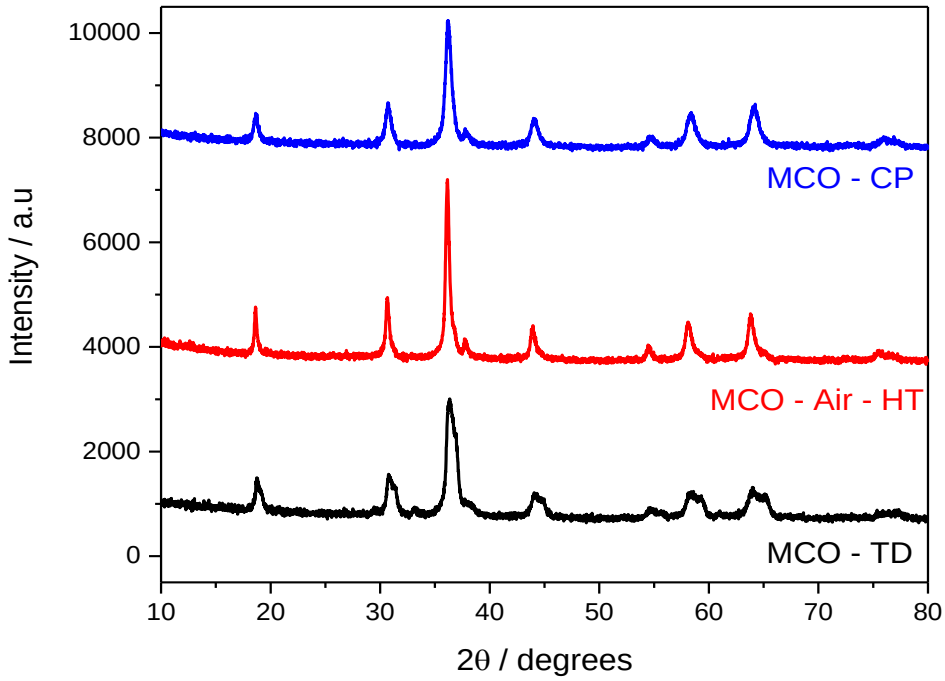

Figure 5.2. XRD patterns of $MnCo_2O_4$ samples synthesised with three different methods; thermal decomposition (MCO – TD), hydrothermal method (MCO – Air – HT) and co-precipitation (MCO – CP).

Rietveld analysis was carried out and the XRD patterns indexed on the basis of cubic space group Fd-3mz (ICSD collection code: 201314). **Figure 5.3** shows the measured diffraction patterns, which fit well with calculated/Rietveld refinement fits, proving the spinel structure. The summary of Rietveld analysis is present in **Table 5.1**, and it shows that the smallest lattice constant was observed with MCO – TD (a = 8.1949), while the largest was obtained with MCO – Air – HT (a = 8.2419). The cell volume per formula units also agree with the order of lattice constants.

It is important to note that fit statistics from the XRD refinement shows that Mn ions prefer to occupy tetrahedral sites rather than octahedral sites in the spinels as previously observed in **Chapter 4**.

Average crystallite sizes were calculated using a variation of the Scherrer equation (see **Equation 4.1** in **Chapter 4)** and the smallest crystallite size (27.1 nm) was obtained with sample (MCO – CP) prepared via co-precipitation method while the largest value was obtained for sample (MCO – TD) prepared via thermal decomposition.

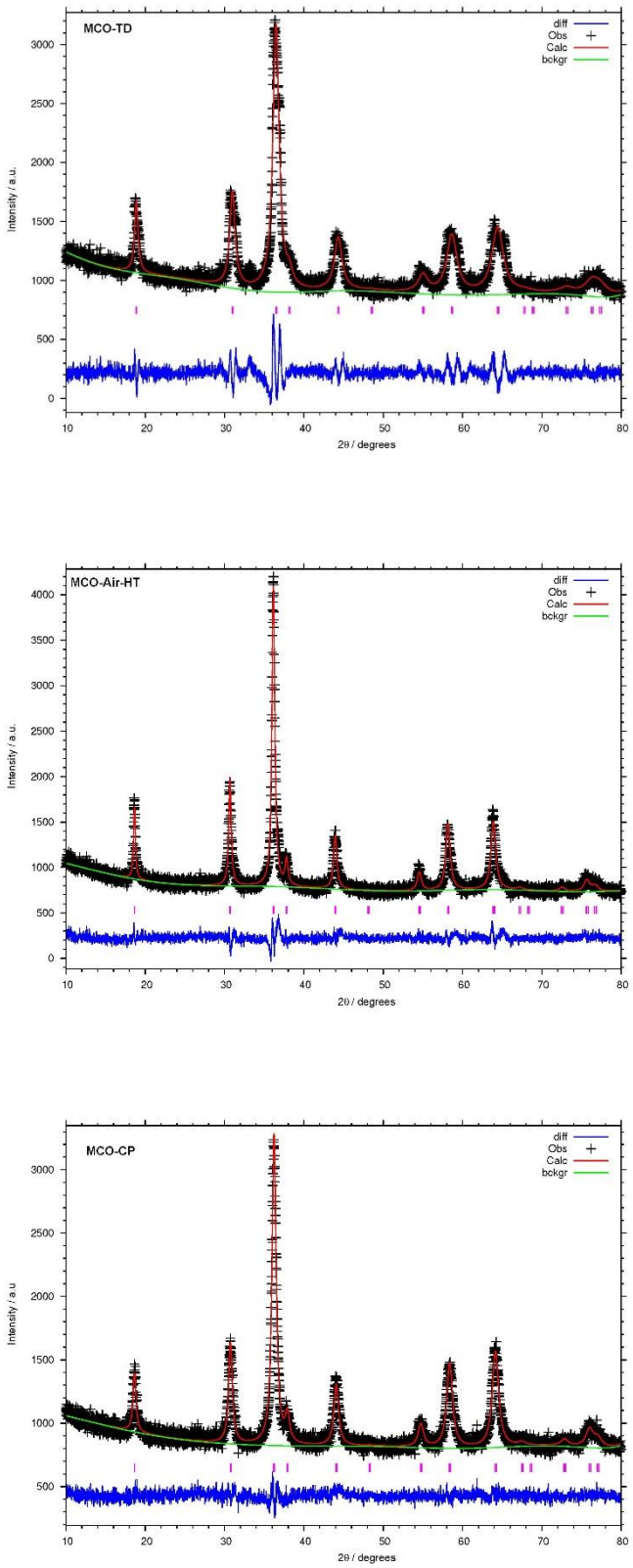

Figure 5.3. XRD patterns of MCO – TD, MCO – Air – HT and MCO – CP. Black crosses: observed intensities; Red line: Rietveld refinement fit; Green line: background fit; Blue line: difference between observed and fitted pattern. Pink line: cubic phase $MnCo_2O_4$ peaks.

Catalyst	**Space Group**	**Lattice Constant a=b=c (Å)**	**Volume per formula unit / (Å^3) (Cubic = V/8)**	**Average crystallite size / nm**	***X*^{2}**	**Fitted wRp / %**	**L_x**
MCO – TD	Fd-3mz	8.195 (2)	68.8(2)	87	2.396	4.70	9.17
MCO – Air – HT	Fd-3mz	8.2419 (7)	69.98(9)	67	1.632	4.31	11.87
MCO – CP	Fd-3mz	8.2026(9)	68.99(10)	27.1	1.216	3.58	29.36

Table 5.1. The summary of Rietveld analysis of $MnCo_2O_4$ samples prepared by three different preparation methods. The value of fitted wRp was kept < 10% in order to do make a fit to be considered acceptable. ICSD collection code for $MnCo_2O_4$ samples is 201314. The values in the parentheses for volume per formula unit and lattice constants are standard deviations.

5.3.2. BET

Brunauer, Emmett and Teller (BET) surface area measurements were carried out and the results for the hydrothermal method samples as well as thermal decomposition and co - precipitation are presented in **Table 5.2**. As shown, the sample with no further thermal treatment (MCO – No Calcination) possesses the highest surface area (43.2 $m^2 g^{-1}$) amongst samples produced via hydrothermal method. With post temperature treatment at ^{o}600 C for 12 hours under air and argon flows, $MnCo_2O_4$ samples have smaller surface areas as expected since increasing calcination temperature decreases the surface area of materials.[23, 26]

Catalyst	BET Surface area (m^2/g)	Average Aggregate Diameter (nm)	Max Pore Volume at P/P^o (0.154) (cm^3/g)	Median Pore Width (nm)
MCO – No Calcination	43.2	138	0.0182	1.35
MCO – Ar – HT	9.5	635	0.0031	1.33
MCO – Air – HT	19.0	317	0.0074	1.23
MCO – TD	28.3	212	0.0112	1.20
MCO – CP	49	123	0.0195	1.18

Table 5.2. BET surface area measurements of $MnCo_2O_4$ samples (MCO – No Calcination, MCO – Ar – HT and MCO – Air – HT) synthesised via hydrothermal method but under different conditions as well as thermal decomposition (MCO – TD) and co - precipitation (MCO – CP).

5.3.3. SEM

Figure 5.4 presents SEM images of MCO – No Calcination, MCO – Air – HT and MCO – Ar – HT samples. All three samples have an amorphous morphology and comprise irregular particles.

MCO – No Calcination

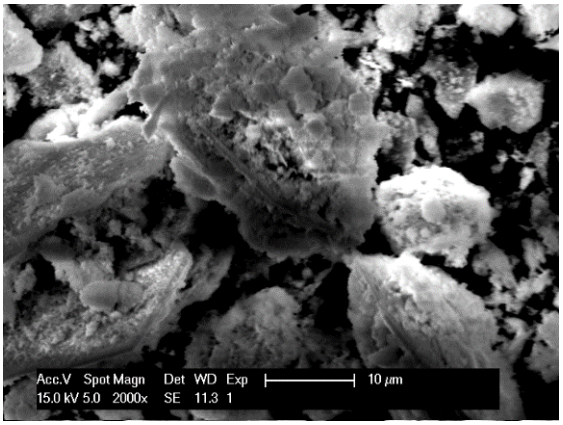

MCO – Air – HT

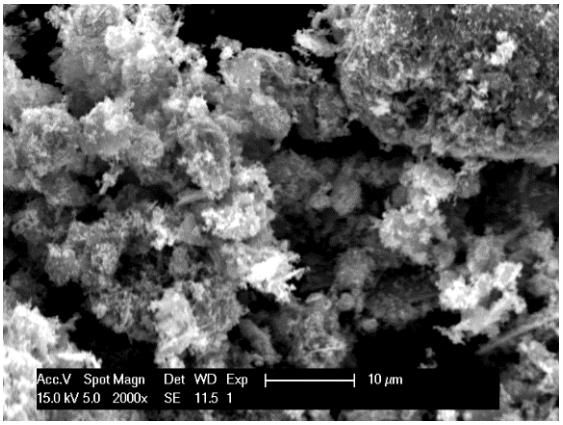

MCO – Ar – HT

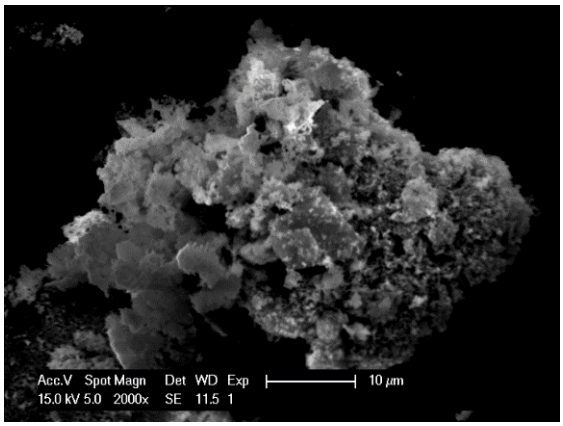

Figure 5.4. SEM images of $MnCo_2O_4$ samples; MCO – No Calcination (**top left**), MCO – Air – HT (**top right**) and MCO – Ar – HT (**bottom**). Scale bar: 10 µm.

5.3.4. TEM

The TEM images of $MnCo_2O_4$ samples are presented in **Figure 5.5**. The crystallinity of MCO – No Calcination is low compared to MCO – Ar – HT and MCO – Air – HT due to the lack of temperature treatment. In contrast, MCO – Ar – HT and MCO – Air – HT have much higher crystallinity and they also show the mixture of cubic and hexagonal shapes particles. These two samples show that there is not a big difference in terms of particle shapes except the size of particles with MCO – Ar – HT having larger sized particles.

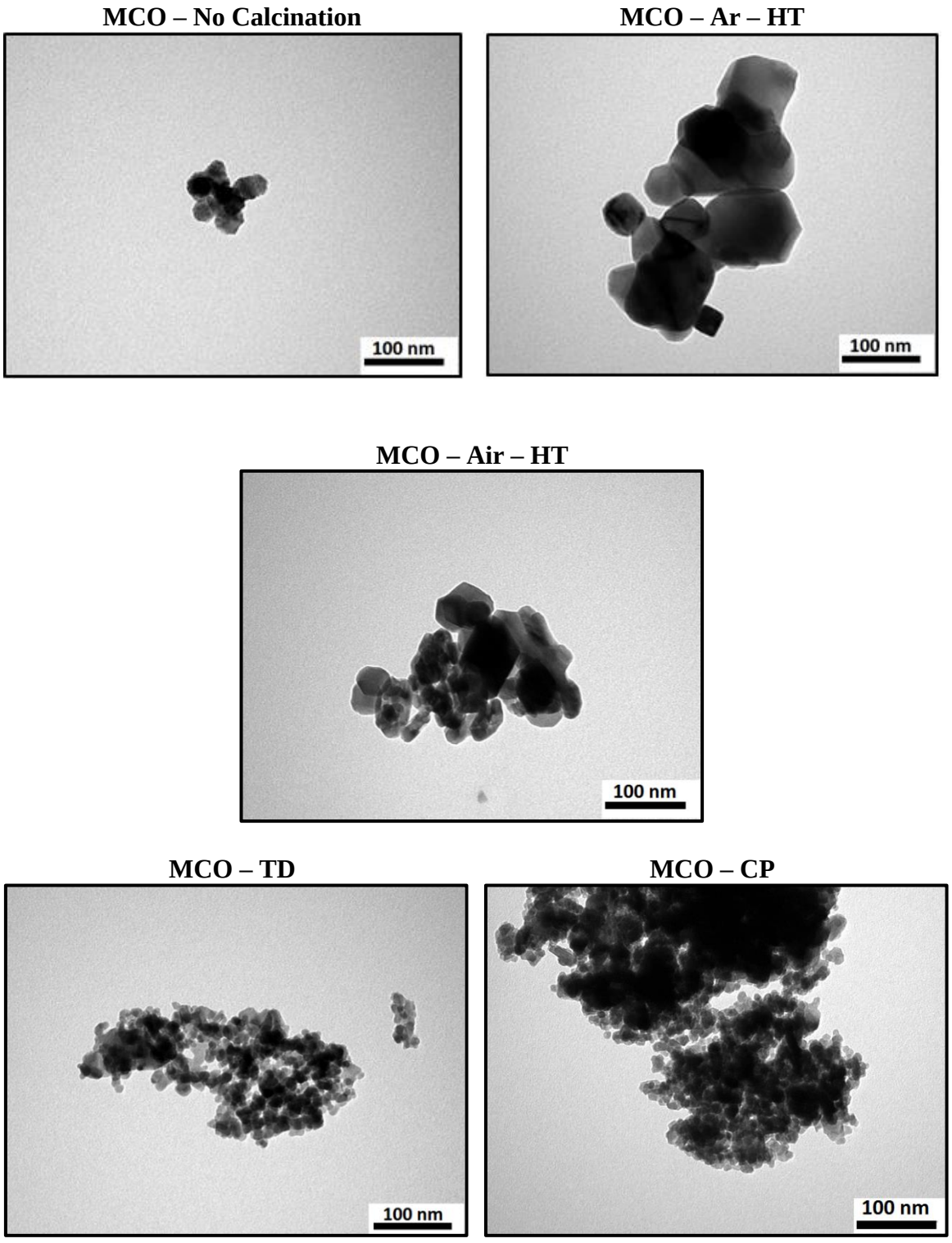

Figure 5.5. TEM images of $MnCo_2O_4$ samples synthesised via hydrothermal method within different preparation conditions (MCO – No Calcination**,** MCO – Ar – HT and MCO – Air – HT) as well as thermal decomposition (MCO – TD) and co - precipitation (MCO – CP). Scale bar: 100nm.

TEM images of MCO – TD and MCO – CP reveal that materials show somewhat similar size and shape particles, however, MCO – CP has smaller size particles compared to MCO – TD. In contrast, MCO – Air – HT shows material with much larger particle size compared to other two (MCO – TD and MCO – CP). It is also worth mentioning that TEM images of MCO – TD, MCO – Air – HT and MCO – CP are consistent with BET and XRD results.

5.3.5. Ex situ XANES

Synchrotron X-ray absorption analysis has been carried out to determine the oxidation states of Co and Mn as well as identifying/comparing the cationic distribution of $MnCo_2O_4$ samples produced via three different preparation methods.[53, 54]

5.3.5.1. Co Edge

Figure 5.6 illustrates Co K-edge X – Ray Absorption Near-Edge Structure (XANES) patterns of all three spinels as well as reference Co oxides.

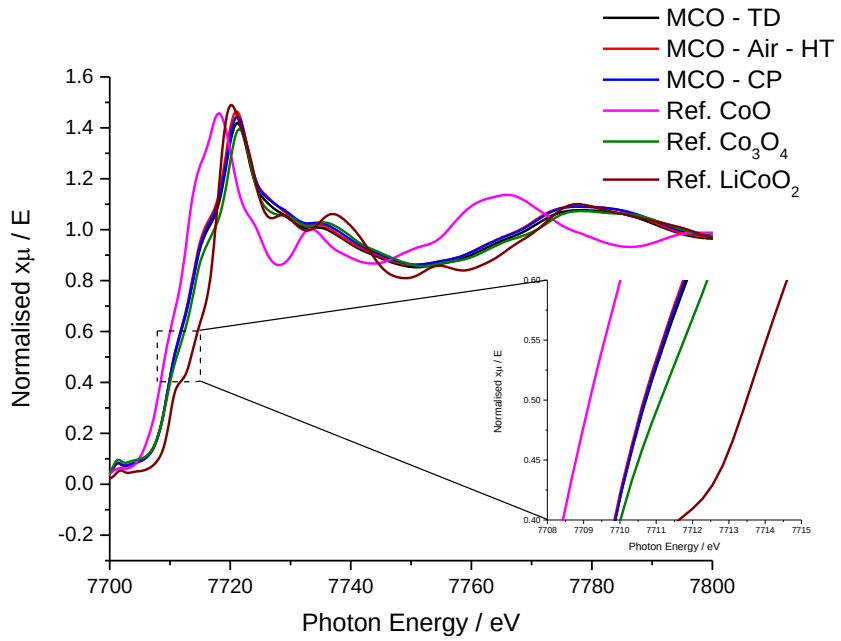

Figure 5.6. K-edge XANES patterns of Co in MCO – TD, MCO – Air – HT, MCO – CP and the reference oxides (CoO, Co_3O_4 and $LiCoO_2$). Inset is shown for more clear difference between patterns in the photon energy scale between 7708 and 7715 eV.

Again, the edge spectra of standard cobalt oxides (CoO (+2), Co_3O_4 (+2.66), and $LiCoO_2$ (+3)) were included for comparison purpose. The inset in the figure shows the difference more clear between spinels and comparing three spinels with reference Co oxides. The reference Co oxides were used to establish linear correlation between K-edge absorption energies and Co oxidation states in three spinels as shown in **Figure 5.7**.[53] The list of Co oxidation states for three spinels and reference Co oxides and their corresponding K-edge energies is reported in **Table 5.3**.

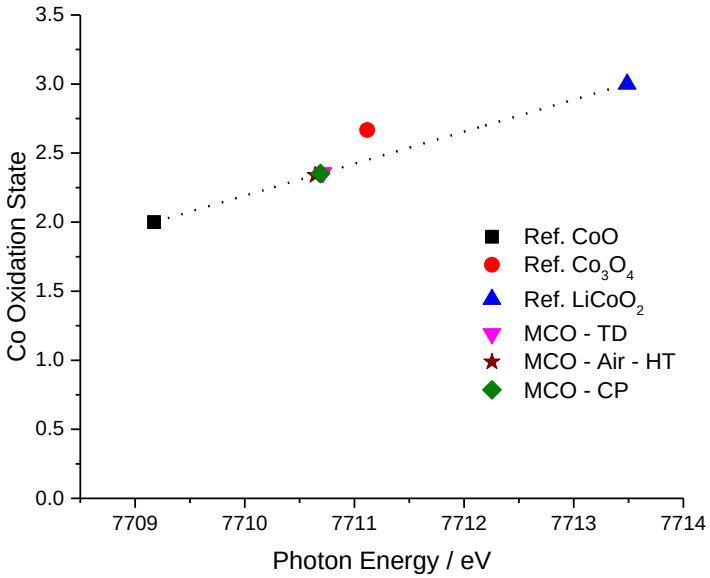

Figure 5.7. Fitted linear relationship between Co oxidation states in three spinels and the photon energies. The plot was made from **Figure 5.6** at 0.5 E, which is commonly selected as half-way up the absorption edge.[55] Linear fit is excluded Ref. Co_3O_4. The same result for Ref. Co_3O_4 is shown by Li et al.[53] Data points for MCO – TD, MCO – Air – HT and MCO – CP samples were placed onto the calibration line.

According to **Figure 5.7** and **Table 5.3**, the mean Co valence values are around 2.35 for all three spinels confirming that adding Mn ions take place in Co^{+3} in three spinels. As previously mentioned in **Chapter 4**, the mean oxidation state for the Co is ≈+2.35 instead of the expected value of +2.5 and this might be coming from small impurity of CoO on the

surface of the spinels or the surface oxidation state of the Co nanoparticles are different from the bulk.

Catalyst	Energy / eV (±0.1)	Oxidation state (±0.023)
Ref. CoO	7709.2	2
Ref. Co_3O_4	7711.1	2.66
Ref. $LiCoO_2$	7713.5	3
MCO - TD	7710.7	2.36
MCO - Air - HT	7710.6	2.34
MCO - CP	7710.7	2.35

Table 5.3. List of the mean Co oxidation states in reference oxides and three spinels, and their corresponding K-edge energies (eV).

By comparing the mean Co valence for three spinels, the difference in the mean Co valence is small, which shows that the preparation methods have a small effect on the oxidation states of Co in the spinel $MnCo_2O_4$ samples.

5.3.5.2. Mn Edge

Mn K-edge XANES patterns of three spinels and Mn oxide references are shown in **Figure 5.8**.

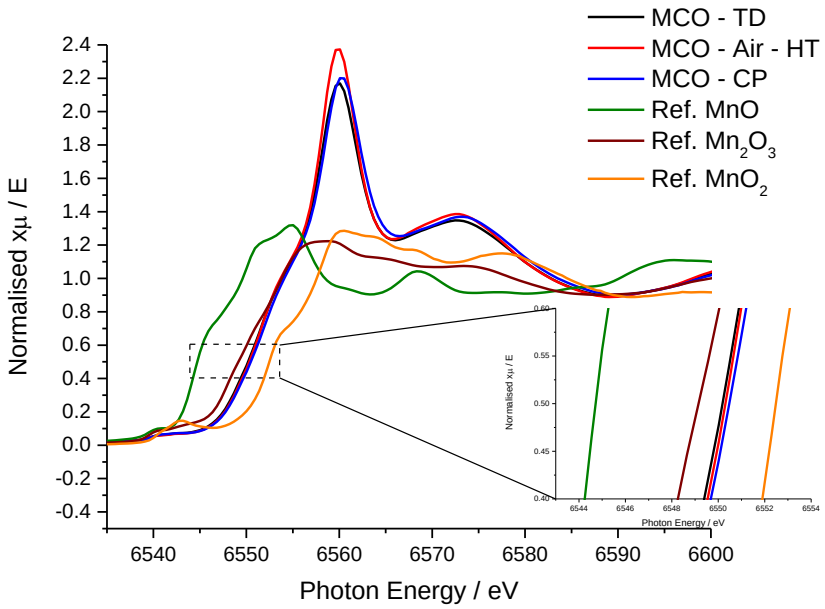

Figure 5.8. K-edge XANES patterns of Mn in MCO – TD, MCO – Air – HT, MCO – CP and the reference oxides (MnO, Mn_2O_3 and MnO_2). Inset is shown for more clear difference between patterns in the photon energy scale between 6543 and 6554 eV.

The absorption energy difference may be seen more obvious in the inset in the figure. Again, the mean Mn oxidation state for each spinel can be found using the Mn oxide references to establish the linear correlation between K-edge absorption energy and the oxide valence.[53, 56] **Table 5.4** reports the mean oxidation states for all three spinels and Mn oxide references and corresponding Mn K-edge adsorption energies. **Figure 5.9** and **Table 5.4** show that Mn oxidation states for all three spinels are between 3 and 4, suggesting that Co^{+3} ions in the spinel are substituted by Mn^{+3} ions. The mean Mn oxidation states are varied from 3.35 to 3.43 for $MnCo_2O_4$ samples. The reason of the mean values of Mn oxidation states is larger than 3 is implying the existence of Mn^{+4}. As this was already pointed out in XPS results in **Chapter 4**, the existence of Mn^{+4} might be coming from the slight excess of Mn on the surface of the samples, which could form MnO_2 in contact with air. Mn edge XANES results are complimentary results with Co-edge XANES. Both results show that Mn^{+3} ions substitute Co^{+3} in the spinels.

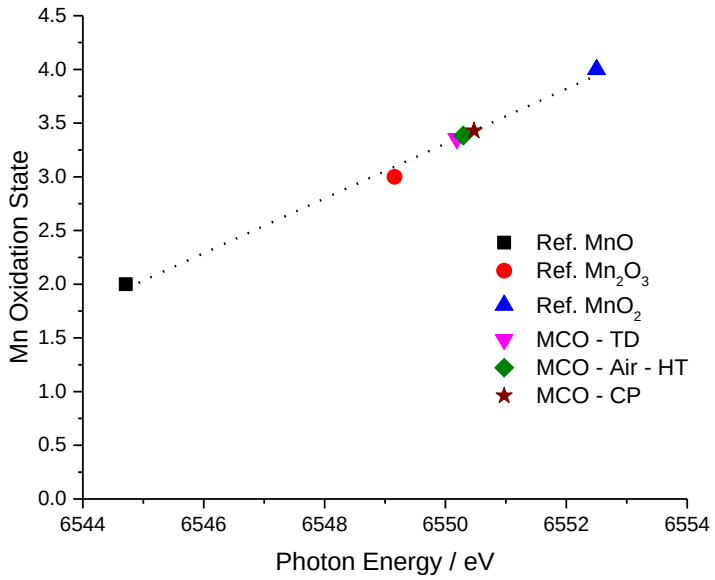

Figure 5.9. Fitted linear relationship between Mn oxidation states in three spinels and the corresponding photon energies. The plot was made from **Figure 5.8** at 0.5 E (half-way up the absorption edge). Data points for MCO – TD, MCO – Air – HT and MCO – CP samples were placed onto the calibration line.

Catalyst	Energy / eV (±0.1)	Oxidation state (±0.025)
Ref. MnO	6544.7	2
Ref. Mn_2O_3	6549.2	3
Ref. MnO_2	6552.5	4
MCO - TD	6550.2	3.36
MCO - Air - HT	6550.3	3.38
MCO - CP	6550.5	3.43

Table 5.4. List of the mean Mn oxidation states in reference oxides and three spinels, and their corresponding K-edge energies (eV).

As shown in **Table 5.4**, the mean Mn oxidation states for all three spinels are varied with different preparation methods, however, the main fact is that the difference is so small, therefore it can be said that the effect of preparation methods is very slight on the oxidation state of Mn and Co in three spinels.

5.4. Electrochemical Characterization

This section will report the electrochemical studies, carried out on $MnCo_2O_4$ samples synthesised under different conditions in hydrothermal method as well as via three different preparation methods (thermal decomposition, hydrothermal, and co-precipitation), in alkaline media. Electrochemical studies were carried out under similar conditions in order to make a reasonable comparison between materials.

5.4.1. Cyclic Voltammetry and Oxidation states

Figure 5.10 presents cyclic voltammograms of MCO – No Calcination, MCO – Air – HT and MCO – Ar – HT in 1 M KOH at 25 ^{o}C with 20 mV s^{-1} potential scan rate.

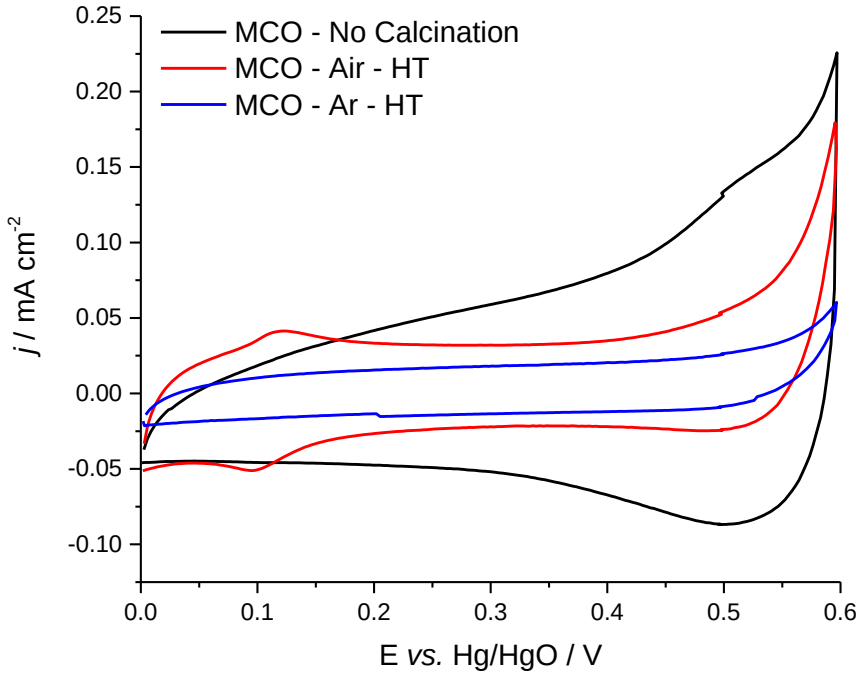

Figure 5.10. Cyclic voltammograms of $MnCo_2O_4$ samples; MCO – No Calcination (black), MCO – Air – HT (red) and MCO – Ar – HT (blue) in 1 M KOH. Temperature: 25 ^{o}C; Potential scan rate: 20 mV s^{-1}.

Unlike some other spinels (such as Co_3O_4, $NiCo_2O_4$), no substantial peaks consistent with a change in metal oxidation state are visible in the potential range 0.2 to + 0.6 V. CV of MCO – Ar – HT shows that there is charging effect, which is expected for a high surface

area sample. More charging effect is observed at CV of MCO – Air – HT due to the larger surface area of MCO – Air – HT than MCO – Ar – HT. There are also two important points to be highlighted in the potential ranges of 0.05 – 0.15 V and 0.4 – 0.6 V:

I) While there are no obvious oxidation and reduction peaks between 0.4 and 0.6 V at all three samples, there are broad oxidation and reduction peaks in the CV for MCO – No Calcination, which is most likely from mixed hydroxide (not from spinel $MnCo_2O_4$). As shown in the XRD data (see **Figure 5.1**), MCO – No Calcination sample does not have spinel structure. A review[42] shows that hydrated metal ions turn into metal hydroxide and then metal hydroxides convert to metal oxides through dehydration. Therefore, it may be said that MCO – No Calcination sample needs dehydration (post heat treatment) to form spinel $MnCo_2O_4$.

II) In the potential range of 0.05 and 0.15 V (see **Figure 5.10**), only the CV of MCO – Air – HT shows oxidation and reduction peaks. As already mentioned in **Chapter 4**, the charge associated with these peaks (≈ 30 μC cm^{-2}) is much less than a monolayer oxidation/reduction charge on a smooth surface (≈ 150 μC cm^{-2}). Therefore, they are not associated with conversion of ions in the bulk structure. These peaks might be from any impurity or iron contamination on the surface of the materials.

Figure 5.11 shows cyclic voltammograms of the three $MnCo_2O_4$ spinel samples (MCO – TD, MCO – Air – HT and MCO – CP) under the conditions of 1 M KOH at 25 ^oC with 20 mV s^{-1} potential scan rate.

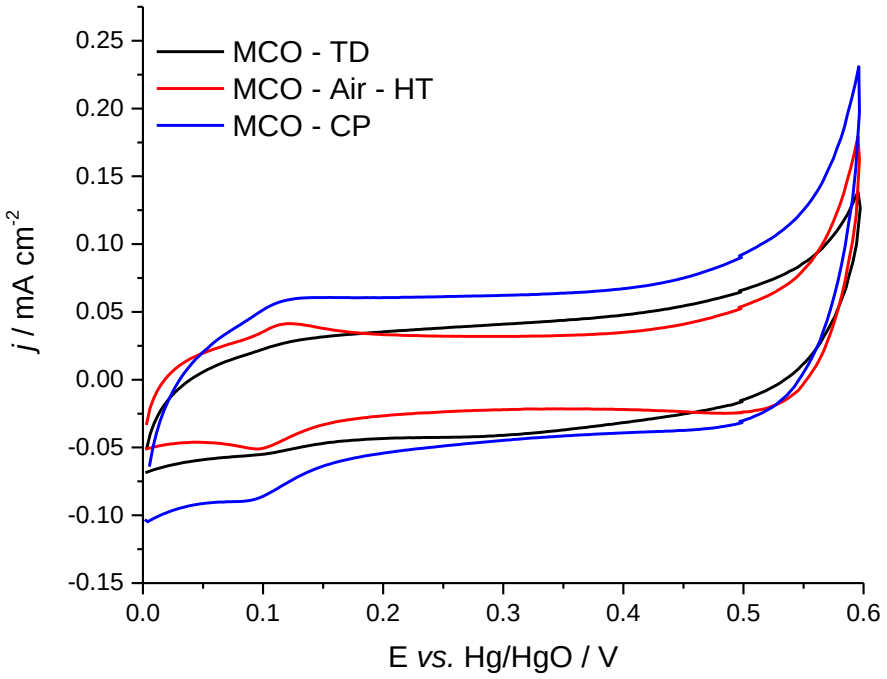

Figure 5.11. Cyclic voltammograms of $MnCo_2O_4$ spinel samples prepared with three different methods; MCO – TD (black), MCO – Air – HT (red) and MCO – CP (blue) in1 M KOH. Temperature: 25 ^oC; Potential scan rate: 20 mv s^{-1}.

Again, there are oxidation and reduction peaks for some samples between 0.05 and 0.15 V in **Figure 5.11**. While these oxidation/reduction peaks are observed at MCO – Air – HT and MCO – CP, there is no peak observed at MCO – TD. As previously mentioned in **Chapter 4**, these peaks could be associated with an iron couple on the surface of these materials. It may be worth pointing out that NaOH (<20 ppm Fe) and NH_4OH (<1 ppm Fe) were used in the preparations of MCO – Air – HT and MCO – CP, respectively. Therefore, the peaks intensities are in accordance with the possibility of Fe collecting at the spinel surfaces. In contrast, MCO – TD is prepared without chemicals containing Fe impurities.

5.4.2. Oxygen Reduction

Oxygen reduction behaviours at MCO – No Calcination, MCO – Air – HT and MCO – Ar – HT samples were investigated under similar conditions and the results are presented in **Figure 5.12.** As shown, the highest activity and lowest onset potential for oxygen reduction was observed with MCO – Air – HT. In contrast, oxygen reduction activity at MCO – Ar – HT shows less activity, which is most likely from less pure spinel structure of this material (see **Figure 5.1**). Probably the most surprising result from **Figure 5.12** is the

ORR activity at MCO – No Calcination sample since this is a high ORR activity to obtain from a most likely mixed hydroxide catalyst.

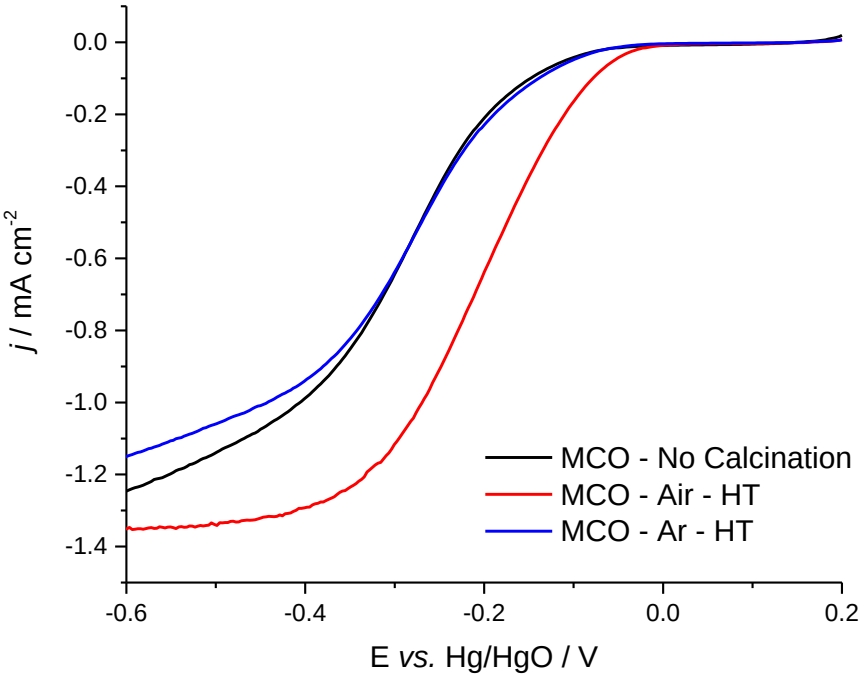

Figure 5.12. ORR voltammograms of $MnCo_2O_4$ samples; MCO – No Calcination (black), MCO – Air – HT (red) and MCO – Ar – HT (blue) in O_2 saturated 1 M KOH. Temperature: 25 ^oC; Potential scan rate: 5 mV s^{-1}; Rotation rate: 400 RPM.

Since the best ORR activity was obtained with MCO – Air – HT sample, it was chosen as the sample prepared via hydrothermal method to compare with other two samples (MCO – TD and MCO – CP) prepared via different preparation methods.

The comparison of oxygen reduction activities at MCO – TD, MCO – Air – HT and MCO – CP under similar conditions is shown in **Figure 5.13**. Pt black and carbon powder were also included as reference electrodes in order to make an assessment for the ORR activities of spinels with reference materials.

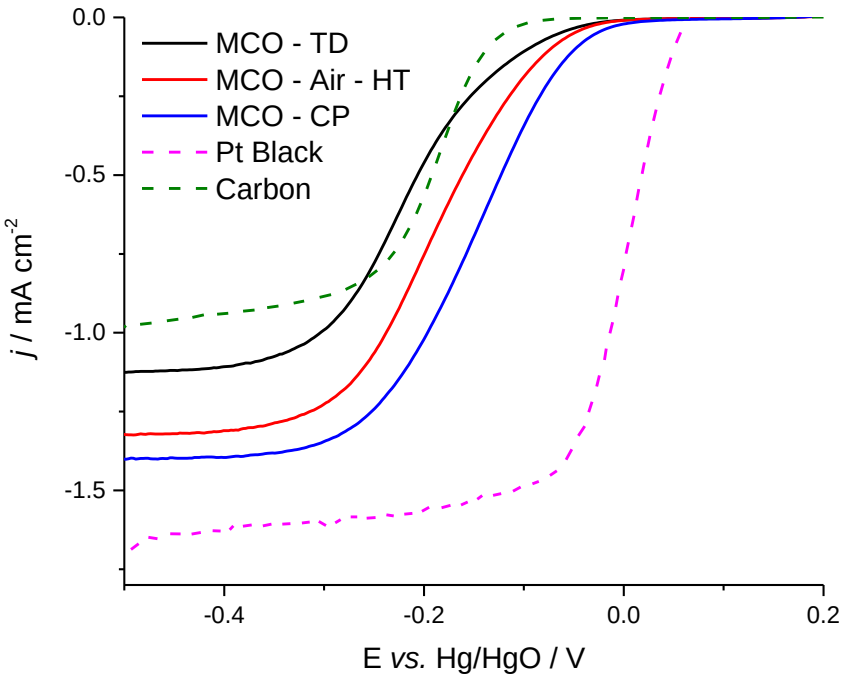

Figure 5.13. ORR voltammograms of $MnCo_2O_4$ samples, produced via three different preparation methods: MCO – TD (black), MCO – Air – HT (red), MCO – CP (blue), Pt black (pink) and Carbon powder (XC – 72R) (green) in O_2 saturated 1 M KOH. Temperature: 25 ^oC; Potential scan rate: 5 mV s^{-1}; Rotation rate: 400 RPM.

After Pt black, MCO – CP shows the highest catalytic activity and lowest onset potential compared to MCO – TD and MCO – Air – HT (see **Table 5.5** for more precise results ($E_{-0.1\ mA\ cm^{-2}}$ and $j_{L\ -0.4\ V}$)). On the other hand, the lowest activity and largest onset potential were observed at MCO – TD amongst spinels. The results in **Figure 5.13** are in agreement with the physical characterisation results. The highest surface area (49 $m^2\ g^{-1}$) and the smallest average particle size (123 nm) were observed with MCO – CP. Therefore, it is not surprising that the highest ORR activity was observed at MCO – CP. However, the ORR activity at MCO – TD is smaller than MCO – Air – HT even though MCO – TD has larger surface area (28.3 $m^2\ g^{-1}$) than MCO – Air – HT (19 $m^2\ g^{-1}$). In general, the larger surface area catalyst shows higher catalytic activity. However, there are some other variables (such as phase, crystallinity etc.), which also effect the overall performance of catalyst. This unusual behaviour most likely comes from the phase and crystallinity of materials. As shown in **Figure 5.2**, MCO – TD contains more than a single phase while MCO – Air – HT sample shows one single phase and much better crystallinity than MCO – TD. Therefore, the better

electrochemical activity at MCO – Air – HT may come from its single phase and much better crystallinity even though it possesses smaller surface area than MCO – TD.

Further investigation is required to compare oxygen reduction kinetics and reduction pathways at these materials. Therefore, rotation rate dependency experiments were carried out and Koutecky – Levich (K – L) plots were produced from the limiting current region to get further insight into the ORR kinetics and reduction pathways ($2e^-$ or $4e^-$).

As also shown in **Chapter 4**, the reduction wave (see **Figure 5.13**) can be investigated in two potential regions: ***a)*** the foot of wave (- 0.1 V *vs* Hg/HgO) and ***b)*** the plateau region (- 0.4 V *vs* Hg/HgO).

5.4.2.1. Foot of Wave

As in **Chapter 4**, there is a potential dependency in this region and an electron transfer reaction must be the rate determining step. The current densities at three samples prepared via different synthesis methods in this potential region (-0.1 V) are as follows; MCO – TD: -0.11, MCO – Air – HT: -0.19 and MCO – CP: -0.35 mA cm^{-2}. According to these results, $MnCo_2O_4$ sample produced via co-precipitation method shows more than three times larger electrochemical activity compared to the sample prepared via thermal decomposition. The difference between electrochemical activities are due to different crystallinity, phase, the specific surface area and particle size.

5.4.2.2. Plateau Region

The rotation rate dependency of voltammograms of the spinel coated electrodes were further investigated and **Figure 5.14** presents the ORR voltammograms with different rotation rates. For all three spinels, well-formed reduction waves were obtained at different rotation rates. The value of limiting currents at each different rotation rates for three spinels also show that the highest catalytic activity was observed with MCO – CP (see **Figure 5.14**). The rate determining step in plateau region can be either mass transport or a chemical step.

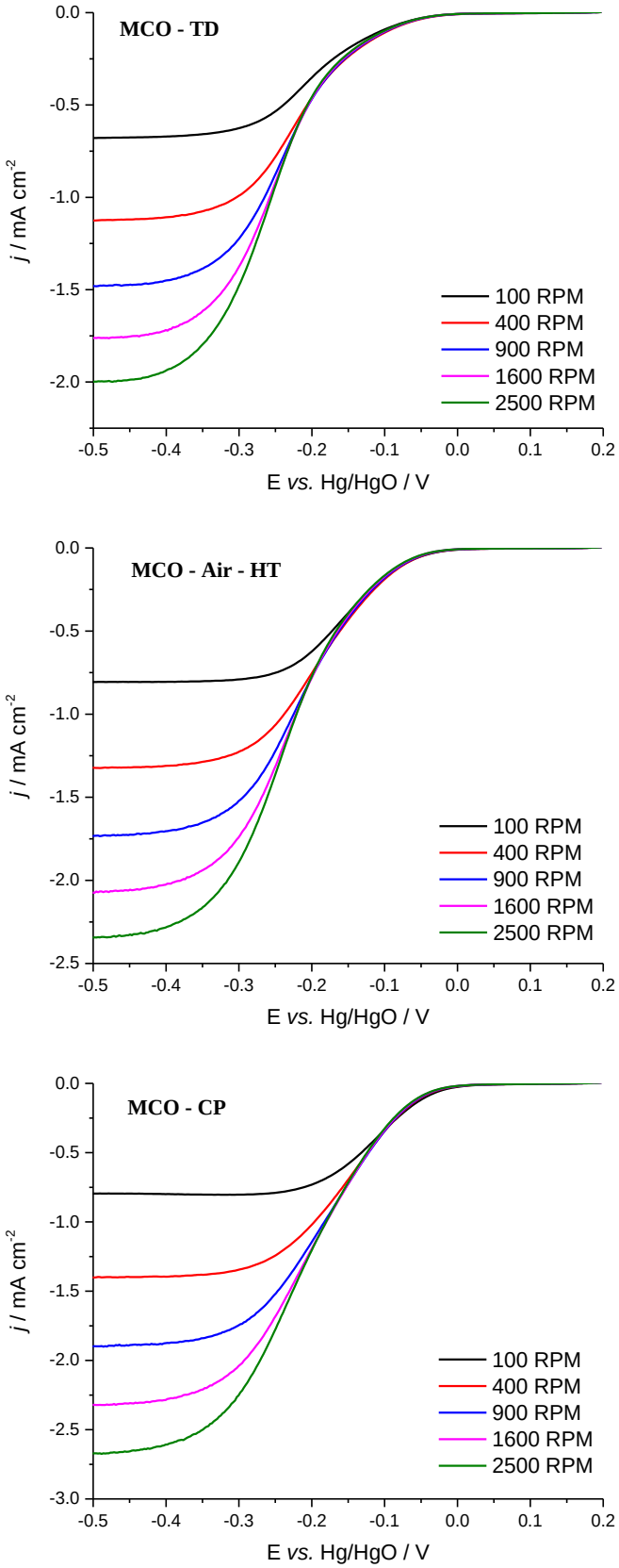

Figure 5.14. ORR voltammograms of $MnCo_2O_4$ samples; MCO – TD (**top**), MCO – Air – HT (**middle**), MCO – CP (**bottom**) in O_2 saturated 1 M KOH. Temperature: 25 ^oC; Potential scan rate: 5 mV s^{-1}. KOH was purged with O_2 for ≈ 8 min prior to each measurement.

Figure 5.14 shows that there is an obvious increase in the limiting current densities at three spinels with increased rotation rates. However, the oxygen reduction is not totally mass transport limited because the limiting current densities versus the square root of rotation rates (Levich Plots, not shown) are obviously not linear passing through the origin. This reveals that the oxygen reduction is limited to a certain extent by a chemical step for all three spinels. Therefore, further analysis was carried out using Koutecky – Levich (K – L) equation (see **Equation 3.1**, in **Chapter 3**) to show/compare the number of transferred electrons (n) per oxygen molecule from K – L slopes and the rate of chemical steps from the intercepts at three spinels. **Figure 5.15** presents K – L plots plotting $1/j_L$ *vs* $1/\omega^{1/2}$ for the three spinels as well as carbon powder and Pt black, which are for comparison purposes. The K – L slopes and intercepts are reported in **Table 5.5**.

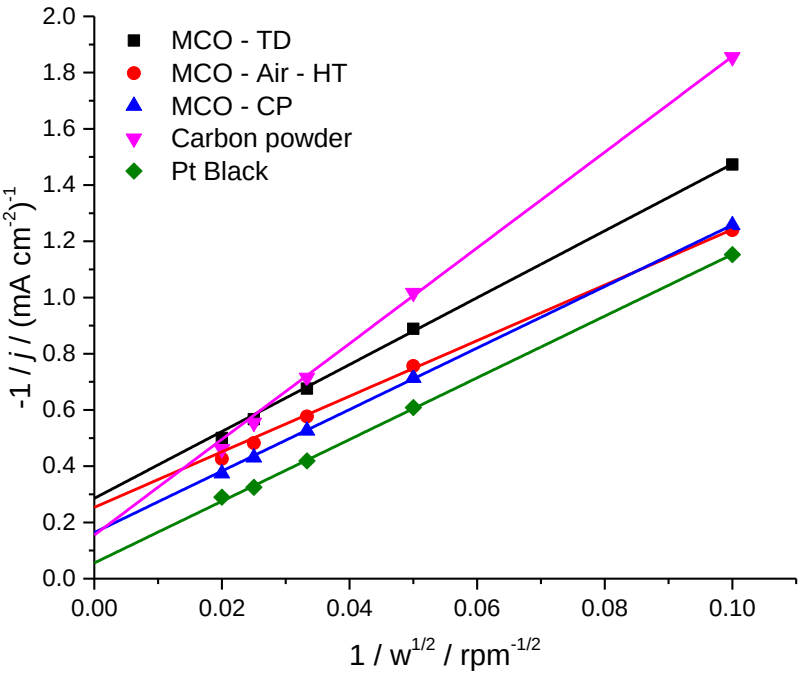

Figure 5.15. Koutecky-Levich plots for O_2 reduction in 1 M KOH with $MnCo_2O_4$ samples (MCO – TD, MCO – Air – HT and MCO – CP), Pt black and carbon powder. Data taken at - 500 mV *vs* Hg/HgO from **Figure 5.14**. Temperature: 25 ^oC; Potential scan rate: 5mV s^{-1}. The fitting for all samples are first 3 points (100, 400 and 900 RPM).

The linear fit passes through first three points (100, 400 and 900 rpm) for all three samples, but it is clear that there is a deviation at higher rotation rates (1600 and 2500 rpm, smaller

$1/\omega^{1/2}$) for each sample. K – L plots of Pt black and carbon were also included in this chapter in order to compare the K – L slopes and intercepts of spinels with Pt black and Carbon powder since oxygen is reduced via $4e^-$ reduction pathway at Pt while it is $2e^-$ reduction pathway on carbon as already mentioned in previous chapters. The intercepts and slopes of the plots are reported in **Table 5.5**.

1) Slopes of K – L plots for three spinels are similar to that of Pt black. The oxygen reduction follows $4e^-$ reduction process at all three samples. Amongst the spinels, MCO – CP shows the same slope with Pt black while there are some deviation observed with other two samples. K – L slope of carbon powder is almost two fold bigger than the one for Pt. Indeed, K – L slope of carbon powder smaller than expected shows that there is some $4e^-$ reduction at carbon. This will be also pointed out in section **5.4.4**.

2) Intercepts are correlated to rates of chemical step (see **Equation 3.1** in **Chapter 3**) and according to results in **Table 5.5**, the highest intercept was observed at MCO – TD, while the smallest value was shown at MCO – CP amongst the spinels. The smallest intercept means the highest rate of chemical step. Therefore, the highest rate of chemical step was observed at MCO – CP, confirming the highest activity of MCO – CP.

Catalyst	**E $_{(-0.1\ mA\ cm^{-2})}$ *vs* Hg/HgO / mV**	**$j_{L\ (-0.4V)}$/ mA cm^{-2}**	**Koutecky – Levich**		**% H_2O_2***	**n_{app}/ Apparent electron number***
			Slope/ mA^{-1} cm^2 rpm$^{-1/2}$	**Intercept/ mA^{-1} cm^2**		
MCO – TD	- 98	-1.1 (± 0.1)	-11.9 (±0.2)	-0.29 (±0.02)	34.6 (±1.7)	3.31
MCO – Air – HT	- 73	-1.3 (± 0.1)	-9.9 (±0.2)	-0.25 (±0.02)	25.4 (±1.3)	3.49
MCO – CP	- 49	-1.4 (± 0.1)	-11 (±0.1)	-0.16 (±0.01)	15.8 (±0.8)	3.68
Pt Black	+ 50	-1.6 (± 0.1)	-11 (±0.1)	-0.06 (±0.01)	<1	-
Carbon powder	- 137	-0.9 (± 0.1)	-17 (±0.3)	-0.16 (±0.02)	59.5 (±3.0)	2.81

Table 5.5. Comparison of catalyst materials with Pt black and Carbon powder (XC – 72R) RDE and RRDE data. O_2 saturated 1 M KOH; Temperature: 25 ^oC; Potential scan rate: 5 mV s^{-1}; Rotation rate: 400 RPM. *****Data were collected at 400 rpm where potential was – 0.5 V. Slopes and intercepts for all materials shown in the table are only from first three points, corresponding to rotation rates of 100, 400 and 900 RPM.

The apparent number of transferred electron (n_{app}), which measures the deviation from mass transport controlled $4e^-/2e^-$ reduction and the hydrogen peroxide formation percentages at materials will be investigated from RRDE data in section **5.4.4**.

5.4.3. Oxygen Evolution

Figure 5.16 present OER voltammograms at the three spinels, Pt black and bare GC in 1 M KOH at room temperature with 5 mV s^{-1} potential scan rate. The three spinels show catalytic activity towards OER, which make all spinels possible bifunctional catalysts. The lowest OER activity and largest onset potential were observed at MCO – TD while the highest activity and lowest onset potential were shown at MCO – CP. Again results from OER also show that $MnCo_2O_4$ synthesised via co-precipitation presents superior catalytic activity for ORR and OER compared to the other synthesis methods. The superior OER activity of $MnCo_2O_4$ produced via co-precipitation (MCO – CP) than Pt and comparable ORR activity of MCO – CP with Pt black make this sample a highly active non-noble bifunctional catalyst.

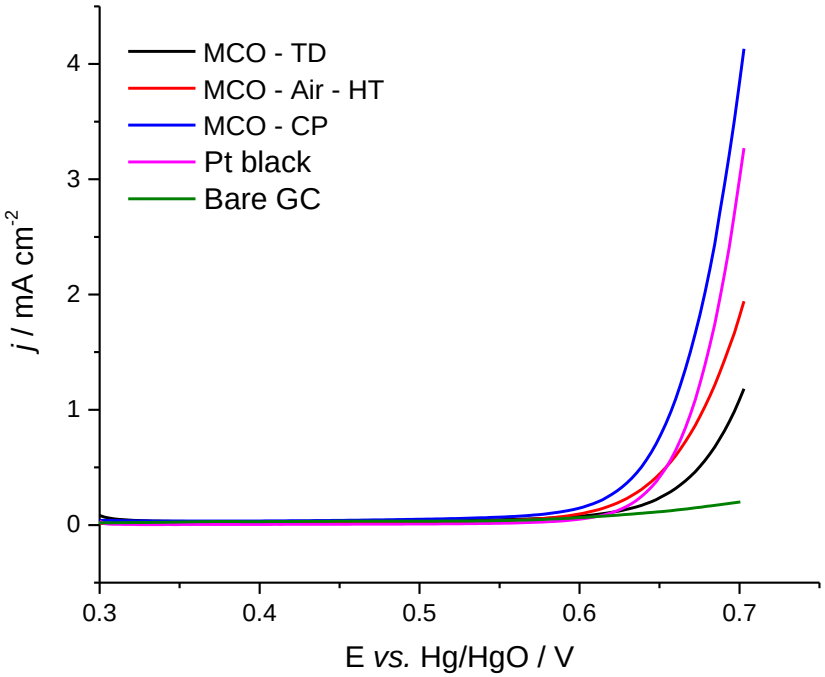

Figure 5.16. OER voltammograms of $MnCo_2O_4$ samples, produced with three different methods: MCO – TD (black), MCO – Air – HT (red), MCO – CP (blue), Pt black (pink) and bare GC (green) in 1 M KOH. Temperature: 25 ^oC; Potential scan rate: 5 mV s^{-1}.

Several papers have reported activity for OER at MCO materials but the conclusions differ, suggesting the different preparations have produced significantly different materials.

5.4.4. Hydrogen Peroxide Formation as an Intermediate Product

Rotating ring disc electrode (RRDE) studies were carried out using the three $MnCo_2O_4$ samples. The glassy carbon (GC) disc electrode was scanned from 0.2 V to -0.5 V *vs* Hg/HgO, while the potential of Pt ring was held at 0.2 V *vs* Hg/HgO, where the H_2O_2 oxidation is mass transport controlled.[26, 48, 57] **Figure 5.17** shows the responses of the ORR at the disc and H_2O_2 oxidation at Pt ring under similar conditions for three spinels. The hydrogen peroxide formation percentages (H_2O_2 %) at these samples as well as Pt black and carbon powder were calculated using **Equation 4.2** in **Chapter 4** and reported in **Table 5.5**. Hydrogen peroxide formation was observed at all three spinels, however, H_2O_2 % at each material are quite different. MCO – TD shows the highest H_2O_2 formation ratio (34.6 %), while MCO – Air – HT and MCO – CP shows much smaller percentages, 25.4 % and 15.8 %, respectively.

As mentioned in previous chapters, the uncovered GC electrode surface was observed from SEM images of GC electrode edges (see **Figure A2.1** in **Appendix**) and the uncovered GC electrode area was calculated as -6.4 % (see **Chapter 2**) and this uncovered GC electrode area added some hydrogen peroxide to the final percentages reported in **Table 5.5**. Hydrogen peroxide percentages at Pt black (support $4e^-$ reduction) and carbon powder (support $2e^-$ reduction) are also reported in **Table 5.5**.

The number of apparent electron (n_{app}) transferred per oxygen molecule was calculated for each spinel using **Equation 4.3** in **Chapter 4** and reported in **Table 5.5**. These results are also consistent with previous electrochemical results. As already shown in section **5.4.2.2**, the rate of chemical step was the smallest at MCO – TD since the intercept was the highest at this material (see **Table 5.5**). Therefore, the smaller the rate of chemical step is the larger deviation from $4e^-$ reduction. These results (from n_{app} values at three spinels) also confirm that $MnCo_2O_4$ produced via co-precipitation is the most favourable catalyst for the ORR.

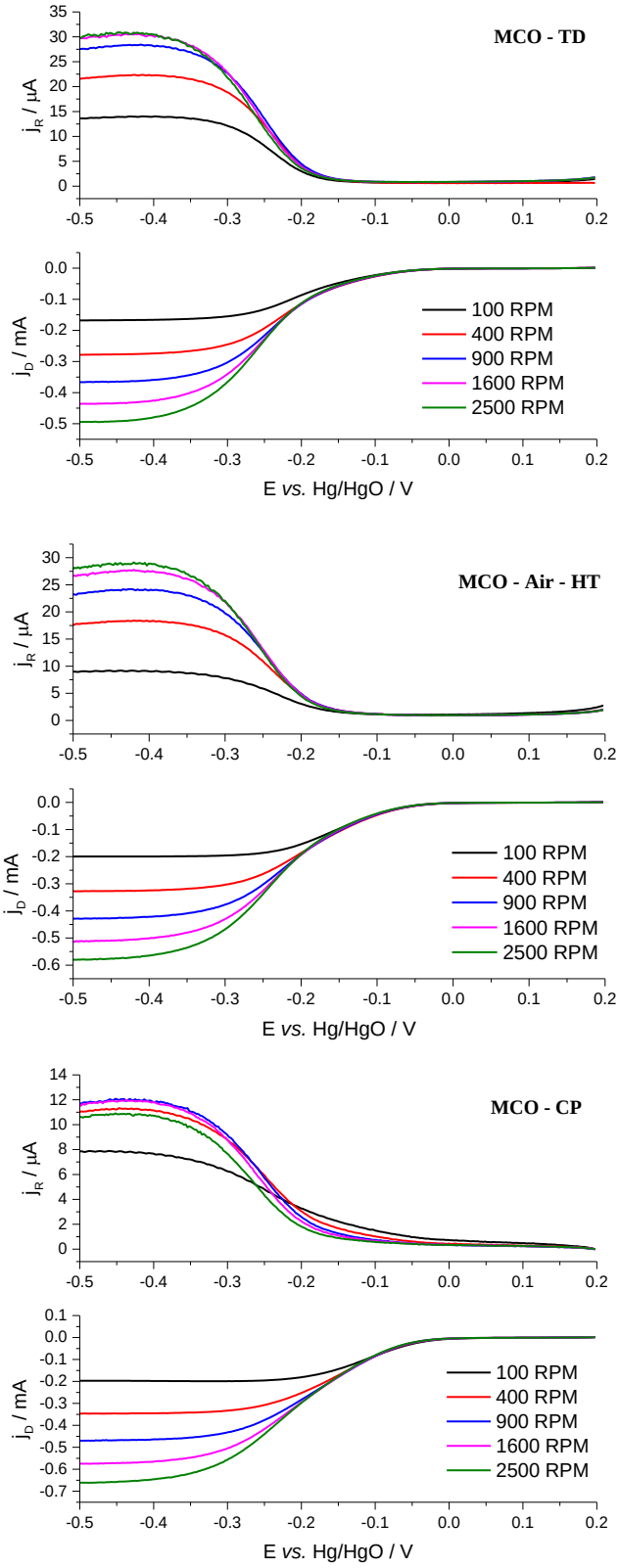

Figure 5.17. Disc and ring responses for O_2 reduction at $MnCo_2O_4$ samples; MCO – TD (**top**), MCO – Air – HT (**middle**) and MCO – CP (**bottom**) coated glassy carbon discs in O_2 saturated 1 M KOH. The potential of the disc is scanned while the Pt ring is held at + 200 mV *vs* Hg/HgO. Temperature: 25 ^oC; Potential scan rate: 5 mV s^{-1}. *N*: 0.37.

As mentioned in section **5.4.2.2** that the K – L slope of carbon powder was smaller than expected, which was showing that oxygen reduction is not pure $2e^-$ reduction at carbon powder. n_{app} for carbon powder is 2.81 (see **Table 5.5**) and this also confirms that n_{app} is larger than expected value for carbon powder, which also indicates that some $4e^-$ reduction is involved at carbon powder even though the oxygen is mainly reduced via $2e^-$.

5.4.5. Hydrogen Peroxide Oxidation and Reduction

To investigate the reduction of H_2O_2 at the three spinels and Pt black, the voltammograms for 10 mM H_2O_2 in 1 M KOH purged with N_2 at room temperature are reported in **Figure 5.18**. The limiting currents for oxidation and reduction at Pt black are equal to each other (as expected since both H_2O_2 oxidation to oxygen and reduction to hydroxide are rapid and involve $2e^-$) and they are much larger than the oxidation and reduction limiting currents obtained at the three spinels, confirming that there is a strong kinetic limitation at these materials.

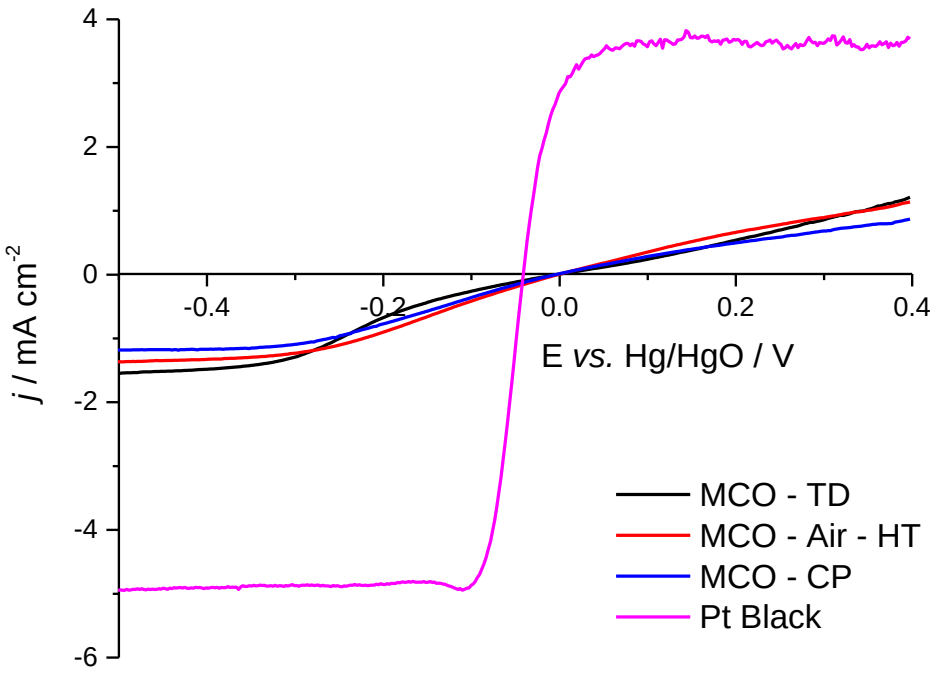

Figure 5.18. Voltammograms for the reduction and oxidation of ≈ 10 mM H_2O_2 in N_2 purged 1 M KOH at MCO – TD (black), MCO – Air – HT (red) and MCO – CP (blue) and Pt black (pink) coated glassy carbon at 400 RPM. Temperature: 25 ^oC; Potential scan rate: 5 mV s^{-1}.

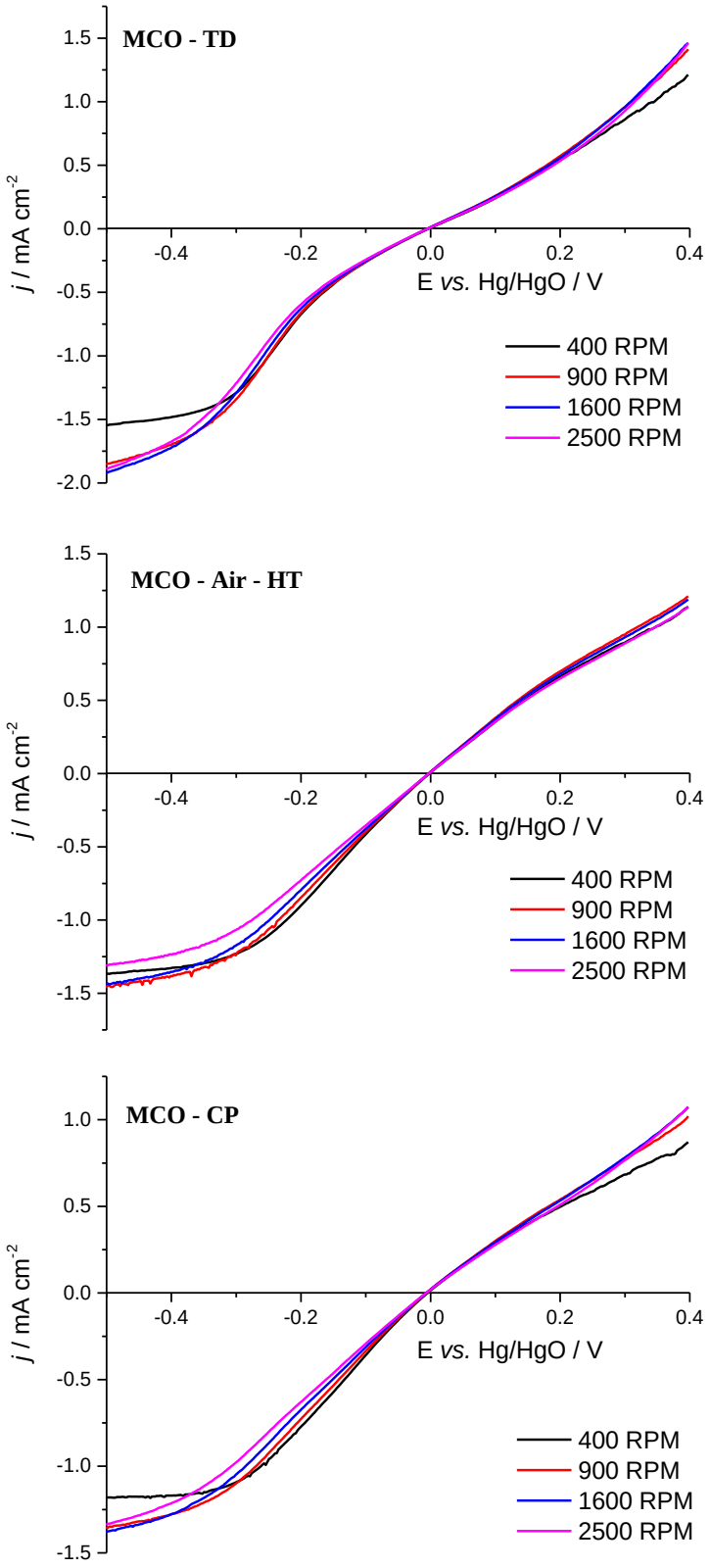

Figure 5.19. Rotation rate dependence of the voltammograms for the reduction and oxidation of 10 mM H_2O_2 in N_2 purged 1 M KOH at MCO – TD (**top**), MCO – Air – HT (**middle**) and MCO – CP (**bottom**) coated glassy carbon. Temperature: 25 ^oC; Potential scan rate: 5 mV s^{-1}. Electrolyte was purged with N_2 (≈ 5 min) before each measurement.

The rotation rate dependency of voltammograms for 10 mM H_2O_2 under similar conditions at the three spinels was also reported and shown in **Figure 5.19**. The limiting currents are almost independent of rotation rates for the three materials. These results also confirm that the reduction of hydrogen peroxide is not a rapid reaction. Therefore, it is certain that $2x2e^-$ mechanism for $4e^-$ reduction is not happening at these materials. The number of apparent electrons for ORR at the spinels (see **Table 5.5**) show that direct $4e^-$ reduction is the case for all three spinels even though there is a chemical step limitation, which varies for each spinel, as already mentioned (see **5.4.2.2**).

5.4.6. Stability

Besides testing the electrocatalytic activities of the three spinels, the stability of activity was evaluated by chronoamperometric measurements since stability/durability is an important parameter for qualification of the performance of catalysts.[20] **Figure 5.20** shows the chronoamperometric responses recorded at a constant potential (-0.5 V) in O_2 saturated 1 M KOH at 900 RPM for 12 hours at the three spinels.

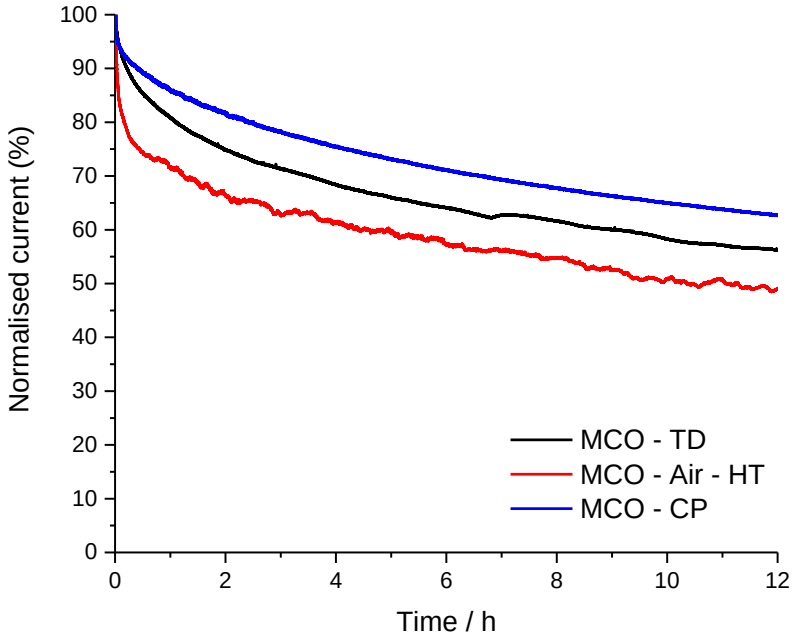

Figure 5.20. Chronoamperometric responses of MCO – TD (black), MCO – Air – HT (red) and MCO – CP (blue) were obtained where the potential was held at -0.5 V *vs* Hg/HgO. Rotation rate: 900 RPM. 1 M KOH was saturated with O_2 and then a continuous flow of O_2 was used above the electrolyte in order to keep a constant O_2 concentration. Duration of measurements: 12 hours; Temperature: 25 ^oC.

Catalyst	The current lost %
MCO – TD	44
MCO – Air – HT	51
MCO – CP	37

Table 5.6. The current lost percentages were reported from **Figure 5.20**.

As shown in **Figure 5.20** and **Table 5.6**, each sample shows different electrochemical stability under similar conditions. In general, these current losses are higher than expected values even though the measurements were carried out for long time (12 hours). It is important to note that the substantial decrease in the current densities is observed in the early stage of measurements (see **Figure 5.20**). The initial fast current loss may be coming from capacitive effects: ***a)*** double layer charge/discharge in the first few seconds and ***b)*** proton insertion in the later minutes.[58] In contrast, the long term losses are Faradaic and this may be due to the decrease in specific area or the lose of active sites.[58]

In order to investigate further about the rapid losses in the activities at spinels, MCO – CP was chosen to do the ORR characterisation before the stability test and using the same electrode to do stability test and then again repeating the ORR measurement as a final stage. Therefore, a voltammogram for ORR before and after the stability test can be compared to have accurate information about the current lost, which is from the material itself or capacitive effects.

Figure 5.21 presents ORR voltammograms before and after chronoamperometric measurement at MCO – CP. As shown, the current density for ORR decreased from 1.4 to 1.2 mA cm^{-2} as well as a slight onset potential shift from positive to more negative potential after the stability test. The current density lost at MCO – CP is around 14.3 % (the current lost between before and after chronoamperometric measurements, see **Figure 5.21**), compared to the result (37 %) that obtained via chronoamperometry in **Figure 5.20**. This result proves that the dramatic decrease in the activities in the beginning of chronoamperometric measurements are most likely from the capacitive effects. Indeed, the current lost at MCO – CP (14.3 %) for 12 hours (43200 seconds) is smaller than the reported result by Yang et al.[59]

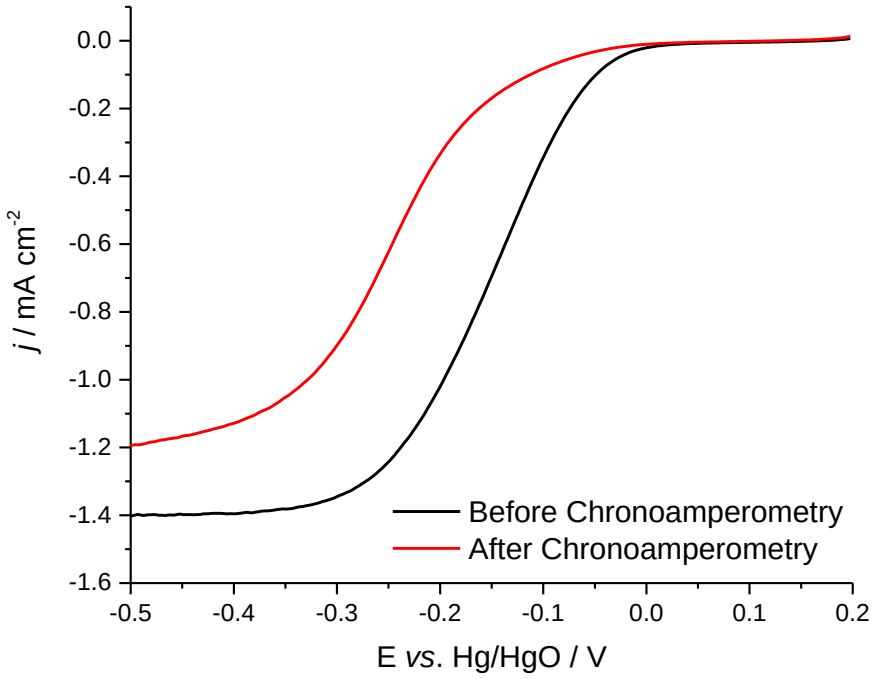

Figure 5.21. ORR voltammograms at MCO – CP coated electrode before and after chronoamperometric measurement in O_2 saturated 1M KOH. Temperature: 25 ^oC; Potential scan rate: 5 mV s^{-1}; Rotation rate: 400 RPM.

5.5. Discussion

$MnCo_2O_4$ samples were synthesised via a hydrothermal method with differing following calcination conditions. Physical characterization techniques show that use of only the hydrothermal method is not enough to produce spinel type $MnCo_2O_4$. Subsequent heat treatment is required under oxygen flow to produce single phase spinel $MnCo_2O_4$ with high crystallinity. Without temperature treatment in hydrothermal method, materials have impurities (these might be coming from undecomposed nitrates in the composition) and amorphous morphology. In contrast, post temperature treatment (especially above 300 ^oC, see TGA analysis in **Chapter 4**) under air flow allows nitrates to be decomposed in the composition and therefore spinel type $MnCo_2O_4$ is synthesised. $MnCo_2O_4$ was synthesised via hydrothermal method and post temperature treatment was applied under argon flow but $MnCo_2O_4$ does not have spinel structure due to oxygen deficiency in the lattice.

Oxygen reduction reaction (ORR) activities of $MnCo_2O_4$ samples produced via hydrothermal method with different post-treatments show that the highest activity and lowest onset potential were observed at MCO – Air – HT ($MnCo_2O_4$ synthesised via hydrothermal

method and under air flow at 600 ºC for 12 hours). A clean spinel structure certainly enhances catalytic activity. Even so, a surprising catalytic activity was observed at MCO – No Calcination (most likely mixed hydroxide catalyst).

The second and major part of this chapter has been reserved for synthesising spinel type $MnCo_2O_4$ samples via three different methods (thermal decomposition, hydrothermal with post temperature treatment and co-precipitation). According to the XRD results, the material produced via thermal decomposition has more than one phase even though it shows a spinel structure. In contrast, single phase spinel type $MnCo_2O_4$ samples with high crystallinities were produced via hydrothermal with post temperature treatment (under air flow) and co-precipitation. The smallest particle size and the highest surface area material was synthesised via co-precipitation method amongst the three preparation methods. As it has been also mentioned in **Chapter 4**, fit statistics from the XRD refinement suggest that Mn ions occupy in tetrahedral sites of the spinels since better fitting is observed when Mn ions occupy tetrahedral sites rather than octahedral sites in the spinel.

Ex-situ XANES studies have shown the mean Co and Mn valence for three spinels are around 2.35 and 3.40, respectively. According to these results, preparation methods have no impact towards the position of Mn^{+3} in the spinels since Mn^{+3} ions substituted Co^{+3} in all three spinels. XANES data are complementary and in a good agreement with XRD data by allowing us to know the mean Co and Mn oxidation states, which improves the input for the XRD refinement. According to XANES and XRD results, the cationic distribution for each spinel could be proposed as $[Mn^{+3}]_{Th}$ $[Co^{+3}\ Co^{+2}]_{Oh}$ O_4^{-2} (where manganese ions (+3) prefer tetrahedral sites in all three spinels).

Electrochemical studies for the $MnCo_2O_4$ spinel samples show that the highest oxygen reduction activity with lowest onset potential was obtained with MCO – CP while MCO – TD shows the lowest activity. The ORR activity of MCO – CP is somewhat close to Pt black with only ≈ 100 mV larger onset potential and slightly less current density in the limiting current region. The ORR current densities at three spinels were compared at a specific potential (-0.1 V) as follow; MCO – TD: -0.11, MCO – Air – HT: -0.19 and MCO – CP: -0.35 mA cm^{-2}. The differences in activity is attributed to the presence of different phases, crystallinity, surface area and particle size, and it hasn't been possible to isolate each effect. It is also worth to draw attention that the surface area of MCO – TD is larger (28.3 $m^2\ g^{-1}$) than MCO – Air – HT (19 $m^2\ g^{-1}$) and therefore the catalytic activity of

MCO – TD was expected to be larger than MCO – Air – HT since the larger surface area material shows higher catalytic activity in general. However, other variables (such as phase, crystallinity etc.) can also effect the overall performance of the material. MCO – Air – HT has a single phase and much better crystallinity compared to MCO – TD (see **Figure 5.2**) even though it has smaller surface area. Therefore, MCO – Air – HT performs better catalytic activity than MCO – TD, which is most likely from its single phase and much better crystallinity.

The mechanistic studies of oxygen reduction at a potential (-500 mV *vs* Hg/HgO) in the plateau region of a voltammogram at three spinels verified that oxygen is reduced via $4e^-$ reduction with different degree of a chemical rate dependency. K – L plots show that the slopes of all three spinels are similar to Pt black, confirming $4e^-$ reduction. The intercepts of three samples show the rate of a chemical step is different at each spinel. The smallest intercept, which means more rapid chemistry, was observed at MCO – CP and the largest intercept (the smallest rate of chemical step) was obtained at MCO – TD (see **Table 5.5**).

Oxygen evolution behaviours at three spinels, Pt black and bare GC were compared under similar conditions and it reveals that the highest OER activity with lowest onset potential was observed at MCO – CP even slightly better than Pt black. The lowest OER activity was observed with MCO – TD confirming that different preparation method has different effects on the OER activities as well.

RRDE studies showed that hydrogen peroxide (H_2O_2 %) formation is observed at each spinel and the amount of hydrogen peroxide varies with the synthesis method. Again MCO – CP shows superior activity compared to other two by producing H_2O_2 as an intermediate product only 15.8 % while MCO – Air – HT and MCO – TD are 25.4 % and 34.6 %, respectively. As previously mentioned, uncovered GC electrode area does also produce some hydrogen peroxide and therefore aforementioned H_2O_2 percentages have already included H_2O_2 formation from uncovered GC electrode since the oxygen reduction follows $2e^-$ reduction (H_2O_2 formation pathway) at GC electrode. The number of apparent electrons (n_{app}) transferred/O_2 for each spinel shows that n_{app} for MCO – CP is 3.68 while it is 3.49 and 3.31 for MCO – Air – HT and MCO – TD, respectively. These results also show that oxygen reduction is $4e^-$ at spinels, however, there are some deviations for each spinels and the smaller rate of chemical step corresponds to a smaller n_{app}.

In order to ensure the oxygen reduction pathway (either direct $4e^-$ or $2x2e^-$ pathway (where H_2O_2 is rapidly converted into hydroxide by a fast reduction kinetics on the surface of the catalyst)) at spinels, the oxidation and reduction studies of 10 mM H_2O_2 in 1 M KOH at the three spinels show that both oxidation and reduction are not mass transport controlled at three materials and the current densities at spinels for both oxidation and reduction are much lower compared to Pt black, confirming that there is a strong kinetic limitation. It can be said that H_2O_2 reduction cannot be so rapid at these spinels and therefore $2x2e^-$ mechanism is ruled out. According to these data, oxygen is reduced via direct $4e^-$ reduction at three spinels.

The stability of the activity of three spinels shows that MCO – CP has the lowest current lost (14.3% for 12 hours) amongst spinels. The rapid losses in the activities at spinels in the beginning of chronoamperometric measurements are most likely due to the capacitive effects.

In conclusion, the comparison of three synthesising methods shows that co-precipitation method is the most suitable preparation method in order to produce spinel $MnCo_2O_4$ with larger surface area, smaller particle size, single phase, higher crystallinity as well as higher electrochemical activity for both ORR and OER in alkaline media.

5.6. References

1. F. Y. Cheng, J. A. Shen, B. Peng, Y. D. Pan, Z. L. Tao and J. Chen, *Nat. Chem.*, 2011, **3**, 79-84.
2. K. Zhang, X. Han, Z. Hu, X. Zhang, Z. Tao and J. Chen, *Chem. Soc. Rev.*, 2015, **44**, 699-728.
3. K. Wang, X. Wu, W. Wu, Y. Hu and S. Liao, *J. Supercond. Novel Magn.*, 2014, **27**, 1249-1256.
4. P. Lavela, J. L. Tirado and C. Vidal-Abarca, *Electrochim. Acta*, 2007, **52**, 7986-7995.
5. A. Restovic, E. Rıos, S. Barbato, J. Ortiz and J. Gautier, *J. Electroanal. Chem.*, 2002, **522**, 141-151.
6. E. Rios, P. Lara, D. Serafini, A. Restovic and J. L. Gautier, *J. Chil. Chem. Soc.*, 2010, **55**, 261-265.
7. T. A. Nissinen, Y. Kiros, M. Gasik and M. Leskela, *Chem. Mat.*, 2003, **15**, 4974-4979.
8. R. Tholkappiyan, A. N. Naveen, S. Sumithra and K. Vishista, *J. Mater. Sci.*, 2015, **50**, 5833-5843.

9. N. Garg, M. Mishra and A. K. Ganguli, *RSC Adv.*, 2015, **5**, 84988-84998.
10. A. J. Esswein, M. J. McMurdo, P. N. Ross, A. T. Bell and T. D. Tilley, *J. Phys. Chem. C*, 2009, **113**, 15068-15072.
11. H. Liu and J. Wang, *J. Electron. Mater.*, 2012, **41**, 3107-3110.
12. P. Boldrin, A. K. Hebb, A. A. Chaudhry, L. Otley, B. Thiebaut, P. Bishop and J. A. Darr, *Ind. Eng. Chem. Res.*, 2007, **46**, 4830-4838.
13. L. F. Duan, F. H. Gao, L. M. Wang, S. Z. Jin and H. Wu, *J. Adv. Ceram.*, 2013, **2**, 266-273.
14. N. Padmanathan and S. Selladurai, *Ionics*, 2014, **20**, 479-487.
15. L. Li, Y. Zhang, X. Liu, S. Shi, X. Zhao, H. Zhang, X. Ge, G. Cai, C. Gu and X. Wang, *Electrochim. Acta*, 2014, **116**, 467-474.
16. Y. Q. Wu, X. Y. Chen, P. T. Ji and Q. Q. Zhou, *Electrochim. Acta*, 2011, **56**, 7517-7522.
17. U. Moralesl, A. Campero and O. Solorza—Feria, *J. New Mater. Electrochem. Syst.*, 1999, **2**, 89-93.
18. X. Cao, C. Jin, F. Lu, Z. Yang, M. Shen and R. Yang, *J. Electrochem. Soc.*, 2014, **161**, H296-H300.
19. L. Zhou, D. Zhao and X. W. Lou, *Adv. Mater.*, 2012, **24**, 745-748.
20. Y. Liu, Y. Wang, X. Xu, P. Sun and T. Chen, *RSC Adv.*, 2014, **4**, 4727-4731.
21. B. Chi, J.-B. Li, Y.-S. Han and J.-H. Dai, *Mater. Lett.*, 2004, **58**, 1415-1418.
22. T. Nissinen, T. Valo, M. Gasik, J. Rantanen and M. Lampinen, *J. Power Sources*, 2002, **106**, 109-115.
23. T. Nissinen, Y. Kiros, M. Gasik and M. Lampinen, *Mater. Res. Bull.*, 2004, **39**, 1195-1208.
24. E. Rios, J. L. Gautier, G. Poillerat and P. Chartier, *Electrochim. Acta*, 1998, **44**, 1491-1497.
25. H. Bordeneuve, C. Tenailleau, S. Guillemet-Fritsch, R. Smith, E. Suard and A. Rousset, *Solid State Sci.*, 2010, **12**, 379-386.
26. M. Sugawara, M. Ohno and K. Matsuki, *J. Mater. Chem.*, 1997, **7**, 833-836.
27. J. J. Mateos, J. Morales and J. Tirado, *J. Solid State Chem.*, 1989, **82**, 87-94.
28. N. Yamamoto, S. Higashi, S. Kawano and N. Achiwa, *J. Mater. Sci. Lett.*, 1983, **2**, 525-526.
29. M. Y. Yoon, E. J. Lee, R. H. Song and H. J. Hwang, *Met. Mater. Int.*, 2011, **17**, 1039-1043.

30. F. Borges, D. Melo, M. Camara, A. Martinelli, J. Soares, J. De Araujo and F. Cabral, *J. Magn. Magn. Mater.*, 2006, **302**, 273-277.
31. M. Hamdani, M. I. S. Pereira, J. Douch, A. A. Addi, Y. Berghoute and M. H. Mendonca, *Electrochim. Acta*, 2004, **49**, 1555-1563.
32. P. S. Patil, *Mater. Chem. Phys.*, 1999, **59**, 185-198.
33. D. Lapham, I. Colbeck, J. Schoonman and Y. Kamlag, *Thin Solid Films*, 2001, **391**, 17-20.
34. M. Hamdani, R. N. Singh and P. Chartier, *Int. J. Electrochem. Sci.*, 2010, **5**, 556-577.
35. S. W. T. Price, S. J. Thompson, X. H. Li, S. F. Gorman, D. Pletcher, A. E. Russell, F. C. Walsh and R. G. A. Wills, *J. Power Sources*, 2014, **259**, 43-49.
36. X. H. Li, D. Pletcher, A. E. Russell, F. C. Walsh, R. G. A. Wills, S. F. Gorman, S. W. T. Price and S. J. Thompson, *Electrochem. Commun.*, 2013, **34**, 228-230.
37. D. Pletcher, X. Li, S. W. Price, A. E. Russell, T. Sönmez and S. J. Thompson, *Electrochim. Acta*, 2016, **188**, 286-293.
38. D. Lapham and A. Tseung, *J. Mater. Sci.*, 2004, **39**, 251-264.
39. M. Schwickardi, T. Johann, W. Schmidt and F. Schüth, *Chem. Mat.*, 2002, **14**, 3913-3919.
40. S. Yuvaraj, L. Fan-Yuan, C. Tsong-Huei and Y. Chuin-Tih, *J. Phys. Chem. B*, 2003, **107**, 1044-1047.
41. H.-C. Dinh, S.-i. Mho, I.-H. Yeo, Y. Kang and D.-W. Kim, *RSC Adv.*, 2015, **5**, 100709-100714.
42. H. Hayashi and Y. Hakuta, *Materials*, 2010, **3**, 3794-3817.
43. Y. Liang, H. Wang, J. Zhou, Y. Li, J. Wang, T. Regier and H. Dai, *J. Am. Chem. Soc.*, 2012, **134**, 3517-3523.
44. X. Ge, Y. Liu, F. T. Goh, T. A. Hor, Y. Zong, P. Xiao, Z. Zhang, S. H. Lim, B. Li and X. Wang, *ACS Appl. Mater. Interfaces*, 2014, **6**, 12684-12691.
45. J. Chen, Y. Cui, X. Wang, M. Zhi, M. Lavorgna, A. P. Baker and J. Wu, *Electrochim. Acta*, 2016, **188**, 704-709.
46. J. M. De Vidales, O. García-Martínez, E. Vila, R. Rojas and M. Torralvo, *Mater. Res. Bull.*, 1993, **28**, 1135-1143.
47. R. M. Rojas, E. Vila, O. García and J. L. M. de Vidales, *J. Mater. Chem.*, 1994, **4**, 1635-1639.

48. T. Sönmez, S. J. Thompson, S. W. Price, D. Pletcher and A. E. Russell, *J. Electrochem. Soc.*, 2016, **163**, H884-H890.
49. T. Poux, F. S. Napolskiy, T. Dintzer, G. Kerangueven, S. Y. Istomin, G. A. Tsirlina, E. V. Antipov and E. R. Savinova, *Catal. Today*, 2012, **189**, 83-92.
50. X. Liu, M. Park, M. G. Kim, S. Gupta, X. Wang, G. Wu and J. Cho, *Nano Energy*, 2016, **20**, 315-325.
51. C. Song and J. Zhang, in *PEM fuel cell electrocatalysts and catalyst layers*, Springer, 2008, pp. 89-134.
52. S. Malkhandi, P. Trinh, A. K. Manohar, K. C. Jayachandrababu, A. Kindler, G. K. S. Prakash and S. R. Narayanan, *J. Electrochem. Soc.*, 2013, **160**, F943-F952.
53. C. Li, X. P. Han, F. Y. Cheng, Y. X. Hu, C. C. Chen and J. Chen, *Nat. Commun.*, 2015, **6**.
54. Y.-Y. Hu, Z. Liu, K.-W. Nam, O. J. Borkiewicz, J. Cheng, X. Hua, M. T. Dunstan, X. Yu, K. M. Wiaderek and L.-S. Du, *Nat. Mater.*, 2013, **12**, 1130-1136.
55. S. Thompson, *Bi-functional oxygen catalysts for metal-air flow-batteries*, PhD Thesis, University of Southampton, 2016.
56. F. Jiao and H. Frei, *Chem. Commun.*, 2010, **46**, 2920-2922.
57. N. M. Marković, H. A. Gasteiger and P. N. Ross, *J. Phys. Chem.*, 1996, **100**, 6715-6721.
58. I. Roche, E. Chaînet, M. Chatenet and J. Vondrák, *J. Appl. Electrochem.*, 2008, **38**, 1195-1201.
59. H. Yang, F. Hu, Y. Zhang, L. Shi and Q. Wang, *Nano Res.*, 2016, **9**, 207-213.

Chapter 6: Conclusions

Co_3O_4, $NiCo_2O_4$ and a series of Mn containing samples ($Mn_xCo_{3-x}O_4$, $0.0 \leq x \leq 2.0$)) with spinel structures were produced and these powdered materials are made of irregular nano scale size particles. In addition, $MnCo_2O_4$ spinel samples were synthesized via different preparation methods and conditions within a synthesis method. All nano-size spinel type powder materials were characterised by a wide range of physical, spectroscopic and electrochemical methods such as XRD, BET, Raman Spectroscopy, SEM-EDX, TEM, XPS, TGA, XANES, RDE and RRDE.

Co_3O_4 is a p-type semiconductor and suffers from low electronic conductivity because of the impossibility of electronic transfer between Co^{+2} and Co^{+3} in tetrahedral and octahedral sites, respectively. It is a poor catalyst for both oxygen reduction and evolution. Its electronic conductivity and also its electrochemical activity towards the ORR and OER can be improved by incorporating metals such as Mn, Ni etc. in a mixed spinel. As shown in this thesis, $NiCo_2O_4$ and Mn containing spinels show much enhanced activity. $NiCo_2O_4$ is shown as the best bifunctional catalyst, however, cubic phase $MnCo_2O_4$ has the greatest the ORR activity.

With Co_3O_4 and $NiCo_2O_4$, O_2 reduction and evolution take place on surfaces with the materials in different oxidation states. In contrast, CVs of Mn containing samples produce no evidence for oxidation and reduction on surfaces of Mn doped Co_3O_4 samples. Oxygen evolution takes place on species with higher oxidation states, which are most favourable for the oxygen evolution process. Therefore, the poor oxygen evolution properties of Mn containing spinels may be correlated with species at lower oxidation sates compared to Ni/Co spinels.

Oxygen reduction properties of all spinels (Mn and Ni containing Co_3O_4) show that the oxygen reduction at cathodes catalysed by $NiCo_2O_4$ and Mn containing spinels are predominantly a $4e^-$ reaction leading to water with early cleavage of the O – O bond in reaction sequence. There are rate limitations observed at $NiCo_2O_4$ and all Mn containing samples in some degree. These rate limitations are controlled by a chemical step, most likely cleavage of the O – O on the surface of the spinels. In contrary, Co_3O_4 supports $2e^-$ reduction with much lower current density. The rate of the cleavage of the O – O and hence the $4e^-$ reduction is much slower and this leads to a significant contribution from a competing

mechanism, initial electron transfer to the oxygen molecule; almost half the charge passed leads to hydrogen peroxide formation.

In the series of $Mn_xCo_{3-x}O_4$, ($0.0 \leq x \leq 2.0$) spinels, studies show the oxidation state of doped Mn ions is +3 and they replace Co^{+3} ions in the spinel. Substituted Mn^{+3} ions occupy tetrahedral sites rather than octahedral sites in the spinel. Therefore, based on XPS, XANES and XRD fit statistics, the cationic distributions for five Mn containing spinels were proposed. The proposed cationic distributions are not the same of those proposed by Crystal Field Theory (CFT). Based on calculations from CFT, the crystal field stabilization energy (CFSE) of $MnCo_2O_4$, to name but one example, is estimated as $-3.53\ \Delta_o+2P$, in which Mn^{+3} is in octahedral site while Co^{+2} and Co^{+3} are in tetrahedral and octahedral sites, respectively. This CFSE ($-3.53\ \Delta_o+2P$) is slightly smaller than CFSE ($-3.37\ \Delta_o+2P$) for those where Mn^{+3} is in tetrahedral site and both Co^{+2} and Co^{+3} are in octahedral sites. It is important to note that Δ_o values vary for the different ions, therefore, the cationic distributions proposed from CFT based on CFSE values are not fully valid. Since the CFSE values are very close, these deviations from the different values of Δ_o could be significant. A recent study by Chao Wei at al.[1] shows that $MnCo_2O_4$ spinels synthesised at different temperatures in which Mn occupy at tetrahedral and octahedral sites (mainly octahedral site) in the spinel structure with different Mn occupation ratio (%). Another recent study[2] of spinel $Mn_{0.3}Co_{2.7}O_4$ assumes Mn^{+3} ions occupy octahedral site from only XPS data. Therefore, it is most likely right to say that proposed cationic distributions for all Mn containing spinels ($Mn_xCo_{3-x}O_4$, ($0.0 \leq x \leq 2.0$)) are clearly correct based on solid evidence from XRD fit statistics, ex-situ XANES and XPS data. This may be considered the main novelty of this work presented in this thesis.

With increase of Mn content in the spinel Co_3O_4, the phase transformation (from cubic to tetragonal) was clearly shown by XRD and Raman. Studies confirm that cubic phase show much better catalytic activity than tetragonal phase. Amongst Mn containing spinels, cubic phase $MnCo_2O_4$ ($x = 1.0$) is the most active ORR catalyst in alkaline media.

Based on all electrochemical data, ternary Ni or Mn based cobalt oxides posses much superior catalytic activity than binary Co_3O_4. This increase in the catalytic activities for ORR/OER at ternary Ni or Mn based oxides is not only correlated with the change in the oxidation states or Mn and Ni ions at the material surfaces, but also with the difference in surface area, particle size, roughness of the material, electrical conductivity, different

crystallinity, different O_2 bonding properties, phase, the exposure of more active sites to the electrolyte, etc. A recent study by Wenqiao Song at al.[3] about Ni and Mn doped Co_3O_4 shows that CV peaks associated with Co^{+2} in the spinel structures were weakened by incorporating Mn and Ni. This was supported by their XPS data that Co^{+2} population at the material surface was decreased after Mn and Ni incorporation to Co_3O_4. They are highlighting that the increase in the ORR activities is not only correlated with the change of ions on the surface but also other structural parameters such as surface area, and oxygen deficiency.

The effect of preparation conditions within hydrothermal method for synthesising spinel $MnCo_2O_4$ samples show that only hydrothermal method is not enough to produce "spinel type" $MnCo_2O_4$. There must be post high temperature treatment under air flow in order to produce single phase spinel $MnCo_2O_4$ with high crystallinity. The comparison of the electrochemical activities show that a clear spinel structure with a high crystallinity enhances catalytic activity.

Different preparation methods (thermal decomposition, co-precipitation and a hydrothermal method) give nanoparticle size spinels with different particle size, surface area, crystallinity, stability and electrochemical activity. The comparison of three preparation methods suggests that spinel $MnCo_2O_4$ should be synthesised via co-precipitation method in order to produce material with a single phase, high crystallinity, high surface area, smaller particle size (up to 7 nm), high stability and the highest ORR activity.

To sum up, in comparing the relative effects of dopants (such as Ni, Mn) and preparation conditions/methods, the dopant effect is much more important for the overall performance of the spinels for the oxygen reduction reaction in alkaline media. The electrochemical performance of cobalt based Ni and Mn containing spinels could be further increased or developed if they can be fabricated with carbon based materials (such as nitrogen-doped reduced graphene oxide (N-rGO), carbon nanotubes (CNT) and carbon powder (XC-72R)) since carbon based materials not only increase conductivity but also help the dispersion of oxide materials to prevent agglomeration, which results in higher surface area and better accessibility of electrolyte to the surface area of metal oxides. However, stable carbon materials must be found that do not degrade at OER potentials, if the materials are to be used as bifunctional catalysts. Similarly, the effect of the $2e^-$ reduction of oxygen on the carbon materials would need to be suppressed or a facile co-catalyst included to achieve the $4e^-$ reduction.

Producing Ni and Mn based spinel type Co_3O_4 without any carbon based materials and investigating the oxygen reduction reaction mechanism at aforementioned spinels in alkaline media in details are another novelty of the work presented in this thesis. As already highlighted in previous chapters, the ORR activity of the carbon or carbon based materials (support $2e^-$ reduction) have been widely ignored in the literature.

For the future work, It could be worth to try some in-situ XAS studies especially of Co_3O_4 and $NiCo_2O_4$ before and after the oxidation/reduction peaks' potentials, which are observed at around 500 mV (*vs* Hg/HgO), since it is still not certain the exact oxidation states of the oxidation/reduction couple, which are widely assigned to Co(III/IV)/Ni(III/IV) couple in the literature.

6.1. References

1. C. Wei, Z. Feng, G. G. Scherer, J. Barber, Y. Shao-Horn and Z. J. Xu, *Adv. Mater.*, 2017, **29**.
2. P. W. Menezes, A. Indra, V. Gutkin and M. Driess, *Chem. Commun.*, 2017, **53**, 8018-8021.
3. W. Song, Z. Ren, S.-Y. Chen, Y. Meng, S. Biswas, P. Nandi, H. A. Elsen, P.-X. Gao and S. L. Suib, *ACS App. Mater. Interfaces*, 2016, **8**, 20802-20813.

Appendix: Figures

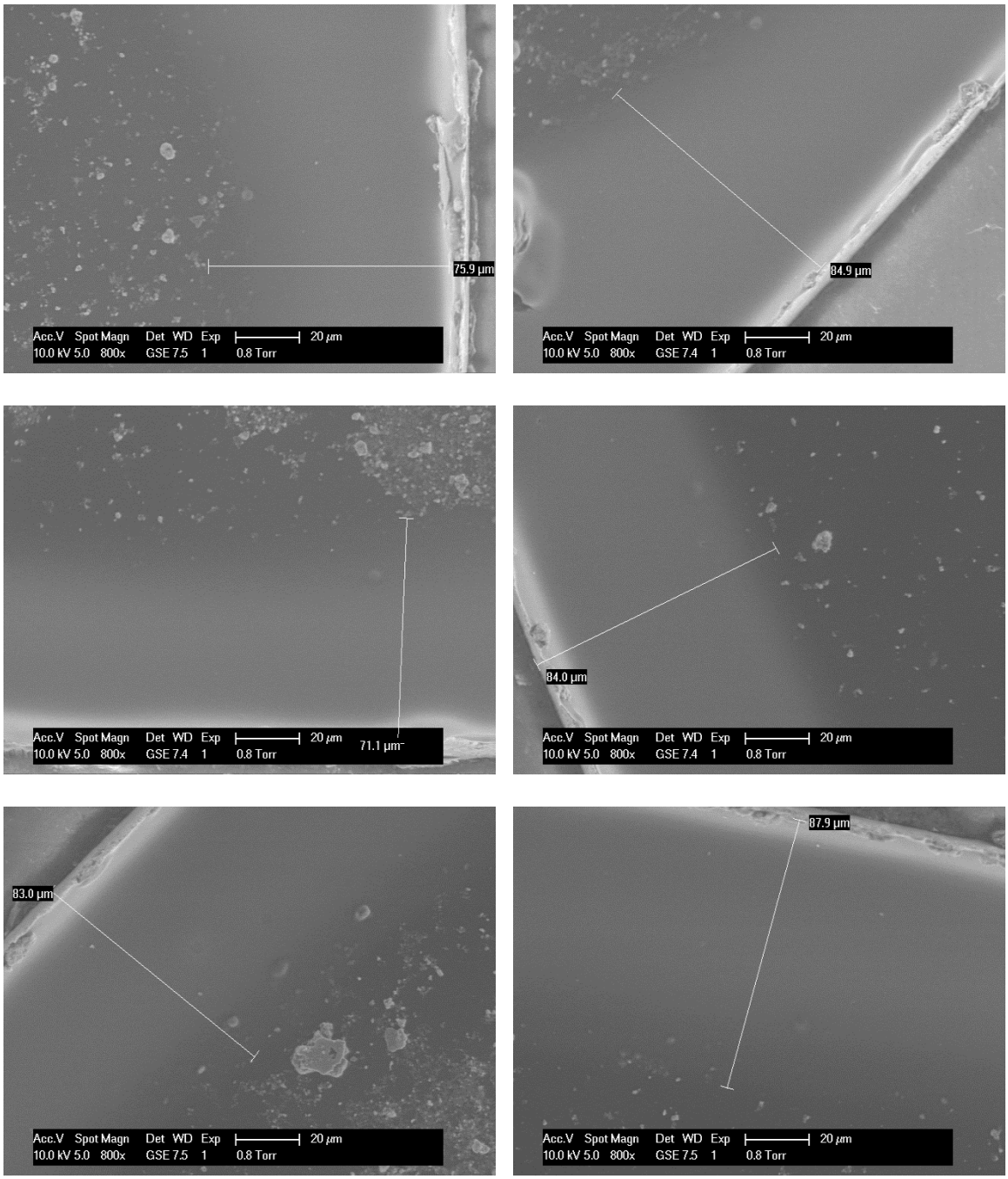

Figure A2.1. SEM images of $MnCo_2O_4$ coated GC electrode edges at 6 different points on the circumference.

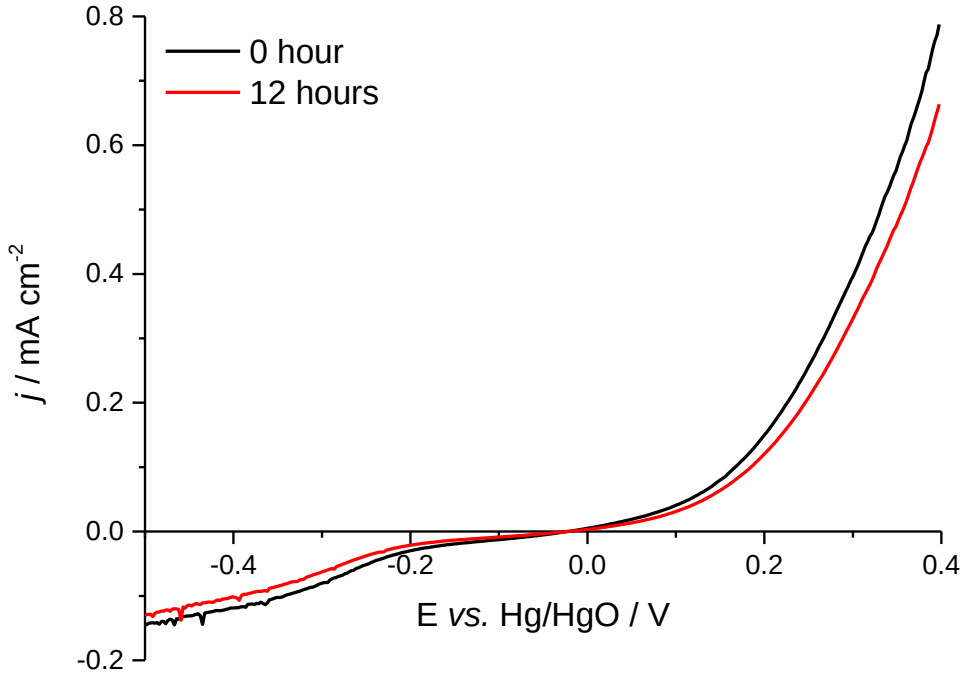

Figure A4.1. The voltammograms for the reduction and oxidation of ≈ 10 mM H_2O_2 in N_2 purged 1 M KOH at Co_3O_4 coated glassy carbon with electrolyte waiting times (0 and 12 hours). Temperature: 25 ^oC; Potential scan rate: 5 mV s^{-1}. For each measurement, 10 mM H_2O_2 in 1 M KOH was used from volumetric flask.